Overview of Advanced Gas Separation Technologies for Gasification-Based Energy Systems

Gary J. Stiegel
National Energy Technology Laboratory
U. S. Department of Energy
P.O. Box 10940
Pittsburgh, PA 15236

Jay Ratafia-Brown
SAIC
8301 Greensboro Dr.
McLean, VA 22102

Massood Ramezan
SAIC
P.O. Box 18689
Pittsburgh, PA 15236

INTRODUCTION

Gasification-based energy systems offer a stable, affordable energy supply for the nation, providing high-efficiency conversion and near zero pollutants, and flexibility in the production of a wide range of commodity and premium products. Perhaps just as important, flexible gasification systems provide for operation on low-cost, widely available feedstocks, such as coal, petroleum coke, and biomass. Building on current operating experience, gasification-based technologies can be refined and improved via application of advanced gas separation technologies that are being developed through DOE's programs. Improved gas separations involving oxygen (O_2), hydrogen (H_2), and carbon dioxide (CO_2) can lead to reduced capital and operating costs, as well as improvements in thermal efficiency and superior environmental performance.

Most of the current commercial gasification projects, as well as those planned for the future, are oxygen-blown and require cryogenic air separation units to provide large quantities of oxygen. These gasifiers allow for lower pressure operation, lower synthesis gas (syngas) volumetric flow rates, and easier adaptability to syngas cleanup systems, which helps reduce the size (and cost) of gas cleanup equipment and improves integration into complete gasification and combined cycle power systems. Unfortunately, the air separation unit can typically represent 12 to 15 percent of the total capital cost of a plant and requires a significant amount of auxiliary power for operation. Thus, air separation represents a major area of opportunity for both cost reduction and performance improvement, making it a key part of DOE's gasifier R&D program. DOE is currently sponsoring projects to develop Ion Transport Membrane Technology (ITM) and Oxygen Transport Membranes (OTM), both of which operate at high temperature and provide a high level of thermal integration with the gasification process. DOE studies indicate that they will offer substantial cost reduction compared with the cryogenic air separation methods now employed.

There is also increasing interest in gasification-based hydrogen production, as well as the capture of CO_2 to help reduce emissions of this climate change agent. Therefore, separation of the H_2 and CO_2 syngas constituents may become vitally important to future applications of gasification. These separations will be of increasing importance for integration with downstream processes, such as fuel cells and Fischer-Tropsch conversions, and producing gas compositions suited to these applications. Significant opportunities to improve upon current separation techniques can result from the use of advanced membrane technologies, and much of the work that DOE supports involves further developing membranes to be consistent with the temperature and pressure requirements of power plant applications, as well as required product specifications. Development of a high-pressure, non-membrane CO_2 separation technology is also being supported.

NETL's gas separation projects primarily support DOE's Vision 21 Program. Two industrial teams are focusing on advanced ceramic membranes for air separation and will begin their first major scale-up effort on the path to commercialization. Development of high temperature membranes for hydrogen separation continues, with two new industrial teams leading the effort. Another industry team has been developing palladium-based composite membrane reactor module for separation of hydrogen and carbon dioxide. This paper describes these technologies and associated R&D projects.

DOE's AIR SEPARATION MEMBRANE PROJECTS

The use of oxygen instead of air in gasification processes is currently burdened by: 1) the high cost of oxygen production, and 2) the loss of thermal efficiency inherent in the low temperatures of the current technology - cryogenic separation. In partnership with the DOE's National Energy Technology Laboratory (NETL), two industry teams are developing advanced, ceramic-based membranes that are well suited for thermal integration with the gasification cycles to achieve major cost reductions and efficiency improvements.

Mixed conductors, which transport both oxygen ions and electrons, can be operated in a pressure-driven mode, negating the need for the electrodes and external circuits that are required for purely ionic-type of conductors. The oxygen chemical potential difference across the membrane provides the driving force for oxygen transport. Oxygen atoms adsorb on the cathode (high oxygen partial pressure side of the membrane), and dissociate into atoms/ions as they pick electrons. These ions travel from cathode to anode (the low oxygen partial pressure side) by jumping through lattice sites and vacancies until they reach the anode side of the membrane. On the anode side, the oxygen ions give up their electrons to become atoms/molecules, which are then desorbed into the gas phase. Electrons from the anode side are carried through the membrane to the cathode side to complete the circuit. The rate of oxygen transport through such membranes is temperature sensitive, and can be very fast at high temperatures. Also, since the flux through the membrane is inversely proportional to the thickness, thin films can enable higher fluxes, leading to compact systems. Thus, the ability to produce pure oxygen at high permeation rates, combined with the thermal integration enabled by high temperature operation, results in significant benefits for integration with gasification-based power systems.

Ion Transport Membrane Technology (ITM) – Air Products and Chemicals, Inc.

ITM technology makes use of non-porous, mixed ion and electron-conducting ceramic membranes operating at high temperature, typically 80-900 ^{o}C. The oxygen ions and electrons flow countercurrent through the membrane, with the driving force for oxygen separation being the relative oxygen partial pressure gradient across the membrane. A thin-film, multi-layer membrane structure has been developed to support the pressure load imposed by gasifier operating conditions.

NETL's Ion Transport Membrane (ITM) Oxygen project will develop, scale-up, and demonstrate this technology for large-scale production of oxygen from air with the co-production of power, and for the integration of ITM Oxygen with IGCC and other advanced power generation systems. The R&D program is being conducted in three phases, with the goal being to cut the cost of oxygen production

by approximately one-third compared to conventional, competing technologies and demonstrate all necessary technical and economic requirements for commercial scale-up in the 2006 to 2008 time-frame. Phase I, initiated in October 1998, focused on materials and process R&D and the design, construction, and operation of a 0.1-TPD Technology Development Unit (TDU) to validate the ITM oxygen process concepts, ITM Oxygen integration schemes with IGCC and other advanced power generation systems, and obtain scale-up data. The work successfully addressed all technical and economic requirements for scale-up by reconfirming the economic benefits of ITM technology, a 30-45% reduction in capital cost; exceeding the target flux with a newly developed material by 25% over baseline; achieving an 8-fold increase in the monthly yield of membrane structures; and demonstrating over 2,300 hours of long-time performance and stability of thin-film membrane structures in several experiments.

The Phase II and Phase III activities will build upon Phase I results to further develop, scale up, and demonstrate the ITM Oxygen technology to an approximately 5-ton-per-day (TPD) design capacity sub-scale engineering prototype facility and a pre-commercial-scale demonstration facility approximating 25-TPD, and obtain materials, engineering, membrane fabrication, operating, performance, and economic data necessary for technology commercialization.

A recent study of IGCC economics, comparing the use of ITM Oxygen technology against a state-of-the-art cryogenic air separation unit (ASU), projects a 7% reduction in overall plant installed capital cost, a 7% improvement in power output, a 35% savings in the installed specific cost of the air separation unit compared to the cryogenic ASU, a 37% improvement in the power requirement of the oxygen plant, and a 2.2% improvement in the overall power plant efficiency.

The project team includes Air Products and Chemicals, Inc., Eltron Research, Inc., Ceramatec, Inc., ChevronTexaco Inc., Concept NREC Inc., McDermott International, Inc., The Pennsylvania State University, and the University of Pennsylvania.

Ceramic Oxygen Transport Membranes (OTM) - Praxair, Inc.

OTM technology is based on ceramic materials that can rapidly and selectively transport oxygen ions at high temperatures (600°C - 1000°C). NETL's OTM project is comprised of a three-year Phase I and two-year Phase II components. The goals are to advance critical technologies for the commercial deployment of OTMs for IGCC oxygen production to enable significant improvements in process economics, efficiency and environmental benefits. Phase I has been completed and has achieved a number of critical milestones. A new, high-performance material has been invented which greatly improves the mechanical properties of the OTM element while maintaining the superior flux performance of an earlier lead candidate. Composite OTM technology capable of high-performance, gas-tight composite OTM membranes capable of sustained operation at 900°C and high-pressure differential has been developed. These elements have demonstrated the production of >99% pure oxygen at fluxes 120% of commercial target in tests conducted at 900°C with a 275 psi pressure differential. A 1000 hr life test and >10 complete thermal cycles were demonstrated on such elements under simulated IGCC conditions with virtually no membrane degradation. Significant progress is also being made in scaling up the manufacturing of the elements. Seal technology has advanced to the point where leak rates are much below commercial target and adverse interactions with the OTM membrane are absent. A multi-element pilot reactor is operational and is being used to understand operational characteristics of the OTM reactor module and validate design concepts for scale-up.

Phase II activities, currently underway, includes advancing OTM reliability to ensure 10-year life, manufacturing of full-size elements for a pilot plant, development of critical components required for efficient thermal and power integration, assessment of advanced process integration concepts, economic modeling and business and marketing studies. This will culminate in the design, construction, and operation of a multi-element pilot reactor that is sufficiently large to confirm scale-up issues, and will feature the elements and design concepts anticipated in the commercial design. It will validate the engineering design basis, startup and shutdown protocols and demonstrate safety, and provide cost data to verify that economic targets are met when scaled to full size. The project team includes Praxair, Inc., and the University of Missouri, Rolla.

DOE's ADVANCED HYDROGEN SEPARATION MEMBRANE PROJECTS

Hydrogen separation in gasification-based systems can be a significant source of low-cost H_2 for use in refineries, as fuel for fuel cells, and for H_2 product gas. These techniques must be suitable for the rapid, selective removal of hydrogen from high-temperature, high-pressure syngas streams, while remaining resistant to chemical impurities such as sulfur. Various ceramic membranes, including both high- and low-temperature membranes, are being tested at laboratory-scale to obtain design and scale-up data.

Mixed-Conducting Dense Ceramic Membranes

Mixed-conducting membranes transport via ion and electron conducting mechanisms. Hydrogen separation is achieved in a non-Galvanic mode without the need for an external power supply to drive the separation, thereby offering potential economic advantages over existing technologies. The membranes are non-porous and therefore, are 100% selective to hydrogen. A hydrogen-permeable membrane must exhibit high electronic and protonic conductivities.

Composite membranes are being developed at Argonne National Laboratories (ANL) containing a metal phase dispersed in a ceramic phase. A preliminary test result using a composite has shown an hydrogen flux of 20 $cm^3/min\text{-}cm^2$ through a 40 micron thick membrane at 900°C using 100% H_2 as the feed gas.

Eltron Research is employing dense ceramic membranes based in part on Eltron-patented materials with a demonstrated ability for rapid proton and electron conduction. Eltron has prepared thick membrane materials that are greater than 95% dense and demonstrated hydrogen separation rates that are roughly 20% of the target (10 $ml/min/cm^2$), and nearly an order of magnitude higher than doped ceramic membranes. These composite materials have been prepared with distinct ceramic and metallic phases by precipitating metal onto a ceramic powder. A tubular-type design concept for this membrane is shown in Figure 1 below.

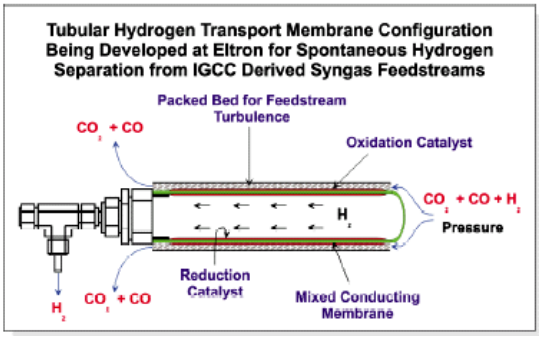

Figure 1

This project was initiated in October of 2000 and will conclude in September 2003 after construction and testing of a sub-engineering scale prototype separation unit. The project team includes Coors Tek, Sud Chemie, McDermott Technologies, and Argonne National Laboratory.

Ion Conducting Ceramic Membranes (ICCM) – ITN Energy Systems

A team led by ITN Energy Systems is pursuing a novel approach to hydrogen separation membrane technology based on Ion Conducting Ceramic Membranes (ICCM) where fundamental engineering material development is fully integrated into module fabrication designs by combining functionally-graded materials, monolithic module concepts and thermal spray manufacturing techniques. The membrane process will also result in a stream of concentrated, sequestration-ready carbon dioxide. (see Figure 2.) The membranes are composed of composites of a proton conducting ceramic and a second metallic phase to promote electrical conductivity.

Functional grading of the membrane components allows for the fabrication of individual membrane layers of different materials, microstructures, and functions directly into a monolithic module. Plasma spray techniques will be used for fabricating ICCM hydrogen separation modules inexpensively, yielding compact membrane modules amenable to large, continuous manufacturing techniques at low costs. The goal of the research program is to demonstrate industrially significant H_2 flux rates of 50 ml/min/cm^2 in a laboratory-scale prototype in the 600 ^oC -900 ^oC temperature range using thin film design. The project was initiated in October of 2000 and will conclude in April 2004 after construction and testing of a sub-engineering scale prototype separation unit. The project team includes Nexant Consulting, Praxair, Argonne National Laboratory, and Idaho National Engineering and Environmental Laboratory.

NETL Hydrogen Gas Separation Program

The overall goal of this project is to develop hydrogen gas separation technology for applications in both the DOE Fuels Program and the Gasification Program. Of particular emphasis are robust hydrogen separation membranes that are suitable for the rapid, selective removal of hydrogen from high-temperature, high-pressure gas streams, while remaining resistant to chemical impurities such as sulfur. This effort comprises four tasks: 1) membrane development, 2) membrane testing, 3) membrane reactor concepts, and 4) computational modeling.

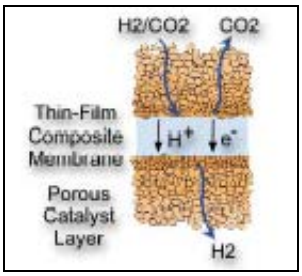

Figure 2 Separation of H2 from Syngas Stream Using an ICCM Membrane Technology

Project activities are centered around two NETL Hydrogen Membrane Testing (HMT) units. These units provide the unique capability of high-pressure, high-temperature hydrogen membrane flux measurements at conditions of up to 400 psi at 900 ^oC. The units can accommodate membrane sizes of 1/4" to 1/2" in both disk and tubular configurations, with a wide range of flow rates for process gases. In addition, they have the flexibility to be used for both membrane separation testing and membrane reactor testing.

CARBON DIOXIDE SEPARATION PROJECTS

Operation of high-pressure, oxygen-blown gasification systems with both high (~350 ^oC) and low (~200 ^oC) temperature shift reactors in series can yield a syngas stream primarily composed of H_2 and CO_2, with some residual CO and H_2O. The concentration of CO_2 in the shifted gas should be about 40%. This syngas composition provides an opportunity to use the previously described hydrogen-selective membranes to separate the H_2 and CO_2 into separate streams.

Palladium-Silver Alloy Composite Membrane - RTI

Research Triangle Institute (RTI) is developing an inorganic palladium-based composite membrane rector that is structurally stable under the fuel reforming conditions with a high selectivity and flux rate for hydrogen permeation through the membrane. The focus of this project is on developing thin palladium-silver alloy composite membranes with a thin protective noble metal coating. Preliminary results form simplified model simulations of the membrane reactor concept has shown hydrogen permeances range from 16 to 80 gmoles/m^2-min (40 to 180 scc/cm^2-min) at 500-600 ^oC temperature and 40 psi hydrogen partial pressure differential depending upon the film thickness and substrate pore size.

CONCLUSIONS

Advanced gas separation research offers the potential for substantial improvement in the thermodynamic, environmental, and cost performance of gasification based energy systems. A major DOE program objective is the development of cost-effective ceramic membranes that can provide substantial cost reduction for oxygen separation, compared to conventional cryogenic methods. Both ITM and OTM types of ion-conducting ceramic membranes offer significant potential to reduce costs by as much as 30 percent and are well suited to integration into plant systems. Based on the current schedules for DOE-sponsored projects, commercial scale-up of the oxygen separation membrane technologies is scheduled to occur in the 2006 – 2008 time frame.

Improved hydrogen recovery and CO_2 removal are also becoming important. Currently, the program is developing high-temperature ceramic membranes and palladium-based dense membrane for H_2 recovery from syngas streams, which can also serve to separate CO_2 when shift reactors are employed with oxygen-blown gasification systems. The hydrogen separation projects are currently operating at the laboratory-scale and further scale-up will depend upon performance results achieved in the current efforts.

For more information visit
http://www.netl.doe.gov/coalpower/gasification/

Particle-Film Structured Dense Dual-Phase Membrane

Weishen Yang[a,], Haihui Wang[a], Y.S. Lin[a,b]*

[a] State Key Laboratory of Catalysis, Dalian Institute of Chemical Physics, Chinese Academy of Sciences

Dalian 116023, China

[b] Department of Chemical Engineering, University of Cincinnati, OH 45221-0171, USA

Dual-phase composite inorganic materials, such as inorganic membranes consisting of an oxygen-ionic conducting ceramic phase and electronically conducting metal or ceramic phase, can find many applications including as membrane separator for oxygen production[1-4], solid oxide fuel cells for power generation[5], and membrane reactors for catalytic conversion of light hydrocarbons[6-11]. If both phases are percolated, such dual-phase membranes offer many unique properties unattainable by the separate single phase. For example, the oxygen permeability for an oxygen ionic conducting (OIC) ceramic membrane (ionic transference number close to one) or an electronic conducting (EC) inorganic membrane (ionic transference number close to zero) is very low because oxygen permeability is determined by the charged species with a lower mobility (conductivity). Combining the two phases would result in a dual-phase membrane with much higher oxygen permeability.

Several research groups[12-18] have reported preparation of dual-phase membranes containing an OIC phase of stabilized zirconia or bismuth oxides and an EC phase of noble metals, such as Ag, Pd. The structure of these dual-phase membranes is defined by random packing of particles of both OIC and EC phases. This structure gives a percolation threshold for the expensive noble metal phase of about 40%, i.e., at least 40 vol% of the electronic conducting phase is required in order to obtain a dual-phase membrane with continuous metal and ceramic phases. This renders the dual-phase membranes too expensive for practical application. Furthermore, the structure of packing particles of two phases of very different properties presents a compatibility issue making such composite membrane mechanically unstable under the conditions of swinging temperature and oxygen pressure.

Kim and Lin [13] reported preparation of dual-phase membrane with an OIC phase formed by close packing of yttria-stabilized-zirconia particles (YSZ) and a continuous phase of Pd as a film covering YSZ particles or filling in the interparticle space of the YSZ phase. They first prepared a mesoporous YSZ membrane by the sol-gel method, and then coated Pd onto the grain surface of YSZ particles by dip-coating and solvent evaporation. Though the Pd phase becomes continuous at low Pd loading they could not obtain a dense dual-phase membrane for effective oxygen transport. In this communication, we report a new structure of dense dual-phase membrane and its preparation method. This new dual-phase membrane consists of an OIC ceramic phase defined by compact packing of OIC ceramic particles and a three dimensional film of an EC phase covering the surface (or grain boundary) of the OIC ceramic particles. This dual-phase membrane requires much lower loading of the EC phase and may also offer improved chemical and mechanical stability.

The primary idea for the formation process of this dual-phase membrane and its structure is shown in Scheme 1 in which the gray particles are an OIC phase and the black one an EC phase. The initial green-body of the dual-phase membrane includes an OIC phase and an EC phase with different but close melting points. It is preferred that the more expensive phase has a lower melting point. The green-body containing particles of two phases are sintered at a temperature between the two melting points. As shown in Scheme 1, the small particles (Scheme 1a) of the OIC-Phase are sintered together to form connected larger grains with clear grain boundaries (Scheme 1b) because the sintering temperature is lower than, but close to, its melting point. At same time, the EC-phase (black one in Scheme 1a) becomes molten and spread over the grain surface of the larger EC particles. Finally, the sintered grains of the OIC-phase develop to a dense bulk particle and the liquid EC-phase forms a continuous three-dimensional film running through the grain-boundaries of the connected OIC phase, as shown in Scheme 1c. Both the EC and OIC phases are expected to be percolated.

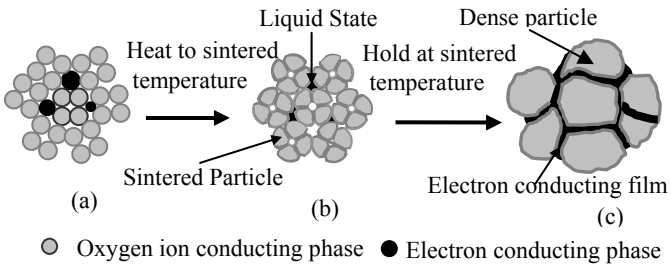

Scheme *1* schematic illustration of structure and formation process of the dual-phase membrane

To verify this concept, we selected $Ba_{0.5}Sr_{0.5}Fe_{0.2}Co_{0.8}O_{3-\delta}$ (BSCF)[3] and $La_{0.15}Sr_{0.85}Ga_{0.3}Fe_{0.7}O_{3-\delta}$ (LSGF)[19] as the OIC and EC phases respectively. BSCF is a mixed oxygen ionic and electronic conductor with electronic-conductivity much higher than the oxygen ionic conductivity[3]. In contract, LSGF developed recently by Eltron[19] exhibits very high oxygen ionic conductivity, low electronic conductivity, and good chemical stability in a reducing atmosphere. But it has very low electronic conductivity and therefore offers very low oxygen permeability. More importantly, the melting point of LSGF (~ 1250°C) is higher than, but close to, that of BSCF (~ 1180°C). We expected that a dual-phase membrane containing a dense LSGF phase and a thin three-dimensional film of BSCF could be prepared from the powders of these two ceramics.

Experimentally, we prepared dual-phase LSGF-BSCF composites by mixing LSGF powder[20] with BSCF powder[3] at a volume ratio of 12.8:1. The powder mixture was ball-milled, pressed into disk-shaped membrane, and then sintered in stagnant air at 1200°C for 10 hours (with a heating and a cooling rate of 1.5°C/min). Low magnification SEM (JEM-5600 LV) analysis of the two dimensional surface of the dual-phase membrane clearly shows a two-dimensional view of the membrane surface characterized by a continuous netlike "wire" running between the boundaries of many grains of about 30-50 μm in size, reassembling the schematic shown in Scheme 1c.

*Corresponding author. Tel: +86-411-4379073; Fax: +86-411-4694447. E-mail address: yangws@dicp.ac.cn (W.S.Yang)

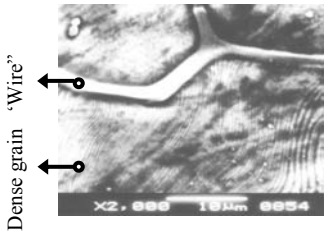

Figure 1 SEM picture of dual phase membrane

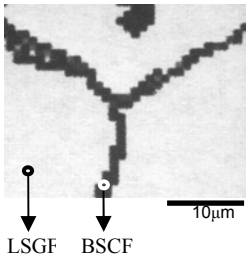

Figure 2 EPMA picture of dual phase membrane

Figure 1 is a higher magnification SEM micrograph of the top view of the dual-phase membrane. This figure shows a section of the continuous netlike "wire" running in the boundaries of three larger ceramic grains. It is important to note that the continuous netlike "wire" is very fine (only 2.5 μm) and uniform throughout the membrane surface observed. Composition of the surface of the dual-phase membrane analyzed by electron probe microanalysis (EPMA, Shimadzu-1600) shows different compositions for the netlike "wire" region and the region of the grains, as shown in Figure 2. The EPMA picture of the two-dimensional view of the dual-phase membrane is very similar to the SEM picture in Figure 1, i.e., a continuous netlike "wire" (black region) running along the boundary of bulk grains (white region). Quantitative EMPA analysis shows only the elements of La, Sr, Ga, Fe, O in the white region, and Ba, Sr, Co, Fe, O in the black region, confirming that the white grains are the LSGF phase and the netlike "wire" is the BSCF phase.

The LSGF-BSCF composite membrane was mechanically fairly strong. It was hermetic to non-oxygen containing gas such as nitrogen or helium. The oxygen permeation flux of the dual-phase LSGF-BSCF membrane was measured in air/helium gradient, and the results are given in Figure 3. Oxygen permeation flux for pure LSGF and BSCF membranes, after being multiplied by the percentage of the phase in the dual-phase composite (92.8% for LSGF and 7.2% for BSCF), are also given in Figure 3 for comparison. As shown the oxygen permeation flux for the dual-phase composite membrane is about one order of magnitude larger than that for the membrane of either pure phase. Such substantial increase in oxygen permeation indicates formation of both percolated phases in the composite membrane and effective electronic transport between the LSGF and BSCF phases and within the BSCF phase.

In conclusion, the above experimental results confirmed successful

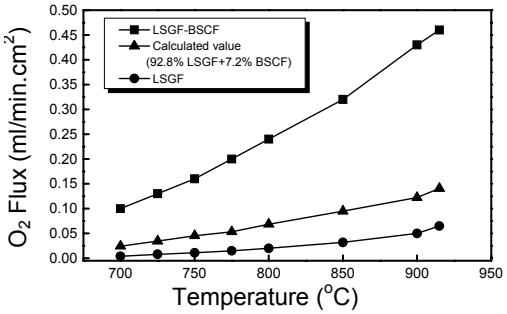

Figure 3 Comparison of oxygen permeation flux at different temperature for the dual-phase membrane with the pure phase membrane.

synthesis of a dual-phase LSGF-BSCF composite membrane with a structure defined by the percolated packing of oxygen ionic conducting LSGF grains with a three-dimensional thin electronic conducting BSCF film running between the boundaries of the connected LSGF grains. The film phase is percolated at a volume percent as low as 7%. Since the majority phase is the chemically more stable LSGF and the second phase is made of a mechanically and chemically compatible BSCF, rather than a metal, the dual phase composite membrane not only exhibit a higher oxygen permeability but also may offer better chemical/mechanical stability than the highly oxygen permeable BSCF membrane. After their structure is further optimized and chemical and physical properties are better understood, the dual-phase membranes will offer many applications including in membrane oxygen separators, fuel cells, and membrane reactors. The concept of the dual-phase membrane and its synthesis method can also be extended to composite materials for other applications.

Acknowledgment. The authors gratefully acknowledge financial supports from the National Advanced Materials Committee of China (Grant No.715-006-0122) and the Ministry of Science and Technology, China (Grant No. G1999022401).

References

(1) Thorogood, R.M.; Srinivasan,R.; Yee,T.F.; Drake,M.P. *U.S.Patent*. 1993, 5240480
(2) Qiu, L.; Lee, T.H.; Liu, L.M.; Yang, Y.L.; Jacobson, A.J. *Solid State Ionics.* 1995, 76, 321
(3) Shao, Z.P.; Yang, W.S.; Cong, Y.; Dong, H.; Tong, J.H.; Xiong, G.X. *J Membr Sci.* 2000, 172, 177
(4) Zeng, Y.; Lin, Y.S.; Swartz, S.L. *J Membr Sci.* 1998, 150, 87
(5) Minth, N.Q. *J.Am.Ceram.Soc.* 1993, 76(2), 563
(6) Balachandran, U.; Dusek, J.T.; Mieville, R.L.; Poeppel, R.B.; Kleefish, M.S.; Pei, S.; Kobylinski, T.P.; Faber, J.; Bose, C.A. *Appl. Catal.A:General.* 1995, 133, 219
(7) Elshof, J.E.; Bouwmeester, H.J.M.; Verweij, H. *Appl Catal A: General.* 1995, 130, 195
(8) Xu, S.; Thomson, W.J.; *AIChE J*. 1997, 43, 2731
(9) Dong, H.; Shao, Z.P.; Xiong, G.X.; Tong, J.H.; Sheng, S.S.; Yang, W.S. *Catal Today*. 2001, 67, 3
(10) Zeng, Y.; Lin, Y.S. *J Catal.* 2000, 193, 58
(11) Tsai, C.Y.; Dixon, A.G.; Moser, W.R.; Ma, Y.H. *AIChE J.* 1997, 43, 2741
(12) Kim, J.; Lin, Y.S. *J Membr Sci*., 2000, 167, 123
(13) Kim, J.; Lin, Y.S. *Ind. Eng. Chem. Res*., 2000, 39, 2124
(14) Chen, C.S.; Kruidhof, H.; M.Bouwmeester, H.J.; Verweij, H.; Burggraaf, A.J.; *Solid State Ionics* 1997, 99, 215.
(15) C.S.Chen, B.A.Boukamp, H.J.M.Bouwmeester, G.Z.Cao, H.Kruidhof, A.J.A.Winnubst, A.J.Burggraaf, *Solid State Ionic.* 1995, 76, 23
(16) Shen, Y.S.; Liu, M.; Taylor, D.; Bolagopal, S. in Proceedings of the 2nd international Symposium on ionic and Mixed Conducting ceramics Vols94-112 (Eds: T.A.Ramanarayanan, W.L. Worrell, H.L.Tuller) *The Electrochemical Society*. Penningeon, NJ, 1994, P. 574
(17) Mazanec, T.J.; Cable, T.L.; Fryer, J.G. *Solid State Ionics* 1992,53-56, 111
(18) Mazanec, T.J.; *Electrochem.Soc.Proc.* 1996, PV95-24, 16.
(19) Schwartz, M.; White, H.James.; Sammells, F.A. *International Patent* WO 1999, 99/21649
(20) Cong, Y.; Shao, Z.P.; Yang, W.S.; Xiong, G.X.; Lin, L.W. *Science in China B*. 2001, 44, 294

ITM Oxygen Membrane Performance and Properties

M. Watson[1], P. Armstrong[1], M. Carolan[1], R. Cutler[2], J. Gordon[2], D. Shelleman[3], R. Tressler[3]

[1]Air Products and Chemicals, Inc.
7201 Hamilton Boulevard
Allentown, PA 18195-1501

[2]Ceramatec, Inc.
2425 South 900 West
Salt Lake City, UT 84119

[3]Department of Materials Science and Engineering
The Pennsylvania State University
110 Steidle Bldg.
University Park, PA 16802

Introduction

Ion Transport Membranes (ITMs) are ceramic materials that conduct oxygen ions at elevated temperatures. The ITM Oxygen process, in which an ITM is used to separate high-purity oxygen from high-pressure air, (Figure 1) has the potential for significant advantages when integrated with power generation cycles. The separation process occurs under high temperature and pressure and places severe demands on the performance and property requirements of the ITM Oxygen material. Air Products and Chemicals has joined with the US Department of Energy, Ceramatec, Penn State University and other partners to develop, scale-up and commercialize this technology.

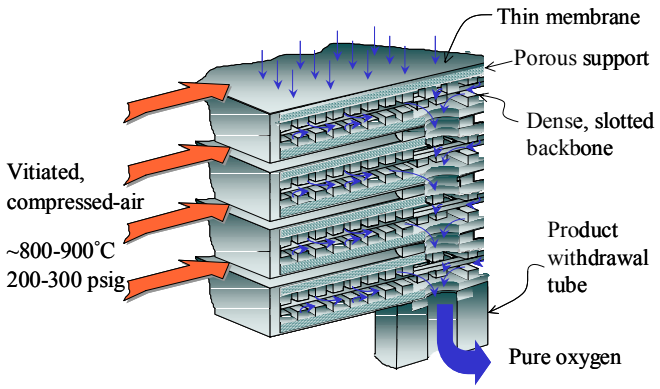

Figure 1. Section of planar membrane modules showing functional layers and process flows.

ITM Oxygen is a pressure-driven process, and the membrane separates oxygen by conducting oxygen ion vacancies from the low-pressure permeate side of the membrane to the high-pressure feed side, causing a counter flow of oxygen anions. Under isothermal conditions, the steady state oxygen flux, N, can be expressed as:[1]

$$N = \frac{D}{4VL}\int_{\ln(P'')}^{\ln(P')} \delta\left(\ln(P)\right)\cdot\partial\left(\ln(P)\right)$$

where V is the material molar volume, D is the vacancy diffusion coefficient, L is the thickness of the separating layer, and δ is the vacancy concentration, expressed as a function of the solid-state oxygen partial pressure, $\ln(P)$, integrated between the feed and permeate oxygen partial pressures, P' and P'', respectively. The oxygen flux is inversely proportional to the separating layer thickness, L, and proportional to the thermodynamic driving force for separation, which is the integrand in the above equation.

Experimental

Membrane and Sample Fabrication. ITM powder processing is carried out by Ceramatec, Inc., and is produced by calcining oxides and carbonates of the cationic species. The calcined powders are milled and mixed with binder/plasticizer/solvent to form a slurry suitable for tape casting. Samples suitable for creep testing are cut from green tape. The membrane consists of multiple functional layers, shown in Figure 1, which are featured and laminated together. The green wafer is then sintered, and one or more wafers are joined to a manifold tube to create an ITM Oxygen module, (Figure 2).

The progression in membrane area from 1996 – 2001 is shown in Figure 2. The disk shaped membrane, first tested in 1996, has approximately 0.9% of the area of a single commercial wafer. Each wafer in the module built in 2001 is commercial scale.

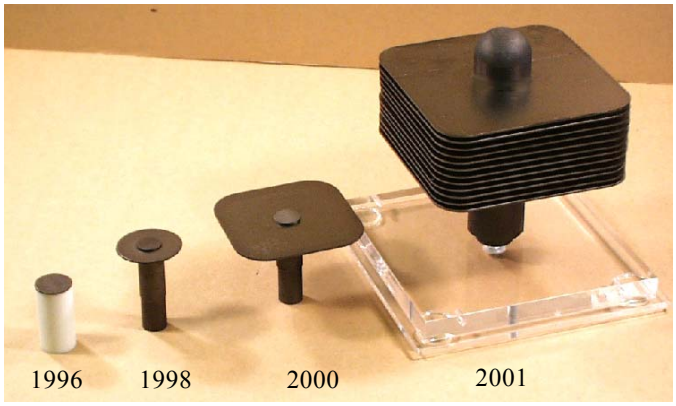

Figure 2. Size-progression of ITM Oxygen modules from 1996 – 2001.

Creep Testing. Rectangular bars were cut from green tape and sintered to full density. Four point flexural creep testing was carried out at Penn State University using standard methods,[2] to ensure the material is able to withstand extended exposure to the high-pressure, high-temperature operating environment without excessive plastic deformation.

Membrane Testing. The ITM wafer is flux tested inside a heated pressure vessel. Hot, pressurized air passes on the outside of the membrane while pure oxygen is collected in the manifold tube, as shown in Figure 1. The flux is measured as a function of feed-side pressure, permeate-side pressure, and thickness of the outermost dense layer of the wafer.

Results

The results presented in this section are given in terms of units relative to the commercial targets. For example, relative flux is the ratio of measured flux to commercial flux target; relative thickness is the ratio of measured thickness to the commercial target for the thickness of the outermost dense layer, and so forth. This approach

[1] H.J.M Bouwmeester and A.J. Burggraaf, "Dense Ceramic Membranes For Oxygen Separation," Chapter 14, pp 527, in P.J. Gellings and H.J.M. Bouwmeester (Editors), *CRC Handbook of Solid State Electrochemistry*, CRC Press, Boca Raton, Florida, 1997.

[2] D. C. Crammer, and D. W. Richerson, *Mechanical Testing Methodology for Ceramic Design and Reliability*, Marcel Dekker, Inc. New York, 1998, p. 171-222

enables the comparison of a number of data sets that have been generated under different experimental conditions.

The effect of the thickness of the outermost dense layer on membrane performance is shown in Figure 3. The membrane performance is expressed in terms of relative flux normalized to relative driving force. As expected from the equation describing flux, (flux)/(driving force) is proportional to the inverse of thickness of the separating layer thickness, and Figure 3 shows that the commercial flux target can be reached and exceeded when the commercial membrane layer thickness is used.

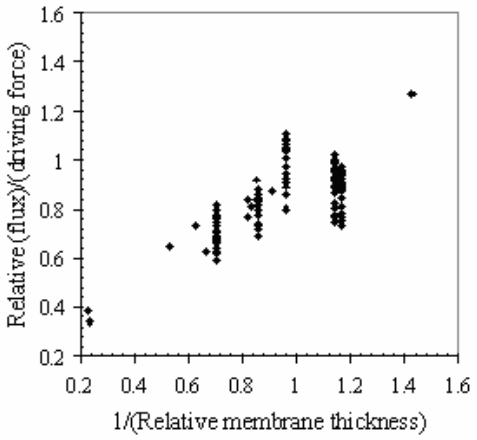

Figure 3. Effect of membrane layer thickness on performance.

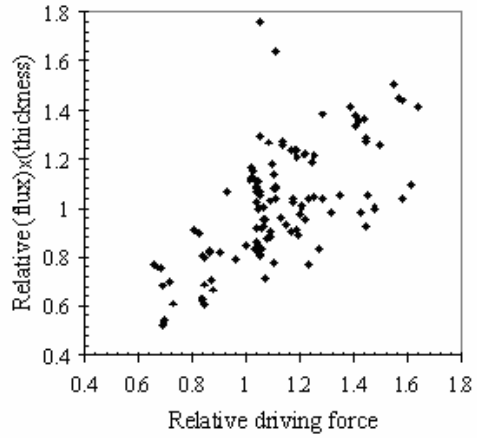

Figure 4. Effect of driving force on performance.

The effect of thermodynamic driving force on the membrane performance is shown in Figure 4. The membrane performance is expressed as relative flux multiplied by the thickness of the dense separating layer. As expected from the equation above (flux)•(thickness) is proportional to the driving force for separation, and Figure 4 shows that the commercial flux target can be reached and exceeded when the commercial driving force is used.

It is important to check that the scale-up from a laminate to wafer module geometry does not negatively impact the membrane performance. During the scale-up, the driving force was increased from ambient pressure to a full commercial pressure gradient; and the thickness of the separating layer decreased to the commercial target. Figure 5 shows that relative flux of the membrane is unchanged by the different geometry. In fact, the sub-scale wafer flux lies within a tighter flux band, which may indicate a more controlled ceramic process.

The scale up of the membrane fabrication and testing processes has occurred simultaneously with the materials development effort. One important property of the membrane material is the ability to withstand extended exposure to a high-pressure, high-temperature environment without excessive plastic deformation, or creep. Figure 6 shows that the latest generation of membrane material (Generation 2) is an order of magnitude more creep resistant than an earlier generation of material (Generation 1).

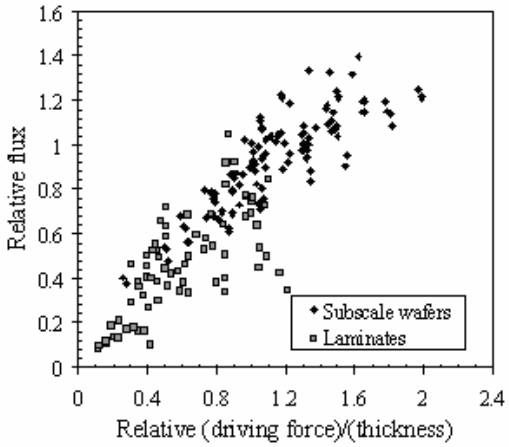

Figure 5. Effect of relative membrane geometry on performance.

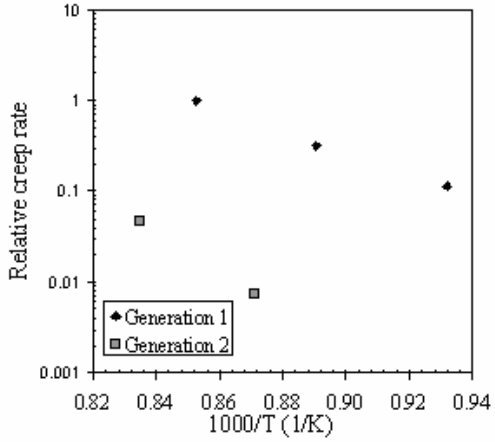

Figure 6. Improvement in creep properties with material development.

Conclusions

The commercial flux target can be reached and exceeded when commercial driving force conditions and separating layer thickness are used. The latest generation of membrane materials are an order of magnitude more creep resistant than an earlier generation.

Disclaimer

A significant portion of this report was prepared by Air Products and Chemicals, Inc. pursuant to a Cooperative Agreement partially funded by the United States Department of Energy, and neither Air Products and Chemicals, Inc. nor any of its contractors or subcontractors nor the United States Department of Energy, nor any person acting on behalf of either:

This paper was written with support of the U.S. Department of Energy under Contract No. DE-FC26-98FT40343.

Effects of ZrO_2 addition on structure, oxygen permeation and stability of $SrCo_{0.4}Fe_{0.6}O_{3-\delta}$ oxides

Li Yang, Liang Tan, Xuehong Gu, Lixiong Zhang, Nanping Xu

Membrane Science & Technology Research Center,
Nanjing University of Technology, Nanjing 210009, P. R. China

Introduction

Mixed-conducting oxides have received considerable attention as possible candidate materials for application in oxygen separation membranes and catalytic membrane reactors. Although the bright future of electronic conducting membrane reactor in the POM reaction, the commercial application of mixed-conductive membranes is often limited by specific disadvantages of the membrane materials known at the present time, for instance, the order-disorder phase transition in the oxygen sublattice. Such a transition is characteristic of most perovskites derived from the strontium cobalites $SrCoO_{3-\delta}$.[1] In addition, a high oxygen chemical potential gradient in the $Sr(Co, Fe)O_{3-\delta}$ type membranes results in a crystal lattice mismatch inside the ceramic, leading to the fracture of the membranes. [2] Thus, the disadvantages of $SrCoO_{3-\delta}$ based ceramics create a necessity to develop new materials and optimizing known materials for oxygen separation and catalytic membrane reactors.

Recently, a novel perovskite-related oxide membrane, which was prepared by addition of 9 wt% ZrO_2 into $SrCo_{0.4}Fe_{0.6}O_{3-\delta}$ (SCFZ), has been reported in our laboratory.[3] The oxygen nonstoichiometry, transport properties and structure stability of SCFZ have been investigated. [4] It showed that the stability of $SrCo_{0.4}Fe_{0.6}O_{3-\delta}$ (SCF) was greatly improved with the addition of ZrO_2, while the oxygen permeability was slightly reduced. The aim of the present study was to investigate the effect of various amounts of ZrO_2 additions on structure, oxygen permeation and stability of SCF in an attempt to search for a suitable composition exhibiting high oxygen flux as well as structural stability in reducing atmosphere.

Experimental

ZrO_2-$SrCo_{0.4}Fe_{0.6}O_{3-\delta}$ (SCFZ) powders with the ZrO_2 additions of 0, 1, 3, 5, 7 and 9 wt% were prepared by conventional solid-state reaction. The required amounts of $SrCO_3$, Co_2O_3, Fe_2O_3 and monoclinic ZrO_2 were mixed and milled for 24 h followed by calcination in air at 1223 K for 4 h. The calcined powders were pressed into disks of 16 mm in diameter with an oil pressure of 200 MPa and then sintered in air at 1473 K for 5 h to form the dense membranes. X-ray diffraction (XRD) was collected on a Bruker D8 Advance diffractometer with Cu Kα radiation. Scanning electron microscopy (SEM) and energy dispersive X-ray (EDX) analysis was performed using a JSM 6300 scanning microscope equipped with a Sigma energy dispersive X-ray microanalysis system. SEM images were recorded in back-scattered electron modes.

Oxygen permeation measurements were performed using a permeation apparatus reported previously. [2] The membrane samples were sealed by two gold rings. Before beginning of the oxygen permeation measurement, the assembly was heated to 1313 K and held for 4 h to form the bonding. One side of the membrane was exposed to air (P_h = 0.209 atm) at a flow rate of 200 ml min^{-1} while the other side was exposed to a lower oxygen partial pressure (Po_2) that was controlled by regulating the He flow rate by mass flow controllers (Models D07/ZM, Beijing Jianzhong Machine Factory, China). A gas chromatograph (GC, Model Shimabzu GC-7A) equipped with a 5 A molecule sieve column was connected to the exit of the sweep side. The amount of oxygen passing through the membrane was calculated from the measured outlet flow rate and the oxygen content.

Results and Discussion

Crystal structure characterization

XRD patterns of the as-synthesized powders with ZrO_2 additions of 1-9% showed the existence of SCF and $SrZrO_3$ phase. But for the sintered membrane (Figure 1), the second phase $SrZrO_3$ was reabsorbed into the perovskite for the compositions with ZrO_2 additions ≤ 7 wt%. Small amount of Co_3O_4 was also detected by XRD analysis. The formation of Co-rich phase may attribute to two parts: the segregation of Co at high temperature[5] and the precipitate of Co to maintain the stoichiometry because of Zr dissolution in SCF as will be discussed below. The presence of these phases in the samples was confirmed by SEM-EDX analysis for the sintered membranes. The results are shown in Figure 2 taking 1% and 9% ZrO_2 addition as examples. Besides, EDX analysis performed on the region corresponding to the SCF phase showed the presence of Zr, indicating the dissolution of Zr in SCF phase took place. The ratio between Sr, Co, Fe, and Zr in five membranes with ZrO_2 addition from 1% to 9% were1:0.48:0.84:0.027, 1:0.42:0.77:0.067, 1:0.38:0.75:0.099, 1:0.51:0.77:0.15, 1:0.38:0.76:0.19, respectively, indicating Zr content in SCF phase increased directly with amount of ZrO_2 additions.

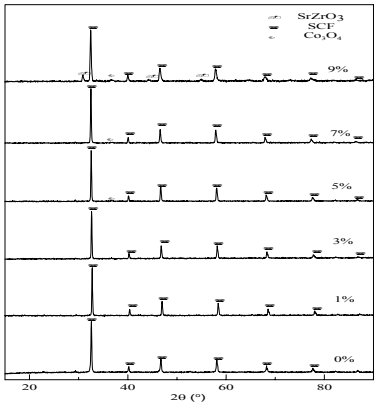

Figure 1. XRD patterns of sintered membranes.

Unit cell dimensions for SCF phase calcined at 1473 K with various amount of ZrO_2 additions are shown in Figure 3. The expanded lattices of SCF phase were found for powders with the addition of ZrO_2 and the lattice parameters increased directly with amount of ZrO_2 addition. Increase of lattice parameter of SCF phase with increasing amount of ZrO_2 addition in these systems could be due to increasing amount of Zr dissolution in B site of SCF phase as indicated by the SEM-EDX analysis. The larger ionic radii of dopant ion Zr^{4+} (0.84 Å) in comparison to the host ions Fe^{3+} (0.65 Å) and Co^{3+} (0.61 Å) resulted in an expanded SCF lattice.

Effect of amount of ZrO_2 addition on phase stability

To study the phase behavior under reducing atmospheres, SCFZ membranes with various amount of ZrO_2 additions were crushed and annealed in helium at 1123 K for 3 h and then applied for XRD analysis. The results are shown in Figure 4. Comparing with the XRD patterns of the fresh powders shown in Figure 1, we could see that the crystal structure of SCF had changed from cubic phase to an oxygen-vacancy ordered, orthorhombic phase Sr_2CoFeO_5. Structure stability of the materials seemed improved with increasing amount of ZrO_2 addition due to increasing amount of Zr dissolution in SCF phase, and when ZrO_2 addition was ≥ 3%, samples could maintain their structure in reducing atmospheres.

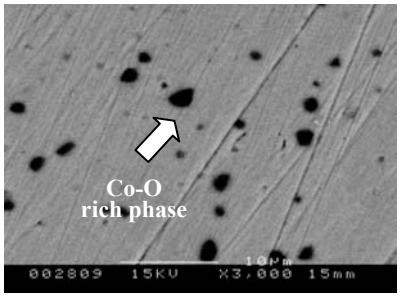

(a)

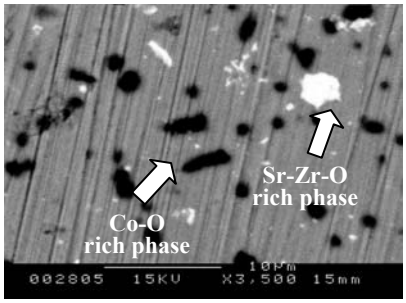

(b)

Figure 2. Back-scattered electron SEM images of membranes for ZrO_2 additions with (a)1%, (b)9%.

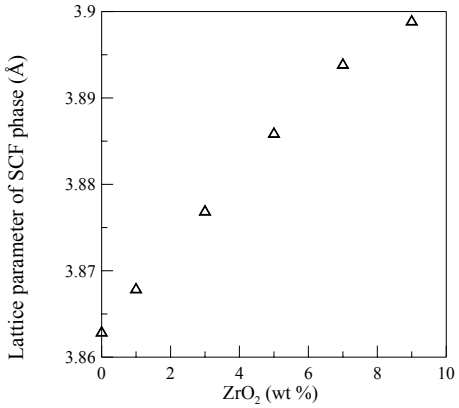

Figure 3. Unit cell dimensions for SCF phase calcined at 1473 K with various amount of ZrO_2 additions.

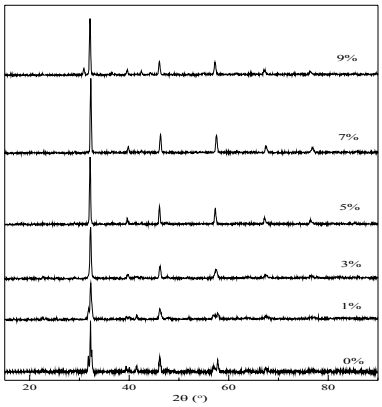

Figure 4. XRD patterns of SCFZ membranes annealed in helium at 1123 K for 3 h.

3.3. Effect of amount of ZrO_2 addition on oxygen permeation

The temperature dependence of oxygen flux through SCFZ membranes is shown in Figure 5 for the ZrO_2 additions of 0, 1, 3, 5, 7 and 9 wt%. The flow rate of He was controlled at 30 ml/min. The oxygen flux was found to decrease monotonically with the increasing amount of ZrO_2 addition due to the more amount of Zr dissolution in SCF phase. Solid solution of Zr in B sites of SCF increased the M-O bonding energy and reduced the concentration of oxide ion vacancies, both leading to a decrease in the oxygen permeability.

Another factor for evaluating the oxygen permeability of the membrane is the activation energy for oxygen permeation. As shown in Figure 5, two activation energies for oxygen permeation in the range of 973-1223K were observed for the compositions with ZrO_2 additions <3%, which was related to the order-disorder transition of oxygen vacancies.[1] In contrast, single activation for oxygen permeation was observed for samples with ZrO_2 addition >3%. The results were in accordance with the XRD analysis of the annealed samples shown in Figure 4. From the dependence of stability and oxygen permeability on the amount of ZrO_2 addition described above, the optimum ZrO_2 addition to greatly improve the structure stability without deleteriously affecting the oxygen permeability has been identified as 3 wt %.

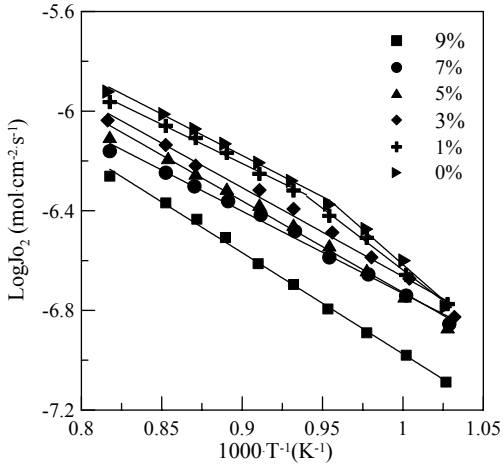

Figure 5. The Temperature dependence of oxygen permeation flux through SCFZ membranes with various ZrO_2 additions.

Acknowledgment

This work is supported by the National Natural Science Foundation of China (NNSFC, No. 20125618) and the Key Laboratory of Chemical Engineering and Technology of Jiangsu Province.

References

1.Kruidhof, H., Boumeester, H. J., Doorn, R. H. E. v., Burggraaf, A. J. *Solid State Ionics* **1994**, ***63-65***, 816-822.

2. Pei, S., Kleefisch, M. S., Kobylinski, T. P., Faber, J., Udovich, C. A., Zhang-Mccoy, V., Dabrowski, B., Balachandran, U., Mieville, R. L., Poeppel, R. B. *Catal. Lett.* **1995**, ***30***, 201-212.

.3. Li, S. G., Jin, W. Q., Huang, P., Xu, N. P., Shi, J., Hu, Z. C., Payzant, E. A., Ma, Y. H. *AIChE J.*, **1999**, ***45***, 276-284.

4. L. Yang, X.H. Gu, L. Tan, W.Q. Jin, L.X. Zhang, N.P. Xu, *Ind. Eng. Chem. Res.* **2002**, *41*, 4273-80.

5. Takeda, Y., Kanno. R., Takada, O., Yamamoto, O., Takano, M., Bando, Y. *Z. Anorg. Allg. Chem.*, **1986**, *9-10*, 259-263.

OXYGEN TRANSPORT KINETICS IN MIXED IONIC AND ELECTRONIC CONDUCTING MEMBRANE MATERIALS

Allan J. Jacobson, Susan Wang and Jiho Yoo

Department of Chemistry, University of Houston, Houston, TX

Introduction

Mixed conducting oxides with high oxygen ion conductivities have potential application in membrane reactors that can produce synthesis gas ($CO + H_2$) by direct conversion of hydrocarbons such as methane (1, 2). A number of perovskites (1-7) and non-perovskite oxide materials (8-10) have been evaluated for membrane reactors. Many of these compositions suffered from poor stability due to phase changes and differential thermal expansion in low oxygen partial pressures. At the present time, iron based compositions are the materials of choice.

The performance of mixed ionic and electronic conducting oxides (MIECs) in oxygen separation membranes is related to the oxygen transport kinetics that include contributions from the surface oxygen exchange rate at the gas-solid interface and oxygen diffusion within the bulk material. For MIEC oxides, electrical conductivity relaxation (ECR) is convenient technique with which to study the kinetics. By analyzing the time dependence of the relative change of the conductivity after an abrupt change in the ambient pO_2, the chemical diffusion coefficient and the surface exchange coefficient can be obtained.

The application of ECR to investigate and compare the oxygen transport kinetics of several perovskite oxide materials with the general composition $(La,Sr)(M,M')O_3$ (M = Fe, Co and M' =Cr, Ga, Co) is described. The long-term stability and the effects of CO_2 on the oxygen transport, which are concerns in practical applications, are discussed for the specific case of $La_{0.2}Sr_{0.8}Fe_{0.8}Cr_{0.2}O_3$.

Experimental

Samples. Sample powders were obtained either from Praxair Specialty Ceramics, or prepared in house by either conventional solid-state methods or by self-propagating high temperature synthesis (11). Phase purity was determined by powder X-ray diffraction and by electron microprobe analysis. Dry powder was pressed into a cylindrical shape by cold isostatic pressing at 40,000 psi. Thin disks were cut using a diamond saw and sintered in air with heating and cooling rates of 1 ºC/min. The sintered disks typically had a density of >95% of the theoretical density. In typical experiments, rectangular samples were used for conductivity relaxation experiments. These were cut from the sintered disks and wound with 4 gold wires (0.025mm, Alfa), which serve as electrodes.

Electrical Conductivity Relaxation. The theory of ECR of MIEC oxides has been described previously (12). Model calculations show that a square bar geometry gives better sensitivity than a thin plate (13). When the ratio of the length to the width is greater than ~10, the sample can be approximated as infinitely long. Analysis of the transients, gives D_{chem} and k_{chem}, the transport parameters measured in a chemical process. They are related to the equilibrium values for MIEC oxides with dominant electronic conductivity by $D_{chem} = \Gamma_O D_{O=}$ and $k_{chem} = \Gamma_O k_{ex}$ where $D_{O=}$ is the self-diffusion coefficient of the oxygen ion, k_{ex} is the surface exchange coefficient at thermal equilibrium and Γ_O is the thermodynamic factor.

Electrical conductivities were measured using the 4-probe method with gold wires as current and voltage electrodes. A model SR830 dual-phase lock-in amplifier (Stanford Research System) with built-in oscillator was used for applying and measuring the AC voltages at a frequency of 13 kHz in the ECR experiments. Instrument control and data acquisition used LabVIEW (National Instruments).

The volume of the ECR apparatus was minimized by using a fine quartz tube (i.d. = 1.0 mm, length = 15 cm, volume = 0.47 cm^3) as the gas inlet line. Gas switching between two streams at the same measured flow rate was performed using a 4-way valve connected to the inlet line through a 3 cm long tube (i. d. = 3 mm). A 6-bore Al_2O_3 tube was used as the sample holder. The holder accommodates a sample with maximum length of 2.5 cm and holds all four gold electrodes and an R-type thermocouple. The gas change-out time in the ECR apparatus was determined by measuring the high temperature conductivity relaxation behavior of a thin film of $La_{0.5}Sr_{0.5}CoO_{3-x}$ (LSCO, ~5000Å) prepared on a $LaAlO_3$ single crystal substrate by laser deposition (14). The results show gas change-out times of <1 second.

Results and Discussion

Oxygen transport kinetics. The results of electrical conductivity measurements for two compositions, $La_{0.5}Sr_{0.5}MO_{3-x}$ (M= Fe, Co), are shown in Figure 1. Because of the differences in conductivity between the two compositions and in the relative magnitudes of D and k, it is not possible to obtain data over the same temperature range. Nevertheless, a comparison can be made. The difference in the diffusion coefficient between the iron and cobalt composition arises in part from differences in the thermodynamic factor but mainly from differences in the vacancy concentration. The extrapolated vacancy diffusion coefficients at the same temperature, determined from the relation $c_O D_O = c_V D_V$, are closely similar (30% difference at 750 °C). In contrast, the equilibrium surface exchange coefficient for $La_{0.5}Sr_{0.5}CoO_{3-x}$ is an order of magnitude higher than for $La_{0.5}Sr_{0.5}FeO_{3-x}$, a difference that cannot be explained solely by the difference in vacancy concentrations.

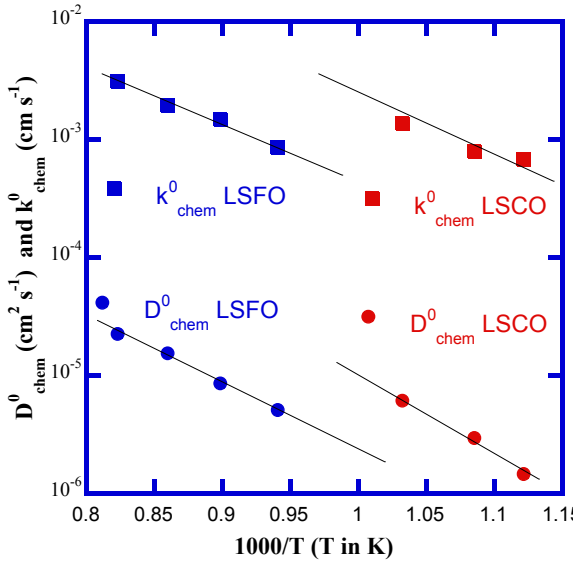

Figure 1. A comparison of the chemical diffusion coefficients and surface exchange rates for $La_{0.5}Sr_{0.5}MO_{3-x}$ (M= Fe, Co), the 0 suffix refers to 1atm oxygen partial pressure.

Long-term performance and surface segregation. The long-term behavior of the oxygen transport kinetics of $La_{0.2}Sr_{0.8}Cr_{0.2}Fe_{0.8}O_{3-x}$ was studied by measuring periodically the relaxation behavior for 1% - 5% O_2 gas switches over a period of

12 d. While the measured surface exchange coefficient was found to decrease monotonically with time, the oxygen chemical diffusivity remained almost constant. The bulk electrical conductivity also remained constant as seen in Figure 2. The behavior indicates a time dependent slow transformation in the sample, which affects the surface exchange kinetics adversely but does not affect bulk transport.

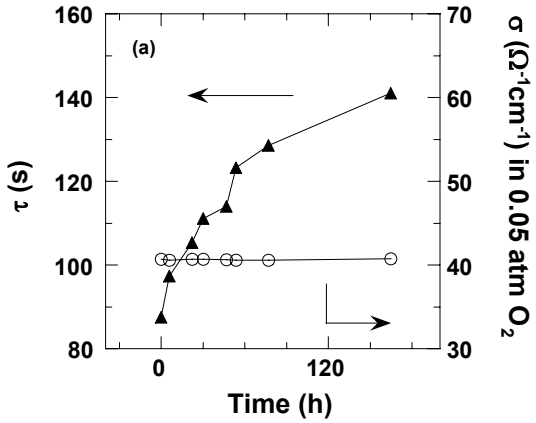

Figure 2. Long time variation of the ECR time constant and the total conductivity for $La_{0.2}Sr_{0.8}Cr_{0.2}Fe_{0.8}O_{3-x}$.

XPS data (15) indicate that the change in the surface exchange kinetics is due to time variations in the surface concentrations of chromium and strontium. Assuming that a varying surface concentration of chromium is responsible for the observed behavior and using a simple analysis of the kinetics of segregation, the diffusivity of chromium can be estimated. We assume that the measured surface exchange coefficient is inversely proportional to concentration of chromium in the surface layer, the thickness of the surface layer is the order of 2 - 3 nm as estimated from the XPS results, and that evaporation of chromium species at the present experimental conditions are negligible. Figure 3 shows the time dependent changes in surface exchange coefficient fitted to the model. The chromium diffusivity, D, in $La_{0.2}Sr_{0.8}Cr_{0.2}Fe_{0.8}O_{3-x}$ is estimated to be ~10^{-19} cm^2/sec at 821 °C.

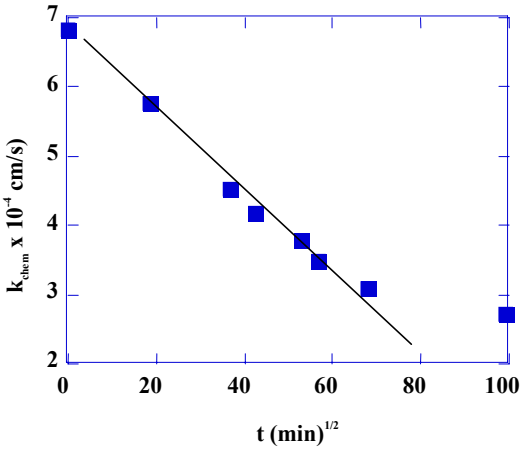

Figure 3. Dependence of k_{chem} at 821°C for $La_{0.2}Sr_{0.8}Cr_{0.2}Fe_{0.8}O_{3-x}$.

A decrease in surface exchange coefficient was also found in a separate study where gas switches where made between 5% O_2 and 15% O_2 over a period of 12 d. During this period, the sample was also exposed to pure CO_2 for short periods. As seen in Figure 4, the exposure of CO_2 temporarily accelerates surface kinetics of the sample. However, the exchange kinetics revert to the original behavior after a short time once the CO_2 is removed.

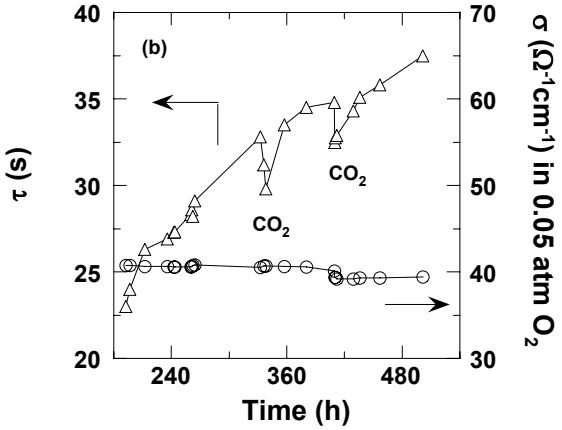

Figure 4 Influence of CO_2 on the ECR time constant and the total conductivity for $La_{0.2}Sr_{0.8}Cr_{0.2}Fe_{0.8}O_{3-x}$ at 821 °C.

Conclusions

Electrical conductivity relaxation is shown to be a useful technique for the determination of the transport properties of mixed electronic ionic conducting membrane materials. Results for $(La,Sr)(M,M')O_3$ (M = Fe, Co) are compared and the long-term stability and the effects of CO_2 are discussed for the specific case of $La_{0.2}Sr_{0.8}Fe_{0.8}Cr_{0.2}O_3$.

Acknowledgement. The work was supported by the Department of Energy, DOE-DE-FC26-99FT40054 and the Robert A. Welch Foundation

References

(1) Mazanec, T. J., *ElectroPox Gas Reforming, Ceramic Membranes*; Anderson, H. U.; Khandkar, A.C.; Liu, M. Eds.; The Electrochem. Soc., 1997; pp 16-28.
(2) *The CRC Handbook of Solid State Electrochemistry*, Eds. P. J. Gellings, P. J.; Bouwmeester, H. J. M., Eds.; CRC Press, USA, 1997, p 413.
(2) Mizusaki, J.; Tabuchi, J.; Matsuura, T.; Yamauchi, S.; Fueki, K. *J. Electrochem. Soc.* **1989**, *136*, 2082.
(4) Kilner, J.A.; De Souza, R.A.; Fullarton, I. C. *Solid State Ionics* **1996**, *86-88*, 703.
(5) Stevenson, J. W.; Armstrong, T. R.; Carneim, R. D.; Pederson L. R.; Weber, W. J. *J. Electrochem. Soc.* **1996**, *143*, 2722.
(6) ten Elshof, J. E.; Lankhorst, M. H. R.; Bouwmeester, H. J. M. *Solid State Ionics* **1997**, *99*, 15.
(7) ten Elshof, J. E.; Lankhorst, M. H. R.; Bouwmeester, H. J. M. *J. Electrochem. Soc.* **1997**, *144*, 1060.
(8) Ma, B.; Balachandran, U.; Park, J.-H.; Segre, C. U. *Solid State Ionics* **1996**, *83*, 65.
(9) Kim, S.; Yang, Y. L.; Christoffersen, R.; Jacobson, A. J. *Solid State Ionics* **1998**, *109*, 187.
(10) Lee, T. H.; Yang, Y. L.; Jacobson, A. J.; Abeles, B.; Zhou, M. *Solid State Ionics* **1997**, *100*, 77.
(11) Ming, Q.; Nersesyan, M.; Wagner, A. L.; Ritchie, J.; Richardson, J. T.; Luss, D.; Jacobson, A.J.; Yang, Y.L. **1999**, *122,* 113.
(12) Yasuda, I; Hishinuma, M. *Solid State Ionics* **1995**, *80*, 141.
(13) Wang, S.; Abeles, B.; Jacobson, A. J. *Mater. Res. Soc. Symp. Proc.* **1999**, *548*, 557.
(14) Kim, S.; Wang, S.; Chen, X.; Yang, Y. L.; Wu, N.; Ignatiev, A.; Jacobson, A. J.; Abeles, B. *J. Electrochem. Soc.* **2000**, *147*, 2398.
(15) van der Heide, P.A.W.; Wang, S.; Verma, A.; Jacobson, A. J. to be published.

Joining $LaMO_3$ Perovskite Ceramics to Nickel-based Super Alloys using Brazing/TLPB Techniques

Raymundo Arroyave, Thomas W. Eagar, Harold Larson*

Massachusetts Institute of Technology
77 Massachusetts Ave. Room 4-134
Cambridge, MA 02139
*raymundo@mit.edu

ABSTRACT

Alternatives to mechanical sealing of perovskite/metal interfaces are explored. Experimental results demonstrating the possibility of using conventional TLPB/brazing techniques for the joining of $LaMO_3$ ceramics with Ni-based super alloys are presented. The nature of the chemical reactions occurring at the $LaMO_3$/metal interfaces is investigated. It is shown that the localized reduction of the perovskite substrate has important consequences regarding the integrity of the joints.

INTRODUCTION

Due to their mixed electronic-ionic conductivity properties, $LaMO_3$ (where M is a transition metal) perovskite ceramics constitute a promising material for emerging energy-related applications such as oxygen transfer membranes (OTM) [1] and electrodes for solid oxide fuel cells (SOFC) [2]. Despite the fact that such applications have been proved to be technically feasible, several engineering challenges must be met in order to make them commercially viable. In both SOFC and OTM-based technologies, the sealing of the process gases and their isolation from the outer environment constitutes a critical step to be resolved.

In particular, OTM technologies used in Gas-to-Liquid (GTL) applications rely heavily on the successful isolation of the syngas from the oxygen-rich external environment. Additionally, the product of the GTL reactors must be transported to further stages of the process and therefore requires the interfacing with metallic pipes capable of withstanding the mechanical stresses undergone in any industrial scale facility.

In this work, we describe the ongoing efforts by our research group regarding the development of reliable alternative sealing techniques for Oxygen Transfer Membrane technologies applied in GTL processes. Particularly, we describe the research aimed at understanding the interactions between Nickel-based brazing alloys and $LaMO_3$ perovskite membranes.

PEROVSKITE/METAL SEALING FOR GTL APPLICATIONS

Mechanical Seals. In GTL technologies using OTM, a perovskite-based membrane separates two regions of highly different oxygen chemical potentials. In order to ensure the proper functioning of the process, it is required to effectively seal the OTM perovskite/metal arrangement. Currently, mechanical compression has been the only effective technique through which this sealing can take place. In order for OTMs to be effective oxygen conductors, the operating temperatures of the GTL reactors must be relatively high ($>900^0$ C) [1] so high oxygen transport rates across the membrane are obtained.

Mechanical seals that rely on compression of the subcomponents of the seal (perovskite and metal substrates) undergo creep processes when subjected to such elevated temperatures for extended times. As time progresses, these creep processes may result in a loss of the compressive force necessary for maintaining a gas-tight seal. In practice, such problems are usually solved by over loading the seals in order to compensate for such mechanical relaxations. However, excessive overloading of the ceramic materials can lead to premature failure of the seals.

Sealing Alternatives. A possible alternative to such mechanical sealing approaches could be the use of liquid-phase based joining techniques such as brazing or transient liquid phase diffusion bonding (TLPB) so that (upon cooling) solid interface between the perovskite membrane and the metallic substrate can be obtained.

Brazing consists of the use of an interlayer with lower melting point than the substrates to be joined [3]. The joint assembly is brought up to a temperature slightly above the melting point of the interlayer so the resulting liquid wets the substrates to be joined. The resulting joint is subsequently cooled down so a solid joint is obtained. TLPB, on the other hand, relies on the isothermal solidification of the interlayer placed between the substrates to be joined and relies on the use of a melting point depressant (MPD) that is also a fast diffuser at least in one of the parent materials [4]. As the joint is held at elevated temperatures for long enough periods of time, the MPD diffuses out of the interlayer and into the base materials, allowing a higher re-melting temperature of the whole joint assembly.

Ceramic/Metal Liquid-based Joining. For brazing or TLPB joining techniques to work, the resulting liquid interlayer must wet both substrates to be joined, since the wetting angle between the liquid and the solid surface is inversely related to the Work of Adhesion, i.e. the energy that must be exerted on the interface to separate both surfaces.

In general, due to the highly different nature of their interatomic bonds, molten metals do not wet ceramic substrates [5] (especially highly stable ones, such as MgO, ZrO_2, Al_2O_3), since the resulting interfaces have a much higher energy than that of the un-joined surfaces. An exception occurs when a chemical reaction between the metal and the ceramic substrate takes place, since this chemical reaction lowers the overall surface energy of the system and therefore increases its stability [6]. In many ceramic/metal joining applications, the promotion of the necessary interfacial reactions is achieved by modifying the interlayer by the addition of active elements, such as titanium, hafnium, zirconium. These active elements ensure the formation of a interfacial reaction product, thus resulting in a chemically stable ceramic/metal interface[7]. In a few cases, particularly when the ceramic substrate has a relatively high surface energy, wetting can be ensured without the use of active elements. As will be seen below, conventional, non-reactive TLPB alloys wet $LaMO_3$ perovskite substrates without the addition of reactive elements. This can be correlated with the relatively low thermodynamic stability (compared to highly stable oxides such as MgO, ZrO_2, etc.) of this family of ceramic materials.

USE OF TLPB ALLOYS FOR JOINING $LaMO_3$ PEROVSKITES TO METALS

In order to select a proper interlayer material for the joining of two particular substrates, special attention must be paid to three different aspects:

a) The melting range of the interlayer material must be lower than that of the parent substrates.

b) The solidus point of the interlayer must lie above the expected operating temperature of the joint.
c) The interlayer material must be able to withstand the operating conditions, such as temperature, chemical environment, etc. of the joint.

As noted above, the melting range of the interlayer material must be above at least 900^0C, which is the minimum temperature in order to ensure fast enough oxygen transfer rates across the perovskite membrane. Moreover, the liquidus of the alloy in question must lie below the solidus of the metallic substrate to be joined to the OTM (for most Ni-based super alloys, the solidus lies somewhere around 1350^0C). This leaves us with a rather limited temperature range of 900^0C-1350^0C.

Of the broad range of commercial metallic brazing and TLPB alloys, copper and nickel-based alloys are the most promising ones. Previously, it has been shown that copper-based brazing alloys do wet perovskite-based substrates [8]. Unfortunately, the poor oxidation resistance of these alloy systems [9] precludes their utilization under the highly oxidizing environments occurring at GTL reactors.

Given the constraints outlined above, it was decided that Ni-based alloys constituted the only commercial alloy system that could lead to the development of a reliable perovskite/metal joint. In general, Ni-based TLPB alloys relay on the use of melting point depressants such as boron, silicon or phosphorus to depress the liquidus surface to temperatures well below the melting point of pure nickel[10].

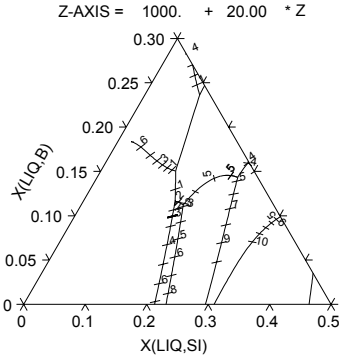

Figure 1. Primary surface of crystallization for the Ni-B-Si system, calculated using the models developed by [10]

Figure 1 shows the liquidus surface for the B-Ni-Si based on the models developed by [10]. As can be seen in the figure, the melting point of the Ni-rich alloys can be reduced by almost 400^0C when considerable amounts of both B and Si are added. Due to the fact that the metallic substrate is a Ni-based super alloy and that boron is a fast interstitial diffuser in nickel, it is expected that by using these alloys it is possible to isothermally solidify the interlayer and thus its re-melting temperature can be even higher than the processing temperature. By modifying these alloys through the addition of chromium their oxidation resistance is increased markedly, which constitutes a clear advantage, given the operating conditions within the GTL reactors.

In the remaining of the paper, we describe the analysis of the nature of the interactions between $LaMO_3$ perovskite substrates and Ni-based super alloys.

EXPERIMENTAL

Perovskite-based ceramic $(La,Sr)FeO_3$ discs were cut from a 0.8 in DIA solid hot-isostatically pressed powders. The discs were cut using a diamond saw and polished down to a 1μm finish using ethanol as the suspension media (water may attack the perovskite materials). Haynes-230® was the Ni-based super alloy selected to work as the metallic substrate due to the fact that its coefficient of thermal expansion (CTE) closely matches (although there is still a difference of about $2x10^{-6}$ /^{0}C) that of the perovskite ceramics used in the present work (~12 x 10^{-6} / ^{0}C at RT). The parent rod was machined down to 0.8" DIA and discs were cut and later polished using standard metallographic techniques. As the TLPB interlayer, a commercial B-Ni5 brazing alloy (3 wt. % Fe, 4.5 wt. % Si, 3.2 wt.% B, 7 wt. % Cr, Ni-balance) in its amorphous foil (2 mils) presentation was used. Both substrate materials and the Ni-based interlayer were ultrasonically cleaned in acetone for about 60 minutes.

Once the joint components were cleaned, a Perovskite/TLPB Alloy/ Haynes230® sandwich assembly was placed inside a high-temperature, high-vacuum furnace (1 x 10^{-6} torr). The temperature of the furnace was increased at a 5 ^{0}C/min rate up to 1090^0C (above the liquidus temperature of the TLPB alloy) and held at that temperature for 30 min. Afterwards, the joint arrangement was cooled at 5 ^{0}C/min until room temperature was reached.

The resulting samples were examined and sectioned. Analyses using optical microscopy, SEM and EDS were performed in order to characterize and understand the reaction mechanisms occurring at the perovskite/braze interfaces.

RESULTS AND DISCUSSION

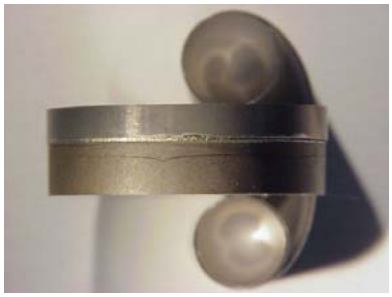

Figure 2. $(La_{0.6}Sr_{0.4})FeO_3$/Haynes230® joint. Joining conditions: 1090^0C, $1x10^{-6}$ torr.

Figure 2 presents typical flat joints created using the TLPB approach. As can be seen, it was possible to create large contact area (disc diameter of approx. 0.8 in) joints. The Ni-based alloy used as an interlayer wetted both substrate materials without the addition of active elements. However, it was observed that cracks appeared in a direction parallel to the ceramic/metal interface. To test the influence of the vacuum pressure on the final integrity of the joints, assemblies were also joined at reduced vacuum pressures of about 10^{-3} torr. In general, cracking of the samples at these reduced vacuum pressures was significantly reduced, as can be seen in Figure 3.

Figure 3. . $(La_{0.6}Sr_{0.4})FeO_3$/Haynes230® joint. Joining conditions: 1090^0C, $1x10^{-3}$ torr.

The effect of the different vacuum pressures may be interpreted as follows: It is well known that perovskite-based ceramics of the $LaMO_3$ class tend to change volume not only with temperature but with the amount of oxygen vacancies present in the lattice. By decreasing the environmental pressure, the oxygen potential was decreased, increasing the degree of non-stoichiometry of the perovskite material. This increased volumetric expansion increased the already present thermally-induced stresses due to the differences in CTE. The greater residual stresses made the formation of cracks parallel to the ceramic/metal interface more likely. However, the fact that a relatively minor change in vacuum pressure had such an effect on the integrity of the resulting joints indicated that the ceramic/metal interfaces created were not stable enough. In order to further examine what was the nature of the perovskite/Ni-based brazing alloy interaction, samples were sectioned and analyzed under SEM.

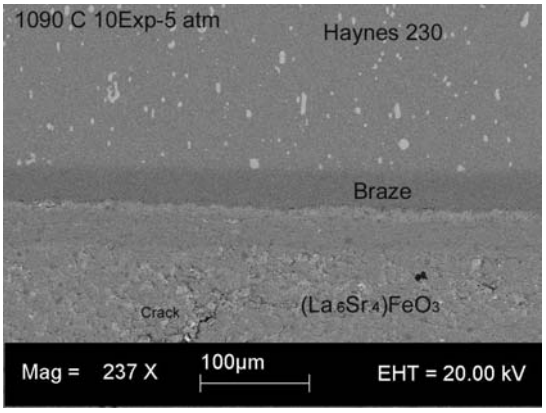

Figure 4. $(La_{0.6}Sr_{0.4})FeO_3$/Haynes230® joint. Joining conditions: 1090^0C, $1x10^{-3}$ torr. SEM Backscattered Image micrograph.

As can be seen from Figure 4, even for some of the samples (approx. 10%) that were joined at reduced vacuum pressures, crack initiation was observed. By using backscattering imaging, it is possible to observe contrast due to differences in composition. From the contrast observed, several regions can be identified. Moreover, it is clear that on the perovskite substrate (below the "Braze" label), at least three clearly identifiable regions have formed due to interactions between the Ni-based brazing alloy and the La-Sr-Fe-O substrate. It can also be seen that cracks tend to nucleate within a region that is relatively far away from the perovskite/braze interface.

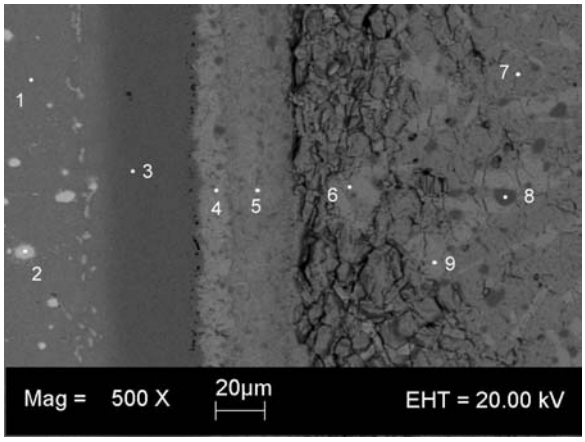

Figure 5. $(La_{0.6}Sr_{0.4})FeO_3$/Haynes230® joint. Joining conditions: 1090^0C, $1x10^{-3}$ torr. SEM Backscattered Image micrograph

Based on Figure 5 and Table 1 it can be seen that the Ni-based alloy reacted with the perovskite substrate in a rather excessive manner. From the compositional analysis (it is important to note that EDS analyses tend to overestimate the presence of light elements such as oxygen) it is possible to determine that the braze/perovskite reaction led to the precipitation of several distinct phases out of the originally single phase ceramic.

Table 1. Compositions through EDS Analysis corresponding to Figure 5 (at %).

	1	**2**	3	4	5	6,9	7	**8**
Ni	56	21	70	0	0	0	0	0
Cr	25	30	9	0	0	0	0	0
W	13	40	0	0	0	0	0	0
Mo	1	0	0	0	0	0	0	0
Ti	0	0	0	0	0	0	0	0
Si	0	0	3	0	0	0	0	0
Fe	2	1	7	1	1	14	15	69
La	0	0	0	23	2	13	15	1
Sr	0	0	8?	1	37	8	8	2
O	0	0	0	76	60	65	62	29
Mn	4	4	0	0	0	0	0	0

The layering of the phases identified as 4 (La_2O_3) and 5 (SrO?) indicates that an oxygen chemical potential gradient was established across the perovskite/braze interface. By establishing this oxygen chemical potential gradient, the original $(La_{0.6}Sr_{0.4})FeO_3$ perovskite substrate close to the interface was decomposed. The localized oxygen potential at that interface must have decreased below $1x10^{-16}$ atm, which is the stability limit of such materials [11]. Under such reducing conditions, the formation of more stable oxides, such as SrO and La_2O_3 becomes thermodynamically favorable. These reducing conditions can be explained by the presence of Fe and Cr dissolved into the Ni-based liquid, since these two elements have

relatively high chemical activities in Ni [12], [13] and additionally have a relatively high oxygen affinity [14]. Although for more stable ceramics, such as ZrO_2 and Al_2O_3, this braze alloy would not have been considered as "active", that is, capable of reducing the ceramic substrate, the relatively low thermodynamic stability of $(La_{0.6}Sr_{0.4})FeO_3$ accounts for the observed decomposition.

Based on purely mass conservation arguments, the formation of La-O and Sr-O compounds must have also led to the segregation of Fe ions. Fe could have been dissolved into the Ni melt, as indicated by the slight increase in the Fe content, compared to the pre-brazing composition. Figure 5, however, shows the formation of Fe-O "islands" within the perovskite matrix (identified as number 8). Thus, the decomposition of $(La_{0.6}Sr_{0.4})FeO_3$ due to the oxygen potential gradient across the perovskite/braze interface led in the first place to the precipitation of La-O and Sr-O layered reaction products and the accompanying segregation of Fe ions both towards the Ni melt and within the perovskite matrix. This localized decomposition of the perovskite matrix led to the formation of an extensive porous network in a well-defined region between points 5 and 6 in Figure 5.

When the joint is created, it can be considered that is stress-free. However, as the joint is cooled, residual stresses generated due to both the CTE mismatch build up. Moreover, since an oxygen potential gradient exists close to the perovskite/braze interface, there should also be a gradient in chemical volumetric expansion, which also contributes to the overall state of stress. Under normal conditions, and given that the actual CTE mismatch between the perovskite and metallic materials used is not significant, one could expect that the joint created would be relatively stable. However, the presence of a localized region of high porosity promotes the nucleation of cracks, which during the normal operating conditions of the interface could grow and eventually would lead to the failure of the seal.

CONCLUSIONS

In the present paper it has been demonstrated that Ni-based liquid alloys wet $LaMO_3$ perovskite substrates without additions of active elements such as Ti, Zr, etc. Moreover, relatively large contact area ceramic/metal joints have been created using such alloys. Under certain joining conditions (low vacuum environments), crack-free specimens were obtained. However, it was observed that, even in these cases, micro-cracks were likely to nucleate in regions close to the ceramic/metal interface.

Through analysis of the interfacial reaction zone it was concluded that the presence of oxygen-active elements such as Cr and Fe in the Ni braze created a relatively large oxygen chemical potential across the ceramic/metal interface. Such a large chemical potential caused the localized decomposition of the perovskite matrix and the formation of a high-porosity region parallel to the ceramic/metal interface.

Approaches such as the use of effective diffusion barriers that would prevent the migration of oxygen ions into the Ni-based melt are under investigation. Alternatively, changes in the chemistry of the Ni-based brazing alloys are being explored so the oxygen affinity of the braze can be reduced. By controlling the extent of the interfacial reactions, it will be possible to use liquid phase-based joining techniques to successfully create $LaMO_3$/metal seals.

REFERENCES

[1] Mazanec, T. Proc. Electrochem. Soc. **1995**, *95*, 24
[2] Skinner, S. J. Int. J. Inorg. Mater. **2001**,*3*, 113-121
[3] Passerone, A.; Muolo, M. L. Mater. Manif. Processes, **2000**, *15*,631-648
[4] McDonald, W. D.; Eagar, T. W. Metall. Trans. A, 1998, *29A*, 315-318
[5] Li, J-G., J. Am. Ceram. Soc., **1992**, *75*, 3118-26
[6] Schwartz, M. M. Ceramic Joining, ASM International, Metals Park, Ohio, 1990.
[7] Eustathopoulos, N.; Drevet, B. Mater. Res. Bull. **1993**, *314*, 15-25
[8] Wilkenhoener, R.; Buckremer, H. P.; Stoever, D.; Stolten, D.; Koch, A. New Materials for Batteries and Fuel Cells, MRS, Warrendale, PA,2000 pp.295-302.
[9] Kapoor, R. R.; Eagar, T.W. J. Am. Ceram. Soc. **1989**, *72*, 448-456.
[10] Tokunaga, T.; Nishio, K.; Hasebe, M. J. Phase Equilib.**2001**, *22*,291-299.
[11] Nakamura, T.; Petzow, G.; Gauckler, L. J. Mater. Res. Bull. **1979**, *14*,649-659
[12] Schuster, J. C.; Du, Y. Metall. Mater. Trans. A. **2000**, *31A*,1795-1803
[13] Larrain, J. M. CALPHAD: Comput. Coupling Phase Diagrams Thermochem. **1980**, *4*, 155-171
[14] Laag, T.; Phser, J.; Janke, D. Steel Res. **1997**, *68*, 341-344

ISOTOPE TRANSIENTS ON OPERATING LSCO OXYGEN SEPARATION MEMBANES

Charles A. Mims and Linjei Hu

Department of Chemical Engineering and Applied Chemistry
University of Toronto, Toronto Ontario CANADA M5S 3E5

Introduction

Mixed oxide ion-electron conducting (MIEC) oxide materials are under intense development for use in membrane processes for air separation, syngas generation and others (1). The performance of the membrane depends on the surface and bulk properties of the material and the membrane geometry. The membrane operates under an oxygen potential gradient, which is in turn shaped by the various surface and bulk resistances.

Isotope exchange - depth profiling (IEDP) has been extensively used to study the kinetics of oxygen activation at the surface and diffusion in the bulk of oxides in the absence of a chemical gradient.(2). Surface exchange coefficient, k*, and tracer diffusion coefficient, D*, are extracted from the isotope distribution profile. Other relaxation techniques measure similar properties under small potential gradients. These techniques provide an accurate and relatively simple way to get valuable parameters for mixed ion-electron conducting (MIEC) materials. Since these parameters are measured under gradientless conditions for oxygen and net oxygen flux is zero, the behavior of the membrane with oxygen chemical gradient may be different from those that are calculated from k* and D*. Conversely, it is not easy to determine the relative contributions of surface and bulk resistances under operating conditions.

Dynamic isotope tracing techniques, which are extensively used in catalysis research, involve placing isotopic labels on reacting atoms. Monitoring these labeled atoms as they become incorporated into reaction intermediates and eventually into reaction products will yield information on the steady state operation of the membrane under a gradient and allow surface and bulk resistances to be separated. An experiment is typically performed by establishing two identical reactant streams (one is fed to the reactor and the other is vented), except that the isotopic labels of one or more of the constituents are different. The transient is initiated by switching feeds while maintaining steady state reactions and monitoring the change in the isotopic composition of products.

We report results here from the first study of isotope transients on MIECs to investigate the oxygen transport parameters across a functioning the membrane. A a pulse of $^{18}O_2$/Ar while maintaining a constant O_2 partial pressure, was introduced to the air side of the sample while maintaining the steady state conditions. The ^{18}O diffuses into the sample as a result of both the existing ^{18}O chemical gradient and oxygen gradient across the membrane. The isotopic ratio $^{18}O/^{16}O$ in the permeated O_2 reveals the residence time distribution of the oxygen transiting the membrane. By fitting the obtained isotopic composition in the permeated oxygen using mathematical models, the surface activation rate, its degree of reversibility (related to the potential drop across the surface, and the bulk mobility under operating conditions can be obtained.

Experimental

The tubular sample of $La_{0.6}Sr_{0.4}Co_{0.2}Fe_{0.8}O_{3-\delta}$ was approximately 6.2 mm outer diameter, 1.0 mm wall thickness, and 8.8 mm length. The both sides of the tube were ground with 800 grit silicon carbide paper to a desired flat and smooth surface. Prior to installing into the reactor, the sample was rinsed and ultrasonically cleansed with distilled water and then acetone to remove any residue and contaminant.

Experimental setup. Figure 1 illustrates the configuration of the internals of the reactor. To minimize the undesired wall reactions, all parts which may contact gas mixture inside and outside of the perovskite membrane in the hot zone of the reactor are made of quartz except the gold seal. The temperature of furnace was controlled by a Omega Type I/32 PID temperature controller with an accuracy of ±0.5 ^oC. Before and after each measurement, the temperature of the sample was measured by a K-type thermocouple as illustrated in Figure 1.

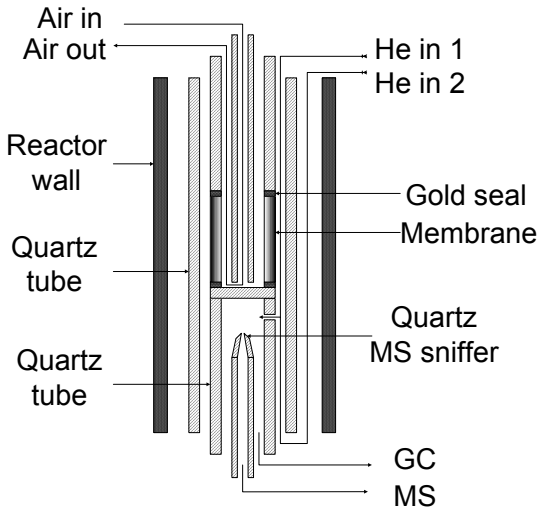

Figure 1: Experimental apparatus for isotope transients

Oxygen permeation measurements. The sample was heated at a ramping rate of ca. 2 ^oC/min to 750 C. The flow rates of air and the sweeping gas He were basically 20 ml/min in our experiments. As illustrated in Figure 1, another He flow (He in 2) was introduced to purge the dead volume between the reactor wall and outer quartz tube, and the flow rate is fixed at 5.0 ml/min. The composition of sweeping gas was analyzed by a SRI 8610C Gas Chromatograph with a 5A molecular-sieve column. A Helium Ionization Detector (HID) was used to measure the oxygen and nitrogen content.

Oxygen isotope transient experiments. The synthesized air, O_2:N_2 = 20:80, was provided by Praxair Products Inc.. The ^{18}O-containing gas, $^{18}O_2$:Ar = 20:80, was supplied by Icon Isotopes. The ^{18}O isotope purity is 97%. The sample was equilibrated at the experimental conditions for at least 24 h in the natural abundance isotope version of the gas mixture. Following this equilibration the gas mixture O_2/N_2 in the air side of the membrane was switched to the ^{18}O containing mixture ($^{18}O2$/Ar) and maintained for 15 min or 60 min. The flow rates of $^{18}O_2$/Ar were 1-3 ml/min for the duration of isotope pulse to avoid depletion of the isotope oxygen, which depend on the experimental temperature and oxygen flux. A "pulse" of ^{18}O was then obtained in the oxygen-rich side. At the end of the pulse, the gas mixture was switched back to O_2/N_2 and kept the same experimental conditions as before for 4-6 days. The sweeping gas was analyzed with an on-line UTI Model 100C Quadrupole Mass Spectrometer (MS). The oxygen fluxes were obtained simultaneously by an on-line GC analysis.

Results

Modelling. The results were simulated by 1-D constant properties computer model to extract values for the transport parameters. The following equations govern the isotope transport:

Transport from gas to air surface (z=0):

$$(k_f' \chi_g^* - k_r' \chi_s^*)\Big|_{z=0} = \frac{j_O}{C_O}\frac{\partial \chi^*}{\partial z}\Big|_{z=0} - D_O \frac{\partial^2 \chi^*}{\partial z^2}\Big|_{z=0} \quad (1)$$

where * denotes the infusing isotope, χ^* is the isotope fraction, C (mol/cm^3) the bulk oxygen atom concentration, j mol/cm^{2}s the oxygen atom flux, D (cm^2/s) is the oxygen diffusion coefficient, k(cm/s) is the transfer coefficient, f = forward, r = reverse. The surface corresponds to $z = 0$. The net oxygen flux is given by C times (k_f - k_r) and the subscripts g and s denote gas and surface respectively. L is the membrane thickness.

Transport in the membrane: (0 # z # L)

$$\frac{\partial \chi_f^*}{\partial t} = D_O \frac{\partial^2 \chi_f^*}{\partial z^2} - \frac{j_O}{C_O}\frac{\partial \chi}{\partial z} \quad (2)$$

and the isotope transport from membrane to the helium sweep side is simply given by $j_O^* \chi_f^*\Big|_{z=L}$.

Figure 2 shows the results of simulations of ^{18}O isotope transients delivered to the sweep side of an oxygen separation membrane. As the diffusion coefficient is reduced, the residence time distribution becomes more and more "plug-flow"–like. Another interesting observation from the simulations is that the shape changes as the reversibility of the air-side reaction changes, thus providing a measure of the reversibility of the air-side surface reaction. The reverse of the air-side oxygen activation provides another path for the isotope to leave the membrane and shortens the residence time distribution of the isotope.

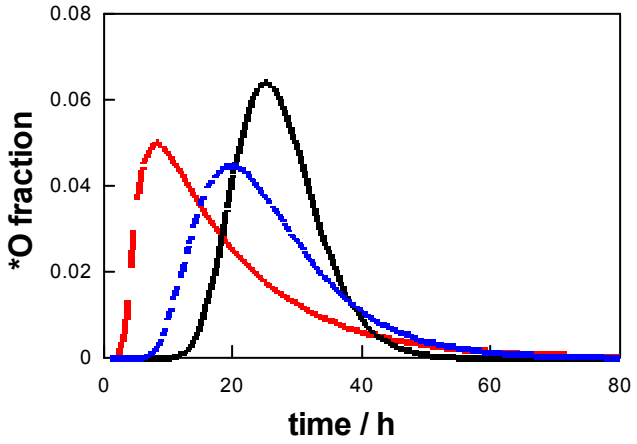

Figure 2: Simulations of isotope transient son delivery (helium sweep) side of an operating membrane at similar flux conditions to this study. Oxygen diffusion coefficient decrease for curves peaking from left to right – 10^{-7}, 10^{-8} and 10^{-9} cm^2 s^{-1} respectively. Oxygen molecule flux = 0.05 sccm for 1 cm^2 area. Air side surface reaction was 50% reversible (forward rate of oxygen activation was twice that of the reverse.

Isotope transient data. Figure 3 presents the time dependent ^{18}O fraction of permeated oxygen in the oxygen-lean side after introducing a pulse (15 min) of 20% $^{18}O_2$ (97% isotopic purity at atom) at 800 ^{0}C . Also shown is a fit to the data by the model described above with the following values. D_O = 1.3 x 10^{-7} cm^2 s^{-1}, $k_{forward}$ = 4 x 10^{-6} cm s^{-1}, $k_{reverse}$ = 2.6 x 10^{-6} cm s^{-1}. The net flux is 0.05 sccm per cm^2. The substantially reversible surface activation rate and the bulk diffusion coefficient are consistent with IEDP measurements on the same material ().

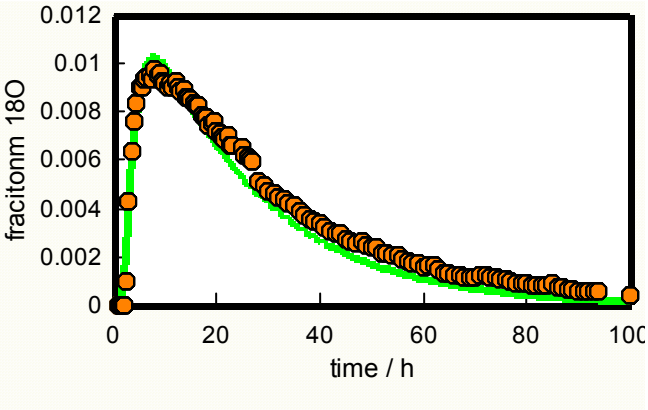

Figure 3: Isotope transient ($^{18}O_2$) on operating membrane. Solid line is given by 1-D model described in text. Natural abundance (0.002) has been subtracted.

Conclusions

The reversibility of the surface reaction together with a finite value fit to the diffusion coefficient shows that both the surface and bulk processes contribute to the overall resistance to oxygen flux through this membrane. The characteristic distance D*/k* measured for this material in IEDP experiments (2,3) is similar to the membrane thickness used here and the substantial reversibility seen in both processes here is consistent with the modest oxygen potential gradients. Future experiments will examine the large gradients present in membranes for syngas production.

Acknowledgments. Support for this work from the UAF membrane consortium under DOE-DE-FC26-99FT40054, the NSF-MRSEC program, and the Natural Sciences and Engineering Research Council (Canada) is gratefully acknowledged.

References

(1) Bouwmeester, H. J. M. and Burggraaf, A. J., Dense Ceramic Membranes for Oxygen Separation. [14], The CRC Handbook of Solid State Electrochemistry, 481-553. Gellings P.J. and Bouwmeester H. J. M, Editors, CRC Press 1997

(2 J.A. Kilner, B.C.H. Steele, L. Ilkov, *Solid State Ionics* **12** (1984) 89. J.A. Kilner, R.A. De Souza, I.C. Fullarton, *Solid State Ionics* **86-88** (1996) 703.

(3) Lane, J.A., Benson, S.J., Waller, D. Kilner, J.A., *Solid State Ionics* 121 (1999) 201: Xu, J.X., Thomson, W.J., *Chemical Engineering Science* **54** (1999) 3839: Li, S. J. , *et.al. J. Membrane Science* **166** (2000) 51.

ATOMIC SCALE CHARACTERIZATION OF OXYGEN VACANCY ORDERING IN OXYGEN CONDUCTING MEMBRANES

R.F. Klie*, N. D. Browning[1]

* Brookhaven National Laboratory, Dept. of Applied Science, Upton, New York 11973

[1] University of Illinois at Chicago, 845 West Taylor Street, Chicago, IL 60607-7059

Introduction

Mixed conductors have been the focus of many studies in the last decade, leading to a detailed understanding of many of the macroscopic bulk properties of these materials.[1] Of particular interest are perovskite oxides for applications as oxygen conducting membranes in syngas reactors. However, there are still many issues that need to be addressed on the fundamental atomic scale. In particular, although the reduced low temperature phase in rare earth perovskite oxides is commonly explained in terms of ordered Brownmillerite (BM) structured micro-domains, the transition to the high temperature phase remains elusive. Here we present an investigation of this transition through atomic resolution annular dark field imaging and electron energy loss spectroscopy of (La, Sr)FeO_3 prepared under different reducing conditions.

Experimental

The STEM and EELS results presented in this paper were obtained using a JEOL 2010F STEM/TEM, having a Schottky field emission gun-source and being operated at 200 kV.[2,3] The microscope is equipped with a standard ultra high resolution objective lens pole piece, a JEOL annular dark-field detector and a post column Gatan imaging filter (GIF).[2] The lens conditions in the microscope were defined for a probe size of 0.2 nm, with a convergence angle of 13 mrad and a collection angle of 52 mrad. With these settings the Z-contrast image is incoherent; i.e., a direct image of the interface is acquired. The experimental setup for this microscope allows us to use low-angle scattered electrons that do not contribute to the Z-contrast image for EELS.[4] As the two techniques do not interfere, Z-contrast images can be used to position the electron probe at the desired spot in the sample to acquire spectra.[5,6,7] This allows us to obtain direct images (spatial resolution of 2 Å) of the atomic structure and to correlate this information with the atomically resolved EELS information (acquisition time 3s, energy resolution 1.2 eV). The in-situ heating experiments performed here utilize a double tilt heating stage with a variable temperature range between 293 K and 1273 K. If the holder is operated above 773 K a water recirculation must be connected, to prevent heat transfer through the rod of the stage. Turbulent flow of water through the recirculation system makes it impossible to achieve atomic resolution for temperatures higher than 773K. The oxygen partial pressure in the microscope column is $P_{O_2} \sim 5*10^{-8}$ Pa during the experiment, which means that at 724 K the oxide samples are in a highly reducing environment. [8]

For (La, Sr)FeO_3 we are primarily interested in the bonding between oxygen and the B-site transition metal atoms. To investigate this, the near edge fine structure of the oxygen K-edge contains valuable information about the nearest neighbor bonding (O 2p with metallic 3d) and the hybridization with the metal sp band.[9] The formal valence-state of the transition metal elements in the structure can be determined from the analysis of the L_2 and L_3 white lines that are visible due to the spin-orbit interaction. More specifically, the L_3 and L_2 lines are the transition of $2p^{3/2} \rightarrow 3d^{3/2}3d^{5/2}$ and $2p^{1/2} \rightarrow 3d^{3/2}$, respectively. However, it needs to be stated that the computed L_3/L_2 white line intensity ratios, used to determine the numerical value for the valence must be compared either with results from the literature or parametric fits calculated from well known materials under similar conditions, to convert the intensities into numerical ionization values.

Results and Discussion

In **Figure 1**, a Z-contrast image of the atomic structure of the sintered but untreated material is shown. The cubic symmetry is clearly visible and the brightest spots represent the mixed (La, Sr), whereas the less bright spots are the Fe-O columns. The pure O-columns are not visible in the image due to the low scattering amplitude of oxygen compared to La, Sr, and Fe. **Figure 1a** also shows a planar defect, commonly found the bulk of the untreated material. Upon investigation, the atomic structure of these planar defects, which run irregularly through the grains, can be identified. The regular lattice above and below the dark line is shifted by half a unit-cell along the direction of this dark feature. EEL spectra taken from the center of the dark line and the adjacent bulk exhibit a significantly lower La M-edge signal (**Figure 1b**). In addition to the decrease of La-M edge intensities, the Fe-$L_{3,2}$ ratio as well as the oxygen K-edge pre-peak is decreased in the defect. The measured Fe valence in the dark lines of 2.4±0.1, as well as the changed O K-edge fine structure originates from the different local atomic environment.

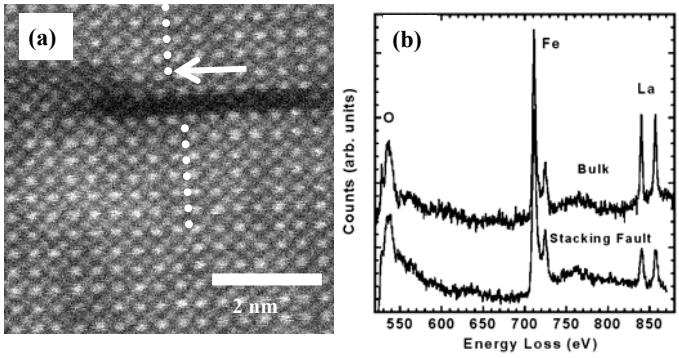

Figure 1. a) Z-contrast image of sintered (La, Sr)FeO_3 [001] showing the cubic perovskite structure and one dark line, revealing the internal structure of this feature and the shift between the adjacent bulk crystal structures. b) EEL spectra from the stacking fault and from the surrounding bulk. The spectra are normalized to the Fe-$L_{3,2}$ intensities.

Figure 2 shows a Z-contrast micrograph of the material after heating to 1023 K in an oxygen partial pressure of $P_{O_2} = 10^{-2}$ Pa for 27h. Ordered structures in the form of contrast variations in every second column can be seen, and one can show that the dark columns represent the reduced valence columns (+2.6± 0.1), whereas in the bright columns the valence is close to +(2.8± 0.1). The results indicate that in the dark FeO_2 lines the point-defect concentration is higher.

After the sample was heated and allowed to stabilized at 724 K for 12 hours in the microscope, the contrast changes appear more distinct in the sample, and can be clearly identified in the

power spectrum of the acquired image (**Figure 3**). We can now observe small micro-domains of 8-16 unit cells width (2.4 nm – 4.8 nm); with no preferential orientation of the boundaries. Note that the EEL spectra at elevated temperatures from the dark and the bright FeO_2 columns (**Figure 3b**), normalized to the intensity of the La M-edges, display different fine structures and intensities of the O K- and Fe L-edges. The pre-peak of the O K-edge in the dark columns of the domains is reduced with respect to the bright ones, indicating a decreased number of available O 2p - Fe 3d orbits, and therefore a lower valence. Also the Fe white line intensity ratios reveal a reduction of the transition metal valence from +(2.8 ± 0.1) in the bright to +(2.3 ± 0.1) in the dark columns respectively. Additionally, the intensity ratio of the iron L-edge to the oxygen K-edge is increased in the dark lines by 10% with respect to the bright line ratio, again showing the lower oxygen content in the dark columns.

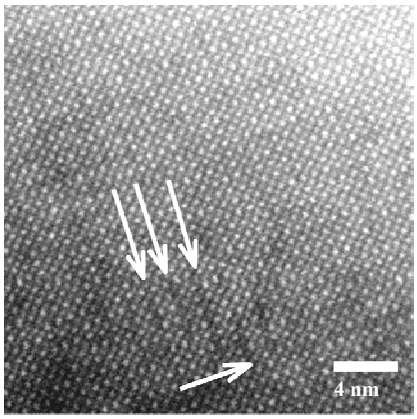

Figure 2. Z-Contrast image showing marked change in contrast in every second FeO_2 column

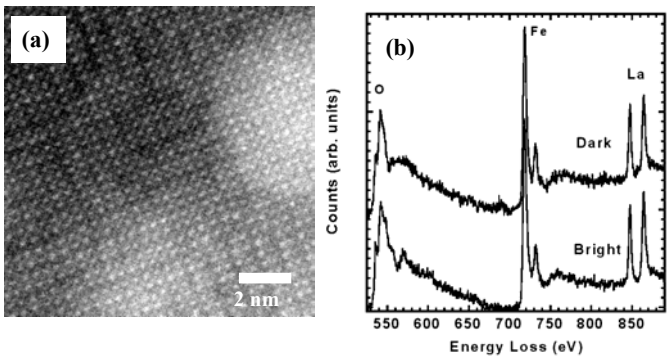

Figure 3. a) Z-Contrast image at 724 K with clearly visible ordered domain. b) EELS of bright and dark columns in LSFO [001] at 724 K.

Following this characterization, the reducing conditions were increased by heating the specimen to 1074 K for 3 hours at an constant oxygen partial pressure of $P_{O_2} = 5*10^{-8}$ Pa in the microscope. **Figure 4** shows a Z-contrast image in which the ordered domains and the interwoven domain-boundaries can be seen very clearly. (Note: The picture appears blurred due to the increased contamination layers from the heating process.) This image suggests that the size of the micro domains is increased dramatically in this environment (~20nm), and also the domain boundaries are more clearly defined. The stronger distinction between the bright and dark columns suggests that the difference in the oxygen concentration between the bright and the dark lines is even higher than before the reduction process. An analysis of the acquired EEL spectra at 724 K reveals that the already reduced, dark columns have an even lower iron valence of +(2.0± 0.1), whereas the bright columns remain at a constant valence of +(2.9± 0.1).

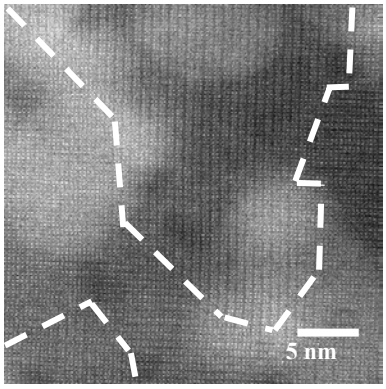

Figure 4. Z-Contrast image of LSFO at 724 K after heating at 1073 K, showing the change in domain size. The diffuse white blobs in the image are caused by contamination built up on the surface during the heating process.

Figure 5 shows the micrographs of the sample at room temperature, after a heat treatment of 1073K at 10^{-10} Pa. The image displays some features that were not observed in the bulk of the untreated or lesser-reduced samples. Two dark lines of one unit cell width, separated by one bright line in the center are oriented along the [010] direction. The EEL data acquired from the dark feature and from the surrounding bulk material is shown in **Figure 5b**. Due to the different Fe/La ratio in these spectra, all the spectra are now normalized to the Fe L-edge intensities. The most striking difference between the bulk spectra and the spectra taken from the defect structure is the drastic decrease in the La M-edge intensity. Hence, it appears to be most likely that the dark lines are caused again by a stacking fault, containing a double layer of FeO_2. The different atomic environment in the stacking fault also gives rise to the observed difference in the O K-edge fine structure. Parallel to these stacking faults the reduced columns form huge domains.

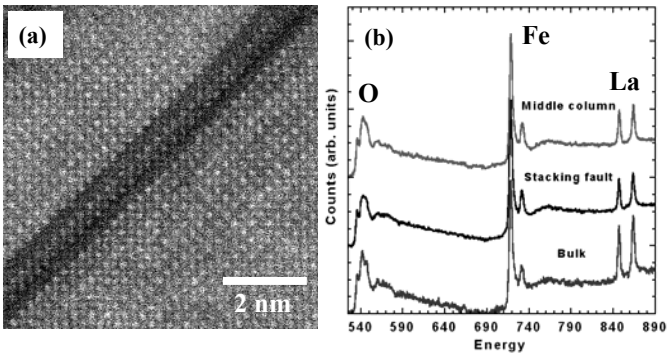

Figure 5. a) Z-Contrast image of LSFO, previously treated at 1073 K in 10^{-10} Pa showing stacking faults and revealing its structure The sandwiched structure of one brighter atomic column surrounded by two darker one can clearly be identified. b) EELS of LSFO from bulk and stacking fault, normalized to oxygen and iron core- loss edge intensity.

Discussion

The atomic scale analysis of (La, Sr)FeO_3 under various ambient pressure and temperature conditions illustrates the formation and evolution processes of ordered vacancy structures in the reduced perovskite oxides. The freshly sintered samples exhibit the ideal cubic perovskite structure in the majority of the grains. However, some grains contain linear stacking faults (**Figure 1**), which can be identified as a Ruddelsden-Popper (RP) phase.[10] These planar defects are usually formed in connection with the planar-type accommodation of excess alkaline-earth oxides by interleaving slabs of the rock-salt structure within the perovskite structure. Here the images suggest that the planar defect formed in the (La, Sr)FeO_3 ceramic is the interleaving a single-layered FeO_2 block within the perovskite structure with a shear vector ½ [110]. Therefore, the occurrence of these RP-phases is closely linked to a deviation from the ideal ***cation*** stoichiometry of the bulk matrix and compensates for the local non-stoichiometry. Most importantly, these defects are not related to oxygen vacancies and are found not to exist in the subsequently annealed samples. The formation of the RP phase in the as sintered materials is clearly not related to changes in ionic conductivity at elevated temperatures.

In fact, the conductivity of the reduced materials appears to be controlled by the formation of the BM- phase. The Z-contrast and EELS results clearly demonstrate that the planar structures observed under reducing conditions are caused by the ordering of oxygen vacancy clusters in every second FeO_2 column (**Figure 2** and **Figure 3**). At temperatures below 1073 K and $P_{O_2} = 1*10^{-6}$ Pa the oxygen vacancy ordered domains are randomly oriented throughout the bulk. Due to the arbitrary direction of this ordering, with no preferential orientation or clustering into larger ordered domains, the overall diffusion performance of the material should be very high (as the reduced planes act as conductivity channels). A disordered arrangement (on the scale of a few nm) of the ordered vacancies is therefore essential for the high oxygen transport material performance. Under higher reducing conditions (lower oxygen partial pressure and higher temperatures) more oxygen vacancies are created. However, the formation of these vacancies does not occur in every position with identical probability. It seems that the already reduced (dark) columns have an increased vacancy formation rate, or from the opposite point of view, a lower vacancy formation energy. The iron valence data for this situation show a decrease in the iron valence from +2.6 to +2.3. The bright columns on the other hand remain mostly unchanged or even a slight increase in the iron valence (i.e. oxygen content) is measured. This means that the two atomic layers in the same material have a different thermodynamic behavior.

A further increase in temperature causes even more oxygen to diffuse out of the material and leave behind continuously growing micro domains of ordered vacant oxygen lattice sites. The oxygen of the already reduced columns is decreased even further, as the iron valence drops from +2.3 to +2.0, while the unreduced columns (bright) keep their original oxygen content (iron valence +2.8). The dark lines represent a further reduction of the BM-phase. At this point the micro domains start to exhibit a distinct bulk and boundary behavior. Under these conditions the huge ordered domains are assumed to not act as high conductivity paths anymore, as oxygen flow is only possible in one direction. Rather than flowing along the shortest line of the concentration gradient, the oxygen atoms must move in the direction of the ordered domains. The grains oriented perpendicular to the oxygen gradient do not contribute to the overall oxygen current across the membrane and the oxygen ions must flow long a percolative path. Four probe conductivity measurements seem to confirm this hypothesis.

At temperatures of 1350 K and pressure around 10^{-9} Pa the concentration of oxygen vacancies in the dark (vacancy containing) columns reaches a critical value. Here the already highly reduced columns cannot host any more oxygen vacancies without losing their structural integrity. Consequently these columns collapse and form the observed stacking faults of double FeO_2 layers, or the Aurivillius phase. [11] These second phases then act as nucleation sites/barriers to preferentially orient the ordered domains, thereby forming huge ordered domains. Four-probe conductivity measurements under these conditions indicate a sudden drop in the ionic and electronic conductivity, consistent with this effect. The decrease in conductivity can be explained by the preferential flow direction in the bulk of a single grain and that fact that practically no oxygen transport occurs perpendicular to the stacking faults.

Conclusions

In conclusion, the ability to observe the structure, characterize the composition and to map valence state changes at atomic resolution in various thermodynamic environments provides an unparalleled capability to understand the effects of oxygen vacancy ordering in electronic and ionic conducting perovskite. This ordering of oxygen vacancies gives rise to the ionic conductivity of the material at elevated temperatures, but the decline in the conductivity can be explained by the progressive growth of the ordered domains. Although we are not able to acquire atomic resolution images at temperatures higher than 724 K, we now have the opportunity to test the predictions of conventional defect chemistry on the atomic scale. The results presented here clearly show that the oxygen formation energy is not constant from one atomic column to another: the defect chemistry differs dramatically from one FeO_2 layer to the next. Ultimately the structure becomes unstable and forms stacking faults, which will prohibit the oxygen diffusion through this grain. Correlations of this structural analysis with conductivity measurements will exhibit this proposed relationship.

Acknowledgements

This research was sponsored by the U.S. Department of Energy under grant numbers DE-FG02-96ER45610 and No. DE-FC26-99FT40054. The experimental results were obtained on the JEOL 2010F operated by the Research Resources Center at UIC and funded by NSF under grant number DMR-9601796. We thank H.U. Anderson and T.J Mazanec for the provision of the samples and A.C. Palanduz for the discussions and conductivity measurements.

(1) Huang, K, Tichy, RS and Goodenough, JB, *J. Am. Ceram. Soc.* **81**, 2565-75 (1998)
(2) James, EM and Browning, ND, Ultramicroscopy 78, 125 (1999)
(3) James, EM Browning, ND Nicholls, AW, Kawasaki, M, Xin, Y, and Stemmer, S, J. Electr. Micr. 47(6), 561 (1998).
(4) Egerton, RF, Electron Energy Loss Spectroscopy in the Electron Microscope, Plenum, New York (1986).
(5) Browning, ND, Chrisholm, MF, and Pennycook, SJ, Nature 366, 143 (1993)
(6) Nellist, PD, and Pennycook, SJ, Ultramicroscopy 78, 111 (1999).
(7) Jesson, DE, and Pennycook, SJ, Proc. R. Soc. Lond. A 449, 273 (1995)
(8) Klie, RF, and Browning, ND, Appl. Phys. Lett., **77 (23)**, 3737, 2000
(9) Browning, ND, Buban, JP, Moltaji, HO, Duscher, G, Pennycook, SJ, Rodrigues, RP, Johnson, K, and Dravid, VP, *Appl Phys Lett.* **74**, 2638-2640. (1999)
(10) Ruddlesden, SN, and Popper P, *Acta Crystallogr.*, **11**, 54 (1958)
(11) Aurivillius, B, *Ark. Kemi*, **2**, 519 (1950)

HYDROGEN TRANSPORT CATALYTIC MEMBRANE REACTORS

Anthony F. Sammells, Michael V. Mundschau, Richard Mackay, and Shane E. Roark

Eltron Research Inc.
4600 Nautilus Court South
Boulder, CO 80301
www.eltronresearch.com

Introduction

Eltron Research Inc. is developing low cost, multi-phase membranes for separating hydrogen from hydrogen containing feedstreams. This is being addressed using material composites which facilitate high proton and electron conduction. Membranes are being developed for high (>750°C) and low (<425°C) temperature applications and have been successfully operated under a high pressure differential (250 psi) for extended times. Under ambient pressure, hydrogen transport rates >25mL/cm^2/min have been achieved at 400°C.

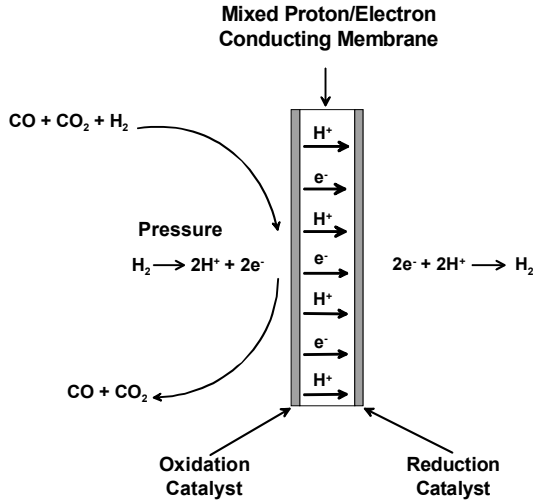

Figure 1. Schematic diagram of the ceramic membrane process for separating hydrogen from a mixture of gases.

Experimental

Doped perovskites $A_{1-x}A_x'B_{1-y}B_y'O_{3-\delta}$, where x and y are the fractions of dopants in the A and B sites, respectively, and δ is the number of oxygen vacancies,[1-3] were prepared using conventional high temperature solid state synthesis techniques. Corresponding cermets $A_{1-x}A_x'B_{1-y}B_y'O_{3-\delta}$/M were prepared by sequential pressing and sintering at elevated temperatures under controlled atmosphere conditions.

The inlet hydrogen source was initially diluted with helium. This facilitated determination of the membrane seal quality. H_2 and He fractions within inlet and sweep streams were determined by TCD-GC using a Shimadzu GC 14-A with a 12-ft. by 1/8-in. stainless steel Carbosphere column. Ultra-high purity Ar was used as the carrier gas to optimize detection limits for hydrogen and helium.

Results and Discussion

Cermet membranes under development at Eltron consist of a proton conducting ceramic phase and a low cost hydrogen permeable metallic phase. Figure 2 shows an SEM image of a cermet membrane.

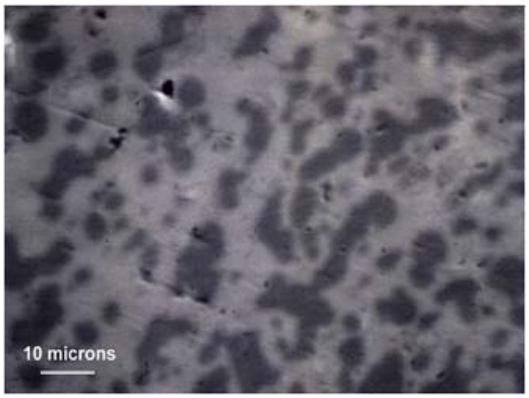

Figure 2. SEM image of a cermet membrane containing 46 wt.% metal phase. The proton-conducting ceramic appears as the light regions and the metal phase as the dark regions.

Hydrogen flux, *J*, through dense mixed proton/electron conducting membranes in the absence of surface kinetic limitations is dependent on the membrane thickness, *t*, according to,

$$J = \frac{\sigma_{amb} E}{t}$$

where *E* is the Nernst potential. Figure 3 contains a plot of theoretical hydrogen transport rates versus membrane thickness.

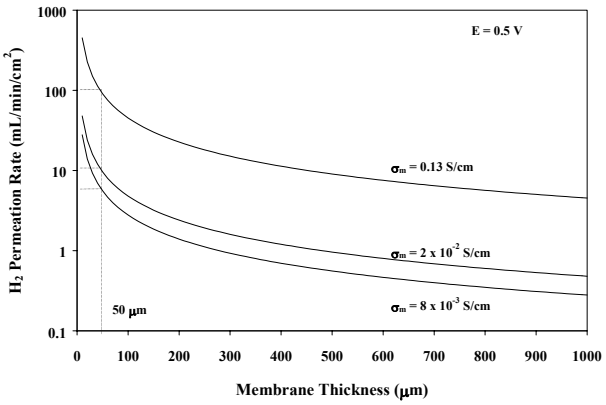

Figure 3. Plot showing H_2 transport rates as a function of membrane thickness for a range of bulk conductivities and a H_2 concentration gradient equivalent to 0.5V.

Several approaches currently are being pursued at Eltron for fabrication of thin film hydrogen separation membranes. The most straightforward strategy is to deposit a thin layer of dense membrane material on a porous support of the same composition. The challenge for this approach is to match the shrinkage rates of the support and thin film to enable sintering without membrane cracking. Shrinkage of the thin film was controlled by varying the surface area of the powder prior to sintering, whereas, shrinkage of the support was controlled by adjusting the material porosity. Using this strategy, the shrinkage mismatch between the thin film and support was

minimized to a only a few percent, and homogenous crack-free thin films approximately 100 Φm thick routinely are prepared. An example is shown in the SEM image in Figure 4.

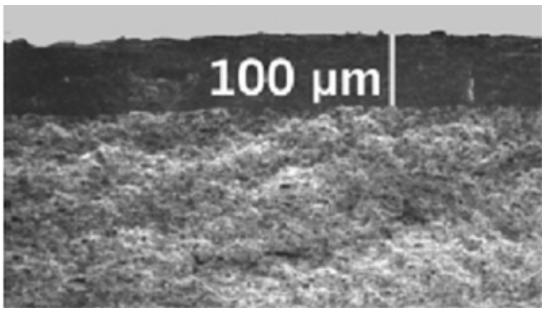

Figure 4. SEM image showing a cross section of a 100 µm thick dense membrane deposited onto a porous support of the same composition.

Hydrogen separation membranes have been operated at 250 psi pressure differential between the hydrogen feed and sweep side at elevated temperatures continuously for >1000 hrs. The performance of our low cost membranes operating under ambient pressure conditions as a function of temperature (Figure 5) and Ar sweep rate (Figure 6) on the hydrogen permeate side are shown below. As can be seen, hydrogen diffusion fluxes >25 mL/cm^2/min have been achieved at 400°C.

A simplified block diagram of a hydrogen separation unit installed in an integrated gasification combined cycle (IGCC) plant is shown in Figure 7. The diagram shows three options for installation, indicated as baseline, alternative 1, and alternative 2. The alternative 1 option assumes the membrane materials will be tolerant to sulfur and particulate material, and that the raw syngas from coal gasification can be sent directly to the unit. The baseline option also assumes sulfur tolerance, but the gas stream must be filtered prior to entering the unit. If the membrane materials are not sulfur tolerant, then alternative 2 will be necessary, and the unit will be inserted after desulfurization. This condition will require reheating the gas stream through a heat exchange prior to entering the hydrogen separation unit.

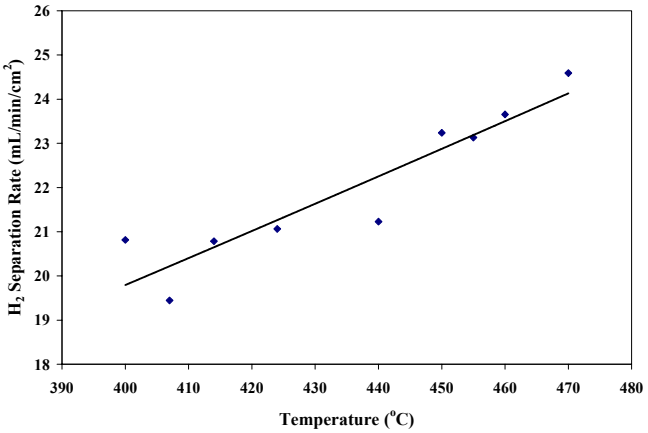

Figure 5. Hydrogen diffusion as a function of operating temperature under ambient pressure conditions. Ar sweep rate on permeate side 300 mL/min.

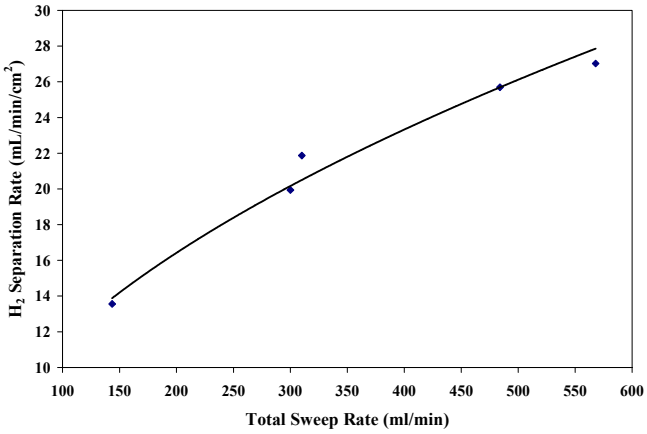

Figure 6. Hydrogen diffusion as a function of Ar sweep rate on the permeate side at 400°C. Ambient pressure conditions.

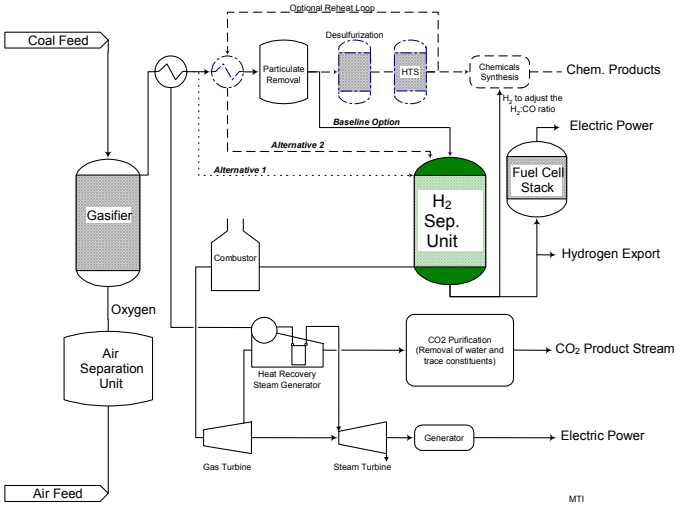

Figure 7. Diagram of an IGCC plant with three installation options for a hydrogen separation unit.

Acknowledgment

This work is supported by DOE/NETL under Contract Number DE-FC26-00NT40762.

References

(1) White, J. H.; Schwartz, M.; and Sammells, A. F. U.S. Patent 5,821,185, October 13, 1998.

(2) White, J. H.; Schwartz, M.; and Sammells, A. F. U.S. Patent 6,037,514, March 14, 2000.

(3) White, J. H.; Schwartz, M.; and Sammells, A. F. U.S. Patent 6,281,403, August 28, 2001.

HYDROGEN SEPARATION THROUGH DENSE MIXED PROTONIC-ELECTRONIC CONDUCTING MEMBRANES

Eric D. Wachsman, Sun-Ju Song and Jamie Rhodes

Department of Materials Science and Engineering
University of Florida, Gainesville, FL 32611-6400

Introduction

Membrane reactor technology holds the promise to circumvent thermodynamic equilibrium limitations by *insitu* removal of product species, resulting in improved chemical yields. Recent advances in mixed-conducting oxide-membrane technology present the possibility for a dramatic reduction in the cost of converting petroleum and coal derived feed stocks to hydrogen and other "value added" hydrocarbons. We have developed mixed protonic-electronic conducting materials for use as solid-state dense high temperature hydrogen permeation membranes. These membrane materials are perovskite ($BaCe_{1-x}M_xO_3$ and $SrCe_{1-x}M_xO_3$) based high temperature protonic conductors Both protonic and electronic conductivity are necessary to achieve hydrogen permeation through the solid-state. Therefore, we are modifying the chemistry of $BaCe_{1-x}M_xO_3$ and $SrCe_{1-x}M_xO_3$ by substitution of a multivalent dopant cation (M = $Eu^{+2/+3}$) in the Ce lattice site to obtain electronic conductivity.

We have studied the defect chemistry of these materials to determine regions of $P_{H2}/P_{H2O}/P_{O2}$ where the membrane exhibits both protonic and n-type electronic conductivity [1-4]. Using this defect chemistry information and conductivity data we determined mobilities and calculated the H_2 flux through 1 mm thick $SrCe_{0.95}Y_{0.05}O_{3-\delta}$ [3,4]. At 700°C the calculated maximum H_2 flux was between 1.5 x10^{-9} and 2.3 x 10^{-8}, depending on feed and sweep $P_{H2}/P_{H2O}/P_{O2}$ conditions [4].

In this paper we report on measured H_2 flux of $BaCe_{1-x}M_xO_3$ and $SrCe_{1-x}M_xO_3$ and compare it to calculated flux.

Experimental

Polycrystalline samples of multivalent and univalent $SrCe_{1-x}M_xO_3$ ($SrCe_{0.95}Eu_{0.05}O_{3-\delta}$ and $SrCe_{0.95}Sm_{0.05}O_{3-\delta}$) and $BaCe_{1-x}M_xO_3$ ($BaCe_{0.85}Eu_{0.15}O_{3-\delta}$ and $BaCe_{0.85}Gd_{0.15}O_{3-\delta}$) were prepared by conventional solid-state reaction methods. High-purity oxide powder of $SrCO_3$ or $BaCO_3$ (99.9% Alfa Aesar), CeO_2 (99.9% Alfa Aesar), and Eu_2O_3, Gd_2O_3 or Sm_2O_3 (99.99%, Alfa Aesar) were mixed, ground in a ball mill with stabilized zirconia balls in ethanol and calcined at 1573K for 10h in air. The calcined oxides were then crushed, sieved to < 45microns, ground in a ball mill again, pressed into pellets, cold-isostatic-pressed, and sintered at 1773K for 10h in air. The densities of the resultant disks were 96% of the theoretical. X-ray diffraction spectra confirmed that all specimens obtained in this way exhibit a single phase perovskite structure.

Hydrogen permeation measurements were performed on dense disks, 24 mm diameter × 1-2 mm thickness. The planar surfaces of the disk were polished down to #1200 grit SiC paper. Polished disks were sealed with ceramic sealant to alumina tubes so that the open surface was exposed to feed gas (H_2/N_2 mixtures). The sweep side had a constant flow of 20ccm helium. The hydrogen content of the permeate stream was measured using a mass spectrometer (Q100MS Dycor Quadlink Mass Spectrometer). Leakage of neutral gas through pores in the sample or through an incomplete seal was checked by measuring the argon content of the permeate stream. No discernible leak was detected. See references 4 and 5 for details.

Results and Discussion

From the hydrogen concentration measurements in the helium sweep side of the permeation assembly and the helium flow rate, the total hydrogen permeation fluxes (mol/sec) were calculated, assuming ideal gas law, and then the permeation fluxes (mol/cm^{2}sec) calculated from the effective surface area of the membrane disks.

The variation in hydrogen flux with temperature for Eu-doped and Sm-doped $SrCeO_3$ is given in Fig. 1. The hydrogen fluxes increase with temperature for both systems and the $SrCe_{0.95}Eu_{0.05}O_{3-\delta}$ exhibits higher permeability in comparison with $SrCe_{0.95}Sm_{0.05}O_{3-\delta}$ over the entire temperature range investigated.

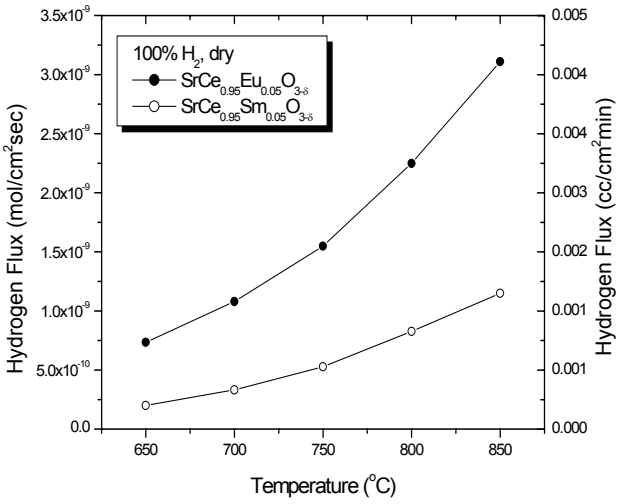

Figure 1. Comaprison of H_2 fluxes through $SrCeEuO_3$ and $SrCeSmO_3$ as a function of temperature.

The influence of an applied hydrogen chemical potential gradient at various P_{H2O} on the hydrogen permeability was also studied [5]. The hydrogen permeation flux of the Eu-doped specimen consistently showed higher hydrogen permeability compared to that of the Sm-doped specimen. The dopant dependence of hydrogen permeability can be explained by the increase in n-type electronic conduction by the multivalent cation under low P_{O2} conditions [1-4].

$BaCeO_3$'s have higher protonic conductivity than $SrCeO_3$'s. Therefrore, we investigated the H_2 permeation of multivalent doped $BaCe_{0.85}Eu_{0.15}O_{3-\delta}$ vs. that of univalent doped $BaCe_{0.85}Gd_{0.15}O_{3-\delta}$ [5]. The $BaCe_{0.85}Eu_{0.15}O_{3-\delta}$ exhibited significantly higher H_2 permeation than $BaCe_{0.85}Gd_{0.15}O_{3-\delta}$ due to it's higher n-type electronic conduction. Further, the $BaCe_{0.85}Eu_{0.15}O_{3-\delta}$ had higher H_2 permeation than $SrCe_{0.95}Eu_{0.05}O_{3-\delta}$ due to it's higher protonic conductivity.

Conclusions

Hydrogen permeability of $BaCe_{1-x}M_xO_3$ and $SrCe_{1-x}M_xO_3$ membranes were studied by gas permeation measurements as a function of temperature, P_{H2} gradient, and P_{H2O} gradient. The measured fluxes with the $SrCe_{1-x}M_xO_3$ membranes are in good agreement with our earlier modeling results [4].

The effect of dopant ion on hydrogen permeability through 1-2 mm thick membranes was investigated. In both cases the membrane

with the multivalent $Eu^{+2/+3}$ dopant exhibited higher hydrogen permeability. Further effort is required to enhance electron conductivity of Eu-doped cerates by adjusting doping level, increasing the effective surface area and/or improving hydrogen exchange properties at the surface.

Acknowledgement. This work was supported by the U.S. Department of Energy, Contract W-31-109-Eng-38, NASA, Contract NAG3-2750, and CANMET, Contract 23341-8-3222/001-SS.

References

(1) S. J. Song, E. D. Wachsman, S. E. Dorris, and U. Balachandran, *Solid State Ionics*, **149**, 1-10 (2002).
(2) S. J. Song, E. D. Wachsman, S. E. Dorris, and U. Balachandran, *J. Electrochem. Soc.,* accepted
(3) S. J. Song, E. D. Wachsman, J. Rhodes, S. E. Dorris, and U. Balachandran, *J. Electrochem. Soc.,* submitted
(4) S. J. Song, E. D. Wachsman, J. Rhodes, S. E. Dorris, and U. Balachandran, *J. Electrochem. Soc.,* submitted
(5) J. Rhodes and E. D. Wachsman In *Solid State Ionic Devices II - Ceramic Sensors*, Proc. Electrochem. Soc., E.D. Wachsman, W. Weppner, E. Traversa, M. Liu, P. Vanysek, and N. Yamazoe, Ed., **2000-32**, 137-147 (2001).

Novel Composite Membranes for Hydrogen Separation from Coal Gasification Streams

Michael Schwartz, Brian S. Berland, Sabina K. Gade and Ronald W. Schaller

ITN Energy Systems, Inc.
8130 Shaffer Parkway
Littleton, CO 80127

Introduction

Hydrogen separation membranes have been identified by the Department of Energy as an "enabling" technology for future "Vision 21" power plants – plants that will be substantially cleaner and more efficient than today's power plants. ITN Energy Systems, Inc. is developing composite membranes for the separation of hydrogen from coal gasification streams for use in the "Vision 21" plant. The fundamental approach is based on Ion Conducting Ceramic Membranes (ICCM) that remove hydrogen from the gasification streams. The membrane process also results in a stream of concentrated carbon dioxide suitable for subsequent sequestration.

The technical approach for achieving the program objectives is three-fold: novel materials development, the integration of materials, module design and fabrication techniques and plant engineering design. The basic building block of the membrane system is a tri-layer consisting of the thin-film, mixed proton and electron conducting membrane and a porous catalyst layer on each side. This structure is illustrated in Figure 1.

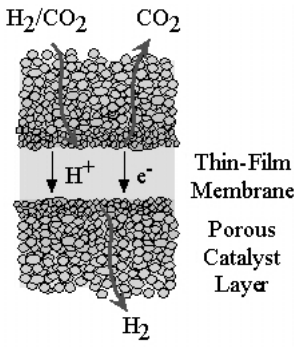

Figure 1. Schematic illustration of hydrogen separation process using an ion conducting ceramic membrane.

As illustrated in Figure 1, the H_2 separation membrane needs to conduct both protons and electrons. In this program, the focus is on cermets consisting of a proton conducting ceramic combined with a metal for electrical conductivity. For proton conducting materials, previous work has focused primarily on rare-earth-doped strontium cerate, strontium zirconate and barium cerate.[1-8] These materials have high ionic conductivities, ~10^{-2} S/cm at 600-800 ^{o}C. However, they are poor electrical conductors, precluding their use in H_2 separation membranes.

Recently, Balachandran and co-workers at Argonne National Laboratory have developed cermet membranes utilizing strontium and barium cerates as the proton conducting phase and nickel as the electron conducting phase.[9,10] They reported quite high H_2 flux rates, $9x10^{-2}$ $cm^3/min\text{-}cm^2$, at 750 ^{o}C with relatively thick membranes, ~0.5 mm. Since the flux rate is inversely proportional to the membrane thickness, commercially attractive flux rates could be achieved with membranes of thickness on the order of tens of microns.

One major concern of membranes comprised of strontium and barium cerates is their chemical stability. Specifically, barium oxide, and to a lesser extent, strontium oxide, react with both water and carbon dioxide, major components of gasification streams, to form hydroxides and carbonates, respectively. This reaction is less of a problem at high temperatures but still can be the deleterious to membrane chemical and mechanical stability during the membrane fabrication process and during membrane module startup and shutdown processes.

To overcome this problem with membrane reactivity, ITN is developing alternate proton conductors that are based on pyrochlore phases with little or no barium or strontium content. Pyrochlore phases are attractive for this application for several reasons. Recent work has pointed to specific pyrochlore phases that exhibit proton conductivity.[11-13] The pyrochlore crystal structure is based on the fluorite structure with additional oxygen vacancies that promote proton conductivity. The fluorite structure typically shows high chemical and mechanical stability which is not expected to be degraded by the presence of additional oxygen vacancies. As an example, the well-known oxide conductor, yttria-stabilized zirconia, crystallizes in the fluorite structure. In this program, ITN is developing new materials by rationally doping the base pyrochlore materials. The goal is to obtain materials which exhibit high ionic conductivity and maintain high chemical and mechanical stability.

Experimental

Pyrochlore membrane powders were prepared by the Pechini process.[14-16] This method starts with an aqueous solution of metal nitrates. Citric acid and ethylene glycol are then added and heated and a gel is formed through a polymerization reaction. The resulting gel is then fired at relatively low temperatures, 700-900 ^{o}C, to yield a fine, homogenous powder of the desired metal oxide phase.

Composite membrane disks were fabricated by uniaxial pressing. In this process, the ceramic powder was ball-milled with Ni powder. An aqueous binder solution (2wt% polyvinyl alcohol) was added and the resulting slurry dried in air. The dried mixture was then passed through a 48 mesh sieve, placed in a cylindrical die and then pressed uniaxially. The resulting membrane disks were then fired at 300 ^{o}C in air for binder burnout followed by sintering at 1400-1450 ^{o}C in 3% H_2 in Ar. Membranes prepared in this manner were typically >90% dense.

Membranes were tested for hydrogen flux by first brazing the membranes into gas-tight holders machined from Inconel 600. Mixtures of H_2, N_2, H_2O and CO_2 were passed over one surface of the membrane while He was passed over the opposite surface. The H_2 concentration in the He stream was determined by gas chromatography. The H_2 flux was determined from the concentration and measured He flow rate. Any leak through the membrane or seal was determined by measuring the N_2 or CO_2 in the He stream. H_2 flux through the membrane was adjusted for this leakage which typically was a few percent of the H_2 flux.

Results and Discussion

Approximately twenty doped pyrochlore materials have been identified as potential proton conductors. To date, several doped pyrochlore phases have been prepared using powders synthesized as above. Figure 2 shows the X-ray diffraction (XRD) pattern of one particular sample. The pattern shows no reflections due to any of the constituent metal oxides, indicating that it is single-phased. Additionally, the broad reflections are indicative of a very fine powder.

The H_2 flux rate through a cermet membrane is shown in Figure 3. This is one particular composition which consists of a pyrochlore proton conductor with 50wt% Ni. The membrane was tested under

several feedstreams containing H_2, N_2, CO_2 and H_2O. Specific feedstreams are shown in Figure 3. At 50% H_2 in N_2, a flux rate greater than 0.3 ml/min-cm^2 (normalized to 1 mm thickness) was achieved. The membrane was stable over operation at 900 ^oC for several days. The sample was also thermally cycled several times over this period with no loss of flux rate. One important point is that these membranes did not have any catalysts on the surfaces and in fact had been polished smooth for the sealing procedure. This would tend to result in lower flux rates as the surface area would be greatly reduced by a lack of roughness.

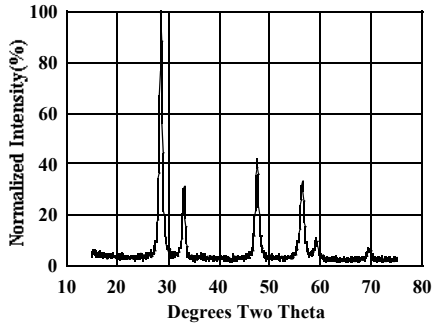

Figure 2. XRD pattern of a doped pyrochlore prepared using the Pechini process.

Figure 3 also shows the effect of the introduction of both CO_2 and H_2O. Here the flux was decreased relative to the dry H_2 in N_2 feedstream. This drop was attributed to a decrease in the H_2 concentration in the feedstream due to the presence of water and the reverse water-gas shift reaction:

$$H_2 + CO_2 \rightarrow H_2O + CO \qquad (1)$$

Measurement of the gases in the feedstream indicated that CO was being produced. At this point, the exact concentration of CO in the feedstream due to the reverse water-gas shift reaction has not been measured. The results in Figure 3 also indicate that the membrane is stable over at least several days with both H_2O and CO_2 in the feedstream.

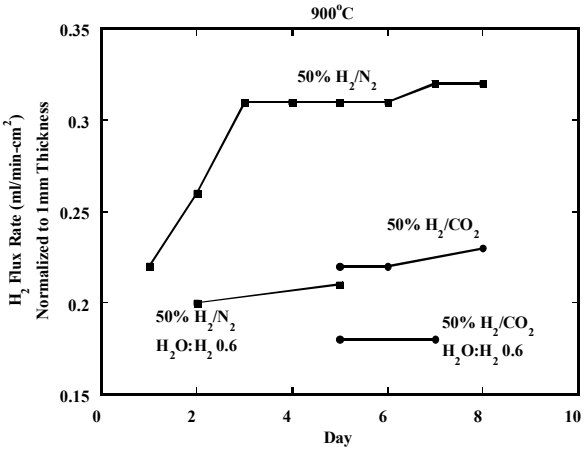

Figure 3. Plot of H_2 flux rate vs. time in different feedstreams.

Conclusion

In conclusion, ITN has identified novel proton-conducting pyrochlore phases. These materials have been incorporated into cermet membranes for the separation of H_2 from mixed gas streams. Initial experiments indicate that these materials do in fact conduct protons and appear to be stable to both H_2O and CO_2 at least over a several day period. The flux rates are roughly a factor of eight lower than what will be required in a commercial process. To enhance the observed flux rates, work is continuing at ITN in two areas. One area is the continued development of novel pyrochlore phases. Here selective doping is being used to increase the overall protonic conductivity. Second, the use of surface catalysts will also be investigated to enhance the surface exchange rates.

Acknowledgement. This work was supported by the U.S. Department of Energy through contract DE-FC26-01NT40793, Dr. Arun Bose, Program Manager.

References

(1) Iwahara, H.; Esaka, T.; Uchida, H.; Maeda, N. *Solid State Ionics* **1981,** *3/4*, 359.
(2) Iwahara, H. *Solid State Ionics* **1988,** *28*, 573.
(3) Lee, W.; Nowick, A.S.; Boatner, L.A. *Solid State Ionics* **1986**, *18/19*, 989.
(4) Iwahara, H.; Uchida, H.; Ono, K.; Ogaki, K. *J. Electrochem. Soc.* **1988**, *135*, 529.
(5) Iwahara, H.; Uchida, H.; Morimoto, K. *J. Electrochem. Soc.* **1990**, *137*, 462.
(6) Taniguchi, N.; Hatoh, K.; Niikura, J.; Gamo, T. *Solid State Ionics* **1992**, *53-56*, 998.
(7) Bonanos, N.; Ellis, B.; Knight, K.S.; Mahmood, M.N. *Solid State Ionics* **1989**, *35*, 179.
(8) Bonanos, N.; Ellis, B.; Mahmood, M.N. *Solid State Ionics* **1991**, *44*, 205.
(9) Balachandran, U.; Lee, T.H.; Zhang, G.; Dorris, S.E.; Rothenberger, K.S.; Martello, D.V.; Cugini, A.V.; Siriwardane, R.V.; Poston, Jr., J.A.; Fisher, E.P. Presented at the 6th Natural Gas Conversion Symposium, Girdwood, AK, June 2001.
(10) Balachandran, U.; Lee, T.H.; Wang, S.; Dorris, S.E.; Rothenberger, K.S. Presented at the 18th Annual International Pittsburgh Coal Conference, Newcastle, Australia, Dec. 2001.
(11) Shimura, T.; Komori, M.; Iwahara, H. *Solid State Ionics* **1996**, *86-88*, 685.
(12) Labrincha, J.A.; Frade, J.R.; Marques, F.M.B. *Solid State Ionics* **1997**, *99*, 33.
(13) Omata, T.; Otsuka-Yao-Matsuo, S. *J. Electrochem. Soc.* **2001**, *148*, E252.
(14) Duran, P.; Capel, F.; Tartaj, J.; Moure, C. *J. Mater. Res.* **2001**, *16*, 197.
(15) Xu, Y.; Chen, X.M.; Wu, Y.J. *J. Mater. Sci.: Mater. Elect.* **2000**, *11*, 633.
(16) Tai, L.-W.; Lessing, P.A. *J. Mater. Res.* **1992**, *7*, 502.

A NOVEL PROCESS FOR HYDROGEN SEPARATION USING MIECS: THEORETICAL ANALYSIS

Srikanth Gopalan and Cui Hengdong

15 St.Mary's Street, Department of Manufacturing Engineering, Boston University, Boston, MA 02215

Introduction

Hydrogen separation from hydrocarbon reformate using mixed proton and electron conductors is presently an active area of research [1-3]. In this process, a pressure differential is maintained across the membrane and hydrogen is transported from the higher hydrogen partial pressure (reformate side) to the lower hydrogen partial pressure side. A few selected examples based on this approach include Balachandran et al. [1], Wachsman and Jiang [2] and White et al. [3]

A different approach described here employs a mixed oxygen ion and electron (or hole) conductor and has not been reported widely in the literature. In this approach, reformate consisting of CO and H_2 is fed to one side of the membrane and water vapor to the other side. Dissociation of water vapor into hydrogen and oxygen ions occurs on the water vapor side of the membrane, followed by ambipolar transport of oxygen across the membrane where the reformate is oxidized to water vapor and carbon dioxide. Thus hydrogen is segregated on the water vapor side. This approach has the potential to generate higher hydrogen fluxes than possible using the mixed proton and electron conductors.

Hydrogen Separation Using Oxygen Ion Conducting MIECs

The concept of using O^{2-} conducting MIECs to separate hydrogen is shown in Figure 1.

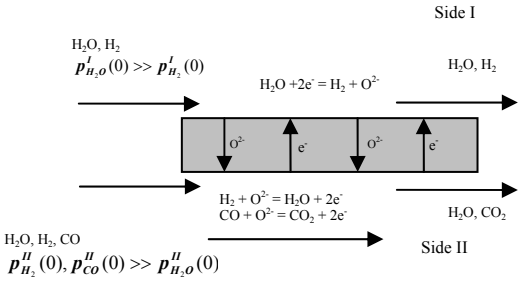

Figure 1. Principle of hydrogen separation using a mixed oxygen ion and electron conductor

Equivalent Circuit Analysis

We have modeled the process shown schematically in Figure 1 using a simple equivalent circuit shown in Figure 2. To simplify the analysis it is assumed that electronic and ionic conductivities (or resistivities) are independent of the partial pressure of O_2, p_{O_2}. In reality these conductivities will depend on the local p_{O_2} in the membrane. However, this complicates the analysis and is not required for a first level estimation of the hydrogen fluxes. The driving Nernst potentials $E_{0,i}$ are a function of position along the direction of gas flow. Each individual leg of the equivalent circuit containing a driving Nernst potential, electronic resistor R_{el} and an ionic resistor R_i has an incremental current dI_x.

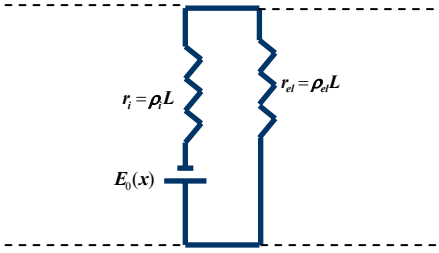

Figure 2. Equivalent circuit model for hydrogen separation using MIECs.

The incremental current is given by,

$$dI_x = \frac{E_0(x)}{R_{el} + R_i} \tag{1}$$

The resistances R_{el} and R_i are given by,

$$R_{el} = \frac{t\rho_{el}}{B.dx} \tag{2a}$$

$$R_i = \frac{t\rho_i}{B.dx} \tag{2b}$$

In equations (2a) and (2b), t is the thickness of the membrane, ρ_{el} and ρ_i are the electronic and ionic resistances which are assumed to be independent of p_{O_2}, B is the width of the membrane (i.e. membrane dimension perpendicular to the plane of the paper) and dx is the incremental dimension in the direction of gas flow. Substituting equations (2a) and (2b) in (1) and summing over the length of the membrane, we get,

$$I_{total} = \sum \frac{E_0(x).B.dx}{t(\rho_{el} + \rho_i)} \tag{3}$$

Since the driving Nernst potential is a function of p_{O_2} which is a continuous function of the position x, the summation can be replaced by an integral as given below.

$$I(x) = \int_{x=0}^{x=x} \frac{E_0(x).B.dx}{t(\rho_{el} + \rho_i)} \tag{4}$$

In equation (4), $I(x)$ represents the cumulative current from the inlet to an arbitrary position along the direction of gas flow. Note that the net current through the membrane is zero, i.e. the current flux due to the transport of the O^{2-} is exactly balanced by the concurrent current flux of holes (or the countercurrent current flux of electrons). The driving Nernst potential is given by,

$$E_0(x) = \frac{RT}{4F} \ln\left[\frac{p_{O_2}^{I}(x)}{p_{O_2}^{II}(x)}\right] \quad (5)$$

For the purposes of this analysis it is assumed that the inlet gas on side II comprises of a mixture of CO and H_2 with trace amounts of H_2O and the inlet gas on side I comprises of H_2O with trace amounts of H_2. The local p_{O_2} s in equation (5) will be determined by the gas phase equilibria. We define two more terms which we use in the analysis, namely the flow ratio λ and the degree of conversion ζ. The flow ratio λ is ratio of the inlet steam flow on side I to the H_2 and CO flow on side II. The degree of conversion ζ is the ratio of exit flow of H_2 on side I to the H_2 and CO flow on side II. It can be shown that assuming that no surface exchange limitations exist,

$$\zeta = \frac{\lambda}{1+\lambda} \quad (16)$$

Results and Discussion

Figure 3 shows the variation of Nernst potential with dimensionless position Γ in the direction of gas flows, for various values of λ. At smaller values of Γ, the Nernst potential is higher for higher values of λ. Further, the slope of the Nernst potential versus Γ is smaller for higher values of λ. This is to be expected since a higher H_2O flow on side I results in a higher Nernst potential. The slower decrease of Nernst potential at higher λ values signifies slower consumption of the driving force for O^{2-} flux (and thus H_2 flux).

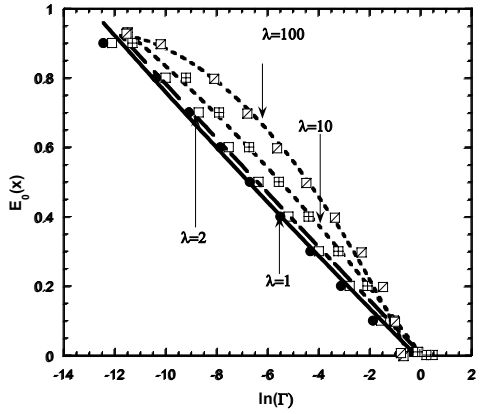

Figure 3. Variation of Nernst potential with dimensionless position for various flow ratios

Figure 4 shows the degree of conversion as a function of the flow ratio calculated from equation (16). As can be seen, the degree of conversion approaches unity only at very large λ values. High values of λ imply higher input of steam which will translate to a higher cost. However, fairly high degrees of conversion (~ζ =0.75) can be achieved at modest flow ratios (λ =3). Table 1 shows the maximum obtainable degree of conversion and hydrogen fluxes (shown as equivalent current density).

Table 1. Maximum Obtainable Degree of Conversion and Current Density (Flux) for Various Flow Ratios

λ	ζ	$J(\max)$: A/cm^2
1	0.5	11.8
2	0.67	12.5
10	0.91	19.7
100	0.99	46.6

The flux calculations shown in Table 1 are based on ionic and electronic conductivities representative of the well known perovskite mixed conductor $La_{1-x}Sr_xCo_yFe_{1-y}O_{3-\delta}$ [4].

Conclusions

A new process for selective separation of hydrogen from reformate using dense MIECs that conduct oxygen ions and electrons (or holes) has been analyzed. The analysis shows that potentially high hydrogen fluxes can be obtained from this process.

Acknowledgment: Seed funding from Boston University for this work is gratefully acknowledged.

References

(1) Balachandran, U.; Guan, J.; Dorris, S.E.; Bose, A.C.; and Stiegel, G.J;and Xu, L. Proc. 5th Int. Conf. on Inorganic Membranes. – Nagoya, Japan, **1998**, p. 192.
(2) Wachsman, E.; and Jiang, N. US Patent # **6,296,687**
(3) White, J.H; Schwartz, M; and Sammels, A.F. US Patent # **6,281,403**
(4) Minh N, Science and Technology of Ceramic Fuel Cells, Elsevier **1995**

DENSE CERMET MEMBRANES FOR HYDROGEN SEPARATION

U. (Balu) Balachandran, T. H. Lee, S. Wang, J. J. Picciolo, J. T. Dusek, and S. E. Dorris

Energy Technology Division
Argonne National Laboratory
Argonne, IL 60439, USA

Introduction

The U.S. Department of Energy's Office of Fossil Energy sponsors a wide variety of research, development, and demonstration programs that aim to maximize the use of the vast domestic fossil resources and ensure a fuel-diverse energy sector while responding to global environmental concerns. Development of cost-effective, membrane-based reactor and separation technologies is of significant interest for applications in advanced fossil-based power and fuel technologies. The purpose of this work is to develop dense hydrogen-permeable membranes for separating hydrogen from mixed gases at commercially significant fluxes under industrially relevant operating conditions. Of particular interest is the separation of hydrogen from product streams that are generated during coal gasification, methane partial oxidation, and water-gas shift reactions.

Membrane development efforts at Argonne National Laboratory (ANL) and the National Energy Technology Laboratory (NETL) have resulted in various ceramic/metal composite (i.e. cermet) membranes that are classified on the basis of the hydrogen transport properties of the ceramic and metal phases. The cermet membranes in this paper are classified as ANL-1, -2, or -3, based on the hydrogen transport properties of the metal and matrix phases. The first class of membranes, ANL-1, contains a metal with low hydrogen permeability in a matrix of $BaCe_{0.8}Y_{0.2}O_{3-\delta}$ (BCY), a mixed proton-electron conductor (1-4). ANL-2 membranes also have a BCY matrix but contain a metal with high hydrogen permeability. In this type of membranes, the metal phase also serves as an additional path for the hydrogen transport. In ANL-3 membranes, the BCY matrix is replaced by a ceramic with superior mechanical properties and thermodynamic stability, e.g., Al_2O_3 or ZrO_2. Specific membranes are identified by a number and a letter, where the number represents the type of the membrane, and the letter indicates a specific combination of metal and matrix phase. For example, ANL-1a is an ANL-1 membrane that contains "metal a" in a matrix of BCY. In this paper, we discuss the results from hydrogen permeation tests of the various cermet membranes.

Experimental

Cermet membranes prepared in this work contain 40 vol.% metal phase unless otherwise noted. BCY powder was prepared at ANL as described elsewhere (5). Powder mixtures were prepared in isopropyl alcohol using a mortar and pestle. They were then pressed uniaxially to prepare disks (22 mm diameter x 2 mm thick) for sintering. ANL-1a and -2a membranes were sintered at 1420°C for 5 h in 4% H_2/balance Ar. ANL-3a membranes were sintered at 1400°C for 5 h in 4% H_2/balance He. ANL-3b membranes were sintered at 1350°C for 12 h in air. For measurement of the hydrogen permeation rate, sintered disks were polished to desired thickness with 600-grit SiC polishing paper. A polished disk was then affixed to an Al_2O_3 tube by using an assembly described elsewhere (6). For the wet condition, feed gas was bubbled through a water bath at room temperature to give ≈0.03 atm H_2O; for the dry condition, feed gas was introduced directly into the furnace from the gas cylinder.

Results and Discussion

The hydrogen permeation rates for ANL-1a, -2a, and -3b are compared in **Figure 1** for a feed gas of 4% H_2/balance He. Among these membranes, ANL-3b exhibited the highest permeation rate, approximately three times that of ANL-1a over the whole temperature range (600-900°C). ANL-3b gave the highest permeation rate because its metal phase had the highest hydrogen permeability of the various metals tested to date.

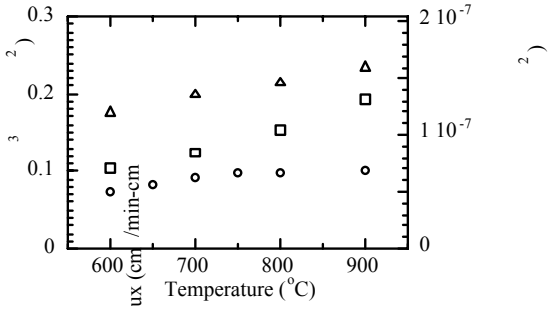

Figure 1. Hydrogen permeation rates through ANL membranes. (○): 0.5-mm-thick ANL-1a. (□): 0.46-mm-thick ANL-2a. (Δ): 0.43-mm-thick ANL-3b.

Figure 2 shows the temperature and thickness dependence of the hydrogen flux through ANL-3b membranes with wet 100% H_2 feed gas. For the 0.1-mm-thick membrane the leakage was high at lower temperatures; therefore, the permeation rate is shown only at 900°C. The hydrogen permeation rate increased with temperature and was proportional to the inverse of membrane thickness, as shown by the inset of **Figure 2**. The inverse dependence of flux on thickness indicates that the bulk diffusion of hydrogen through the metal phase is rate-limiting for thicknesses >0.1 mm.

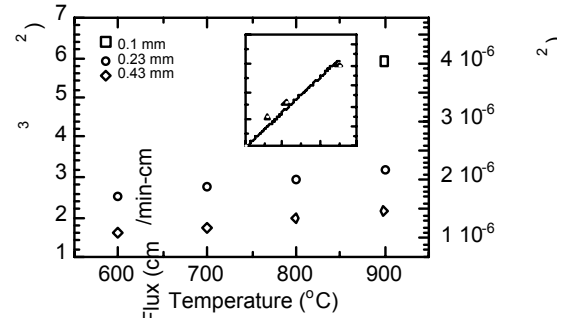

Figure 2. Hydrogen permeation rate through ANL-3b membranes. Inset shows the thickness dependence of permeation rate.

The bulk-limited hydrogen diffusion was further confirmed by measuring the pressure dependence of hydrogen permeation through ANL-3b membrane. **Figure 3** shows the effect of hydrogen partial pressure on the permeation rates through a 0.23-mm-thick ANL-3b membrane at 800 and 900°C. At both temperatures, the flux varies linearly with the difference in square root of hydrogen partial pressure of the feed gas and sweep gas; this relationship is characteristic of bulk-limited hydrogen diffusion through metals (7).

Figure 4 shows the temperature dependence of hydrogen fluxfor a 40-μm-thick ANL-3a membrane, which contained 50 vol.% hydrogen transport metal, before and after it was conditioned in air. Before the conditioning, the membrane gave high hydrogen flux [16.2 cm^3 (STP)/min-cm^2 at 900°C]. However, the flux at 400°C [0.8 cm^3 (STP)/min-cm^2] was much lower than expected based on the known hydrogen permeabilities for the materials in the membrane.

Previous study of the hydrogen transport metal in the ANL-3a membrane suggested that conditioning it in oxygen may increase its hydrogen flux, so it was heated for ≈250 h in air at 800°C. While it is not presently understood how conditioning in oxygen influences the hydrogen flux, the flux increased to 20.0 and 7.6 cm^3 (STP)/min-cm^2 at 900 and 400°C, respectively; the flux at 600°C increased only marginally. Although this membrane contained a higher concentration (50 vol.%) of metal phase, which was different from the one used in ANL-3b membrane, its significantly higher permeation rate can be related primarily to its reduced thickness.

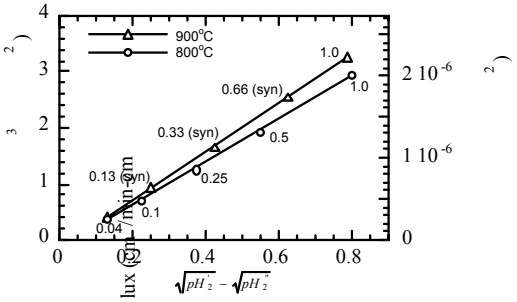

Figure 3. Hydrogen flux through ANL-3b vs. partial pressure of hydrogen (pH_2). pH_2' = pH_2 of feed gas; pH_2'' = pH_2 of sweep gas; values for pH_2 of feed gas is shown on curves; syn = gas mixtures made with simulated syngas.

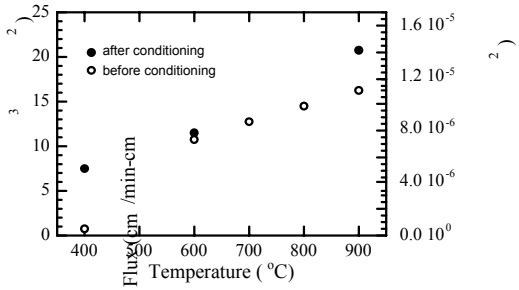

Figure 4. Hydrogen flux through ANL-3a membrane before and after conditioning in air.

The chemical stability of membranes was investigated in simulated syngas. **Figure 5** shows the permeation rates through ANL-2a and -3d as a function of time at 900°C in dry syngas of composition 2.0% CH_4, 19.6% H_2, 19.6% CO, and 58.8% CO_2 (mol.%). The permeation rate through ANL-2a decreased dramatically after only several minutes, whereas the hydrogen flux through ANL-3d was stable for >3 h. Examination of the ANL-2a surface by scanning electron microscopy and X-ray diffraction after the permeation measurements showed that the BCY matrix had decomposed to form $BaCO_3$ and other phases. These results indicate that a chemically stable matrix such as Al_2O_3 or ZrO_2 will be required for application of the membrane in atmospheres with high CO_2 concentrations. The chemical stability of 0.43-mm-thick ANL-3b in simulated syngas (66% H_2, 33% CO, and 1% CO_2) was tested by measuring its hydrogen flux at several temperatures for times up to 190 h. As can be seen in **Figure 6**, no noticeable decrease in flux was observed during testing. Similar tests with 0.23-mm-thick ANL-3b showed no decrease in the hydrogen flux during 120 h of exposure to syngas at 900°C.

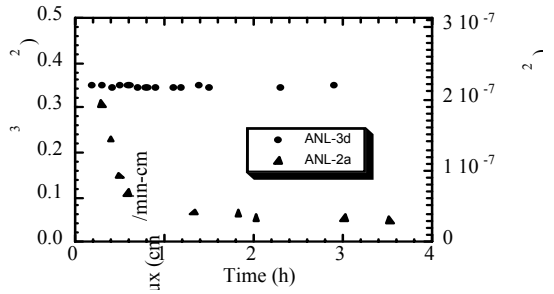

Figure 5. Permeation rates through Al_2O_3-based ANL-3d and BCY-based ANL-2a. Thickness of ANL-3d membrane was 0.53 mm; thickness of ANL-2a, 0.43 mm.

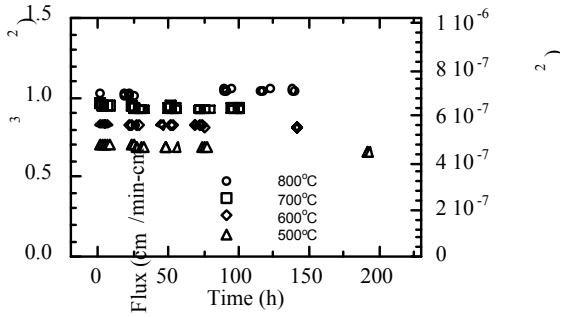

Figure 6. Hydrogen permeation rates through ANL-3b membrane vs. time in simulated syngas at various temperatures.

Conclusions

Various types of cermet membranes have been developed at ANL. The highest measured hydrogen flux was 20 cm^3 (STP)/min-cm^2 for an ANL-3a membrane at 900°C. For ANL-3 membranes with thickness of 0.04-0.5 mm, the permeation rate is limited by the bulk diffusion of hydrogen through the metal phase. The permeation rates in a syngas atmosphere for times up to 190 h showed no degradation in performance, indicating that ANL-3 membranes may be suitable for long-term, practical hydrogen separation.

Acknowledgment This work is supported by the U.S. Department of Energy, National Energy Technology Laboratory, under Contract W-31-109-Eng-38.

References

(1) Iwahara, H.; Yajima, T.; and Uchida, H. *Solid State Ionics*, **1994**, *70/71*, 267.
(2) Iwahara, H. *Solid State Ionics*, **1995**, *77*, 289.
(3) Guan, J.; Dorris, S. E.; Balachandran, U.; and Liu, M. *Solid State Ionics*, **1997**, *100*, 45.
(4) Guan, J.; Dorris, S. E.; Balachandran, U.; and Liu, M. *J. Electrochem. Soc.*, **1998**, *145*, 1780.
(5) Guan, J.; Dorris, S. E.; Balachandran, U.; and Liu, M. *Ceram. Trans.*, **1998**, *92*, 1.
(6) Balachandran, U.; Lee, T. H.; Zhang, G.; Dorris, S. E.; Rothenberger, K. S.; Howard, B. H.; Morreale, B.; Cugini, A. V.; Siriwardane, R. V.; Poston Jr., J. A.; and Fisher, E. P. In *Proc. 26th Intl. Technical Conf. on Coal Utilization and Fuel Systems*, Clearwater, FL, Mar. 5-8, **2001**, Coal Technical Association, Gaithersburg, MD, pp. 751-761.
(7) Buxbaum, R. E. and Marker, T. L. *J. Membr. Sci.*, **1993**, *85*, 29.

MIXED CONDUCTING MEMBRANES FOR PRESSURE-DRIVEN HYDROGEN SEPARATION FROM SYNGAS

S. Elangovan, B. Nair, J. Hartvigsen and T. Small
Ceramatec Inc.
Salt Lake City, UT

Introduction

Integrated Gasification Combined Cycle (IGCC) systems show tremendous potential for very efficient, environmentally friendly power generation.[1] In IGCC systems, a combined cycle is employed in which syngas ($CO+H_2$) is used to drive a gas turbine and the exhaust gases are then used to heat water/steam to generate superheated steam that drives a steam turbine. IGCC systems typically operate at efficiencies higher than 40%, whereas coal-burning plants that employ flue gas desulfurization processes reach a maximum efficiency of 34%. A number of demonstration projects, such as the Wabash River Coal Gasification Repowering Project in Indiana and the Pinon Pine IGCC Power Project in Nevada, have been carried out as part of the Department of Energy (DOE) Clean Coal Technology Program.[2,3]

Despite the significant potential of IGCC systems, economic considerations still limit their wide-spread commercial applicability. Fortunately, the total hydrogen in raw syngas is usually greater than 200% of the required amount. Thus, one critical advance that would significantly enhance the commercial viability of IGCC systems is the recovery of hydrogen fuel from syngas as a by-product.[4] There are a number of technologies and combinations of technologies being considered as alternatives for recovery of hydrogen from syngas. These technologies include membrane separation, pressure swing adsorption (PSA), methanation and nitrogen wash techniques. Each of these techniques has its strong points, and the choice of the specific technique is usually dictated by the economics of the process and the purity of hydrogen desired. Since ultra-high purity (>99 %) H_2 is a high value commodity, a technique that could generate such a high purity gas stream would be most attractive from an economic standpoint.

Technical Approach

Membrane separation, especially with ceramic membranes that separate H_2 by selectively transporting H+ ions (protons), offers the potential for generation of very high purity hydrogen (>99.9%), and is clearly superior in this regard compared with the other techniques mentioned above. Studies at SK Corporation in Ulsan, Korea have shown that the highest purities attainable by other techniques such as PSA, methanation and nitrogen wash techniques are only 97%, 85% and 97% respectively.[4]

A high-temperature, pressure-driven membrane-based separation system would be ideal for separation of hydrogen from the hot, high-pressure syngas stream typical of IGCC systems. Ceramic membranes are the only alternatives for operation under the high-temperature, high-pressure environment expected in IGCC systems, and can be designed to have very good thermomechanical and thermochemical stability under IGCC operating conditions. Our approach is to use a dense ceramic mixed-conducting membrane that can generate a stream of very high-purity H_2. The proposed concept, when fully developed, will be compatible with the temperature and pressure conditions in IGCC systems, and thus will be amenable for process and physical system integration.

One category of ceramic membranes that has received a good deal of attention in the preceding decade is mixed protonic/electronic conducting perovskite type oxide ceramics.[5,6] The stoichiometric chemical composition of perovskites can be represented as ABO_3, where A is a bivalent ion (A^{2+}) such as calcium, magnesium, barium or strontium and B is a tetravalent ion (B^{4+}) such as cerium or zirconium. While simple perovskites such as barium cerate ($BaCeO_3$) and strontium cerate ($SrCeO_3$) have some proton conductivity, it is now well known that doping these perovskites at the B sites can significantly enhance their protonic conductivities. The most common examples are structures of the form $AB_xD_{1-x}O_{3-\delta}$ formed by doping ABO_3 with trivalent ions such as yttrium (Y^{3+}) and ytterbium (Yb^{3+}). For example, $BaCe_{0.95}Y_{0.05}O_{3-\delta}$ has been shown to have a proton conductivity as high as 1.27×10^{-2} S/cm at 800°C in a H_2/H_2O atmosphere.[7]

In a pressure driven system, both hydrogen ions and electrons generated by dissociation of H_2 molecules at the high-pressure surface must be transported through the membrane to recombine at the low-pressure surface. Since these two are parallel kinetic processes, the overall kinetics are limited by the slowest process. In the case of a conventional mixed conducting membrane, the paths for proton conduction and electron conduction are the same. However, the electronic conductivity of mixed perovskites is very low and therefore is usually the limiting factor to these materials being used effectively as pressure-driven hydrogen separation membranes. For example, Phillips et al have shown that the electronic conductivity of $SrCe_{1-x}Y_xO_\delta$ was 2 to 3 orders of magnitude lower than its protonic conductivity at 800°C.[8] Our approach is to increase the electronic conductivities of these perovskite-based membranes through compositional and microstructural modifications.

In addition to being a good electronic conductor at these temperatures, the membrane material should also possess good thermomechanical and thermochemical stability at testing conditions involving temperatures as high as 900°C and high pressures of up to 5-10 atm. It has been reported that barium and strontium cerates are thermochemical unstable in H_2O and CO_2 containing atmospheres, due to carbonate formation as indicated in Equation (2).[9]

$$BaCeO_3 + CO_2 \rightarrow BaCO_3 + CeO_2 \qquad (2)$$

We are also addressing methods of increasing the thermochemical stability of the cerate-based membranes in CO_2-containing atmospheres. A membrane system that displays good mixed conductivity and thermochemical stability has been chosen for a proof-of-concept demonstration using said perovskite-ceria composite mixed conducting membranes for pressure-driven gas separation.

Experimental Approach

Membrane materials were synthesized with optimized compositions for mixed conductivity and thermochemical stability, using conventional powder processing routes. The powders were uniaxially pressed with appropriate binder additions in the shape of bars for conductivity measurements and as pellets for thermochemical stability measurements in simulated syngas. The bars and pellets were subjected through a prescribed sintering schedule and the densities of the sintered parts was measured through an Archimedes measurements, to ensure that the porosities in all parts was less than 1%, and that the densities corresponded to expected values for the chosen compositions. The specimens were studied by x-ray diffraction and scanning electron microscopy respectively to ensure that the targeted phases and microstructures were obtained in the sintered pellets.

The conductivity of the baseline cerate compositions and the modified compositions were evaluated using a conductivity test station, which is schematically shown in Figure 1. The apparatus has the ability to measure conductivities of bar specimens in various dry or wet gases. Conductivities of various bar specimens were measured at 800°C, 850°C and 900°C in wet hydrogen, and dry argon so that the protonic and electronic conductivities of the material could be assessed.

Membrane material stability under conditions expected in an IGCC system will be tested using a simulated syngas produced by steam reforming of natural gas. A mixture of steam/methane (2:1 ratio), and carbon dioxide (CO_2/CH_4=1.4) calculated to match the carbon/hydrogen ratio found in IGCC syngas, will be passed over a commercial nickel steam reforming catalyst at 800°C and 7.8 bar. Space velocity of less than 500 volume methane (stp conditions) per volume catalyst per hour will be used. This is low enough that the reformate composition is expected to closely match the equilibrium composition (1.5% CH_4, 21.4% CO, 15.3% CO_2, 36.2% H_2, 1.1% N_2, 24.5% H_2O) calculated for a steam/CO_2 reformed natural gas.

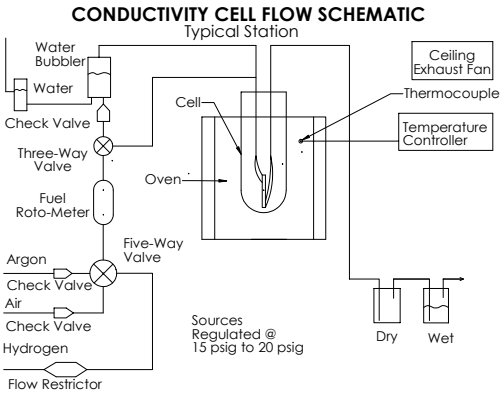

Figure 1. Schematic of test set-up for measuring conductivity of perovskite-based materials in various atmospheres.

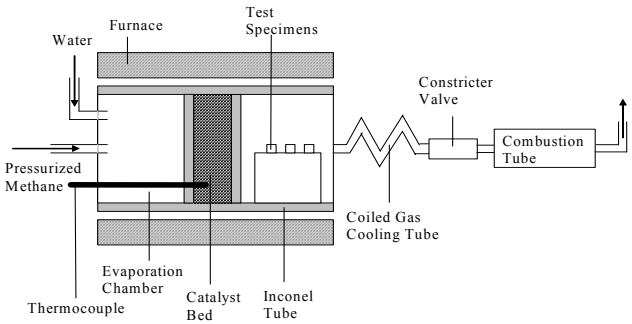

Figure 2. Schematic of test set-up for performing thermochemical stability experiments on perovskite-based membrane materials in pressurized syngas environment.

Results and Discussion

The results of preliminary conductivity testing of BaCeO3 and SrCeO3 based materials in moist H_2 are shown in Figure 3. The protonic conductivities of ≈0.9-1.3×10^{-2} S/cm in the temperature range of 800-900°C obtained for our baseline compositions (c.f. Figure 3(a)) of doped $BaCeO_3$ compare very favorably with conductivity values reported for similar compositions in the literature.[8] Based on the slopes of Arrhenius plots shown in Figure 3(b), we calculated activation energies of 50-75 KJ/mol for these perovskite compositions, which also compares very favorably with values reported in the literature.

Ongoing work includes measurement of conductivities of baseline and modified perovkite-based candidate membrane materials in dry argon and moist H_2 to study the effect of our microstructural/ compositional modifications on electronic and protonic conductivity. In parallel, experiments to study thermochemical stability of the baseline and modified compositions will be carried out. Based on the conductivity measurements and thermochemical stability studies, compositions will be selected for membrane fabrication on porous supports. Experiments will then be carried out to demonstrate the feasibility of H_2 separation from simulated syngas by use of these mixed conducting membranes.

Summary

A novel, dense, mixed-conducting ceramic membrane is being developed. These membranes will allow pressure-driven hydrogen separation at 800-900°C, resulting in a very high purity hydrogen stream. The electronic conductivity and thermochemical stability of cerate-based perovskite membranes is enhanced through compositional/microstructural modifications. Hydrogen separation membranes were fabricated and protonic and electronic conductivity through the membrane will be characterized. The thermochemical stability of candidate membranes materials under simulated operating

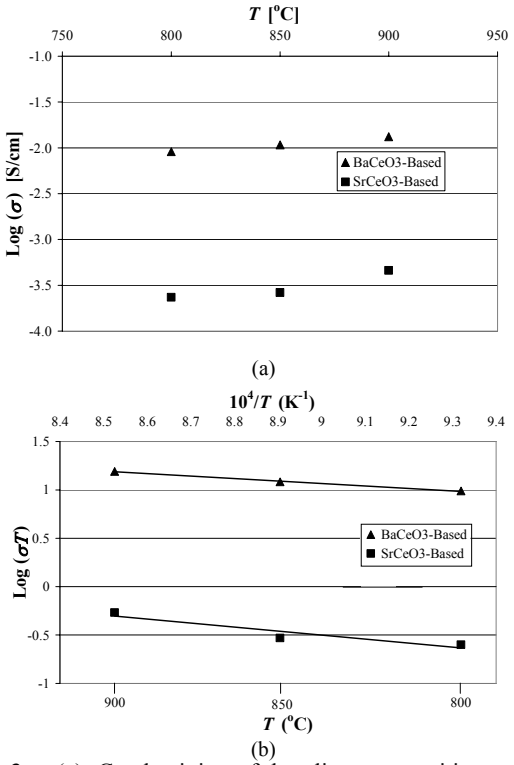

Figure 3. (a) Conductivity of baseline compositions of doped $BaCeO_3$ and $SrCeO_3$ in moist H_2 as a function of temperature; (b) Arrhenius plots of the data in (a).

conditions will be evaluated. The performance of the membrane as a mixed ionic-electronic conducting membrane will be evaluated through feasibility studies of pressure-driven hydrogen separation from simulated syngas. This hydrogen separation technique is expected to have a major impact on enhancing the commercial feasibility of IGCC systems.

Acknowledgement

This work was funded by the U.S. Department of Energy (DOE) through SBIR Grant No. DE-FG03-02ER83386.

References

(1) Campbell, P. E., McMullan, J. T. and Williams, B. C. *Fuel* **2000** *79* [9] 1031.
(2) Brdar, R. D., and Cicero, D. C., DOE Report No: DOE/METC/C-69/7231.
(3) Ness, H. M. and Brdar, R. D., DOE Report No. DOE/METC/C-96/7236.
(4) Kwon, S H., Shin, J. W., Oh, J. K., Heaven, D. L., and Condorelli, P. *Hydrocarbon Processing*, **1999** *78* [4] 73.
(5) Norby, T. and Larring, Y., *Solid State Ionics* **2000** *136-137* 139.
(6) Sata, N., Yugami, H., Akiyama, Y., Sone, H., Kitamura, N., Hattori, T., and Ishigame, M., *Solid State Ionics* **1999** *125* 383.
(7) Guan, J. Dorris, S. E., Balachandran, U., and Liu, M., *Solid State Ionics*, **1997** *100* 45.
(8) Phillips, R. J., Bonanos, N., Poulsen, F. W., and Ahlgren, E. O., *Solid State Ionics* **1999** *125* 389.
(9) Bhide, S. V., and Virkar, A. V., *J. Electrochem. Soc.* **1999** *146* [6] 2038.

SORPTION IN PROTON EXCHANGE MEMBRANES: AN EXPLANATION OF SCHROEDER'S PARADOX

Pyoungho Choi and Ravindra Datta

Fuel Cell Center, Department of Chemical Engineering, Worcester Polytechnic Institute, Worcester, MA 01609, USA.

Introduction

Fuel cells based on the proton-exchange membranes (PEMs) are of great potential as efficient and largely pollution-free power generators for mobile and stationary applications.[1] The PFSA membranes typically consist of a polytetrafluoroethylene (PTFE) backbone with side-chains terminating in SO_3H groups. They possess little porosity in the dry state. However, in the presence of water or other polar solvents, the membrane swells and the sulfonic acid groups ionize protonating the sorbed solvent molecules that are responsible for conducting the protons. The conductivity of Nafion® is highly dependent upon hydration level[2] being essentially an insulator below a threshold and rising through several orders of magnitude to about 0.07 ~ 0.1 Siemens/cm at 80 ºC when it is fully hydrated.

The water uptake in Nafion® expressed in terms of λ, the number of moles of water per equivalent of polymer, upon contact with liquid or its saturated vapor as reported in the literature[3] There is an unexplained discrepancy in the water uptake in Nafion® from pure liquid ($\lambda_{i,L} \approx 22\sim23$) versus that from its saturated vapor ($\lambda_{i,V} \approx 13.5\sim14.0$), even though both possess unit activity. In fact, when a liquid water-equilibrated membrane was removed and exposed to saturated water vapor, λ dropped from 22 to 14, thus indicating that the two states are thermodynamically stable. The phenomena, known as Schroeder's paradox,[4] is apparently not uncommon in polymer systems, but has not so far been satisfactorily explained although many different explanations have been advanced.

A sorption model of water in Nation® is proposed here based on that the sorption isotherm is controlled by the swelling pressure determined by the matrix and surface forces of the polymer membrane and sorbed solvent.

Model Description

When the ion exchange membrane, *e.g.,* Nafion®, is in equilibrium with a solvent, *e.g.,* water, some of the sorbed solvent molecules are in a physicochemical state that is different from the bulk solvent molecules depending upon their interaction with surroundings. The model developed here simply assumes that the sorbed solvent molecules are of two types; *i*) those that are strongly, or chemically, bound to the acid sites, akin to chemisorption, and *ii*) others that are physically equilibrated between the fluid and the membrane phases, akin to physisorption. It is further assumed that as the membrane swells due to solvent uptake, the solvent molecules meet increasing resistance from the hydrophobic backbone as well as the stretched polymer chains resulting in a swelling pressure on the pore liquid. The model, thus, involves a balance of forces.[5] Equilibrium is achieved when the elastic forces of the polymer matrix counterbalance the increased pressure within the pore liquid in an effort of solvent molecules to equalize the chemical potential of the fluid inside and outside of the pore. The spring constant κ of the spring is assumed to depend upon the temperature (*e.g.,* proximity to the glass-transition temperature, T_g), and pretreatment procedures.

Liquid-Membrane Phase Equilibria For equilibration between a liquid and membrane phases for an uncharged species *i*

$$\ln \frac{a_{i,M}^{F}}{a_{i,L}} = -\left(\frac{\overline{V}_i}{RT}\right)\Pi_{\mathrm{M}} \tag{1}$$

where the membrane swelling, or osmotic pressure, $\Pi_{\mathrm{M}} = P_M - P_L$, is the pressure rise within the membrane exerted by the membrane polymer matrix due to stretching to accommodate the imbibed pore liquid The activity of species *i* within the membrane $a_{i,M}^{F}$ corresponds to the 'free', or non-chemically bound, molecules of *i*, as denoted by the superscript *'F'*.

Vapor-Membrane Phase Equilibria. When the membrane equilibrates with a vapor phase, assuming that the pressure changes within the condensed phase in the pore is caused both due to the stretching of the polymer chains upon solvent uptake, Π_{M}, as well as that exerted by the curved vapor-liquid interface within the pores, Π_σ,

$$\ln \frac{a_{i,M}^{F}}{a_{i,V}} = -\left(\frac{\overline{V}_i}{RT}\right)\left(\Pi_{\mathrm{M}}+\Pi_\sigma\right) \tag{2}$$

where the vapor phase activity $a_{i,V} = P_i/P_i^{sat}$ and Π_σ is provided by the equation of Young and Laplace[6]

$$\Pi_\sigma = -\frac{2\sigma\cos\theta}{r_p} \tag{3}$$

where θ is the liquid-membrane contact angle and r_p is the mean pore radius of liquid-filled pores. For the case of saturated vapor, $P_i=P_i^{sat}$, then Eq. (2) gives

$$\ln a_{i,M}^{F} = -\left(\frac{\overline{V}_i}{RT}\right)\left(\Pi_{\mathrm{M}}+\Pi_\sigma\right) \tag{4}$$

whereas for the case of pure liquid solvent *i*, from Eq. (1)

$$\ln a_{i,M}^{F} = -\left(\frac{\overline{V}_i}{RT}\right)\Pi_{\mathrm{M}} \tag{5}$$

It is then clear from the Eq. (4) and (5) that, in general, the amount sorbed from a saturated vapor would be different from that sorbed from a pure liquid, both possessing unit activity. This simple result, thus, provides a reasonable explanation for the Schroeder's paradox for the sorption in polymers.

The final expression for the liquid-phase sorption in the proton exchange membrane is obtained as

$$\left\{\lambda_{i,L} - \frac{\lambda_{i,m}K_1 a_{i,L}}{(1-a_{i,L})}\left[\frac{1-(\nu+1)(a_{i,L})^{\nu}+\nu(a_{i,L})^{\nu+1}}{1+(K_1-1)a_{i,L}-K_1(a_{i,L})^{\nu+1}}\right]\right\}^{-1} =$$

$$a_{i,L}^{-1}\exp\left\{\frac{\overline{V}_i}{RT}\left[\frac{\kappa\lambda_{i,L}}{\lambda_{i,L}+\overline{V}_M/\overline{V}_i}\right]\right\} - 1 \tag{6}$$

where $\lambda_{i,m}$ is the monolayer coverage being bound, K_1 is the equilibrium constant of water molecules with ion exchange site of the polymer and ν is the number of equilibrium steps chemical equilibrium between the ion exchange site and each water molecules.

For the vapor-phase sorption, surface energy term is included in the isotherm expression as

$$\left\{\lambda_{i,V}-\frac{\lambda_{i,m}K_1 a_{i,V}}{(1-a_{i,V})}\left[\frac{1-(\nu+1)(a_{i,V})^{\nu}+\nu(a_{i,V})^{\nu+1}}{1+(K_1-1)a_{i,V}-K_1(a_{i,V})^{\nu+1}}\right]\right\}^{-1} =$$

$$a_{i,V}^{-1}\exp\left\{\frac{\overline{V}_i}{RT}\left[\frac{\kappa\lambda_{i,V}}{\lambda_{i,V}+\overline{V}_M/\overline{V}_i}-(S\sigma\cos\theta)\left(1+\frac{\overline{V}_M}{\overline{V}_i}\frac{1}{\lambda_{i,V}}\right)\right]\right\}-1 \quad (7)$$

For given $\lambda_{i,m}$, K_1, ν, $\overline{V}_i$, κ, S, σ, θ and $\overline{V}_M$, thus, the sorption isotherm, namely versus a_i can be determined for vapor or liquid phase sorption. Further, it is then clear from the Eq. (6) and (7) that the solvent loading in liquid sorption, $\lambda_{i,L}$, would in general be different from the solvent loading from the vapor sorption $\lambda_{i,V}$.

Results and Discussion

In order to apply this model into water sorption in Nafion®, the parameters of the equations, K_1, $\lambda_{i,m}$, and ν, are obtained based on the following considerations. The equilibrium constant K_1 between water and the side chain of SO_3^- ion is approximated by that of sulfuric acids in water for the first ionization. The solvent loading parameter, $\lambda_{i,m}$, is taken as a monolayer coverage being bound in the proton exchange membrane. The number of equilibrium steps, ν, for hydration of the ions is related to the number of solvent molecules in the hydration shell. For sulfonated styrene-type ion exchanger, six hydration number for SO_3H group is reported experimentally and recent molecular modeling studies also results in 5 to 6 hydration number for SO_3H. The activity of water in Nafion®, which is osmotically active, is limited to the water molecules that are outside of the first hydration shell.[7] In the dry or low humidity conditions, a few water molecules are in the hydration shell and are not enough to shield the ions and as the humidity of the membrane increases, more water molecules are involved in the shielding of sulfonic acid and hydronium ion.

Figure 1 shows the predicted isotherm of water in Nafion® by Eq. (7), the solid line, as well as the experimental data. The model represents the sorption of water in Nation® and predicts quite precisely all the features of the isotherm throughout the entire range of vapor phase activity; it predicts the high initial slope, gradual increase of the slope after the sorption of the first a few molecules and high slope at high activities after about $a_{i,V} = 0.7 \sim 0.8$.

In order to explain the Schroeder's paradox for the sorption of water in Nafion®, Eq. (6) and (7) can be further modified for the sorption of pure liquid *i*, $a_{i,L} = 1.0$. The model predicts the loading of water in water solution $\lambda_{i,L} = 22 \sim 23$ and $\lambda_{i,V} = 15 \sim 16$ for saturated vapor condition. There is a clear difference in solvent loading between liquid and saturated vapor sorption; *that is*, the solvent loading of vapor phase sorption is less than that of liquid phase, in this case the difference is about seven. This means that seven water molecules per acid site on average are less sorbed in Nafion® when the molecules are sorbed from the vapor compared with the liquid molecules contacting the membrane. The reason for this difference is that the surface energy of the sorption phase affects the chemical potential of the sorption phase in different extents in the liquid and saturated vapor sorption.

The simplified model presented here predicts the isotherms, the solvent loadings from the vapor and liquid phase sorption, and explains the Schroeder's paradox for the water sorption in Nafion® satisfactorily. It is based on the difference in the states, which are stable in thermodynamic means, of the sorption phases where the sorption phases interact with different environments of the bulk liquid and its saturated vapor phases.

Conclusions

A theoretical model is developed for the sorption of solvent in proton exchange membrane. This model predicts isotherm of water in Nation® quite precisely and provides insight into the sorption phenomena in the ion exchange polymer. The sorption isotherm is a result of equilibrium conditions that are established between the elastic forces of the polymer matrix and swelling pressure in the membrane. The swelling pressure is derived from the solvent activity inside of the polymer membrane and the dissociation characteristics of the solvent in the presence of the acid exchange site.

The isotherm equations clearly show the difference in the sorption amount from liquid and its saturated vapor, which is known as Schroeder's paradox. The paradox could well be explained in terms of surface energy that leads different energy states of sorption molecules for the liquid immersion and saturated vapor conditions.

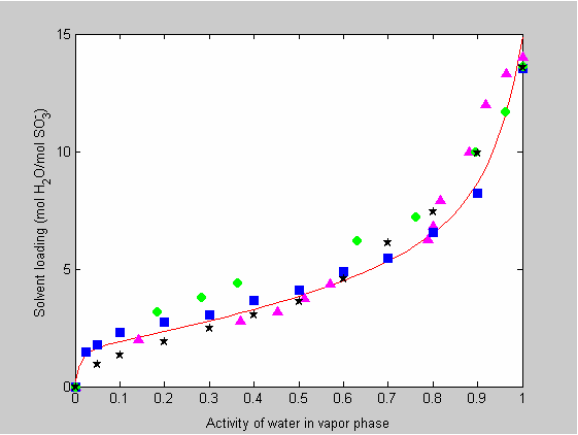

Figure 1. Isotherm of water vapor in Nafion: experimental reports (symbols) from four different groups with model prediction (solid line).

References

1. Perry. M. L.; Fuller. T. F. *J. Electrochem. Soc.* **2002**, 149, S59.
2. Anantaraman, A. V.; Gardner, C. L. *J. Electroanal. Chem.*, **1996**, 414, 115.
3. Zawodzinski, T. A.; Springer, T. E.; Davey, J.; Jestel, R.; Lopez, C.; Valerio, J.; Gottesfeld, S. *J. Electrochem. Soc.*, **1993**, 140, 1981.
4. Schroeder, P. V. *Z. Phys. Chem.*, **1903**, 45, 75.
5. Gregor, H. P. *J. Am. Chem. Soc.*, **1951**, 73, 642.
6. Adamson, A. W.; Gast, A. P. *Physical Chemistry of Surfaces*; John Wiley & Sons, Inc.: NY, 1997.
7. Helfferich, H. *Ion Exchange*; McGraw-Hill; NY, 1960.

CHEMICAL STABILITY OF BARIUM CERATE–BASED HIGH-TEMPERATURE PROTON CONDUCTORS

R. D. Carneim and T. R. Armstrong

Metals and Ceramics Division
Oak Ridge National Laboratory
PO Box 2008
Oak Ridge, TN 37831

Introduction

Proton conducting ion transport membranes are required to extract absolutely pure hydrogen from mixed gas streams in the processing of fossil fuels and other petroleum and petrochemical processes. Ceramic materials are required to withstand these high-temperature processes. Yttrium-doped barium cerate ($BaCe_{0.80}Y_{0.20}O_{3-\delta}$) is currently one of the best materials when considering only proton conductivity. However, this material is very sensitive to the carbon dioxide (CO_2) and sulfur (H_2S) contamination found in the fossil fuel process stream. Barium cerate will decompose into barium carbonate ($BaCO_3$) and ceria (CeO_2) in the presence of CO_2; and CeO_2 reacts with H_2S to produce a sulfided phase, particularly in the highly reducing fuel environment. Two approaches for improving the stability of barium cerate are examined: manipulation of the A- to B-site stoichiometry and partial substitution of Ce with Zr. Individually these techniques have been previously shown to enhance stability. In the present work, the effect of applying both modifications simultaneously is explored. High-temperature x-ray diffraction (HTXRD) and thermogravimetric analysis (TGA) are used to determine decomposition temperatures, extent of decomposition, and reaction kinetics of various yttrium-doped barium cerate compositions in CO_2-contaminated environments.

Experimental

Sample preparation. Small batches (≈ 10 g) of powders were prepared by the glycine–nitrate process (GNP).[1] The resulting ash was sieved (100-mesh) and calcined for 20 min to 30 min at 1200 °C to produce the desired single-phase perovskite. The following compositions were synthesized:

BCY—: Four barium-deficient compositions: $Ba_xCe_{0.80}Y_{0.20}O_{3-\delta}$ with x = 1.00, 0.98, 0.95, and 0.90; designated BCY108, BCY88, BCY58, and BCY08, respectively.

BCZ—: Three barium-deficient, non-acceptor-doped zirconium-substituted compositions: $Ba_{0.98}Ce_{1-y}Zr_yO_{3-\delta}$ with y = 0.15, 0.10, and 0.05; designated BCZ885, BCZ89, and BCZ895, respectively.

BCZY: One barium-deficient, acceptor-doped, zirconium-substituted composition: $Ba_{0.98}Ce_{0.65}Zr_{0.15}Y_{0.20}O_{3-\delta}$; designated BCZY.

High-temperature x-ray diffraction. The bulk of the HTXRD measurements were conducted in a Phillips X'Pert diffractometer with a Pt-Rh strip heater/sample stage in an environmentally controllable sample chamber (HTK 16 High-Temperature Camera) with Capton x-ray windows.

Resistance to degradation due to the presence of CO_2 was determined by measuring the temperatures at which $BaCO_3$ formed during heating and cooling of the single-phase perovskite in flowing CO_2 ($p[CO_2] = p$ = 101 kPa [1 atm]). The procedure used was: heat sample in N_2 to t = 1400 °C and cool to room temperature; perform scan; change sample environment to flowing CO_2 and hold 20 min; perform scan; raise temperature by 50 °C and hold 5 min; perform scan; repeat preceding two steps until t = 1400 °C; lower temperature by 100 °C and hold 10 min; perform scan; repeat preceding two steps until t = 500 °C. Measurements were taken over the range from 2θ = 20° to 2θ = 44°.

The HTXRD data is presented by plotting the common logarithms of the peak ratios (areas under peaks attributable to only the perovskite phase vs. those attributable to only non-perovskite phases; background intensity and noise ensure finite results), , versus temperature during heating and cooling (figure 1). A cut-off value of $\lg(r_{p/c}) = -0.25$ was used to define transition temperatures ($\lg(r_{p/c}) > 0$ indicates no observable $BaCO_3$ and $\lg(r_{p/c}) < -0.5$ indicates the presence of a significant amount of $BaCO_3$). The temperatures at which carbonate phase forms and disappears on heating, and forms again on cooling can be easily seen and compared. Additionally, the relative extent of conversion to $BaCO_3$ can be seen by the magnitude of the deflection into the carbonate side of the plot.

An additional feature that stands out in this representation of the data is hysteresis in the high-temperature transition (i.e., the temperature at which $BaCO_3$ disappears on heating or appears on cooling). The high-temperature transition hysteresis, Δt_{hyst}, is defined as the difference between the transition temperatures measured during heating and cooling. This quantity may be used for comparing reaction kinetics between related materials undergoing the same reaction at comparable temperatures.

Thermal analysis. Simultaneous thermogravimetric analysis and differential thermal analysis (TGA and DTA) were performed on the three modified compositions BCY88, BCZ885, and BCZY (T/A Instruments). Sample and α-Al_2O_3 reference powders of $m \approx 25$ mg each were used. Multiple scans were performed on each composition at different heating/cooling rates (ϕ = 4 °C·min^{-1}, 10 °C·min^{-1}, and 20 °C·min^{-1}) to allow estimation of the reaction activation energies using the Kissinger method.[2, 3] Derivatives of the TGA data were used for these calculations rather than the DTA data due to significantly greater signal intensity.

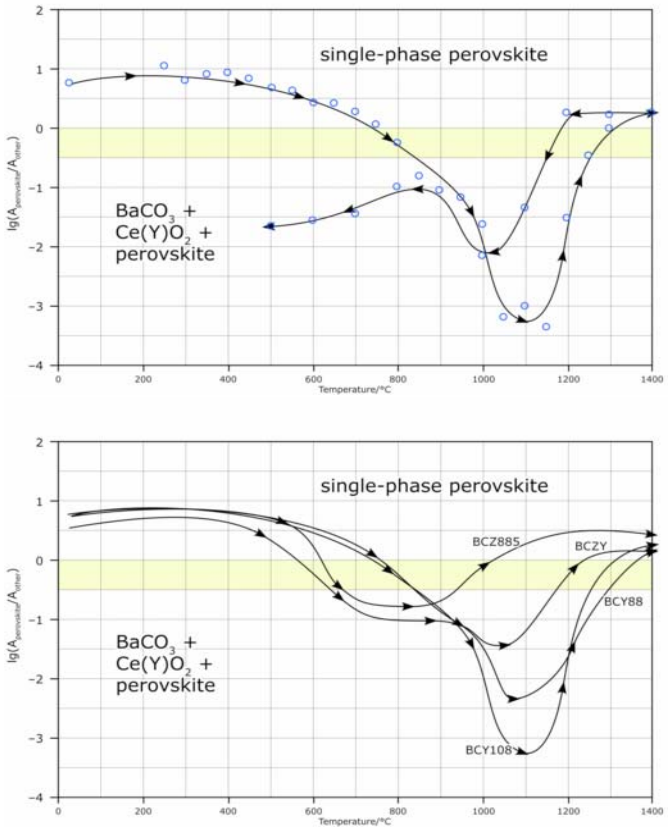

Figure 1. The results of HTXRD in CO_2 are represented as the common logarithm of the ratio of perovskite to non-perovskite (i.e., $BaCO_3$) peak areas. Values > 0 indicate no detectable $BaCO_3$ and values < –0.5 indicate significant $BaCO_3$ formation. ***Top:*** sample complete data set for BCY108, heating and cooling. ***Bottom:*** data on heating only for BCY108 and the three modified compositions BCY88, BCZ885, and BCZY.

Results and Discussion

Barium Stoichiometry. Earlier cursory measurements showed no difference in the behavior of the three barium-deficient compositions (BCY88, BCY58, and BCY08). For the purpose of stability in CO_2, any of the barium-deficient compositions would serve to realize the improvement over the stoichiometric composition and stay well clear of a barium-excess situation (which previous work reports as detrimental [4]); however, an extreme barium deficiency would result in severe degradation of electrical properties[4]. Therefore, the least (non-zero) barium-deficient composition was chosen for propagation through this study: $x = 0.98$.

The measurements reported here for BCY108 and BCY88 reveal details of the differences in behavior of the stoichiometric and barium-deficient compositions with respect to degradation in CO_2. The various transition temperatures are nearly identical for these two compositions. The temperature range in which $BaCO_3$ is present and the high-temperature transition hysteresis were similar for these two materials. The consequential difference between these two compositions is the extent of transformation: the peak ratio, $\lg(r_{p/c})$, is nearly one order of magnitude larger (i.e., indicating significantly less $BaCO_3$ formation) for BCY88 than for BCY108.

Zirconium substitution, undoped. Published work[5] and previous experiments indicated that the BCZ samples showed significantly less carbonate formation relative to the BCY samples, though the carbonate appears at higher temperatures in the BCZ samples than in the BCY samples. The highest zirconium-content composition, BCZ885, had no measurable $BaCO_3$ peaks on cooling, though on heating BCZ885 clearly showed $BaCO_3$ formation at approximately the same temperature as the BCY compositions ($t \approx 550$ °C).

Current results clearly reveals considerable improvements in the chemical stability of BCZ885 over the most similar non-zirconium-substituted composition, acceptor-doped BCY88. The data barely enters the $BaCO_3$ region of the $\lg(r_{p/c})$ vs. t plot during both heating and cooling. Furthermore, the temperature range in which $BaCO_3$ is present is smaller and occurs at lower temperatures (Table 1).

The high-temperature transition hysteresis, however, is greater: $\Delta t_{hyst} \approx 230$ °C for BCZ885 vs. $\Delta t_{hyst} \approx 150$ °C for BCY88. Such an increase in this quantity indicates a slowing of the reaction kinetics. It is not clear at this point whether this effect on the kinetics is a direct result of the chemical effects of the Zr_{Ce} substitution or merely due to the fact that the transition occurs at a lower temperature (an *indirect* result of the Zr_{Ce} substitution).

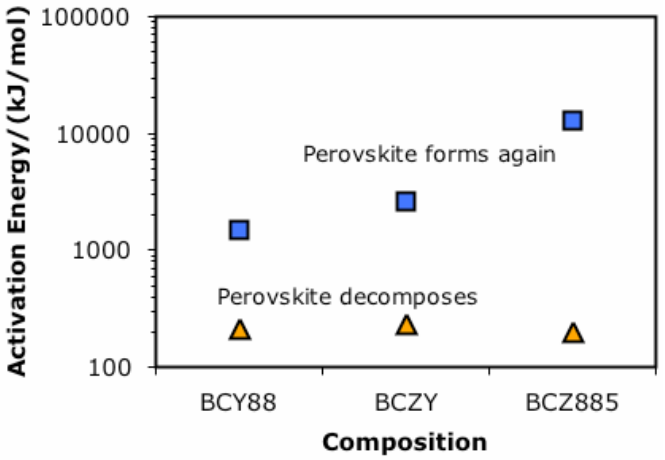

Figure 2. The activation energies are shown for the three modified barium cerate compositions: (▲) initial decomposition of the single phase perovskite into $BaCO_3$ and CeO_2, (■) formation of perovskite as CO_2 is lost at high temperature. Values were calculated using the Kissinger method from TGA data on heating in $p = p(CO_2) = 101$ kPa (1 atm).

Table 1. Summary of Transition Temperatures from HTXRD*

Composition	$BaCO_3$ appears on heating: t/°C	$BaCO_3$ disappears on heating: t/°C	$BaCO_3$ temperature range: t_{range}/°C	$BaCO_3$ appears on cooling: t/°C	High-temperature transition hysteresis: Δt_{hyst}/°C	Maximum $\lg(r_{p/c})$ peak deflection to $BaCO_3$†
BCY108	780	1280	500	1160	120	–3.25
BCY88	780	1330	550	1180	150	–2.35
BCZ885	640	980	340	750	230	–0.80
BCZY	600	1200	600	950	250	–1.45

* Tabulated values were extracted from data as in figure 1 using $\lg(r_{p/c}) = -0.25$ cutoff.
† N.B., $\lg(r_{p/c}) < -0.5 \equiv$ significant formation of $BaCO_3$

Zirconium substitution, yttrium-doped. The composition BCZY incorporates all the stability-enhancing modifications examined earlier, plus the standard 0.20 Y doping. On heating, BCYZ possesses characteristics of both component compositions (i.e., BCY88 and BCZ885): a minor excursion into the $BaCO_3$ field at $t \approx 600$ °C, similar to BCZ885; then further $BaCO_3$ formation above $t \approx 1000$ °C, approximately the temperature of maximum conversion to $BaCO_3$ of BCY88. The extent of conversion also falls between that of the two simple compositions. On cooling, BCZY behaves slightly differently. Barium carbonate begins to form at a temperature approximately midway between the onset temperatures for BCY88 and BCZ885. But rather than distinct peaks in the $\lg(r_{p/c})$ data, BCZY displays a gradual, monotone decrease in $\lg(r_{p/c})$ to the lowest temperature.

Since BCZY behaves approximately as a combination of the two component compositions, the magnitudes of the $BaCO_3$-presence temperature range and high-temperature transition hysteresis are approximately equal to the greater of the two corresponding values for the simple compositions: $t_{range} \approx 600$ °C, comparable to the t_{range} value for BCY88; and $\Delta t_{hyst} \approx 250$ °C, similar to the Δt_{hyst} value of BCZ885. Furthermore, the high-temperature transition temperatures of BCZY fall between those of BCY88 and BCZ885 while the hysteresis is still comparable to that of BCZ885. This indicates that the effect on the kinetics is principally due to chemical differences resulting from the Zr_{Ce} substitution. This is corroborated by the calculated activation energies shown in figure 2. While activation energy of the low-temperature transition (▲ in figure 2) is nearly independent of the composition, the high-temperature transition (■ in figure 2) has a significantly higher energy barrier in the BCZ885 composition.

Conclusions

Two methods for improving the stability of yttrium-doped barium cerate in CO_2 have been investigated. Producing slightly barium-deficient compositions and partial substitution of Zr for Ce have previously and in this work been shown to increase the resistance to decomposition in the presence of CO_2. The effects of the individual modifications as well as their combined effects have been shown utilizing thermal analysis and high-temperature x-ray diffraction. While definite improvements in CO_2-tolerance were observed, absolute immunity was not achieved at the levels of modification studied. Since it is known[4, 5] that significant amounts of Zr_{Ce} substitution or Ba-deficiency severely decrease conductivity, the prospect of producing a practical, durable high-temperature proton conductor in this system with these techniques is unlikely.

Acknowledgement. Research at Oak Ridge National Laboratory sponsored by the Office of Fossil Energy, U.S. Department of Energy under contract DE-AC05-00OR22725 with UT–Battelle, LLC.

References

(1) Chick, L. A.; Pederson, L. R.; Maupin, G. D.; Bates, J. L.; Thomas, L. E.; Exarhos, G. J. , *Materials Letters,* **1990,** *44* (1, 2) 6–12.
(2) Kissinger, H. E., *J. Res. National Bureau of Standards,* **1956,** *57*(4), 217–21.
(3) Kissinger, H. E., *Anal. Chem.,* **1957,** *29* (11), 1702–6.
(4) Ma, G.; Shimura, T.; Iwahara, H., *Solid State Ionics,* **1998,** *107,* 221–29.
(5) Ryu, K. H.; Haile, S. M., *Solid State Ionics,* **1999,** *125,* 355–67.

Composite Palladium and Palladium-alloy Membranes for High Temperature Hydrogen Separations

Yi Hua Ma, Erik E. Engwall and Ivan P. Mardilovich

Center for Inorganic Membrane Studies
Department of Chemical Engineering
Worcester Polytechnic Institute
Worcester, MA 01609

Introduction

As we are approaching the era of the hydrogen economy, hydrogen is not only an important industrial chemical but also becoming one of the future's key energy resources. It is expected that the future worldwide demand for hydrogen will increase greatly. Dense composite Pd and Pd/alloy membranes supported on a porous substrate, in particular, porous stainless steel (PSS), are especially suited for high temperature hydrogen separation and membrane reactor applications.

Most early work on hydrogen permeation in palladium involved the use of palladium foils as summarized in detail by Lewis (1). However, there are a number of advantages of using composite palladium membranes supported on porous substrates, in particular, porous stainless steel, over palladium foils and tubes. These advantages include thinner membrane layer, better mechanical strength and higher hydrogen flux. Furthermore, there are additional main advantages for using porous stainless steel (PSS) supports that include the resistance to cracking and the simplicity of module construction. Composite Pd/PSS membranes, welded from both ends with non-porous stainless steel tubes, can be very easily assembled and integrated into a process. Additionally, the thermal expansion coefficient of stainless steel is very close to that of palladium, insuring good mechanical properties of the composite membrane during temperature cycling.

This paper reviews the synthesis by electroless plating and characterization of composite Pd and Pd-alloy with a special emphasis on porous stainless steel (PSS) support, and long-term thermal stability. In addition, the unique features of the controlled in-situ oxidation technique to create an intermetallic diffusion barrier are discussed.

Electroless Plating

The advantages of electroless plating include uniform deposition on complex shapes and large substrate areas, hardness of the deposited film, and very simple equipment. Electroless plating (2) generally consists of pre-treatment of the porous stainless steel (PSS) support, surface activation and plating. The pre-treatment of the PSS support includes complete removal of foreign contaminants (grease, oil, dirt, corrosion products) while surface activation consists of seeding the support surface with palladium nuclei, which during the electroless plating initiate an autocatalytic process of the reduction of a metastable Pd salt complex on the target surface. Electroless plating is carried out at constant temperature with a plating solution typically consisting of a plating agent $(Pd(NH_3)_4)Cl_2H_2O$, stabilizing agent Na_2EDTA, and a reducing agent H_2NNH_2 with NH_4OH for pH adjustment.

One of the problems associated with electroless plating of palladium on porous metal substrates is the intermetallic diffusion of metal elements into the palladium layer at high temperatures causing deterioration of the hydrogen flux. We have developed a unique technology to create an intermediate intermetallic diffusion barrier layer by controlled in-situ oxidation prior to the plating (3). Furthermore, there are added benefits that the intermediate barrier layer also provides surface sites for easy activation and plating as well as improved adhesion (4). Typical Pd/PSS membranes plated by the electroless plating technique with an in-situ barrier layer are shown in Fig.1. Non-porous stainless steel tubes of the same diameter were welded to the membrane tubes on both ends and the white sleeves were used to facilitate the handling of the membranes.

Figure 1. Composite Pd/PSS membranes 1" OD (2.54 cm), Membrane area: 24.7 in^2 (159 cm^2)

Hydrogen Permeation Flux as a Function of Membrane Thickness

Since the permeation of hydrogen through Pd and Pd/alloy is by the solution and diffusion mechanism and is, in most cases, controlled by the diffusion of dissociated hydrogen molecules through the Pd bulk, the hydrogen flux is proportional to the difference of the square root of the pressures, known as the Sievert's law. A typical plot of permeance vs. the difference of the square root of pressure (Sievert's law) is shown in Figure 2 for a membrane of

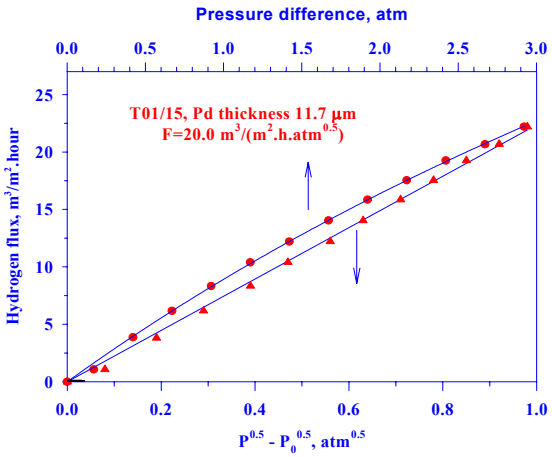

Figure 2. The hydrogen Flux as a function of the difference of the square root of the pressure (Sievert's law) at 350°C)

thickness of 11.7 µm at 350°C. In addition, when the permeation is controlled by the diffusion of hydrogen in the bulk palladium layer, the permeation flux and thus the permeance, is inversely proportional to the membrane thickness. We have performed a systematic study of the permeation of hydrogen through composite Pd/PSS membranes with different Pd layer thickness and showed the inverse relationship between the hydrogen permeance and the Pd layer thickness at 350°C[4]. As shown in Fig. 3, these experimental

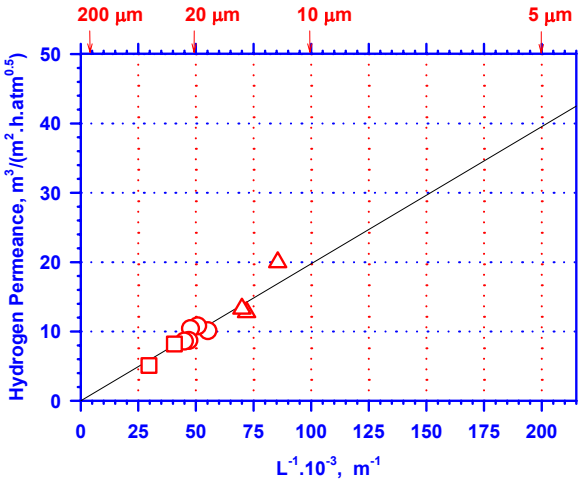

Figure 3. Hydrogen permeance versus reciprocal palladium thickness for a pressure difference of 1 atm and a temperature of 350 ºC. The Pd layer thickness is indicated along the top. The grade of the supports from Mott Metallurgical Corporation were: **squares**-grade 0.5 µm; **circles**-grade 0.2 µm; **triangles**-grade 0.1µm.

results covered the range of the Pd layer thickness between 11.7 µm and 33.8 µm, an almost three-fold difference in membrane thickness. This inverse relationship provides additional evidence that even at such small membrane thickness, the flux was still controlled by the hydrogen permeation through the Pd bulk without any influence by the mass transport at the membrane surface or through the pores of the support.

Palladium Alloys for Improving Hydrogen Permeation Flux and Thermally Stability

It has long been recognized that Pd alloys may have advantages over Pd for use in hydrogen separation and membrane reactor applications. In general, Pd alloys have a reduced critical temperature for the α-β phase transition (1). For example, Pd/Ag alloy membranes may be operated in the presence of H_2 at temperatures below 300ºC without the hydrogen embrittlement observed for pure Pd membranes (6). In some cases, the hydrogen permeability of alloys is greater than that of Pd. This is true for binary palladium alloys with yttrium, cerium, silver, copper and gold for the appropriate compositions as shown in Table 1 based on data from Knapton (7). Several tertiary Pd alloys such as Pd-Ru-In, Pd-Ag-Ru and Pd-Ag-Rh reported to have high hydrogen permeability as well (7, 8) are also included in the table. Finally, some Pd alloys may produce membranes with enhanced chemical resistance. It has been suggested that both the Pd-Cu and Pd-Au systems can be used to produce membranes with enhanced resistance to H_2S (9, 10).

Of the metals listed above for binary palladium alloys, Cu and Ag represent the least expensive alternatives from the standpoint of materials costs. Palladium-silver alloys are attractive because they have good hydrogen permeability relative to pure palladium. In the case of Pd-Ag alloys, the solubility of hydrogen increases with increasing Ag content reaching a maximum at an Ag content between 20-40 wt % (1). However, the diffusivity of hydrogen in Pd-Ag alloys decreases with increasing silver content. The simultaneous changes in solubility and diffusivity result in a maximum in the hydrogen permeability of 1.7 times the permeability of pure palladium, at a silver content of 23 wt % and a temperature of 350 ºC (10). Recently, Roa et al. (11) also reported highest hydrogen permeability for a Pd(60)/Cu(40) alloy membrane on porous ceramic supports.

Table 1. Improvement in hydrogen permeability of various binary Pd alloys at 350 ºC (7, 8)

Alloy Metal	wt % for Maximum Permeability	Normalized Permeability (P_{alloy}/P_{Pd})
Y	10	3.8
Ag	23	1.7
Ce	7.7	1.6
Cu	40	1.1
Au	5	1.1
Ru, In	0.5, 6.0	2.8
Ag, Ru	30, 2	2.2
Ag, Rh	19, 1	2.6
Pure Pd	-	1.0

Palladium-copper alloys are attractive from the standpoint of relatively high permabilities coupled with their enhanced sulfur resistance. In the case of Pd-Cu alloys, the formation of a solid phase with a BCC structure at 40 wt % copper, leads to an increase in the hydrogen diffusivity of two orders of magnitude, and thus a sharp maximum in permeability for this composition (6). More detailed discussion can be found in Ma et al. (12).

Conclusions

Dense composite palladium, especially palladium/alloy, membranes will play an important and essential role in the production of pure hydrogen in the 21st century of hydrogen economy. The use of porous metal as substrates will facilitate the membrane module fabrication and process integration. Many technical issues, such as producing thin membranes with good separation characteristics and long term thermal and mechanical stability, remain to be solved. Further exploration of the use of palladium alloys to increase the hydrogen permeability and at the same time, to enhance the thermal stability can expedite the implementation of these composite membranes into hydrogen production processes.

References

(1) Lewis, F.A., The Palladium Hydrogen System, **1967**, Ac. Press. London.
(2) Mardilovich, P. P., She, Y. and Ma, Y. H., AIChE J, **1998**, 44, 310.
(3) Ma, Y.H., Mardilovich, P. .P. and She, Ying, **2000**, US Patent 6,152,987.
(4) Akis, B. C., Engwall, E. E., Mardilovich, I. P. and Ma, Y. H., **2003**, Fuel Chemistry Preprints, 47(1), the 225th ACS National Meeting, New Orleans, LA, March 23-27, 2003.
(5) Mardilovich, I. P., Engwall, E. E. and Ma, Y. H., Desalination, **2002**, 144(1), 85.
(6) Shu, J., B.P.A. Grandjean, A. Van Neste and Kaliaguine, S., Can. J. Chem. Eng.. **1991**. 69: 1036-1060.
(7) Knapton, A.G.. Plat. Met. Rev., **1977**, 21: 44.
(8) Gryaznov, V.M.. Separation and Purification Methods. **2000**. 29: 171-187
(9) McKinley, D.L. and Nitro, W.Va., **1967**. US patent 3,350,845.
(10) McKinley, D.L. and Nitro, W.Va., **1969**. US patent 3,439,474.
(11) Roa, F., Block, M. J. and Way, J. D., Desalination, **2002**, 144(4), 411.
(12) Ma, Y.H., Mardilovich, I.P. and Engwall, E.E., Annals of the New York Academy of Science, **2002**, In press.

ALLOY COMPOSITION EFFECT ON THE N-VALUE FOR H_2-SELECTIVE Pd MEMBRANES

Fernando Roa, J. Douglas Way

Colorado School of Mines, Chemical Engineering Department
1500 Illinois St, Golden, CO 80401-1887

1. Introduction

Hydrogen is known to be highly soluble in palladium and in some of its alloys [1]. This characteristic makes those Pd alloys suitable to be used as hydrogen selective membranes [2].

For reasonably thick Pd membranes (thickness ≥ 10μm), the H_2 flux can be calculated from Sievert's Law [3]:

$$J_{H_2} = \frac{\rho_{H_2}}{X_{metal}} \left(P^n_{H,feed} - P^n_{H,perm} \right) \qquad (1)$$

The dependence of the H_2 flux on feed and permeate pressures is represented in Equation 1 by the exponent 'n'. For thick Pd films, the rate-controlling step for the permeation process is the bulk metal diffusion of atomic hydrogen, for which the n-value should be 0.5 [4]. Changes in the crystalline structure of the membrane, large external mass transfer resistances, very thin films, gradients in alloy composition or the dominance of other transport mechanism have shown to cause deviations from that value [5].

Pure palladium, however, presents an embrittlement problem if in contact with H_2 at temperatures below 310°C, is easily poisoned by sulfur compounds and doesn't withstand temperature cycling. The Pd-Cu alloy has been found to show improved resistance to all of these problems while exhibiting superior permeation to cost performance at the $Pd_{60}Cu_{40}$ composition [6-8]. N-values and fluxes were calculated for a $Pd_{60}Cu_{40}$ and a $Pd_{90}Cu_{10}$.

Pd membranes should show infinite H_2 selectivity. However the presence of grain boundaries, cracks and pinholes, as well as imperfect seals cause finite permeation of insoluble species[9]. We discuss why differences in plating procedures led to a membrane exhibiting H_2/N_2 ideal selectivity over 7000.

2. Experimental

Materials. Composite Pd alloy membranes were fabricated by sequential deposition of commercially available palladium and copper electroless plating baths onto asymmetric 0.05 cut-off zirconia coated α-alumina tubes (US Filter, T1-70). All gases used were nominally 99.999% pure (UHP grade).

Preparation. A seeding procedure has to be used prior to the palladium plating. That step involves impregnation of the ceramic support with an organic Pd salt solution, followed by calcination and reduction in flowing hydrogen.

Pd and Cu electroless plating baths were then used in combination with osmotic pressure gradients to deposit films ranging from 1 to 5 microns in thickness. The osmotic pressure, generated by circulating concentrated sucrose solutions on the outside of the tubes, insured reduced porosity and promoted surface homogeneity and densification of the plated Pd film [10].

High Temperature Permeation Tests. The membrane to be tested was loaded into a stainless steel module, which in turn was mounted in a tube furnace. To avoid embrittlement, the membranes were heated under helium and no H_2 was introduced until the membrane reached 350°C. Annealing the two metals was achieved while conducting the single gas permeability tests, run at transmembrane pressure differentials of 345 and 172 kPa and temperature varying from 350°C to 500°C. Permeate pressure was local atmospheric pressure (~83 kPa) and no sweep gas was used.

Characterization. Scanning electron microscopy (SEM) was carried out to determine film thickness; Atomic Force Microscopy (AFM) was used to study surface morphology; X-ray diffraction (XRD) and energy dispersive X-ray spectroscopy (EDAX) were used to study crystal structure and determine Pd alloy composition.

3. Results and Discussion

Alloy Composition and Flux. For Pd-Cu membranes, the H_2 flux is strongly influenced by the alloy composition and it has a maximum at about 40-wt% Cu. This behavior is attributed to a favorable phase transition occurring at about this composition in the solid phase [11]. We targeted that specific composition; however, given that our current membrane fabrication procedure mandates each metal to be deposited separately and that we could only calibrate the deposition time after testing the membrane, several membranes of different compositions were made.

Table 1. Permeation Data for Pd-Cu Membranes at 350°C

Membrane	Metal Thickness (μm)	Pd/Cu Alloy Composition (wt%)	Max. Permeance $\left(\frac{mol}{m^2 min Hg^{0.5} s}\right)$	Max. Selectivity
20	1.0± 0.2	90/10	0.061	2000
22	1.5± 0.2	70/30	0.138	48
25b	1.5± 0.2	60/40	0.312	93
28	3.5± 0.5	90/10	0.035	≥7000

Table 1 summarizes the permeation experiments results for our recent membranes. Of the membranes shown there, membrane 25b clearly exhibits the highest permeance; in agreement with the literature, it has a $Pd_{60}Cu_{40}$ alloy as its selective layer. Figure 1 shows the influence of alloy composition on the permeance values for membranes studied in this work. Hydrogen permeance values for 10-25μm-thick Pd-Cu foils from the literature are also plotted on Figure 1 for comparison. As can be seen in that plot, both membrane 25b and the $Pd_{60}Cu_{40}$ foils exhibited higher hydrogen permeance than their comparable membranes having different alloy compositions. Moreover, the H_2 permeance of membrane 25b is more than twice that of an equivalent foil.

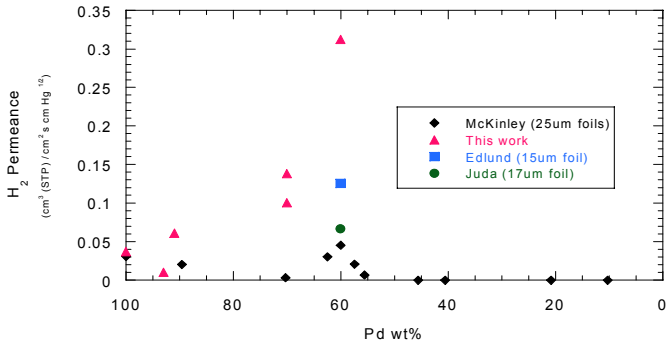

Figure 1. Alloy composition influence on H_2 permeance for Pd-Cu composite membranes and Pd-Cu foils.

Among the factors contributing to the differences in permeance are: the use of supports for making our membranes; these being thinner than the foils; that their surface morphologies are different according to AFM images, and that their bulk crystalline structures are also different as our membranes exhibit domains for both the fcc and bcc phases as opposed to just bcc for the foils (from XRD data).

N-value and Temperature. Figure 2 presents the transport data for membrane 25b at 350°C. Non-linear regression of the data gives an n-value of 0.515. Given that the experimental n-value is very close to the theoretical value of 0.5, it is likely that the H_2 transport through this membrane is controlled by the diffusion of hydrogen atoms through the metal bulk film. By contrast, the n-value for nitrogen permeation through the same membrane was 1.05; presumably indicating that nitrogen transport occurred mainly by Knudsen diffusion through defects in the metal film and seals. The ideal H_2/N_2 separation factor at 350°C for a feed pressure of 25 psig was 100.

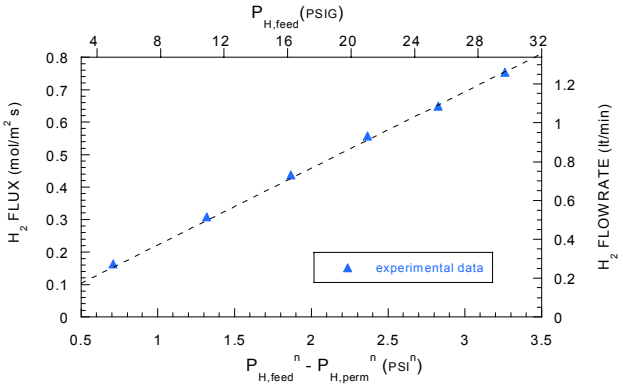

Figure 2. Permeation data for membrane 25b at 350°C. The dotted line shows predicted H_2 fluxes using eq. 1 with n equal to 0.515.

The n-value dependence on temperature was observed for membrane 28 and it is plotted in Figure 3. This membrane was not typically prepared, as it had to be plated again because it failed after air was accidentally let in for an extended period, during the high temperature experiments. As seen in Figure 3, the n-values for membrane 28 departed significantly from the ideal value, 0.5, in contrast with membrane 25b. Moreover, the ideal H_2/N_2 ideal selectivity for membrane 28 was very high, well over 7000.

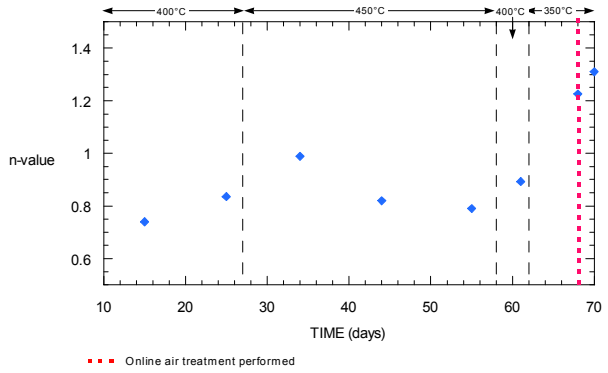

Figure 3. Effect of temperature and time in the n-value for #28.

That discrepancy may be related to the different preparation histories for the two membranes. Based on recently published results for controlled oxidation of on palladium films [12], it is thought that the prolonged air exposure made the original metal film rearrange to form a pattern of conically shaped structures, much like a range of hills and valleys, schematically illustrated in Figure 4, creating a metal oxide layer of very small pore size on top of the ceramic support. These micropores in the sieve-like structure developed would then be easily and completely covered with the subsequent metal depositions, essentially forming a pore-free film, which would thus explain the high selectivity membrane 28 showed. Note, however, that inside those micropores the formation of micro voids underneath the newly deposited film was likely, due to less than perfect wetting between the metallic and oxidized layers, a consequence of the different electronic nature of each surface.

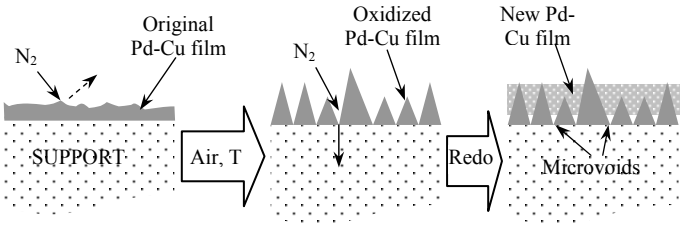

Figure 4. Sketch of what is thought happened to membrane 28.

As a consequence, we hypothesize that there are two different rate processes in series limiting the permeation through the metal film in membrane 28 rather than just one as was the case for membrane 25b: proton diffusion through the metal film and gas phase mass transfer resistance in the voids; each would in turn become dominant depending on the transport conditions.

4. Conclusions

A range of Pd-Cu composite membranes of different alloy composition were fabricated and they exhibited a hydrogen permeation trend consistent with the literature.

A $Pd_{60}Cu_{40}$ membrane was made that showed higher permeance than other composite membranes of different alloy composition and than $Pd_{60}Cu_{40}$ foils. A $Pd_{90}Cu_{10}$ exhibited selectivity over 7000.

The transport mechanism for H_2 through Pd-Cu membranes is affected by alloy composition, temperature and preparation history.

Acknowledgements. This work was supported by the U.S. Dept. of Energy (DOE) University Coal Research Program under grant No. DE-FG2699 – FT 40585. The authors are grateful to Dr. David Edlund of IdaTech, LLC for donating the $Pd_{60}Cu_{40}$ foil membrane used in this work. The authors are also grateful to Michael J. Block for his help with membrane preparation and transport experiments.

5. References

1. Linkov, V. Membrane Technology, 2001. **132**: p. 4-8.
2. Paglieri, S., D. Way, and J. Collins. Ind. Eng. Chem. Res., 1999. **38**(10): p. 1925-1936.
3. Ward, T. and T. Dao. J. Membrane Sci., 1998. **153**(1): p. 211-231.
4. Uemiya, S., T. Matsuda, and E. Kikuchi. J. Membr. Sci. 1991. **56**: p. 315-325.
5. de Rosset, A.J. 1960: U.S. Patent 2,958,391
6. McKinley, D.L. 1967: U.S. Patent 3,439,474
7. Edlund, D.J. and D.T. Friesen. 1993: U.S. Patent 5,217,506
8. Juda, W., Krueger, C.W., and Bombard, R.T. 2000: U.S. Patent 6,103,028
9. Roa, F., D. Way, and S. Paglieri. Chem. Eng. J., 2002. **4047**: p. 1-12.
10. Varma, A. and R. Souleimanova. J. Membrane Sci., 2000. **166**(4): p. 249-257.
11. Piper, J. J. Appl. Phys., 1966. **37**(2): p. 715-21.
12. Aggarwal, S., *et al.* Science, 2000. **287**: p. 2235-2237.

EFFECTS OF THE IN-SITU FORMATION OF AN INTERMETALLIC DIFFUSION BARRIER LAYER ON THE PROPERTIES OF COMPOSITE PALLADIUM MEMBRANES

B. Ceylan Akis, Erik E. Engwall, Ivan P. Mardilovich and Y.H. Ma

Center for Inorganic Membrane Studies
Department of Chemical Engineering
Worcester Polytechnic Institute
Worcester, Massachusetts 01609

Introduction

Composite palladium and palladium/alloy membranes are especially suited for high temperature hydrogen separation and membrane reactor applications. However, when porous metal supports are used at high temperatures, the intermetallic diffusion between metal elements in the substrate and the palladium separation layer causes the hydrogen flux to deteriorate. One way to improve the membrane stability is to create an intermediate intermetallic diffusion barrier layer. This barrier layer can be created by the in-situ controlled oxidation of the substrate prior to plating, developed recently by Ma *et al*. (1). The technique consists of the oxidation of the metal substrate (e.g., porous stainless steel) followed by electroless plating. A detailed description of the technique can be found in Ma *et al*. (1).

The objective of this work was to investigate the effect of oxidation time and temperature on the surface of porous stainless steel (PSS), thus on the thickness of the Pd dense layer and hydrogen flux. Specifically, the effects of the oxidation temperature and time on the pore size and porosity of the porous stainless steel support were systematically investigated. In addition, the effects of the oxidized layer on the surface sties required for activation and plating were studied by scanning electron microscopy (SEM) to provide better understanding of plating mechanisms on the oxidized layer.

Experimental

Electroless plating was used to plate Pd on porous stainless steel supports of Grade 0.5 μm produced by Mott Metallurgical Corporation. Both porous cups and cups welded to non-porous stainless steel tubes were used in the study. The porous stainless steel supports were oxidized in a high temperature furnace at constant temperature. The uniformity of the temperature in the furnace was carefully monitored and controlled. The cups were oxidized at three different temperatures: 400, 600 and 800°C for six hours. An additional cup was oxidized at 400°C for 18 hours to study the effect of the oxidation time. The procedure for cleaning, activation and electroless plating has been described in detail by Mardilovich *et al*. (2). The surface of the support was examined by SEM (AMRAY model 1610).

Results and Discussion

For the PSS supports, a high He flux before plating indicates low resistance to hydrogen permeation. Table 1 shows the mass gains Δm, changes in He flux ΔJ, median pore size D_p and porosity ε of the 0.5 μm grade PSS cups after oxidation at various temperatures. There were no significant changes in porosity and He flux, between the unoxidized blank and the support oxidized at 400°C. Between the oxidation temperatures of 400 °C and 800 °C the pore size and porosity decrease slightly with increasing T_{ox}. However, between the oxidation temperatures of 400°C and 800°C the reduction in He flux was too drastic to be explained by the changes in porosity. This is particularly true for changes observed between 600 and 800°C. As the oxidation temperature was increased, the weight gain increased indicating the formation of more oxide at higher temperatures. The formation of greater quantities of oxide gave a larger resistance to the He permeation.

The oxidation of PSS supports of smaller grades resulted in higher declines in the He flux after oxidation. With a 0.2 μm grade support over 90% reduction in He flux was observed after oxidizing at 800 °C for 4h. The characterization of this membrane showed that the maximum H_2 flux that could be achieved was limited by the reduced support porosity.

Table 1. Flux Decline and % Weight Gain of the Supports After Oxidation.

T_{ox} [°C]	Time [h]	Δm [%]	D_p [μm]	ε	Δ J [%]
25	-	unoxidized	3.9	0.22	0.0
400	6	~0.0	4.1	0.22	0.0
600	6	0.5	3.9	0.21	-10.4
800	6	1.4	3.7	0.20	-73.5
400	18	~0.1	-	-	0.0

Figure 1 shows the scanning electron micrographs of the four PSS cups oxidized at different temperatures for 6h. It can be seen from Figure 1 that higher oxidation temperatures appeared to increase the surface roughness. Figure 2 shows the scanning electron micrographs of the same oxidized cups after 1 hour of the Pd deposition. As shown in the figure, the size of the Pd clusters was bigger on the supports oxidized at higher temperatures. Aggressive oxidation caused enhanced formation of a porous oxide layer which provided more surface area. Furthermore, the oxidized surface appeared to enhance the absorption of $SnCl_2$ and nucleation of Pd seeds during activation and increased the surface roughness for easy attachment of Pd ions during plating.

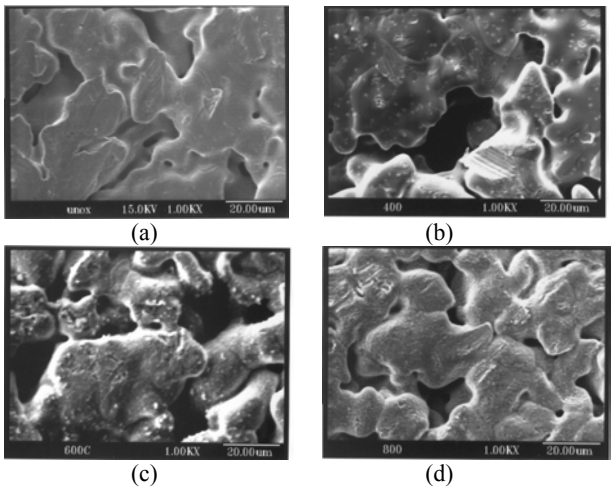

Figure 1. Scanning electron micrographs of PSS cups after oxidation: (a) unoxidized, (b) 400°C, (c) 600°C and (d) 800°C.

Another support was oxidized at 400°C for 18 h to study the effect of longer oxidation time on the surface morphology, thus the microstructure of the Pd layer. The surface morphology and cluster size of Pd deposited on cup5 were almost the same as the one oxidized at 400°C for 4 h. Furthermore, as shown in Table 1, the weight gain and He flux decline also are essentially the same as those of cup2.

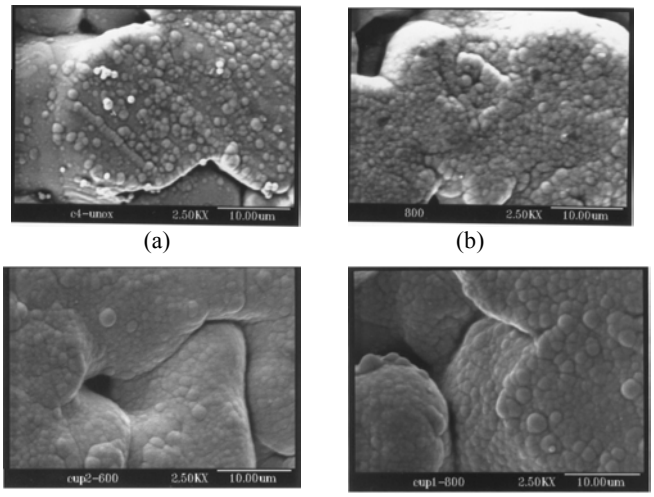

(a) (b) (c) (d)

Figure 2. Scanning electron micrographs of oxidized cups after 1 hour Pd plating: (a) unoxidized (1.8μm), (b) 400°C (2.7μm), (c) 600°C (2.8μm) and (d) 800°C (2.54μm). Note: Numbers in the parentheses indicate the Pd layer thickness at the end of one hour plating.

The He flux was used to check if the Pd layer was dense. The membrane is deemed 'dense' when there was no He flux at room temperature under a pressure difference of 1 atm. Three PSS supports welded to nonporous tubes were oxidized at three different temperatures, 400°C, 600°C, 800°C, and electroless-plated with Pd until they were dense. As shown in Figure 3, the He flux declines after oxidation showed similar behavior as the cups shown in Table 1. The final thicknesses of the dense Pd layers were about the same for the supports oxidized at 600 and 800°C and appeared independent of the oxidation temperature as shown in Table 2. The slightly thicker Pd layer for the support oxidized at 400°C appeared to be due to the lower extent of oxidation that provided less active oxide area for absorption and plating.

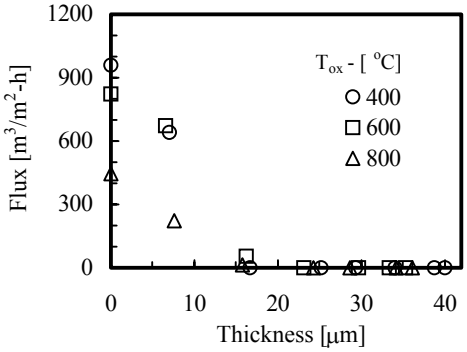

Figure 3. He flux at 1 atm difference as a function of Pd layer thickness for membranes oxidized at different temperatures.

The typical behavior of the He flux as a function of the Pd layer thickness is shown in Figure 3 for the three prepared membranes. The curves can be divided into two parts. The first part is the linear decline of He flux with the plated Pd thickness, where all the small pores were being plugged. All three membranes had different initial He fluxes as a result of the oxidation at different temperatures, however they intersected the abscissa at essentially the same point. The second part of the curves is the exponential decline of the He flux with the thickness, where the largest pores were being gradually plugged. The fact that the exponential decline starts at a similar Pd layer thickness for all oxidation conditions indicates that the pores being blocked in this portion of the curve are too large to be significantly affected by the oxidation conditions. These pores may be regarded as defect pores for the purpose of Pd membrane fabrication. Our previous works also showed that the dense Pd layer thickness was dependent on the largest pore size (3). Therefore, for large grade supports, the oxidation temperature will not affect the size of the pore enough to cause a significant reduction of the plated Pd layer thickness.

Table 2. Thickness of Dense Pd Layer on Supports Oxidized at Different Temperatures.

#	T_{ox} [^{0}C]	Time [h]	l [μm]
1	400	6	40.00
2	600	6	35.32
3	800	6	36.16

Although the oxide layer is used as a barrier for the intermetallic diffusion, it could also act as a barrier for hydrogen diffusion through the pores if the oxide layer were too thick. Therefore, the thickness of the oxide layer should be thick enough to prevent intermetallic diffusion, thereby increasing the thermal stability of the membrane but thin enough not to block the flow of hydrogen through the pores of the PSS support.

Conclusions

The oxidation of PSS supports should have an optimum time and temperature at which stable, uniform oxide layer is formed without plugging pores, thus without producing a hydrogen diffusion barrier, yet sufficient to prevent intermetallic diffusion. For relatively low oxidation temperatures, the time of oxidation does not affect the He flux appreciably.

Higher oxidation temperatures cause a larger reduction of the He flux resulting possibly from either the pores been blocked or the formation of a thicker oxide layer. Although the final thickness of the dense palladium layer does not appear to be affected appreciably by the oxidation temperature, the oxide layer not only acts as a diffusion barrier but also provides surface sites for easy activation and plating and improved adhesion.

References

(1) Ma, Y.H., Mardilovich, P. .P. and She, Ying, **2000**, US Patent 6,152,987.
(2) Mardilovich, P. P., She, Y. and Ma, Y. H., AIChE J, **1998**, 44, 310.
(3) Mardilovich, I.P.; Engwall, E.; & Ma, Y.H. *Desalination*. **2002**, *144*, 85.

NOVEL METHOD FOR FABRICATION OF SUPPORTED PALLADIUM MEMBRANES FOR MEMBRANE REACTOR

Shigeyuki Uemiya[1)], Shogo Mishima[2)], Yutaka Makino[2)], Ikumi Miyazaki[1)], Hiroshi Moritomi[2)], Makoto Nishimura[1)]

1) Department of Human and Information Systems, Faculty of Engineering,
2) Environmental and Renewable Energy Systems Division, Graduate School of Engineering,
Gifu University
Yanagido 1-1, Gifu, 501-1193 JAPAN

Introduction

In most chemical reactions there is the thermodynamically limited level of conversion attainable for a given reaction condition. Among them hydrogen producing reactions, for example steam reforming and dehydrogenation of hydrocarbon, require relatively high reaction temperatures; however, in some cases the level of equilibrium conversion is not so high even at high temperatures that the recycle operation of unconverted reactant is required in industrial-scale plants.

Membrane reactor has been proposed as one of novel reactors that will be able to solve the problems existing in thermodynamically limited reactions. Membrane reactor is defined as a reactor incorporating with a functional membrane, and enables the simultaneous separation of product with chemical reaction. Membrane reactor leads to an environmentally friendly compact and simple chemical process. Development of novel membrane material, fabrication technique of thin film, and screening of highly active catalyst even at milder reaction conditions are required for the realization and commercialization of novel membrane reactor system. We have reported the fabrication technique of supported palladium and palladium-alloy membranes[1,2] and the applicability of hydrogen permeable palladium membrane reactor[3], and have experimentally demonstrated importance of improving hydrogen permeance of supported palladium-based membranes. In this paper we will present novel methods for fabrication of a supported palladium membrane in order to decrease the thickness of palladium film.

Experimental

A porous alumina tube with asymmetric structure (o.d., 10 mm; mean pore size of effective layer, 0.2 μm) was used as a supporting material for palladium thin film. First, the tube was cleaned using a solvent in an ultrasonic condition. Palladium thin film was formed on the outer surface of the tube by the electroless-plating technique. Just before plating, the surface was activated and catalyzed in two step activation involving repeated immersing into stannous chloride and palladium chloride aqueous solutions with pure water washing between them. During this procedure, palladium ions were reduced into metallic form. The deposited utrafine palladium particles worked as a catalyst for the electroless-plating. The plating conditions are shown in Table 1.

In the improved procedure of membrane fabrication proposed here, there were five different points:

1. The temperature of activation procedure was changed from room temperature to 35°C.
2. The immersion procedure of the support into distilled water was added just before the activation procedure.
3. The immersion into hydrazine aqueous solution was added just before electroless-plating.
4. The time of the repeated activation procedure was decreased from 10 to 3.

Table 1. Composition of Electroless Plating, Sensitization and Activation Solutions

Electroless plating solution	
$Pd(NH_3)_4Cl_2$	5.4 g L^{-1}
EDTA 2Na	67.2 g L^{-1}
NH_3 H_2O [28%]	651.3 mL L^{-1}
N_2H_4 H_2O	0.35 mL L^{-1}
Sensitization solution	
$SnCl_2$ $2H_2O$	1.0 g L^{-1}
HCl [37%]	1.0 mL L^{-1}
Activation solution	
$PdCl_2$	0.1 g L^{-1}
HCl [37%]	1.0 mL L^{-1}

Plating temperature, 50°C

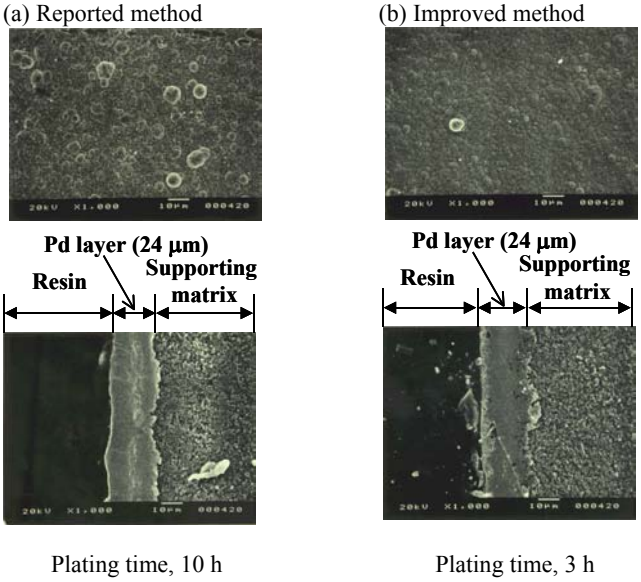

Figure 1. Surface and cross section view of supported palladium membranes.

5. Bath load, namely the ratio of the surface area of a support to the volume of the plating bath, was changed from 785 cm^2 L^{-1} to 167 cm^2 L^{-1}.

Furthermore, the effect of hydrazine concentration in the immersion procedure conducted just before electroless-plating was investigated.

The resulting membranes were characterized by SEM, XPS, and gas permeation tests. For the purpose of checking formation of pinholes and cracks, gas leakage test was conducted using helium. Hydrogen permeance of the membrane was evaluated by a traditional permeation test using pure hydrogen.

Results and Discussion

The surface of the porous alumina tube used as a support was completely covered without any pinholes by 10-hour electroless plating in the previously reported method. On the other hand, only 3 hour plating was required in the improved method. The morphology of the surface and the cross section of the both supported palladium membranes were almost same, as shown in Figure 1. The difference is found to be only plating rate.

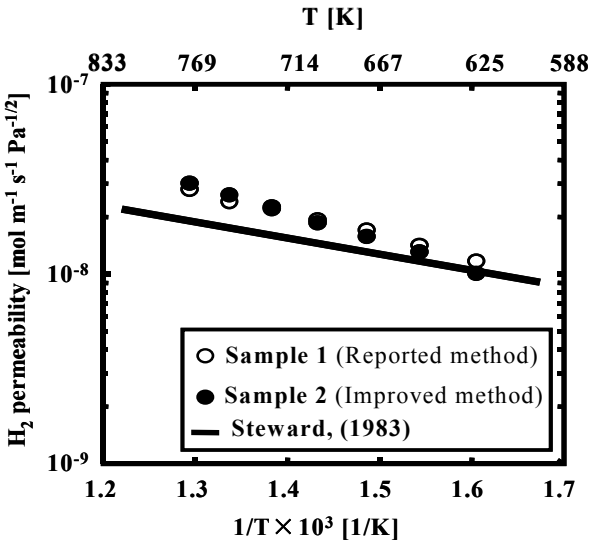

Figure 2. Comparison in hydrogen permeability between the supported palladium membranes prepared by reported and improved methods.

Table 2. Effect of Hydrazine Concentration on the Thickness of Palladium Film

Hydrazine conc. [mol L^{-1}]	Palladium thickness[1)] [μm]	Standard deviation
3.6 x 10^{-3}	3.02	0.27
7.2 x 10^{-3}	2.83	0.12
14.4 x 10^{-3}	4.66	0.21

1) Ten data obtained from the cross section view were averaged.

Figure 2 demonstrates the comparison in hydrogen permeability between two membranes. Here, hydrogen permeability means hydrogen permeance per unit area, unit thickness, unit transpressure, and unit thickness. The line in the figure indicates reported values refereed from Steward's review article[4]. The plots of hydrogen permeability are overlapped and the values are nearly equal to the reported ones. This indicates that hydrogen permeance is independent of preparation procedure.

The effect of plating method on palladium plating rate has not investigated yet; however, we may speculate that the immersion into hydrazine aqueous solution greatly affects the plating rate among five different factors between the reported and improved fabrication methods. In the reported method, a considerable amount of palladium ions, which were not reacted with stannous ions, still existed on the surface of support besides active palladium metallic ultrafine particles in electroless plating. On the other hand, in the improved method, most palladium ions were probably reduced by the reaction with hydrazine; therefore, active palladium fine particles worked as a catalyst for electroless-plating adsorbed densely on the surface, leading to the shorten preparation time of a dense supported palladium membranes applicable to membrane.

As aforementioned, the density of palladium ultrafine particles was increased in case of the improved method. This means that the adoption of the improved method possibly leads to decrease the thickness of palladium film for covering the surface of the support completely. Table 2 summarizes the effect of hydrazine concentration in the immersion procedure conducted just before electroless-plating on the thickness of palladium film. Here, a porous

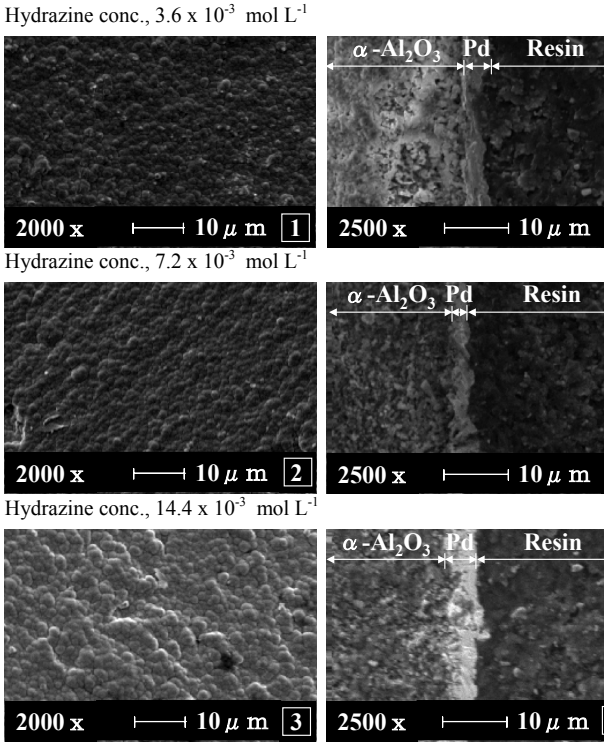

Figure 3. Surface and cross section view of supported palladium membranes prepared by improved method with different hydrazine concentration.

alumina tube with relatively short length (5 cm) was used. Fortunately, helium leakage was hardly observed in these membranes, indicating that the thickness of 2.8 μm will be enough to cover completely the surface of the porous alumina support with the mean pore size of 0.2 μm. When hydrazine concentration is 14.4 x 10^{-3} mol L^{-1}, the plating time will be shorten for the fabrication of thin palladium film with the thickness of 2.8 μm. However, stannous ions still coexisted with active palladium fine particles. Paglieri et al. demonstrated that the amount of tin presented at the interface of palladium and porous support was qualitatively related to stability of a resulting supported palladium membrane at high temperatures. Further study will be necessary to remove stannous ions from the surface of the support.

Acknowledgement. This work has been partly carried out as a research project of The Japan Petroleum Institute commissioned by the Petroleum Energy Center with the subsidy of the Ministry of Economy, Trade and Industry, and partly supported by Grants-in-Aid for Scientific Research from the Ministry of Education, Culture, Sports, Science and Technology and Japan Society for the Promotion of Science.

References

(1) Kikuchi, E.; Uemiya, S, *Gas Separation & Purification*, **1991**, 5, 261-266.
(2) Uemiya, S.; Kajiwara, M.; Kojima, T., *AIChE J.,* **1997**, 43(11A), 2715-2723.
(3) Kikuchi, E.; Uemiya, S.; Matsuda, T.; *Stud. Surf. Sci. Catal.,* **1991**, 61, 509-515.
(4) Steward, S.A.; Lawrence Livermore National Laboratory Report UCRL-53441 (1993).
(5) Paglieri, S.N.; Foo, K.Y.; Way, J.D.; Collins, J.P.; Harper-Nixon, D.L.; *Ind. Eng. Chem. Res.,* **1999**, 38, 1925-1936.

CATALYTIC MEMBRANE REACTORS FOR GAS, LIQUID AND SOLID REFORMING TO SYNGAS

Anthony F. Sammells, Thomas F. Barton, and Michael V. Mundschau

Eltron Research Inc.
4600 Nautilus Court South
Boulder, CO 80301
www.eltronresearch.com

Introduction

Catalytic Membrane Reactor (CMR) technology, under development at Eltron Research Inc., facilitates the exclusive mediation of oxygen from the atmosphere to a desired reaction site. As a consequence of this, many CMR-driven hydrocarbon partial oxidation chemistries become exothermic while at the same time eliminating the need for a separate oxygen plant - a significant reduction in overall production costs compared to currently available technology. An additional feature is that in such chemical processing NO_x emissions are eliminated, since N_2 in the air is separated from O_2 via the membrane.

In particular, this technology is being developed for the respective spontaneous reforming of natural gas, liquid fuels and coal into synthesis gas. Principles behind the membrane technology and its current status for the partial oxidation of these feedstocks will be discussed.

Experimental

Proprietary oxygen deficient metal oxides possessing the general stoichiometry $A_{2-x}A'_xB_{2-y}B'_yO_{5+z}$ were prepared following conventional high temperature solid-state synthesis techniques until subsequent XRD analysis indicated that the desired single phase material had been obtained. Membranes were prepared into closed-one-end tubes using isostatic pressing techniques followed by sintering at elevated temperatures in the atmosphere. Mixed conducting catalysts were then subsequently deposited on respectively the oxidizing and reducing membrane surfaces using either dip coating, silk screening or spray pyrolysis techniques. Following incorporation of the resulting CMR into experimental test stands, a seal was formed at the open-end of the membrane tube to ensure gas-tight separation between respective membrane compartments. Hydrogen, carbon monoxide, methane, and carbon dioxide gas constituents were analyzed using a Gow-Mac series 580 TCD gas chromatograph equipped with a carbosphere column. Helium was used as the carrier gas. Pre-analyzed standard gas samples were used for calibration purposes in order to quantify all products. Gas analyses from each membrane compartment were performed with the aid of air tight syringes (Pressure-Lok, Alltech Associates). The amount of products measured was compared to the feed in order to calculate the overall conversion efficiency of the membrane reactor system towards promoting the subject partial oxidation reactions.

Results and Discussion

Dense mixed oxygen anion and electron conducting ceramic membranes are derived from oxygen-deficient metal oxides possessing the general stoichiometry $A_{2-x}A'_xB_{2-y}B'_yO_{5+z}$. This CMR technology will facilitate spontaneous reforming of respectively natural gas (methane), liquid hydrocarbon fuels and coal into synthesis gas feeds, as shown schematically in Figure 1.

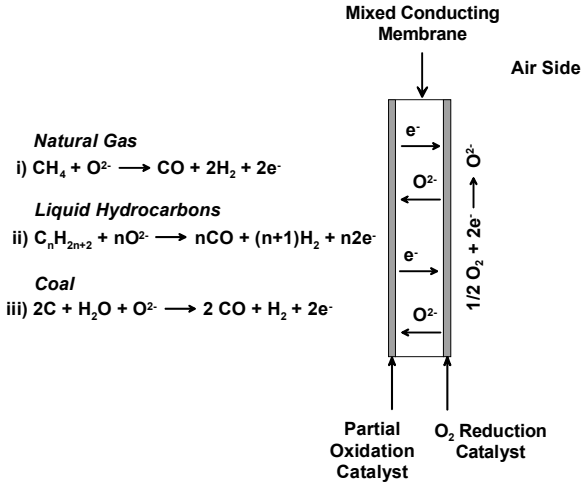

Figure 1. Schematic of spontaneous processes occurring on the membrane partial oxidation surface for the respective reforming of i) natural gas, ii) liquid hydrocarbons, and iii) coal into synthesis gas.

To achieve high oxygen flux in membrane materials which possess high stability, Eltron[1-6] has developed mixed oxygen anion and electron conducting membranes $A_{2-x}A\rho_xB_{2-y}B\rho_yO_{5+z}$ where:

A is an alkaline earth metal ion or mixture of alkaline earth metal ions; Aρ is a metal ion or mixture of metal ions where the metal is selected from the group consisting of the lanthanide series or is yttrium; B is a metal ion or mixture of metal ions wherein the metal is selected from the group consisting of 3d transition metals, and the group 13 metals; Bρ is a metal ion or mixture of metal ions where the metal is selected from the group consisting of the 3d transition metals, the lanthanides and yttrium.

The rationale for selecting specific A and B lattice substituents has evolved from work performed at Eltron which identified clear correlations between crystallographic and thermodynamic parameters relating to the activation energy for ionic transport. These parameters include: 1) the average metal-oxygen bond energy within the lattice, 2) lattice free volumes, obtained by subtracting the ionic volumes of cations and O^{2-} in the unit cell from the overall crystallographic unit cell, 3) the parameter $r_{critical}$ (r_c) which corresponds to the radius of the opening between the two A site cations and one B site cation through which the mobile anion must pass, and 4) lattice polarizability towards ionic migration.

Of all the potential applications for mixed oxygen anion and electronic conducting materials, the partial oxidation of methane to syngas is one of the most commercially important. Syngas can serve as a precursor for a variety of products such as methanol, higher alcohols or Fischer-Tropsch products. Current commercially available technology for syngas production from natural gas is based on the endothermic steam reforming reaction which may be represented by:

$$CH_4 + H_2O \rightarrow 3H_2 + CO$$

with CO also reacting with water via the water-gas shift reaction:

$$CO + H_2O \rightarrow CO_2 + H_2$$

In contrast, the methane partial oxidation reaction:

$$2CH_4 + O_2 \rightarrow 2CO + 4H_2$$

proceeding across mixed conducting membranes is exothermic, with oxygen being separated from the atmosphere at the membrane reducing surface for subsequent participation in the natural gas partial oxidative reforming reaction at the membrane oxidizing surface.

CMRs have been successfully operated under ambient pressure conditions for over one year at 900°C for natural gas reforming with no evidence of instability. Performance realized for ambient pressure CMRs may be summarized as: Syn Gas Production Rate - 60 mL/min•cm^2, Equivalent O_2 Flux 10-12 mL/min•cm^2 (corresponding oxygen anion conductivity > 1S cm$^{!1}$), H_2: CO Ratio - ~ 1.9 - 2.0, CO Selectivity - >96%, Throughput Conversion - 90% CH_4, 70% O_2 (air). Additionally, Eltron has accumulated over eight years of experimental experience for CMRs operating at elevated temperatures with a 250 psi pressure differential between the hydrocarbon and the air side of the membrane.

The spontaneous reforming of liquid hydrocarbon fuels into H_2/CO mixtures provides a feedstock compatible for subsequent electrochemical oxidation in the anode compartment of a Solid Oxide Fuel Cell (SOFC). The overall reforming process may be represented by:

$$C_nH_{2n+2} + n/2O_2 \rightarrow nCO + (n+1)H_2$$

Ceramic membrane partial oxidation process operating conditions have been systematically evaluated using: i) the respective logistic fuel model constituents dodecane, hexadecane, octane, branched chain hydrocarbons and aromatic hydrocarbons, and ii) representative diesel and jet fuels. At 900°C, synthesis gas production rates approaching 40 mL/min-cm^2 were achieved when converting dodecane as a simulant for diesel fuel. Throughput conversions were 99%. This corresponded to an oxygen flux rate across the membrane >6.3 mL/min-cm^2. CMRs were also operated directly on both diesel and jet fuels. For diesel fuel, the synthesis gas production rate was >27mL/min-cm^2 with stoichiometric (100%) throughput conversion. In the case of jet fuel, the synthesis gas production rate was >22 mL/min-cm^2 with a throughput conversion of >80%. Diesel fuel partial oxidation to synthesis gas at a rate of 27 mL/min-cm^2 when used for SOFC fuel would produce an equivalent current of 3.9A/cm^2. Assuming the SOFC operates at 0.75V per cell, this would correspond to a power output of 2.9W/cm^2 of membrane reactor surface area.

Eltron's CMR technology is also being applied towards oxygen separation for reaction with coal fines. Membrane-based coal gasifiers are being developed for both the direct catalytic gasification of coal with mediated oxygen anions as well as for coal gasification with molecular oxygen evolved from the membrane's oxidation catalyst. This is requiring the development of two catalysis strategies. Gasification reactions occurring between coal and mediated oxygen are a combination of the partial oxidation and complete combustion of coal as shown below:

$$C + \tfrac{1}{2}O_2 \rightarrow CO$$

$$C + O_2 \rightarrow CO_2$$

where C is used as an empirical representation for coal. Using coal as the sole component of the feedstream requires consideration of two issues. The first is that since the above reactions are highly exothermic (ΔH = -110.5 J/mol and -393.8 J/mol respectively), any reactor system using this approach must be designed to account for proper heat transfer. Secondly, the sole product of this process is not very versatile, useful only as a fuel or as a feedstock in chemical processes requiring carbon monoxide.

In order to address these two issues, steam is being added to the coal feedstream. Since the steam reforming of coal, given below,

$$C + H_2O \rightarrow H_2 + CO$$

is endothermic in nature (ΔH = 175.4 J/mol), this process can then be used to absorb the heat generated by the exothermic coal oxidation process.

Furthermore, the introduction of steam serves to form hydrogen. The resulting product, a mixture of hydrogen and carbon monoxide, has a high BTU value making it more valuable as a fuel or as a feedstock for the production of liquid fuels such as methanol or diesel.

The following reaction, which is a combination of the partial oxidation and steam reforming of coal, summarizes the catalytic process being developed at Eltron utilizing CMRs with a humidified coal feed stream to yield a product containing hydrogen and carbon monoxide.

$$2C + \tfrac{1}{2}O_2 + H_2O \rightarrow 2CO + H_2$$

For the process to be self-sustaining it needs to be operated at the thermoneutral point or exothermically. The thermoneutral point is represented by:

$$1.8\ C + 0.5\ O_2 + 0.8\ H_2O \rightarrow 0.8\ H_2 + 1.8\ CO$$

which yields a product gas with a H_2:CO ratio of 0.44:1.

For fixed-bed coal gasifiers, coal gasification rates as high as 4.9 mL/min/cm^2 (61.3 ml/min) were obtained. A corresponding oxygen depletion of greater than 60% was found on the air side confirming the utility and role of the mixed conducting membrane. There was never any sign of melting of the coal ash which was recovered following experimentation. This indicates that this membrane-based gasifier operates below the slagging temperature. Coal gasification production rates of up to 17.8 mL/min/cm^2 (188 mL/min) were achieved with a continuous feed reactor operating at 900°C. Experimentation without an oxidation/reforming catalyst on the surface of the membrane showed similar results to when a catalyst layer was deposited on the oxidation surface. This indicates that intimate contact between coal, oxygen anions, and steam on the membrane surface is not essential, greatly simplifying future gasifier designs.

Acknowledgment. This work is supported by the U.S. Department of Energy (DOE) and the Defense Advanced Research Projects Agency (DARPA).

References

(1) Schwartz, M.; White, J. H.; and Sammells, A. F. U.S. Patent 6,033,632, March 7, 2000.
(2) Mackay, R.; Schwartz, M.; and Sammells, A. F. U.S. Patent 6,165,431, December 26, 2000.
(3) Mackay, R.; and Sammells, A. F. U.S. Patent 6,146,549, November 14, 2000.
(4) Schwartz, M.; White, J. H.; and Sammells, A. F. U.S. Patent 6,355,093, March 12, 2002.
(5) Schwartz, M.; White, J. H.; and Sammells, A. F. U.S. Patent 6,214,757, April 10, 2001.
(6) Van Calcar, P.; Mackay, R.; and Sammells, A. F. U.S. Patent 6,471,921, October 29, 2002.

DEVELOPMENT OF THE CERAMIC MEMBRANE ITM SYNGAS/ITM HYDROGEN PROCESS

Michael F. Carolan, Christopher M. Chen and Steven W. Rynders*

Advanced Gas Separation Department
Air Products and Chemicals, Inc.
7201 Hamilton Boulevard
Allentown, PA 18195

Introduction

The ITM Syngas Team led by Air Products and Chemicals and including Ceramatec, ChevronTexaco, Eltron Research, McDermott Technology and other partners, in collaboration with the U.S. Department of Energy, is developing ceramic Ion Transport Membrane (ITM) technology for the production of synthesis gas and hydrogen from natural gas. The ITM Syngas technology is in the fifth year and Phase 2 of a co-funded $90 MM, nine year, three phase development program.

ITM membranes are fabricated from non-porous, multi-component metallic oxides that operate at high temperatures and have exceptionally high oxygen flux and selectivity. A conceptualization of the ITM Syngas process is illustrated in Figure 1. The membrane structure incorporates a non-porous ITM and reduction and reforming catalyst layers. The membrane material must show long-term stability in reducing and oxidizing atmospheres, and long-term compatibility with the reduction and reforming catalysts.

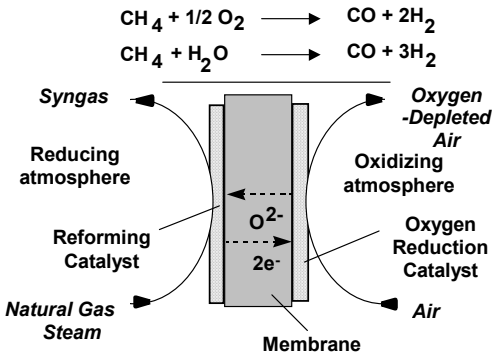

Figure 1. The conceptual ITM Syngas technology.

ITM Syngas Process Design

The ITM Syngas process combines air separation and high-temperature syngas generation processes into a single, compact ceramic membrane reactor, resulting in significant savings when compared to conventional technology. In contrast to conventional oxygen-blown Autothermal Reformer (ATR) processes that require high-pressure oxygen typically supplied by a cryogenic Air Separation Unit (ASU), the ITM process uses low pressure air directly, resulting in significant capital and operating cost savings. The ITM Syngas process is outlined in Figure 2 [1-4]. The process has several important features: production of syngas at high pressure while consuming air delivered at low pressure, use of an upstream prereformer, non-isothermal operation of the ITM Syngas reactor, and integration with the downstream Fischer-Tropsch (FT) process. The ITM Syngas reactor operates in the 200 to 500 psig pressure range, and produces syngas at pressure suitable for downstream Fischer-Tropsch processes without the need for further compression. The air supplied to the ITM Syngas reactor is delivered at low pressure (approximately 5 to 10 psig), resulting in additional significant capital and operating cost savings.

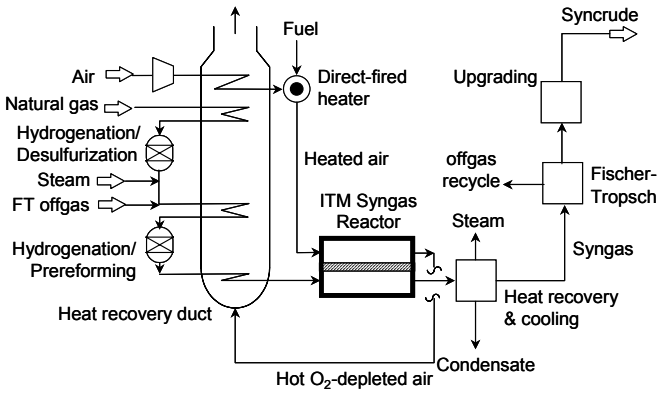

Figure 2. The ITM Syngas process with adiabatic prereformer.

The natural gas feed is converted into syngas in a two-stage process comprising a steam reforming step followed by conversion to syngas in the ITM Syngas reactor. The prereforming step converts a portion of the methane and essentially all of the heavier hydrocarbons into hydrogen, carbon monoxide, carbon dioxide, and methane. This step minimizes processing problems, such as carbon formation, in the downstream heat exchanger and the ITM Syngas reactor.

The ITM Syngas reactor operates non-isothermally, with a prereformed natural gas inlet temperature of 550 – 750 °C and a syngas exit temperature of > 800 °C. The exit temperature is in the preferred range for oxidative reforming while the cooler inlet temperature minimizes carbon formation in the inlet piping and permits a wider choice of piping materials.

CO_2-containing offgas from a downstream Fischer-Tropsch plant may be recycled to the feed of the ITM Syngas process to adjust the product syngas H_2/CO molar ratio to about 2, suitable for FT GTL. This avoids an acid gas removal system to recycle CO_2; instead, the FT offgas containing CO_2 is recovered at high pressure along with other useful components to be recycled, such as light hydrocarbons, hydrogen, and carbon oxides.

Economic Analysis

Air Products, ChevronTexaco, and McDermott developed an ITM Syngas process design and cost estimate for an offshore GTL facility that processes 55 million SCFD of associated gas and produces approximately 6,400 barrels per day of syncrude. The economic evaluation compared an ITM Syngas process to an oxygen-blown ATR process that included a cryogenic ASU. Capital cost savings of greater than 30% are predicted with the ITM Syngas process over a conventional ATR with ASU. Other advantages of the ITM Syngas process include an increase in overall fuel efficiency to 61% versus 58% for ATR/ASU; and up to 40% less deck space required for syngas process and power generation equipment.

Ceramic Fabrication and Testing

The ITM Syngas/ITM Hydrogen team has developed stable ITM Syngas material compositions and successfully fabricated planar membranes from these materials. The membranes are based on microchannel device designs developed by Air Products, Ceramatec, and McDermott and are fabricated at Ceramatec using methods that provide good scalability for commercial application.

Laboratory-scale membranes have been used extensively to evaluate the properties and performance of candidate ITM materials

developed by Air Products, Ceramatec, and Eltron Research. Several generations of ITM Syngas material compositions have been evaluated and compositions that achieve the commercial flux targets have been identified.

Pilot-scale membranes are used to evaluate membrane performance at commercial process conditions. The membranes are assembled into single or multi-membrane modules and are mounted into superalloy holders using double U-ring ceramic/metal seal assemblies developed by Air Products and Ceramatec [5]. A representative pilot-scale membrane module, prior to installation, is illustrated in Figure 3.

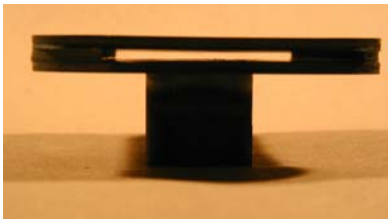

Figure 3. A pilot-scale Membrane Module

Development activities at Ceramatec have also focused on the implementation of fabrication processes to produce large area membranes. These activities have led to a rapid development of scalable fabrication processes and a nearly 200 fold increase in the area of membranes that can be fabricated. Figure 4 illustrates the significant increase in the area of membranes, up to and including full-sized membranes, fabricated using the processes developed at Ceramatec.

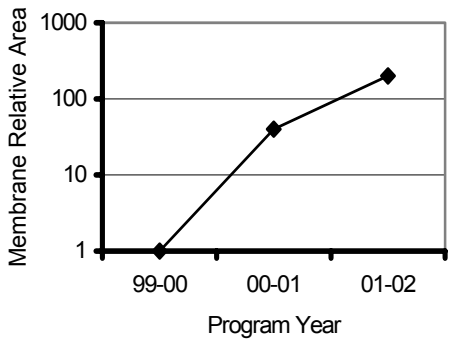

Figure 4. Progression of ITM Syngas/ITM H_2 Ceramic Membranes from Laboratory-scale to Full-sized Components.

Air Products and McDermott have jointly developed and installed a 24,000 SCFD ITM Syngas/ITM H_2 Process Development Unit (PDU) to evaluate membrane performance throughout the full range of ITM Syngas and ITM H_2 process conditions. The PDU, illustrated in Figure 5, is suitable for testing pilot and full-sized membranes and is currently in use for membrane performance testing and membrane design verification.

Conclusions

Significant progress has been made to develop the ITM Syngas/ITM H_2 technology. Membrane modules and seal assemblies have been fabricated for testing in the PDU and ceramic fabrication scaleup is continuing the progression from lab-scale to full-size membranes. A database is being built up of performance data from membrane testing in the laboratory and PDU. Excellent progress

Figure 5. The ITM Syngas/ITM H_2 Process Development Unit.

continues to be made against the remaining technical challenges in the demonstration and scale-up of the ITM Syngas and ITM H_2 technology.

Acknowledgement The authors gratefully acknowledge the work of ITM Syngas team members at Air Products and Chemicals Inc., Ceramatec Inc., ChevronTexaco Energy Research and Technology Co., Eltron Research Inc., and McDermott Technology Inc. The co-funding by the U.S. DOE (DE-FC26-97FT96052) is also gratefully acknowledged.

Disclaimer A significant portion of this report was prepared by Air Products and Chemicals, Inc. pursuant to a Cooperative Agreement partially funded by the United States Department of Energy, and neither Air Products and Chemicals, Inc. nor any of its contractors or subcontractors nor the United States Department of Energy, nor any person acting on behalf of either:

1. Makes any warranty or representation, express or implied, with respect to the accuracy, completeness, or usefulness of the information contained in this report, or that the use of any information, apparatus, method, or process disclosed in this report may not infringe privately owned rights; or
2. Assumes any liabilities with respect to the use of, or for damages resulting from the use of, any information, apparatus, method, or process disclosed in this report. Reference herein to any specific commercial products, process, or service by trade name, trademark, manufacturer, or otherwise, does not necessarily constitute or imply its endorsement, recommendation, or favoring by the United States Department of Energy. The views and opinions of authors expressed herein do not necessarily state or reflect those of the United States Department of Energy.

References

(1) Nataraj, S.; Moore, R. B.; Russek, S. L. U.S. Patent 6048472, **2000**.
(2) Nataraj, S.; Russek, S. L. U.S. Patent 6077323, **2000**.
(3) Nataraj, S.; Russek, S. L. U.S. Patent 6110979, **2000**.
(4) Nataraj, S.; Dyer, P. N.; Russek, S. L. U.S.Patent 6114400, **2000**.
(5) Minford, E.; Rynders, S. W.; Taylor, D. M.; Tressler, R. E. US Patent 6302402, **2001**.

This paper was written with support of the U.S. Department of Energy under Contract no. DE-FC26-97FT96052.

HYDROGEN RECOVERY FROM FLUID CATALYTIC CRACKING UNITS USING MEMBRANES OR CATALYTIC MEMBRANE REACTORS

Christophe CHAU, Thierry GAUTHIER°*

Institut Français du Pétrole,
1 & 4, avenue de Bois-Préau, 92852 Rueil-Malmaison - France,
*Catalysis and Separation Division, christophe.chau@ifp.fr
°Process Development Division, Chemical Engineering Department

Introduction

Hydrogen consumption and demand are increasing, due to more severe specifications on gasolines and highly hydrogen consuming units like hydrotreating, hydroconverting and hydrocracking. To face this increasing demand, refiners can invest in hydrogen production units (methane to naphtha steam reforming and partial oxidation) and/or optimize hydrogen consumption and recycle (*e.g.* catalytic reforming). In this context, hydrogen recovery from refining and petrochemical off gases has a great potential.

Fluid catalytic cracking (FCC) units are used worldwide to convert heavy hydrocarbons (typically with boiling points above 360°C at atmospheric pressure) into lighter products. Among the reaction products, dry gas contains the lighter molecules typically lighter than C3. After postreatment (absorption and further washing), dry gas contains typically 0.2 to 0.5 t/h of hydrogen (*e.g.* 0.4 t/h for FCC units with a 65,000 BPSD capacity and 27% mol. hydrogen) and this dry gas is generally used as fuel gas. Besides hydrogen, light olefins (25% mol.) and carbon oxides (0.6%) are found in these hydrogen containing gaseous streams. Considering the high FCC capacities in refineries, hydrogen recovery from dry gas can be of great economical and technical interest. A schematic flowsheet of a R2R catalytic cracking unit, licensed by Axens (of IFP's Group) and SWEC is depicted in Fig. 1.

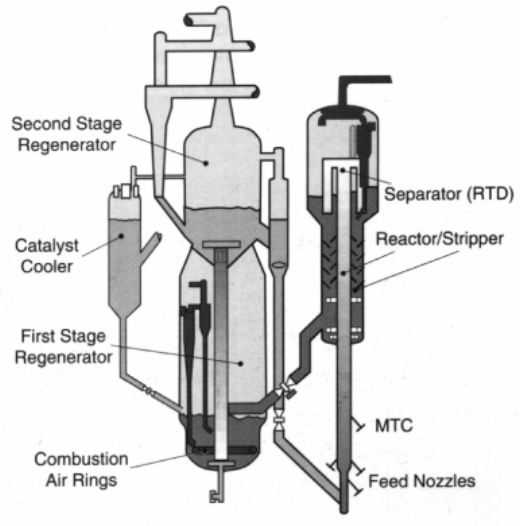

Figure 1. Flowsheet of a R2R Fluid Catalytic Cracking unit

Experimental

Hydrogen recovery from FCC units can be considered using either a separation unit with a membrane module used alone (gas permeation) or in combination with a catalyst (catalytic membrane reactor). In this latter case, the permeation driving force can be considerably increased by hydrogen consumption through a catalytic hydrogenation. The coupling effect gas permeation/catalytic reaction can compensate for the low or moderate pressures of hydrogen and the moderate permeation driving force. IFP highlights a new process flowsheet that integrates a hydrogen selective membrane and a catalytic hydrogenation of aromatics from a reforming unit.

Simulation has been carried out using Matlab software. Membrane performances were taken from literature, industrial or commercial data. Kinetic data were determined in previous IFP's studies on heterogeneous catalysis at pilot scale.

Results and discussion

Gas permeation. Requirements on hydrogen selective membranes are related to selectivity (in the presence of *e.g.* olefins, CO and H_2S), permeability (necessarily high, due to high gas flowrates) and commercial availability. Dense metallic membranes with hydrogen specificity are too expensive and their manufacture is strongly limited by palladium availability and fabrication technology. To date, only hollow fibers made of polymeric materials can be considered for this application, with their high surface to volume ratio and their commercial availability and maturity.

Our studies revealed that a sweep gas is required to increase hydrogen recovery, unless a compression stage of the hydrogen streams from FCC units is used (with high associated CAPEX and OPEX). Moreover a sweep gas would have to be integrated in the full-scale industrial process, separated from hydrogen and recycled. This alternative is seemingly not economically feasible.

Separation/catalytic reaction coupling. To improve the separation process, we have considered an integrated flowsheet (disclosed in IFP's patent applications) based on: a selective hydrogen separation using a membrane, contacting this hydrogen with a hydrogenation catalyst and a naphtha reforming containing *e.g.* 15% of aromatics. Part of these aromatics is hydrogenated and this hydrogen consumption favors hydrogen transfer through the hydrogen selective membrane by increasing permeation driving force. Lastly hydrogenated aromatics are converted in a reforming unit, thus allowing aromatics recycle and hydrogen recovery. Hydrogen is therefore recovered at a higher pressure with a high purity for further use (see Fig. 2), without any compression stage.

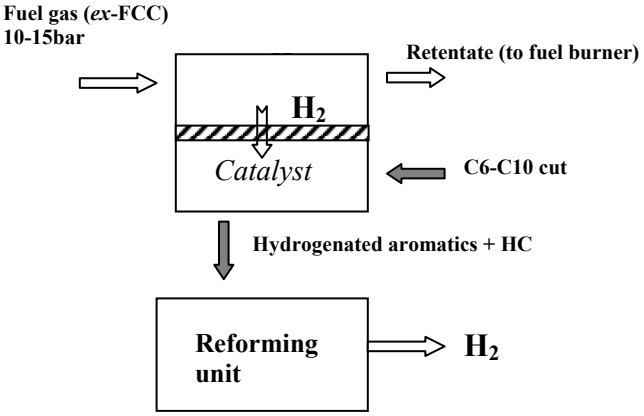

Figure 2. Hydrogen recovery from FCC units using membrane reactors

The membrane implemented has a high selectivity to hydrogen and thus limits the permeation of unsatured hydrocarbons and carbon oxides, which can affect catalyst activity. Operating conditions allow both hydrogen permeation and catalytic conversion in the catalytic membrane reactor.

A sensitivity study has been carried out and highlighted operating conditions to increase the synergetic effect of hydrogen separation (by membrane) and catalytic reaction. Space velocity at the reaction side and membrane performances determines the efficiency of hydrogen recovery. Co-current and counter-current modes are of great importance in the combined system and affect membrane surface area. Moreover, the catalytic activity can limit hydrogen recovery.

Conclusions

In hydrogen-containing streams from refining and petrochemistry, gas permeation allows partial hydrogen recovery, as soon as the hydrogen selective membrane performances (permeability, high selectivity) and the modular compacity and membrane specific surface area are very high. With hydrogen streams from FCC units, delivered at moderate to low pressures, hydrogen compression is required to reach hydrogen recoveries that are economically feasible.

Membrane/catalyst coupling allows increased hydrogen recovery rates by hydrogen consumption through a catalytic reaction. IFP proposed flowsheet is an integrated and combined system in which hydrogen recovery is higher than that of a permeation system. Catalyst activity is of significant importance as it affects hydrogen permeation driving force and the closer the coupling effect, the higher the hydrogen recovery rate.

Oxygen transport membranes for ultra-clean fuel production

E.T. Robinson
Torix, Inc.
7165 Hart. St., Ste. B, Mentor, Oh. 44060

Introduction

Natural gas is an abundant, inexpensive hydrocarbon resource that can be converted to clean burning liquid fuels. Most gas to liquid (GTL) processes require two steps: conversion of natural gas to a mixture of hydrogen and carbon monoxide (syngas), followed by an upgrading process such as Fischer-Tropsch (FT) synthesis, methanol synthesis or water-gas shift to hydrogen. The Fischer – Tropsch process converts syngas to a highly paraffinic synthetic crude oil that is free of sulfur and aromatics. The synthetic crude can be refined to yield a clean, high cetane diesel fuel. In the overall GTL process scheme, the syngas production consumes about 60% of the capital and therefore has been the focus of extensive research to reduce costs. The conventional syngas process, autothermal reforming, requires high purity oxygen, which is normally produced by cryogenic distillation. Ceramic oxygen transport membranes can replace cryogenic oxygen and thus offer a potentially lower cost, higher efficiency method for producing syngas from natural gas in ultra-clean fuel applications.

Oxygen Transport in Mixed Conducting Membranes

A commercial OTM process exploits the unique properties of mixed conducting ceramic materials, which transport both oxygen ions and electrons across a gas impermeable membrane. The membranes are typically made of inorganic crystalline metal oxides with the general composition ABOx, where A and B are cations and x is a number that satisfies the valences of A and B. Numerous compositions have been patented for various oxygen separation and oxidation applications[1, 2].

The oxygen separation process, **Figure 1**, involves at least four steps: 1) molecular oxygen diffuses to the membrane surface on the air side, 2) molecular oxygen dissociates to oxide ions, consuming electrons, 3) oxide ions diffuse across the membrane by moving through oxygen vacancies, electrons move in the opposite direction, and 4) oxygen ions recombine or react with process gas on the fuel side, liberating electrons. The driving force for oxygen transport is the chemical activity or oxygen partial pressure gradient from the air to fuel side. However, other factors can be rate limiting. At high oxygen flux rates, diffusion or mass transport of oxygen to the membrane surface, or oxidation products away from the membrane surface, can be rate controlling. The electronic and ionic conductivity of the ceramic membrane materials are rate determining at lower temperatures. Most materials require temperatures in excess of 700C and partial pressure gradients (pO2 air/pO2 fuel) exceeding 10,000 to achieve commercial significance.

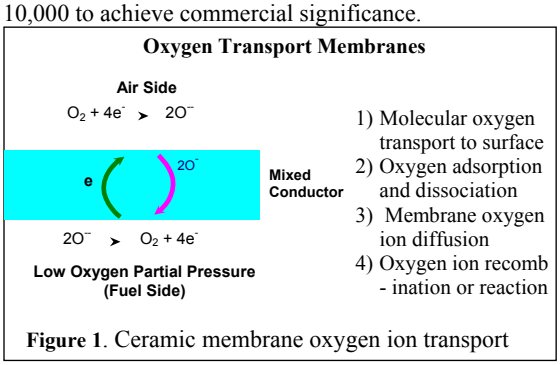

Figure 1. Ceramic membrane oxygen ion transport

Application of OTM to Syngas Production

The benchmark syngas technology for the Fischer Tropsch (FT) process is autothermal reforming (ATR). ATR reacts high purity oxygen with natural gas and steam at pressures of 15 to 40 bar and temperatures above 950C. The ATR process employs a catalyst to ensure the product gases achieve equilibrium conversion. Product gas composition is determined by the process conditions, (temperature and pressure) and relative amounts of steam, oxygen and carbon dioxide fed to the reactor. For FT, a H_2/CO ratio of about two is desired, with minimum quantities of CO_2. The major cost component for ATR is the air separation unit, which includes air compression to about 6 bar, cryogenic oxygen distillation and product oxygen compression to about 30 bar.

OTM can in principal reduce or eliminate the cost of all three of these unit operations if the mixed conducting materials can achieve certain oxygen flux and durability targets. A significant advantage of OTM is the ability to transport oxygen from a low pressure air source to a high pressure fuel stream without mechanical compression. Oxygen partial pressure on the fuel side of the membrane is on the order of 10^{-12} to 10^{-16} bar, regardless of total pressure of the fuel gas. Thus, a substantial driving force is established across the membrane, irrespective of the actual pressure differential. With OTM, air compression is minimal, just enough to overcome the pressure drop through the OTM reactor and air heat exchangers. Obviously no oxygen compressor is required if the membrane is operated above the FT pressure. And, of greatest significance, OTM eliminates cryogenic distillation.

Oxygen Transport Membrane and Reactor Design Challenges

The critical performance factors for an OTM based syngas process are oxygen flux and membrane durability. Oxygen flux, often reported in units of standard cubic centimeter of oxygen per minute per square centimeter (scc/min./cm^2), directly determines the surface area of oxygen transport membrane required to achieve the target oxygen flow rates. Fluxes exceeding 10 scc/min/cm^2 have been reported as minimum requirements for an economical syngas process[3]. A much greater challenge is to build an OTM element that can withstand the extreme temperatures and stresses of an ATR environment, while resisting creep, corrosion and poisoning.

In an ATR or OTM syngas reactor, at least five reactions are occurring:

1) CH4 + ½ O2 → CO + 2H2
2) H2 + ½ O2 → H2O
3) CO + ½ O2 → CO2
4) CH4 + H2O → CO + 2 H2
5) CO + H2O → CO2 + H2

The first three oxidation reactions are exothermic, the steam methane reforming (SMR) reaction (4), is endothermic, and the water gas shift reaction (5) is about thermally neutral, depending on operating conditions.

Oxidation on the fuel side is very rapid and has an "autocatalytic like" effect: oxidation reduces the oxygen partial pressure and increases the temperature, both of which increase oxygen flux. With no controls, thermal runaways and formation of local hot spots are major concerns. The steam methane reforming reaction will adsorb the heat of oxidation. Catalyst deployment to promote SMR in the hot zones is a primary design consideration. Adequate temperature monitoring and control mechanisms must be in place to ensure safe and reliable operation.

OTM Element

The element is the means of deploying the oxygen transport membrane in a chemical reactor. Both planar and tubular designs have been considered. Both must withstand the pressure load across the membrane of 15 to 40 bars and be capable of achieving a reliable

seal. The OTM Alliance has selected a tubular element design, primarily because successful seals have been developed, and many manufacturing hurdles have already been overcome.[4] Eight foot tubular elements have been made and 5 foot elements have been tested in a mutli-tube pilot plant reactor.

However, the most serious challenge facing these elements is the capability to withstand the stresses created by the process pressure, mechanical loads and the thermal and chemical gradients inherent in the system. The trans- membrane pressure of 15 to 40 bars is a significant, yet static force on the membrane. Membranes can be made thick enough to withstand the pressure, but at the expense of oxygen flux. At high operating temperatures, creep is a concern. An extremely low creep material is needed to achieve element life times in excess of 5 years.

Of greater concern are the stresses created by thermal and chemical gradients. Thermal stresses are dynamic and can be enormous. Thermal stresses are created by temperature gradients or connected materials with different thermal expansion properties. In the former case, a temperature gradient causes one part of the membrane to expand more than the cooler side, creating stresses in the element. Another issue is supporting the element and providing room for thermal growth. A closed end tubular element requires only one seal and allows unimpeded expansion in the axial direction.

An OTM element made of materials with dissimilar rates of thermal expansion can generate considerable stresses, even if all materials are at the same temperature. As a rule of thumb, the coefficient of thermal expansion (CTE), measured as parts per million per degree C, should match within ~< 1 ppm/C over the entire temperature range, from a cold start to full operation. Managing these same types of thermal stresses is also a major issue for planar solid oxide fuel cells.[5]

A third source of stress in an OTM element is the volumetric change of the material under different oxygen partial pressures. As the oxygen partial pressure decreases, an OTM material will lose oxygen ions, creating vacancies in the crystalline lattice. Oxygen vacancies are the mechanism for ionic transport through the membrane. The penalty however is the crystal will expand, creating internal stresses.

An example of dynamic stress creation and relaxation is shown in **Figure 2.** A rapid, short change in oxygen partial pressure[4] will develop significant stress gradients that decay with time. Under steady state conditions, a significant stress gradient can also be created in response to the large oxygen partial pressure drop across the membrane, as shown in **Figure 3**. In both cases the inherent strength of the materials must exceed the stresses created, or the element will fail.

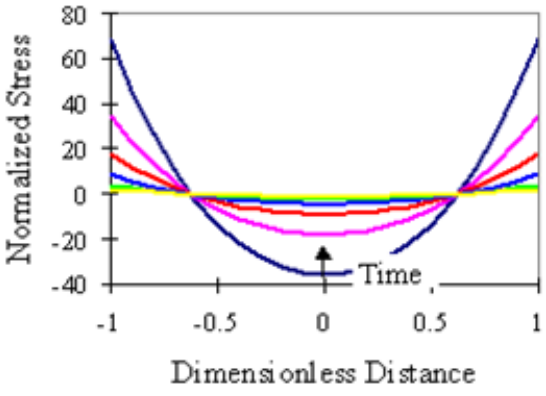

Figure 2. Calculated stress response to a pulse change in oxygen partial pressure. Zero distance is the membrane centerline

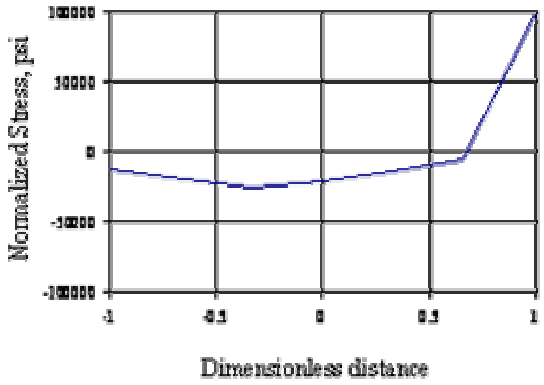

Figure 3: Steady state stress gradient with air on one side and process gas on the opposite side

In addition, an OTM element must resist attack by carbon dioxide and steam. Some metal oxides will form carbonates at elevated CO_2 partial pressures and moderate temperatures. Long term ionic diffusion and phase stability may also be issues, especially in the high temperature region of the element.

Technical Solutions to Challenging Problems

As discussed above, the technical challenges of an OTM based syngas technology are formidable. It is unlikely that a single breakthrough or development will resolve all of the issues. We have therefore adopted a systems approach that focuses on three aspects of the technology:

- Process and reactor design
- Materials development
- Element development

Process and Reactor Design

The broad objectives of the process and reactor design program are: 1) achieve cost and performance targets and 2) ensure safe operation with responsive control. Obviously, the OTM syngas process must reliably and economically deliver a high quality product gas. Key targets are high methane conversion (>97%), consistent H_2/CO ratio of two, high oxygen utilization (~80%) and a competitive capital cost. The reactor and control system must minimize hot spots, prevent thermal runaways, be responsive to load changes, and be entirely safe under both normal and abnormal operating conditions and scenarios.

Reactor development has focused on a progressive scale-up from bench units to pilot plants, coupled with concurrent development and verification of mathematical models. Computational fluid dynamic models have been successfully linked with gaseous diffusion and solid state kinetic models to provide a fairly accurate view of the complex chemical and physical phenomenon in the OTM element and reactor. Thermal and chemical composition maps from the CFD kinetic models are inputs to finite element models to predict stress gradients in OTM elements. The kinetic models assist the development of catalysts and catalyst deployment strategies, which are essential for achieving the close-coupled thermal integration required to control local temperature and achieve maximum efficiency. These tools are important for scale-up, troubleshooting and guiding the technical program.

Materials Development

The OTM material is the "secret ingredient" of the OTM syngas process. The key hurdle is developing a material or suite of materials that collectively are stable, strong, and creep resistant and can deliver

high oxygen flux. The OTM approach has been to develop combinations of materials that can complement each other without compromising performance. These materials will be in close proximity and thus must be physically and chemically compatible. We have successfully developed suites of materials that have similar thermal expansion properties, are minimally reactive, and yet are strong and creep resistant. Several "suites" have completed test runs exceeding 2000 hours and tens of thermal and chemical cycles without degradation. One example is shown in **Figure 4**. Note that even after 10 thermal cycles, numerous compositional cycles and almost 2500 hours on-stream, the flux has not degraded.

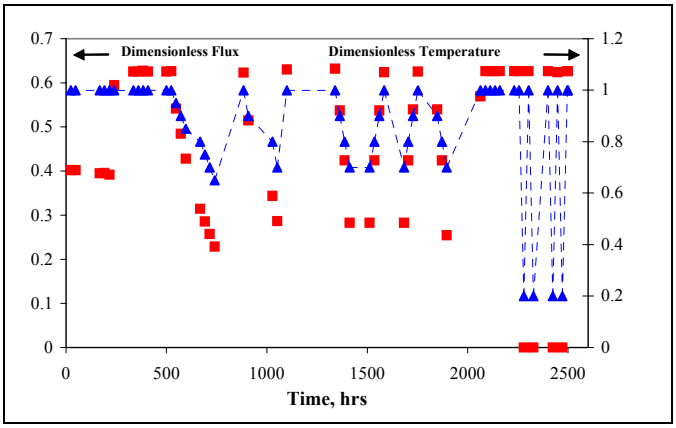

Figure 4: Life and cycle test of an advanced OTM material system

Element Development

The element is the means of deploying the OTM materials in a reactor. Element architecture (design) can have a profound impact on material durability, reactor performance, control and safety. An advanced element design has been developed that exhibits a flat response of oxygen flux to temperature as shown in **Figure 5**. This clearly reduces the risk of thermal runaway. Other architectures have been developed that resist creep or improve flux. We believe architecture also plays a key role in managing the mechanical, thermal and chemical gradient induced stresses.

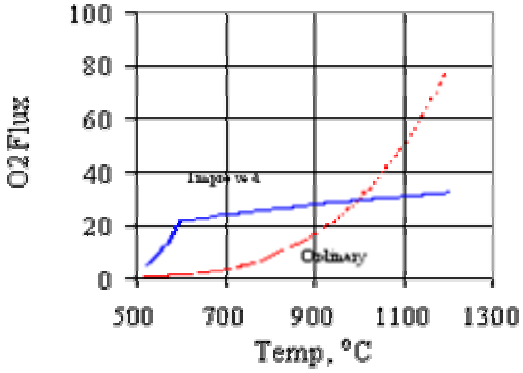

Figure 5: Oxygen flux versus temperature

In addition, element development includes the means to commercially fabricate the elements. Several techniques are under study. High quality tubular elements five feet long can be routinely manufactured as shown in **Figure 6**. Work continues on improving quality and reducing costs and building alternative architectures.

Figure 6: Large scale OTM elements

Conclusions

Exploiting the unique properties of ceramic oxygen transport membranes to develop a syngas process that is more economical than large scale autothermal reforming is a formidable, but achievable goal. Parallel and systemic improvements in the OTM materials, reactor and process design, and element architecture and element manufacturing processes are required for commercial success. Significant advances in all of these arenas have been achieved by the OTM Alliance. OTM syngas coupled with other clean fuel technologies is a promising path for energy independence and a cleaner environment.

Acknowledgements

This work was supported by the National Energy Technology Laboratory, U.S Department of Energy under contract DE-FC26-01NT41096.

The author is grateful for the contributions from all of the OTM alliance scientists and engineers, and in particular Siv Aasland, Morten Brustad, Bente Krogh, Kjersti Kleveland of Statoil; Jack Chen, Hancun Chen, Prasad Apte, Bart van Hassel, John Sirman and Jon Lane of Praxair , Charles Besecker, Sherman Xu, and Mark Kleefisch of BP and John Hemmings of Foster Wheeler.

References

[1]Cable, T.L., Frye, T.G., Jr., Kliewer, W.R., Mazanec, T.J., U.S. Patent 5,591,315, 1997

[2] Cable, T.L., Mazanec, T.J., U.S. Patent 5,788,748, 1998

[3] Bredesen, R; Sogge, J; "A Technical and Economic Assessment of Membrane Reactors for Hydrogen and Syngas Production" presented at Seminar on the Ecol. Applic. Of Innovative Membrane Technology in the Chemistry Industry", Cetraro, Calabria, Italy, May 1-4, 1996

[4] Mazanec, T.J., Prasad, R., Steyn, C., Robinson, E., "Oxygen Transport Membranes for Syngas Production", 6th Natural Gas Conversion Symposium, June, 2001

[5] Chen, Emmeline, Science & Technology Review, Sept. 2002, p. 19

Hydrogen-butane separation through MFI-type zeolite membrane grown by a secondary growth method

Masahiko Matsukata, Hikokazu Akimoto, Yasushi Sekine and Eiichi Kikuchi

Department of Applied Chemistry
Waseda University
3-4-1 Okubo
Shinjyuku-ku
Tokyo, 169-8555, Japan

Introduction

Zeolite is an inorganic membrane material which has heat resistance, chemical resistance, durability, mechanical strength, and selective adsorption properties. Zeolite membrane attracts attention as an inorganic membrane with which separation on a molecular level is possible.

The secondary growth method is a method of growing up seed crystals secondarily and obtaining a compact membrane. In order to obtain a compact membrane, it is necessary to control a mount of and a density of seed crystals on a surface of support. But, researches that are focused on seeding conditions are few.

In this study, the conditions which can synthesize a compact membrane were established and the influence of the seeding conditions on membrane properties was examined. The membrane structure and its permeation properties were examined. In the present study, a dip coating method was used for seeding the surface of a porous alumina support. The effect of the seed concentration in a suspension and the speed of the suspension on membrane property were focused on.

Experimental

Membrane preparation. Silicalite-1 seeds approximately 100 nm in size were hydrothermally synthesized. A mixture with a molar composition of TPAOH (tetrapropylammonium hydroxide): SiO_2:H_2O:NaOH = 2.4 : 10 : 110 : 1.0 was prepared and crystallized[1] at 408 K for 4 h. In order to obtain seed particles with a uniform size, seeds in a suspension was separated by using a centrifuge. The seed concentration in a suspension and the speed of the suspension were changed in the ranges of 3-107 g/l, and 0.08-3.0 cm/s, respectively. Seeding an α-alumina tubular support with the average pore size of the outer top layer of 0.1μm and 3 cm long was performed by a dip coating method. A clear solution with the composition of TPAOH:SiO_2:H_2O=3:25:1500 was prepared[2]. The seeded support was immersed in the clear solution and crystallized at 448 K for 24 h. As-synthesized MFI-type zeolite membranes were calcined in air at 798 K for 5 h.

Characterization. Support surfaces before and after the seeding were observed by field emission scanning electron microscopy (FE-SEM). The structure of product was analyzed by X-ray diffraction (XRD) with Cu Kα radiation. The morphology of product was examined by scanning electron microscopy (SEM). For evaluating the compactness of all MFI-type zeolite membranes, N_2 single gas permeation was carried out at 423 K. The separation properties of membrane were tested by using binary gas mixtures, H_2/iso-butane(i-C_4) and H_2/n-butane(n-C_4), at 423-673 K. Before starting the binary gas mixtures tests, distilled water was charged into both feed and permeate sides of membrane. The membrane was then dried in air for 30 min.

Results and Discussion

Figure 1 shows the relation between the seed crystal concentration and the compactness of membrane prepared. Figure 2 gives the effect of the speed of the suspension on the compactness of membranes. The compactness of membrane was evaluated by the N_2 single gas permeation. Figures 1 and 2 led us to a conclusion that seeding conditions significantly influenced the permeation property. When the seeding was performed with a seed concentration of 22 g/l or above and a speed of the suspension of 0.5 cm/s or above, the membranes became compact.

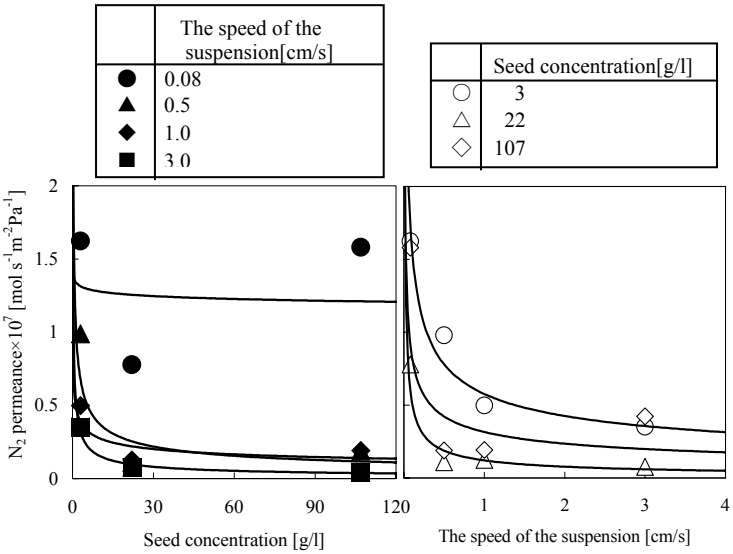

Figure 1. Relation between seed concentration and N_2 permeance.

Figure 2. Relation between the speed of suspension and N_2 permeance.

The seed crystals attached on the surface of support were observed. Figure 3 gives a typical FE-SEM image of the seeded support. In the cases of seeding performed under the conditions determined above, a sufficient amount of seed crystals was densely loaded on the support surface, as shown in Fig. 3. Such seeds could grew up secondarily during crystallization, resulting in the formation of compact membrane.

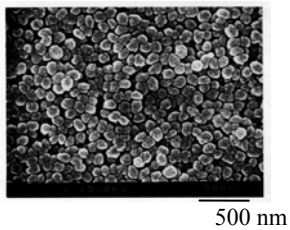

Figure 3. Typical FE-SEM image for the top view of seeded support (seed concentration : 22 g/l, speed of the suspension : 3.0 cm/s).

The formation of MFI-type zeolite on the porous alumina support was confirmed by using XRD, as shown in Figure 5. Irrespective of the compactness of membrane, the (002) plane of MFI-type zeolite was oriented in parallel with the surface of support, that is, its c-axis was grown vertically against the support surface, as

often observed in literature[1,2]. The top surfaces and the cross sections of membranes prepared under different seeding conditions were observed by using SEM. A typical SEM image of MFI-type zeolite membrane is shown in Figure 4. The structure of all the membranes observed was quite similar. As described above, it was difficult observe obvious structural and morphological differences between compact and incompact membranes.

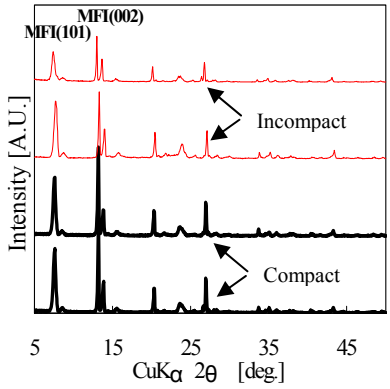

Figure 4. XRD patterns for MFI-type zeolite membranes.

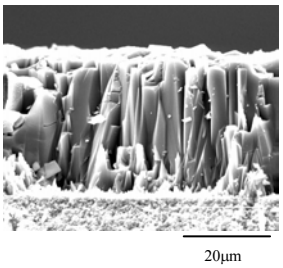

Figure 5. SEM images of the cross-section of MFI-type zeolite membrane (seed concentration : 22 g/l, speed of the suspension : 1.0 cm/s).

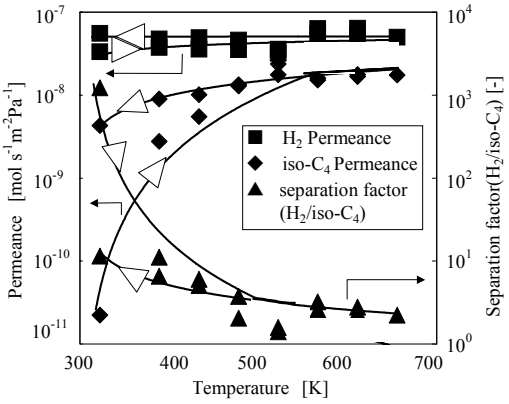

Figure 6. Temperature dependence of the permeances of H_2 and i-C_4 in the binary (50:50) mixture permeation.

The separation properties of the most compact membrane were evaluated. Figure 6 shows the permeation results of a binary 50:50 gas mixture, H_2/iso-C_4. The permeation test was started at 303 K after the water treatment of membrane. The temperature was raised up to 673 K and then fell to 303 K. The permeances of H_2 and i-C_4 were measured after the permeation reached a steady-state at each temperature. The maximum of separation factor as high as 1,200 was observed at 323 K before raising temperature. It is considered that water adsorbed in the membrane blocked i-C_4 permeation. The separation factor decreased with increasing temperature because the permeance of i-C_4 markedly increased with temperature. During cooling, the H_2 and i-C_4 permeances were greater than those observed during heating. The difference in the permeances measured during heating and cooling the membrane would be caused by the desorption of water adsorbed in advance. The permeation of i-C_4 was strongly hindered by the adsorbed water in comparison with H_2 permeation.

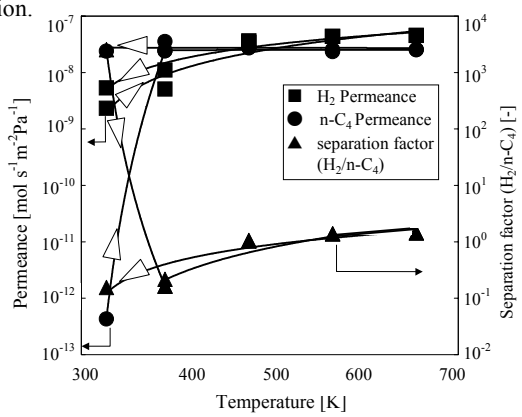

Figure 7. Temperature dependence of the permeances of H_2 and iso-C_4 for mixture.

The binary gas mixture of H_2/n-C_4 was also used for evaluating the separation properties of membrane. The experimental procedure was the same as that for the H_2/n-C_4 permeation test. The results were shown in Figure 7. Similarly to the case of H_2/i-C_4 permeation, the maximum of separation factor of 2,500 was observed at 323 K before raising temperature. It is suggested that the water adsorbed in the membrane also blocked n-C_4 permeation. It is worth noting that upon heating to 373 K the separation factor became less than unity and such a n-C_4 selectivity was held at 323 K after the removal of water. We presume that n-C_4 is strongly adsorbed in the micropore of MFI-type zeolite and thus hinder the H_2 permeation at lower temperature while micropore blockage with n-C_4 was interfered with water.

Conclusions

In the present study, seeding conditions were successfully optimized to prepare a compact MFI-type membrane by the secondary growth method. In the permeation tests of the binary gas mixtures of H_2/i-C_4 and H_2/n-C_4, both i- and n-C_4 permeation was remarkably decreased by the adsorption of water in the membrane, resulting in very high separation factors exceeding 10^3 at 323 K. After the removal of adsorbed water, the membrane was H_2 selective in the H_2/i-C_4 mixture and n-C_4 selective in the H_2/n-C_4 mixture.

References

1. M. C. Lavollo, M. Tsapatsis, *AIChE J.* , 42, 3020, **1996**
2. G. Xomeritakis, S. Nair, M. Tsapatsis, *Micropor. Mesopor. Mater.* , 38, 63, **2000**

CHARACTERIZATION OF SULFONATED CATION-EXCHANGE MEMBRANES MODIFIED WITH POLYANILINE

Sophie Tan, Alexis Laforgue, and Daniel Bélanger

Département de Chimie, Université du Québec à Montréal, C.P. 8888, Succursale Centre-Ville, Montréal (QC) H3C 3P8

Introduction

Different types of membrane surface modifications have been studied in order to obtain selective transport of molecules or ions. For example, membrane surfaces were modified to improve membrane filtration performance,[1] biocompatibility,[2] membrane selectivity for specific proteins,[3] for protons versus solvent[4] or other ions.[5-8]

For some of these applications, a recent approach consisted in the formation of a composite membrane based on a commercially available ion-exchange membrane and electronically conducting polymers such as polypyrrole[5] and polyaniline.[6-8]

In this study, commercial cation-exchange membranes bearing sulfonate groups are modified on a single side by chemical polymerization of aniline. The composite membranes prepared under different polymerization parameters are characterized by several techniques including X-ray photoelectron spectroscopy (XPS), scanning-electron microscopy, cyclic voltammetry and exchange-capacity measurements. Their permselectivity is evaluated by electrodialysis (ED) in acidic media.

Experimental

Materials and Chemicals. Neosepta® CMX membranes were stored in 0.5 M NaCl prior to modification. $(NH_4)_2S_2O_8$, HCl, HNO_3, NaCl, H_2SO_4, $ZnSO_4{\cdot}7H_2O$ and $CuSO_4{\cdot}5H_2O$ were of A.C.S. reagent grade and used as received. Aniline was distilled twice or until a colorless monomer is obtained prior its to use. Millipore water (18 MΩ) was used for the preparation of all solutions.

Modification of cation-exchange membranes. Single-side modifications were done in a two-compartment cell containing the reagents in one compartment and water in the other. The chemical polymerization was performed in two steps: 1) protons within the membranes are exchanged with charged aniline (10 % aniline in 1 M HCl solution) and 2) polymerization is induced by chemical oxidation with ammonium peroxodisulfate, $(NH_4)_2S_2O_8$.

X-ray photoelectron spectroscopy. After conditioning the membranes in 1 M HCl and drying these membranes under vacuum at room temperature, XPS analyses were performed using a VG Escalab 220i-XL system equipped with an hemispherical analyzer and an Al anode (Kα X-rays at 1486.6 eV) used at 10 kV and 15 mA. The data were recorded at room temperature and at a pressure below 10^{-8} Torr.

Electrodialysis experiments. Electrodialysis was performed in a two-compartment cell which contained, in the anodic compartment, 15 g/L of $ZnSO_4{\cdot}7H_2O$ or $CuSO_4{\cdot}5H_2O$ in 0.5 M H_2SO_4 and in the cathodic compartment, 0.5 M H_2SO_4. A current density of 100 mA/cm^2 was applied between two platinum plates for 3 hours. The surface of the membrane exposed to the solutions is 5.1 cm^2.

Results and Discussion

Using various modification parameters, we have obtained two main types of CMX-PANI composite membranes. The XPS survey spectra of these two types of composite membranes along with the spectrum of the unmodified CMX are given in Figure 1. The XPS spectrum of the bare CMX membrane exhibits the following characteristic peaks: O1s at 531 eV, S2s at 228 eV and S2p at 169 eV from the sulfonate (SO_3^-) groups, Cl2s at 271 eV and Cl2p at 200 eV attributed to the poly(vinyl chloride) (PVC) support. The peak at 400 eV indicates the presence of a small amount of nitrogen at the surface of the unmodified CMX membrane. When a PANI layer covers the surface of the membrane, the peaks attributed to PVC and sulfonate groups nearly disappear and are replaced by an enhancement of the nitrogen peak, confirming the presence of polyaniline on the surface of the membrane. It should be recalled here that XPS analysis only allow measurements down to 5-10 nm depth which explains the disappearance of the peaks attributed to the bare CMX membrane upon coverage with PANI chains. The top XPS spectrum shows an intermediate case between the first two spectra where there is still nitrogen attributed to PANI as well as chlorine and sulfur attributed to PVC and the sulfonate groups of the basal membrane.

Hence, the first type of CMX-PANI composite membranes can be described as a three-section membrane:[8] 1) an outermost layer consisting of PANI chains doped with chloride ions 2) an intermediate layer in which PANI chains are doped with sulfonate groups present on the bare membrane and 3) the bulk of the CMX membrane. The second type of composite membranes is obtained under longer polymerization times and at higher concentration of oxidant. In this case, the outermost layer of PANI is almost completely degraded and we believe that more PANI chains and/or oligomers are found within the membrane. Indeed, less nitrogen is found at the surface by XPS, and exchange capacity results demonstrate the presence of a larger PANI content inside the membrane. Therefore, for this second type of CMX-PANI membranes, most of the PANI chains and/or oligomers are found within the bulk of the membrane.

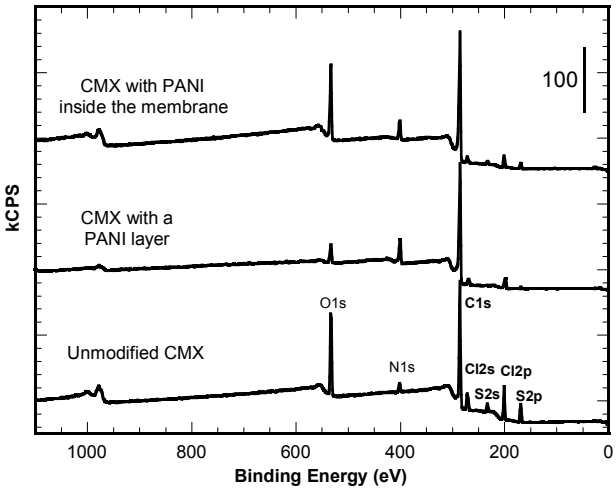

Figure 1. XPS survey spectra of an unmodified CMX membrane, a CMX-PANI composite membrane with PANI at the surface, and a CMX-PANI composite membrane with PANI within the membrane.

In addition, these two types of composite membrane show different permselectivity behaviors. Figure 2 compares metal leakage after electrodialysis in acidic medium for the unmodified CMX, CMX-PANI (type 1) and CMX-PANI with a degraded layer (type 2). It is demonstrated that the presence of a PANI layer on a CMX membrane decreases the Zn^{2+} and Cu^{2+} transport from about

10% to less than 0.5%. However, when the PANI found on the surface is degraded, the permselectivity of the composite membrane for protons decreases significantly with a metal leakage increasing back to 7.4% and 8.6% for Cu^{2+} and Zn^{2+}, respectively. These results suggest that in order to obtain good permselectivity behaviors for protons against bivalent cations in acidic solution, a good PANI surface coverage is required. Nevertheless, the CMX-PANI composite membrane that possesses a higher PANI content within the membrane can be studied for its blocking behavior towards other types of reagents or solvents such as methanol for methanol fuel cells.

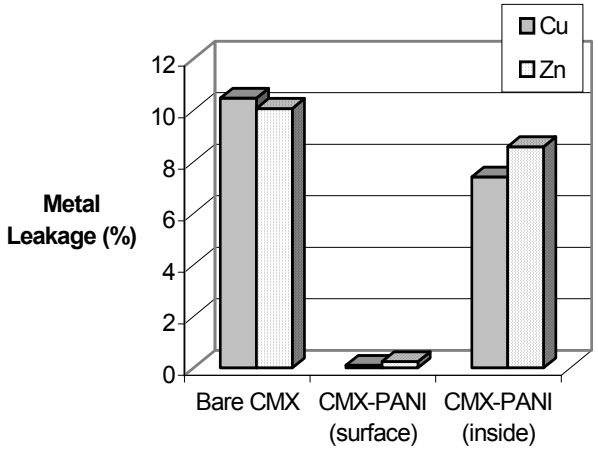

Figure 2. Metal leakage after a 3 h electrodialysis at 100 mA/cm^2 using a bare CMX, and CMX-PANI membranes (with PANI found on the surface and inside the CMX membrane).

Conclusions

We have demonstrated that two main classes of CMX-PANI composite membranes can be prepared under different polymerization times. These two type of membranes are distinguished by the location of the PANI chains or oligomers at the surface or inside the CMX membrane and exhibit very different permeability properties.

To improve our understanding of the structural effect of PANI composite membranes on the permselectivity behavior, the polymerization of aniline will also be studied on Nafion.

Acknowledgments. This research was funded by the Natural Science and Engineering Research Council of Canada through a strategic grant (234959-00) and an equipment grant for an XPS spectrometer (to D.B. and nine others. S.T. acknowledges the "Fonds Québécois de Recherche sur la Nature et les Technologies" for a graduate student fellowship. The financial contribution of UQAM is also acknowledged.

References

(1) Ma, H.M.; Nielsen, D.R.; Bowman, C.N.; Davis, R.H. *Separation Science and Technology*, **2001**, *36*, 1557.
(2) Song, Y.Q.; Sheng, J.; Wei, M.; Yuan, X.B. *J. Appl. Polym. Sc.*, **2000**, *78*, 979.
(3) Li, R.H.; Barbari, T.A. *J. Membr. Sci*., **1994**, *88*, 115.
(4) Easton, E.B.; Pickup, P.G. *Electrochem. and Solid-State Lett.*, **2000**, *3*, 359.
(5) Sata, T; Sata, T.; Yang, W., *J. Membr. Sci.*, **2002**, *206*, 31.
(6) Sata, T.; Ishii, Y.; Kawamura, K.; Matsusaki, K. *J. Electrochem. Soc.* **1999**, *146*, 585.
(7) Tan, S; Laforgue, A.; Bélanger, D., *Electrochem. and Solid-State Lett.*, **2002**, *5*, E55.
(8) Tan, S; Laforgue, A.; Bélanger, D. *Langmuir*, **2003**, in press.

PHASE CHANGE OF $SrCo_{0.5}FeO_X$ OXIDE ION CONDUCTOR IN REDUCING AND OXIDIZING ATMOSPHERE

Rajesh Sharma[1], David Caldwell[2], David A. Lindquist[2], Caner U. Yurteri[1], and Malay K Mazumder[1]

[1]Department of Applied Science
[2]Department of Chemistry
University of Arkansas at Little Rock
Little Rock, AR 72204

Introduction

Ceramic membranes exhibiting both electronic as well as ionic conductivity have generated a significant interest due to their potential applications in high temperature electrochemical devices such as electrodes in solid oxide fuel cell (SOFC) and oxygen separation membranes. Mixed conducting perovskite oxides such as La-Sr-Co-Fe (LSCFO) were extensively studied followed by their discovery by Teroaka et al (1,2). Further Balachandran et al (3) showed that Sr-Fe-Co oxides (SFCO) not only have high ionic and electronic conductivity, but also have structural stability. Extruded tubes of these materials have successfully operated in methane conversion reactors at 850°C for more than 1000 hrs (4). Most of these materials have been studied for their oxygen permeation properties as well as structural stability in oxidizing and reducing atmospheres (5,6). But a limited work has been reported on the effect of microstructure on electrochemical properties of these materials. Zhang et al (7) commented on the effect of surface microstructure on oxygen permeation flux of LSFCO and SFCO. They found out that the microstructure of SFCO exhibited good stability at elevated temperature for as long as 7 days. Since surface exchange kinetics is equally important to bulk diffusion in oxygen permeation through these membranes, the effect of high temperatures on surface microstructure of reducing side of the membranes is of significant interest. In this work we report on the effect of reducing conditions at elevated temperature on the microstructure of Sr-Fe-Co membranes, which simulates the oxygen lean side of the membranes in oxygen permeation reactor. We also report some preliminary results on the reversibility of the effects caused by reducing conditions.

Experimental

SFCO samples were synthesized using solid-state reaction method. Appropriate amounts of $SrCO_3$, $Co(NO_3)_2$. $6H_2O$ and Fe_2O_3 were mixed in isopropanol and ball milled using WC media for 24 hrs. The mixture was dried to remove isopropanol. The powder obtained was ground followed by calcination at 850°C for 8 hrs. The heating and cooling rates were 5°C/min. The calcined powder was ground and mixed with the binder. The binder was comprised of 2 wt% Butavar® B-98 as binder and 0.5 wt% stearic acid as plasticizer dissolved in isopropanol. The mixture with binder system was allowed to dry off isopropanol. This powder was again ground and used for pressing pellets. The resulting powder was then pressed into 13-mm diameter disks by applying a uniaxial pressure of 675 Mpa. These green disks were then sintered at 1250°C for 8 hrs. The heating and cooling rates were 2°C/min.

These pellets were exposed to a reducing atmosphere at 850°C. Two sets of samples were taken out after 24, 48, 72, 96 and 168 hrs of exposure. One set of these samples was observed under scanning electron microscope (Aspex personal SEM 2000). The SEM pictures were used to calculate average grain size using linear intercept method. Another set of the samples was used for X-ray diffraction (XRD) analysis. X-ray patterns for these membranes were obtained using a Rigaku Geigerflex X-ray generator equipped with a theta – theta goniometer and sample rotator (step size 0.05° 2θ, 1 second per step, range 10° to 75° 2θ).

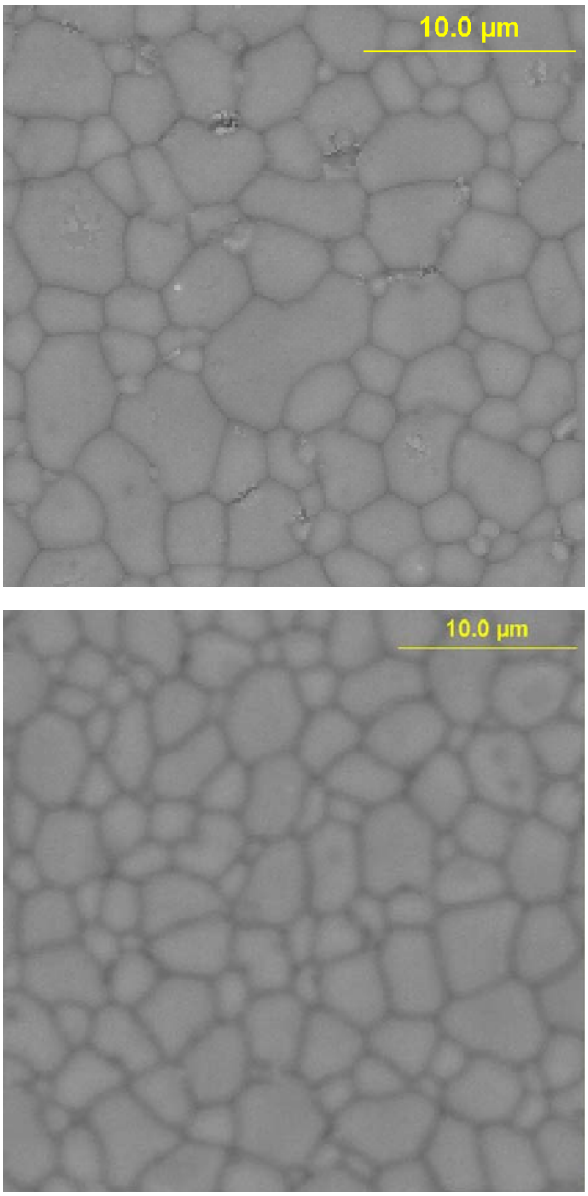

Figure 1. SEM micrograph of membrane surface before (upper plate) and after reduction (lower plate).

To study the reversibility of this composition, the powder was exposed to reducing atmosphere at 850°C. The powder was heated in oxidizing conditions at 850°C and samples were taken after 1, 2, 5, 10 and 30 minutes. These samples were used for generating X-ray patterns.

Results and Discussion

The SEM images of the membrane surfaces show little changes in surface microstructure when exposed to reducing atmosphere at elevated temperature. Figure 1 shows the microstructure of the unmodified and reduced membrane surface. A bimodal grain size distribution is observed for all these images. Although there was no significant change in average grain size, the grain boundaries of reduced surface are coarser than unmodified surface. Probably this

reflects the poor integrity of the membranes during prolonged exposure to reducing conditions in oxygen permeation reactors. The membranes were exposed to reducing atmosphere for different durations up to 168 hrs, but there was no significant change in average grain size. Figure 2 shows the phase behavior of SFCO. The material was cubic perovskite in it original state. When exposed to reducing conditions at 850°C the cubic phase transformed into an oxygen-vacancy-ordered phase.

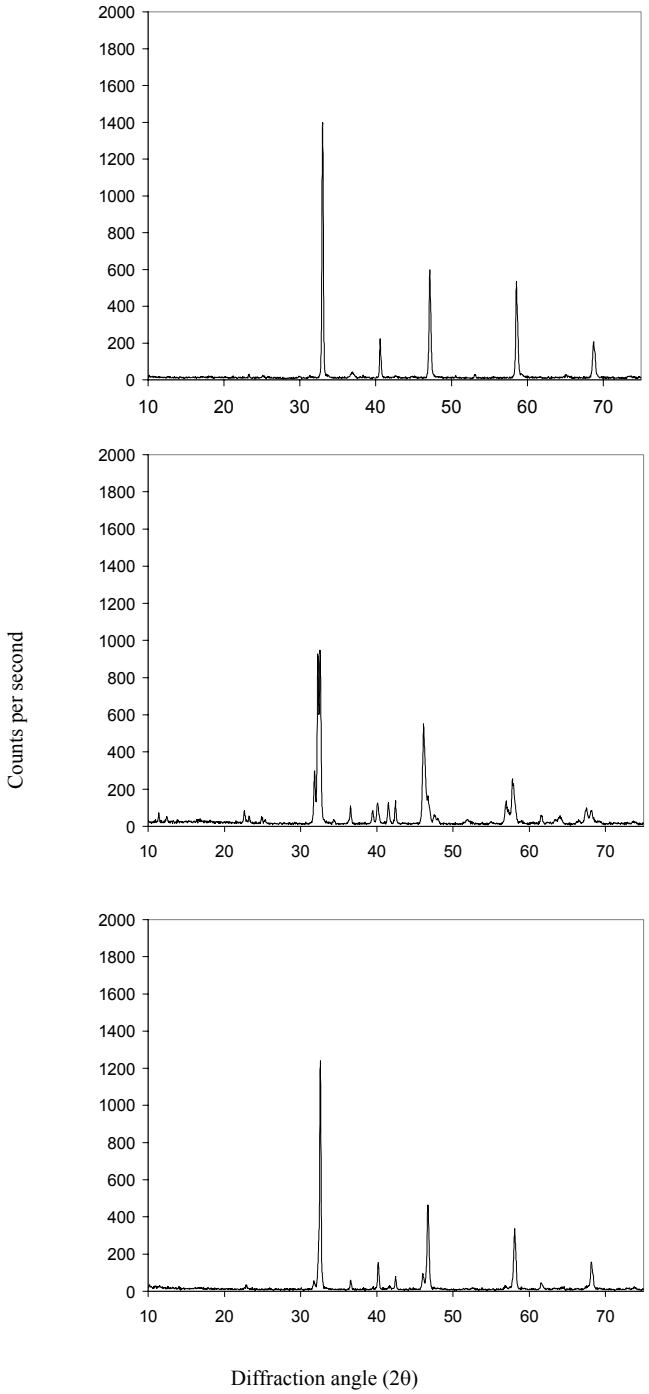

Figure 2. XRD patterns of original SFCO membrane surface (upper plate), after reduction (middle plate) and after oxidation of reduced surface (lower plate).

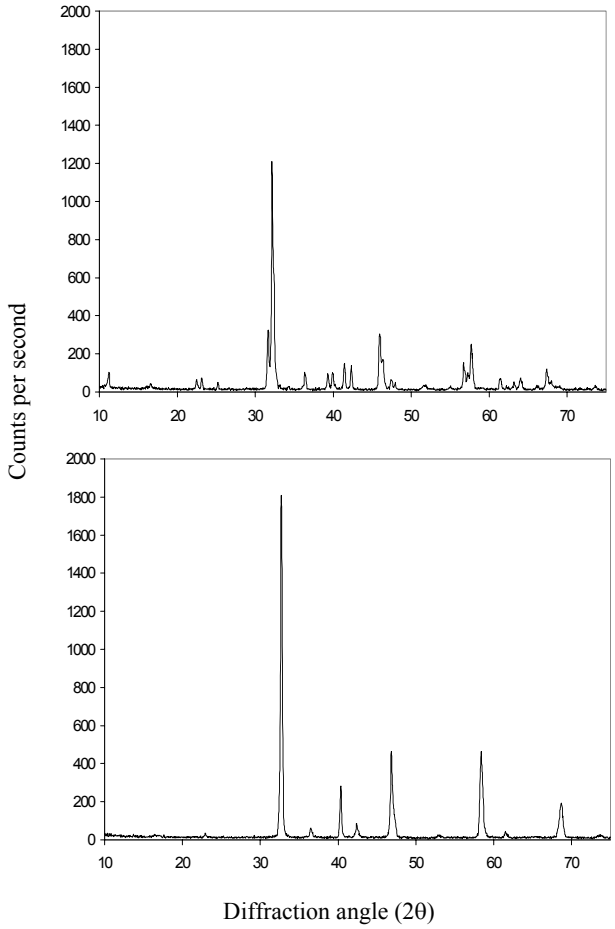

Figure 3. XRD patterns of SFCO powder sample reduced for 24 hrs (upper plate) and after 2-minute oxidation (lower plate).

XRD patterns show new reflections were formed for every characteristic peak of the cubic phase perovskite. Similar patterns were observed when the material was exposed to reducing conditions for various durations between 24 and 168 hrs. When this reduced material was oxidized at 850°C, it reverted back to the original cubic perovskite phase. This reversibility of the membrane surface crystal structure could play an important role in increasing the life span of these membranes.

Another set of experiments was performed to determine the kinetics of oxidation. SFCO membranes were crushed and the powder obtained was reduced at 850°C for 24 hrs. This powder was then oxidized 850°C for different durations between 1 and 30 minutes. Figure 3 shows the XRD patterns of powder, which was reduced and then oxidized. It was observed that there was no change in XRD patterns of the powder, which was oxidized for 1 minute. But XRD patterns of the powder that was oxidized for 2 minutes show that the crystal structure reverts back to its original state. There were no more changes in the XRD patterns with further oxidation.

Conclusions

SEM micrographs of SFCO membranes, exposed to reducing conditions at elevated temperature, show coarser grain boundaries, reflecting deterioration of the membrane surface. The SFCO powder samples were reduced for 24 hrs, followed by oxidation. XRD patterns showed that crystal structure of oxidized samples reverted back to its original state.

Acknowledgement. This work was supported by U.S. Department of Energy/EPSCoR Grant # DE-F602-01ER45865. The authors would also like to acknowledge Dr. Rahul Mehta of SEM Lab at University of Central Arkansas for helping with SEM imaging.

References

(1) Teroaka, Y., Zhang, H., Furukawa, S., Yamazoe, N., Chem. *Lett*., **1985**, 1743.
(2) Teroaka, Y., Zhang, H., Okamoto, K., Yamazoe, N., Mater. Res. Bull., 23, **1988**, 51.
(3) Balachandran, U.; Ma, B.; Maiya, P. S.; Mieville, R. L.; Dusek, J. T.; Picciolo, J. J.; Guan, J.; Dorris, S. E.; Liu, M., *Solid State Ionics*, **1998**, 108, 363-370.
(4) Balachandran, U; Dusek, J. T.; Maiya, P. S.; Ma, B.; Mieville, R. L..; Kleefisch, M. S.; Guan, J.; Udovich, C. A., *Catalysis Today*, **1997**, *36*, 265.
(5) Minh, N. Q., *J. Am. Ceram. Soc.,* **1993***,* 76,563.
(6) Kruidhof, H., Bouwmeester, H. J. M., Doorn, R. H. E. V., Burggraff, A. L., *Solid State Ionics*, **1993**, 816, 63-65.
(7) Zhang, K., Yang, Y. L., Jaconson, A. J., Salama, K., Mater. Res. Soc. Symp. Proc., **1998**, 496, 341-346.

TRANSPORT RESISTANCE FOR OXIDE DIFFUSION BARRIERS ON POROUS METAL SUPPORTS USED IN COMPOSITE Pd AND Pd-ALLOY MEMBRANES

Erik E. Engwall, Ivan P. Mardilovich and Y.H. Ma

Center for Inorganic Membrane Studies
Department of Chemical Engineering
Worcester Polytechnic Institute
Worcester, MA 01609

Introduction

Thin oxide layers may be used as barriers to prevent intermetalic diffusion between a porous stainless steel support (PSS) and the dense Pd layer of a composite Pd-PSS membrane (1,2). An oxide diffusion barrier may be created by heating the PSS support in air prior to application of the Pd layer. The simplicity of this in-situ oxidation (1) approach and the benefits of the barrier must be weighed against an increase in transport resistance caused by oxide formation. In this study, the effects of the oxidation temperature were experimentally evaluated for a series of 316L PSS supports oxidized at 400, 500 and 600°C. The effects of oxidation conditions were determined experimentally by the measurement of support helium flux versus pressure drop at room temperature, before and after oxidation.

For the simple case where a Pd-PSS membrane is used in hydrogen separations with no sweep gases, the contribution of the support to the transport resistance of the membrane may be measured by the trans-support pressure drop ΔP. The measurement of ΔP at process conditions (H_2, 350-450°C) prior to Pd plating, is not convenient as a routine step during membrane synthesis. However, the helium flux of the supports is routinely measured at room temperature before and after support oxidation. It is therefore convenient to have a means to predict the behavior of the support at process conditions from the data taken during synthesis. This was done for the porous disks using a model based on Darcy's law.

Experimental

The supports for this study were disks of 0.1μ grade porous 316L stainless steel with a thickness (z) of 0.071 in. and a diameter of 1.17 in. The pore size and porosity of these disks was determined prior to oxidation by Hg porosimitry on a representative sample. The disks were subjected to the same cleaning procedures as applied to membrane supports used in this laboratory (2). Following cleaning, the disks were oxidized at 400, 500 and 600°C in air. The oxidation treatments were 6 hours in duration with 10°C/min heating and cooling ramps. Three samples were oxidized at each temperature. The sample mass and helium flux versus ΔP at 25°C were obtained before and after oxidation for all samples.

Results and Discussion

Mercury porosimitry on a single unoxidized support indicated a median pore diameter of 1.86 μm and a porosity of 0.31. This result is consistent with Mardilovich *et al*. (2) who have observed that the pore sizes obtained by mercury porosimetry for 316L PSS supports from Mott are typically about an order of magnitude larger than the reported grade, which is determined by other criteria.

The mass of the samples increased following oxidation as indicated in Table 1. These increases in mass indicate the formation of oxide on the support surface and on the pore walls of the support. The increases in mass were relatively small and the composition of the oxide was not determined experimentally. Additionally, the the estimation of ΔP at process conditions does not require the estimation of pore size and porosity for the oxidized supports. For these reasons no effort was made to calculate change in pore size and porosity based on changes in sample mass.

Table 1. Mass increase following oxidations of PSS supports

Oxidation Temperature [°C]	Mass Increase [%]
400	0.12 ± 0.01
500	0.32 ± 0.04
600	1.21 ± 0.04

Figure 1 shows the helium flux J $[m^3/m^2\text{-}h]_{STP}$ before and after oxidation, over a range of trans-support pressure drops for a sample oxidized at 600 °C. There was an excellent linear fit between the flux J and the product of the trans-support pressure drop ΔP and the average of the upstream and downstream pressures P_M. This was typical of all the support samples studied and indicates that the He flux followed a viscous mechanism described by Darcy's law for compressible fluids (3), which may be expressed as follows:

$$J = (B/\eta RT)(\Delta PP_M/z) = m(\Delta PP_M/z) \qquad (1)$$

where B is a constant dependent on the geometry of the pore system, η is the viscosity of the gas, R is the gas constant and m is the slope of a plot of J versus $(\Delta PP_M/z)$.

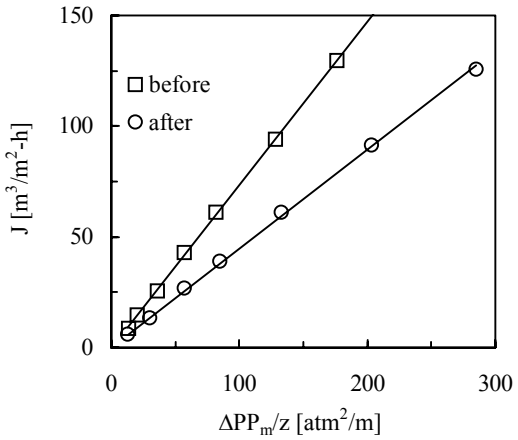

Figure 1. The He flux versus $(\Delta PP_m/z)$ measured at 25°C for a PSS disk oxidized at 600°C for 6 hours. Excellent linear fits for these coordinates confirm Darcy's law behavior, m = (B/ηRT).

The effect of oxidation temperature on He permeability at 25°C may be seen in Figure 2. The permeability, indicated as the group (B/ηRT), decreases by 2, 14 and 40 % for oxidation temperatures of 400, 500 and 600°C respectively. This indicates an increase in support resistance with increasing oxidation temperature. To evaluate the significance of the loss in permeance at process conditions, the Darcy's law slope m_1 obtained with He at room temperature was used to predict the slope m_2 for H_2 at the process temperature.

$$m_2 = m_1(\eta_1 T_1/\eta_2 T_2) \qquad (2)$$

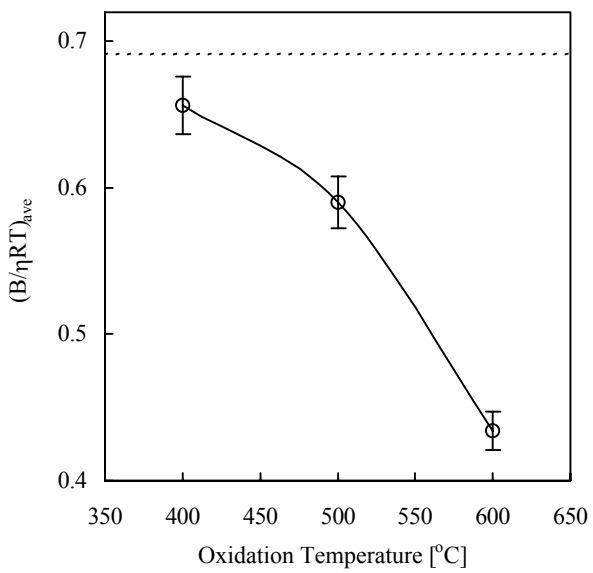

Figure 2. Average He permeability at 25°C $(B/\eta RT)_{ave}$ versus support oxidation temperature. The dashed line indicates the $(B/\eta RT)_{ave}$ for all nine supports before oxidation.

Equation 2 was used in conjunction with published data for the temperature dependence of the viscosities of He and H_2 (4). In this way an estimate for m_2 or $(B/\eta RT)$ was obtained for H_2 at 350°C for each of the oxidized supports. Based on previous results from this laboratory (2), a H_2 flux of 3 $[m^3/m^2\text{-h}]_{STP}$ could be expected from a membrane with a Pd layer thickness of about 30μm at total membrane pressure drop ΔP_T of 1 atm and an permeate side (tube side) absolute pressure P_P of 1 atm. This performance estimate is based on measurments using pure hydrogen on the retante side (shell side). Note that in the case of an actual membrane assembly the pressure drop across the support ΔP could not be determined directly from experimental data because the pressure at the interface between the Pd and the support could not be measured. However, with an estimated of m_2 at process conditions, the following equation may be solved for ΔP, if z, P_P and J are also known.

$$\mathbf{J = (m_2/2z)(\Delta P)(\Delta P + 2P_P)} \qquad \mathbf{(3)}$$

Figure 3 gives the estimates for the expected trans-support pressure drop for oxidized supports based on equation 3, and the realistic process conditions listed above. The predicted trans-support pressure drop for supports oxidized at 600 °C was 0.019 atm. This is nearly double the value expected for unoxidized supports. The total membrane pressure drop for this flux was 1 atm. The estimated support contributions to the total membrane pressure drop are 1.3, 1.4 and 1.9 % of the total membrane pressure drop for supports oxidized at 400, 500 and 600°C respectively. For applications where pure hydrogen is being obtained as a permeate stream from a Pd-PSS membrane module, the trans-support pressure drop provides a good measure of the resistance of the support. Based on these calculations even a 40% reduction of the permeability of the support will not have a significant impact on membrane performance.

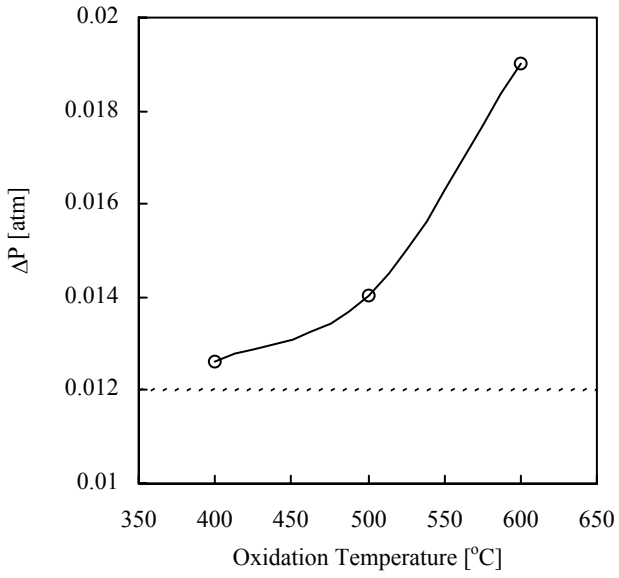

Figure 3. Predicted support pressure drop ΔP for typical hydrogen flux conditions (2). H_2 flux: 3 m^3/m^2-h, temperature: 350°C, total membrane ΔP_T: 1 atm. The dashed line indicates the expected behavior of unoxidized supports.

Conclusions

The He flux vs ΔP behavior of Mott 0.1μ grade 316L PSS supports follows Darcy's law before and after oxidation, over a wide range of flux values. Air oxidation treatments at 400, 500 and 600°C were effective in producing an oxide covering on the supports as indicated by the increasing mass and decreasing helium permeability of the supports after oxidation. The degree of oxidation increases dramatically for this support material at higher oxidation temperatures. At an oxidation temperature of 600°C the room temperature He permeability was decreased by 40%. While this represents a partial blockage of the pore system, the support contribution to the total membrane pressure drop was estimated to be only 1.9% under these conditions. This indicates that higher oxidation temperatures should not cause a significant increase in relative support resistance for applications where a pure hydrogen permeate is withdrawn from the membrane.

References

(1) Ma, Y.H.; Mardilovich, P.P.; & She, Y. *US Patent 6,152,987*, **2000**
(2) Mardilovich, I.P.; Engwall, E.; & Ma, Y.H. *Desalination*. **2002**, *144*, 85.
(3) Cunningham, R. E.; & Williams, R.J.J. In *Diffusion in Gases and Porous Media*; Plenum Press: New York, 1980; pp. 47-48.
(4) *Perry's Chemical Engineers' Handbook Sixth Edition*; Green D.W., Ed.; McGraw-Hill: New York, 1984; pp. 3-247.

ORDERED MESOPOROUS SILICA MEMBRANES FOR CO_2 SEPARATION FROM FLUE GAS

Sangil Kim, Vadim V. Guliants, Junichi Ida, and Y.S. Lin

Department of Chemical and Materials Engineering
University of Cincinnati
Cincinnati, OH 45221-0171

Introduction

Reducing CO_2 emissions for addressing climate change concerns is becoming increasingly important as the CO_2 concentration in the atmosphere has increased rapidly since the industrial revolution. Most of currently investigated mitigation processes require CO_2 in a concentrated form. However, CO_2 is emitted from large sources, such as coal-fired power plants, at ~15% concentration. Therefore, capturing CO_2 from dilute streams is an important step for many mitigation methods. Membrane separation methods are particularly promising due to potentially high CO_2 selectivities and fluxes.[1] By a proper choice of the pore size and surface properties, the CO_2 transport across a membrane can be facilitated with respect to those of N_2 and O_2 leading to an efficient CO_2 separation process. However, current membranes suffer from a poor control over the pore size on the 2-4 nm scale and surface properties required for CO_2 separation.[2]

We describe here novel mesoporous silica membranes containing surface-attached amino groups promising for CO_2 separation from dilute sources. Defect-free mesoporous silica membranes on porous alumina supports exhibiting 26~28Å pores were obtained by spin-coating (~5-7 μm thick) and solution growth methods. Several kind of amino groups were attached to the membrane surface using amino-containing silicon alkoxides, such as 3-aminopropyltriethoxysilane.

Smaller pores (~18-22Å) were obtained by silylating the original calcined membranes with silane coupling agents. The characterization of the silylated silica membranes by BET surface area measurements, N_2 adsorption pore size analysis and TGA confirmed that silylation technique was successful in decreasing the membrane pore size by ~8 Å which is required for completely filling the pore volume with surface attached aminopropylsilyl groups and achieving facilitated transport of CO_2.

CO_2/N_2 separation on amine-modified silica membranes was investigated at 20-70^{o}C and transmembrane pressure drop of 0.2-1 atm as a function of the pore size and the nature of the amino group using a Wicke-Kalenbach permeability cell. The membrane performance was evaluated with respect to permeance and separation selectivity, determined by a GC/MS analysis of the feed, permeate, and retentate streams.

Experimental

Membrane synthesis and amino group attachment. Mesoporous 3D hexagonal/MCM48 silica membranes were fabricated on disc-shaped porous alumina supports by a spin coating and solution grown method according to a previously published procedure.[3,4] In the spin-coating method, the polymeric silica sol was prepared under acidic conditions by mixing TEOS, water (pH=1.25) and ethanol in the 1:5:3.8 molar ratio. After stirring for 10h, CTAB diluted with ethanol was added to the sol. and the sol was aged at room temperature for 10h. The final molar composition of solution was 1.0 TEOS: 0.1 CTAB: 13.6 ethanol: 5.0 H_2O. Porous alumina supports were spin-coated at ~1000 rpm with this solution. Typically, 4-5 coats were required to obtain ordered mesoporous membranes ~2-6 μm thick. The pores of the silica membrane were opened by the thermal removal of the organic surfactant at ~500 ^{o}C in air, which left an ordered array of ~1-3 nm pores.

The MCM-48 membranes were prepared by the solution-growth technique as follows. A porous alumina support was placed in TEOS. Then, a solution containing CTAB, NaOH and water was added to TEOS. The molar composition of the mixture was 1.0 TEOS: 0.59 CTAB: 0.5 NaOH: 61 H_2O. After the mixture was stirred for 2 h, the mixture and alumina support were transferred to an autoclave. The reaction was carried out at 90 ^{o}C for 96 h. The membranes were washed with deionized water and dried at room temperature in air. Then, the membranes were calcined in air at 500 ^{o}C for 5h with heating and cooling rate of 1 ^{o}C /min.

3-aminopropyl groups, NH_2-$(CH_2)_3$-, were attached to the membrane surface by reacting the surface silanol groups with aminopropyltriethoxysilane in toluene under reflux. After distillation of a toluene fraction containing ethanol, the heating and distillation sequences were repeated two times. The functionalized membranes were washed in a Soxhlet apparatus with dichloromethane, and then dried at 100 ^{o}C.[5]

Silylation of Mesoporous Membranes. The silylation of the original calcined MCM-48 membranes was carried out at room temperature for 48hr in a liquid phase of trimethylchlorosilane.[6] The membranes were washed several times with n-hexane to remove the residual silylating agent. After silylation and washing, the membranes were calcined at 530 ^{o}C to oxidize surface trimethyl silyl groups into silanol groups, and a second silylation treatment was conducted in order to further decrease the pore diameter.

Membrane Characterization. The structure, the absence of "pinhole" defects and the presence of amino groups in mesoporous silica membranes were characterized by the X-ray diffraction, SEM, and He permeation studies. The presence and surface concentration of amino groups in the silica membrane upon attachment was investigated by IR spectroscopy and TGA. For the TGA analysis, samples were heated to 700 ^{o}C at a rate of 10 ^{o}C /min under O_2. In order to investigate the effect of trimethyl silyl and amino groups in silica membrane on pore size, pore volumes, N_2 adsorption/desorption isotherms and BET surface areas were investigated using Micromeritics TriStar 3000 porosimeter.

Results and Discussion

The X-ray diffraction patterns of calcined mesoporous membranes synthesized on porous alumina support indicated that the presence of low angle reflections corresponding to the ordered mesoporous MCM-48 structures.

The gas permeation properties of as-synthesized, calcined, and amine-attached membranes were characterized by He and CO_2 permeation tests under unsteady state at room temperature. **Figure 1** indicated that the as-synthesized mesoporous membranes were gas-tight prior to the removal of the organic surfactant from the pores as expected with the absence of "pinhole" defects. The He permeation increased dramatically after the pores of the silica membrane were opened by the thermal removal of the surfactant. In addition, the CO_2 permeation data showed higher CO_2 flux, $P(CO_2)$~$7\cdot10^{-7}$ $mol/m^2\cdot s\cdot Pa$, than the DOE target of $3\cdot10^{-7} mol/m^2\cdot s\cdot Pa$.

The SEM image of a silica membrane prepared by 5-fold spin coating the γ-alumina/α-alumina support showed that the support surface is covered with a continuous ~6 μm thick mesoporous silica layer.

The presence of amino groups in the silica membrane upon attachment was confirmed by IR spectroscopy. **Figure 2** shows IR spectra of the silica membranes before and after amino group

attachment. The presence of amino groups is indicated by strong IR peaks in the 1300-1700 cm^{-1} range.

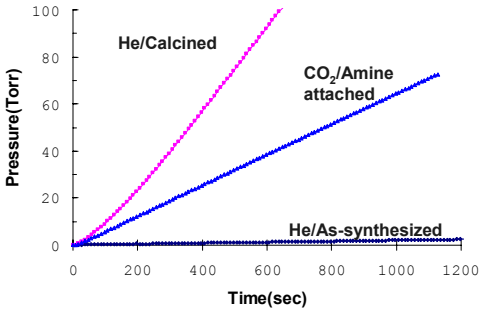

Figure 1. He and CO_2 permeation data for spin coated silica membrane.

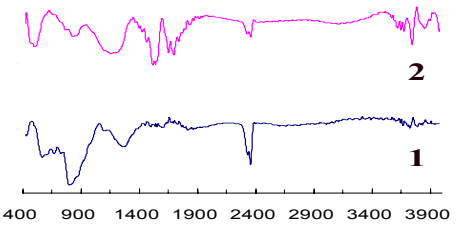

Figure 2. IR spectra of silica membrane prepared by spin-coating the γ-alumina/α-alumina support (1) before and (2) after amino group attachment.

The surface concentration of amino groups was investigated by TGA. **Figure 3** shows TGA derivative data for the mesoporous silica before and after amino group attachment. Above 100 ^oC, MCM-48 suffered very little weight loss, while the amine-modified MCM-48 showed a rather pronounced weight loss at 300~500^oC. This can be explained by the combustion of the amino groups. Derivative TGA curves in **Figure 3** indicated that the attached amino groups are stable up to at least 250 ^oC. Therefore, the surface concentration of amino groups attached to MCM-48 can be measured from the weight loss in this temperature range. TGA indicated high surface amine concentration of ~0.88 mmol/g.

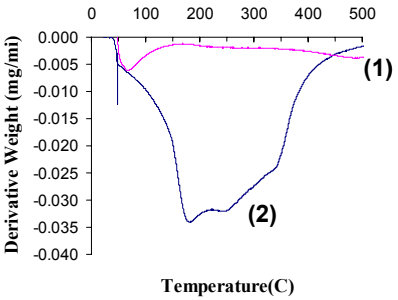

Figure 3. TGA derivative data MCM-48 type membrane (1) before and (2) after amino group attachment.

Single component CO_2 and N_2 studies and binary permeation studies showed that CO_2 and N_2 displayed similar trans-membrane fluxes indicating that the pore size needs to be reduced in order to achieve facilitated transport of CO_2 and its separation from N_2. In order to enhance the CO_2/N_2 separation, the membrane pore was decreased by the silylation process using silane coupling agents.

Figure 4 shows the pore size distributions determined by the BJH method using N_2 adsorption isotherms. The original MCM-48 powder and once-silylated and calcined materials showed the presence of mesoporosity; however, after the second silylation procedure the pore diameters decreased to below 20Å, which is the smallest pore size detectable by the TriStar 3000 porosimeter. The pore size after each silylation was reduced by ca. 6Å and increased slightly after calcination to remove the bulky trimethyl groups. There were no considerable changes in the BET surface areas for the original and silylated materials. These results indicated that the trimethyl silyl groups were uniformly dispersed on the pore surface of MCM-48 samples. These findings further indicated that the pore diameter in mesoporous silica membranes can be fine-tuned by sequential silylation/calcination steps.

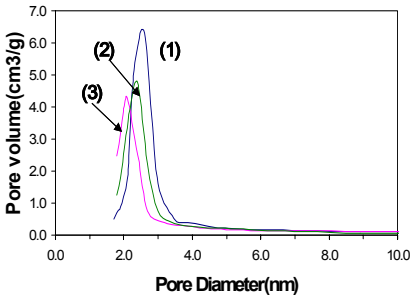

Figure 4. Pore size distribution in the (1) original MCM-48, (2) once silylated MCM-48, and (3) once silylated and calcined MCM-48.

The TGA data for the silylated MCM-48 samples in air indicated that the decomposition of the trimethylsilyl group of once-silylated MCM-48 occurred at ~520 ^oC, but the decomposition of the trimethylsilyl group of twice-silylated material started at a much lower temperature (~325 ^oC). The single component and binary CO_2/N_2 permeation studies of these silylated membranes are currently under investigation

Acknowledgment. This work was supported by the Ohio Coal Development Office grant OCRC3-00-1.C3.14.

References

(1) Feron, P.H.M; Jansen, A.E.; Herzog, H.J., *Energy Conversion and Management*, 1997, 38, S98
(2) Hsieh, H.P. *Inorganic Membranes for Separation and Reaction*, Elsevier: New York, 1996
(3) Besson, S.; Ricolleau, C.; Gacoin, T.; Jacquiod, C.; Boilot, J.-P., *J. Phys.Chem.B*, **2000**, 104(51), 12095
(4) Nishiyama, N.; Park, D.; Koide, A.;Egashira, Y.; Ueyama, K, *J.Mem.Sci*., **2001**, 182(2), 235
(5) Lin, X.; Chuah, G.K.; Jaenicke, S., *J.Mol.Cat.A: Chemical*, **1999**, 150(2), 287
(6) Park, D.; Nishiyama, N.; Egashira, Y.; Ueyama, K., *Ind. Eng. Chem. Res*., **2001**, 40, 6105

MFI-alumina composite membrane. Influence of the support porous structure on the separative performance.

E. Landrivon[1], S. Miachon[1], I. Kumakiri[1], M. Matsukata[2] and J-A. Dalmon[1]

[1]Institut de Recherches sur la Catalyse, 2 av. A. Einstein
69626 Villeurbanne Cedex France
[2]Waseda University, 3-4-1 Okubo, Shinjyuku,
Tokyo, 169-8555, Japan

Introduction

Owing to their very narrow pore-size distribution, zeolite-based membranes are currently considered for separative applications. Besides A-zeolite membranes, mainly developed for pervaporation processes, MFI-based membranes have been the subject of numerous studies, mostly in relation with gas separation applications. Gas separations require high quality materials, as the selectivity of the transport through the membrane is deeply dependent on the presence of defects in the separative layer.

Most of the materials combine a porous support (ceramic, metallic, carbon) and a thin continuous zeolite film deposited on top of it. In the present paper, we report on a composite MFI-alumina membrane obtained by growing zeolite crystals inside the pores of the support (pore-plugging method). Such systems, made of discrete zeolite particles embedded in the alumina matrix, may present advantages on the viewpoint of thermal stability (no long-range stresses in the zeolite phase). The present study analyses the influence of the support porous structure on the membrane separative performance.

Experimental

Supports were commercial macroporous alpha-alumina tubes obtained from Pall-Exekia (T1-70 type). They consist of concentric layers, with pore sizes decreasing from the outside. The external layer, thickness 1500 µm, pore size 12 µm, is present in all samples. Support 1 is obtained after coating this material with a 40 µm thick inner layer, average pore size 0.8 µm. Supports 2 and 3 are obtained after application on Support 1 of a final 20 µm thick toplayer, average pore size 0.5 µm (Support 2) or 0.2 µm (Support 3).

Tubes (15 cm length) have endings enameled on 1 cm to ensure gas-tight sealing (carbon seals + compression fittings) in the test module.

The precursor solution of the MFI zeolite was obtained by mixing silica (Aerosil 380) and a template (tetrapropylammonium hydroxide, TPAOH). After a 3-day ageing period at room temperature, that solution was poured in a Teflon-lined autoclave containing the Pall-Exekia porous ceramic tube. Hydrothermal synthesis was then performed at 443 K for 3 days. It was then checked that no gas permeation could occur through the precursor-plugged tube. The membrane was calcined at 773 K under a flow of 5% O_2 diluted in N_2, in order to remove organics coming from the template [1].

Pure gas permeation and mixture separation experiments were carried out in the 20-450°C temperature range. The shell side was used as permeate side.

For pure gas permeation measurements, hydrogen was used at 120 kPa feed pressure and 7.6 kPa pressure difference across the membrane, for n-butane these parameters were 148 and 39 kPa.

In gas mixture separation experiments, a mixture of 15% n-butane, 12% hydrogen and 73% nitrogen at about 120 kPa, was used in Wicke-Kallenbach mode in order to determine the separation factor Sf of n-butane over hydrogen, defined as the ratio:

$$Sf = (XC_4H_{10,permeate}/XC_4H_{10,feed}) / (XH_{2,permeate}/XH_{2,feed})$$

where X is the molar fraction. Permeate composition was analyzed by GC. Sf has been used as a reference for measuring the performance of the membrane.

Scanning Electron Microscopy analyses were performed using a Hitachi S800 microscope equipped with a EDX analyzer. Tubes were broken using a hammer and small pieces were glued to a sample holder.

Results and Discussion

Electron Microscopy. In all cases, after zeolite hydrothermal synthesis, SEM micrographs showed the presence of typical MFI crystals on top of the final internal (smallest pores) toplayer. However, it is quite clear these crystals are not well connected. Therefore, they do not form a continuous supported film that might act as a separative layer.

Separated MFI crystals are also observed on top of the very large alumina particles of the external (12 µm pore size) layer. However, the large pores of this layer are still undoubtedly open and this zone also cannot contribute to the separative performance.

According to these SEM observations, if existing, the separative zone should be located in the 0.8 - 0.2 µm pore area. Though SEM micrographs did not allow a clear identification of zeolite crystals in these layers, EDX analyses revealed the presence of Si in all this 0.8 - 0.2 µm pore area. Moreover, an analytical probe including both the material present in these pores and the support, gave a Si/Al ratio close to that calculated on the basis of the complete filling of the porous volume by the MFI phase. In another recent study [2], TEM-FFT structure analysis confirmed the presence of MFI zeolite in the toplayer pores of the host material.

Gas Transport Experiments. The transmembrane transfers were studied using both adsorbing (n-butane) and non-adsorbing (hydrogen) species. Figure 1 shows typical results of single gas measurements obtained with a MFI membrane formed with Support 3 (0.2 µm toplayer).

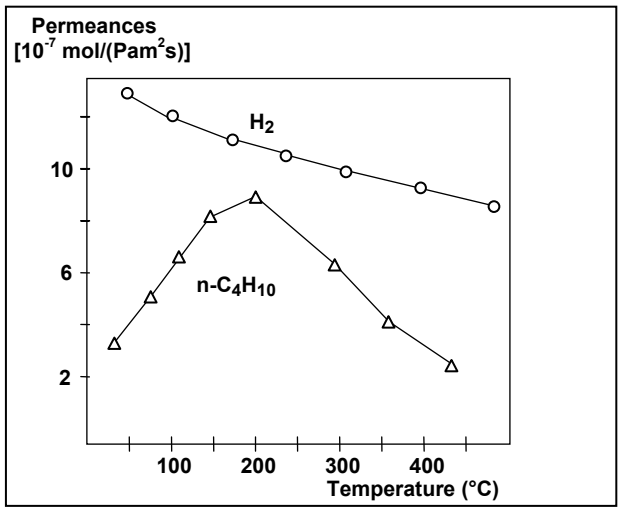

Figure 1. Typical single-gas permeances of a MFI membrane obtained with Support 3. Feed pressure and pressure difference across the membrane (kPa), H_2: 120, 7.6; n-C_4H_{10}: 125, 39.

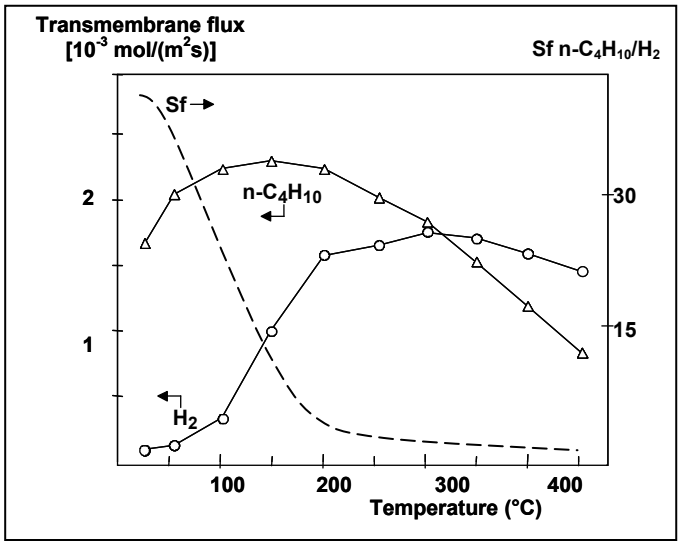

Figure 2. Typical $n\text{-}C_4H_{10}/H_2$ separative performance of a MFI membrane obtained with Support 3. Conditions: P=125 kPa, ΔP=0, Feed flow: 5.410^{-5}mol.s^{-1} (H_2 :$n\text{-}C_4H_{10}$:N_2 =12 :15::73), Sweep flow (countercurrent) 5.410^{-5}mol.s^{-1}.

Figure 2 gives permeating fluxes and Sf ($n\text{-}C_4H_{10}/H_2$) as a function of the temperature.

In single gas permeation experiments (Figure 1), the hydrogen permeance is higher than that of n-butane, which shows a maximum, typical of adsorbing species [3].

However, when mixtures of the two gases are considered (Figure 2), mainly n-butane permeates at room temperature [1, 3]. This is due to the strong adsorption of n-butane, which, owing to its molecular size close to that of the MFI pores, hinders the hydrogen penetration in the zeolite structure. When temperature increases, n-butane adsorption decreases, and the hydrogen flux increases progressively and finally overtakes that of n-butane (however, even at 450°C, there is still some n-butane hindering effect, as the $H_2/n\text{-}C_4H_{10}$ selectivity is much lower than that calculated from single-gas permeances).

If, at low temperature, the strong n-butane adsorption completely blocks hydrogen permeation through the zeolite pores, the value of Sf obtained at room temperature can be used as a quality measurement of the material. As a matter of fact, hydrogen will only permeate through defects of the zeolite separative layer. However, this is only true if n-butane, due to capillary condensation phenomena, does not also block at room temperature pores larger than those of the MFI zeolite. Though, in principle, only valid for larger pores, the Kelvin equation indicates that n-butane should, for the present conditions, only condensate in micropores. It seems therefore that the room temperature value of Sf is a way to evaluate the quality of the membrane, as hydrogen would only permeate through pores larger than micropores.

This Sf criterion has been used for the optimization of the MFI membrane synthesis. This resulted in a net progress in the membrane performance.

Among the various parameters involved in the membrane preparation, the porous structure of the support may play an important role. This should be especially the case in the present synthesis, where zeolite crystals are growing in the porous volume of the support, till plugging the pores. As a matter of fact, it seems reasonable to think there is a critical pore diameter above which the complete pore plugging will not occur.

A comparative study of Sf performances of MFI-alumina composite membranes prepared using Supports 1 (smallest pores 0.8 µm) , 2 (0.5 µm) or 3 (0.2 µm) undoubtedly showed that complete pore plugging did not occur in supports 1 and 2. As a matter of fact, typical Sf values with Support 3 are in the 20-50 range, when Sf is close to 1 (no separation) when the zeolite synthesis is performed in presence of Supports 1 or 2.

The definition of a critical pore diameter (the largest pore size where plugging by zeolite crystals occurs) is not easy. If it is likely between 0.5 and 0.2 µm, it seems difficult to be more precise, as all supports present a pore size distribution. It is clear that both Supports 1 and 2 have a large part of the pore distribution above the critical diameter.

Contrariwise, Support 3 has certainly most of its pores under the critical value. The fraction of pores above the critical value should affect negatively the separative performance of membranes based on Support 3. Moreover, these supports may present some small variations in the pores size distribution. This could contribute to the reproducibility problems observed during the zeolite membrane preparation. Verification of such hypothesis would require a detailed study of the pore distribution of several samples of Support 3 and comparison with the observed values of Sf. However, there are certainly many other parameters that may affect the final separative performance.

Conclusion

The preparation of composite MFI-alumina membranes by growing zeolite crystals inside the pores of a macroporous alumina host material (pore-plugging method) has been successfully achieved. Among other parameters, the porous structure of the alumina support has a great influence on the final separative performance of the composite membrane. There is a critical support pore diameter above which the pore plugging does not occur. As a consequence, the thickness of the layer with pores under the critical diameter should control the thickness of the separative layer. This can be used for further optimization of the zeolite membrane.

References

(1) Giroir-Fendler, A.; Peureux, J.; Mozzanega, H.; Dalmon J-A. *Studies Surf. Sc. Cat.*, **1996**, *101(A)*, 127.
(2) Aouine, M.; Miachon, S.; and Dalmon J-A. *to be published.*
(3) Kapteijn, F.; Bakker, W.J.W.; Zheng, G.; Moulijn J.A..; van Bekkum, H. *Catal. Today*, **1995**, *25 (3-4)*, 213.

THERMAL MECHANOCHEMICAL STABILITY OF OXYGEN TRANSPORT PEROVSKITE MEMBRANES

N. Nagendra[1], W.F. Haslebacher[2], V.K. Venkataraman[2] and S. Bandopadhyay[1]

[1]School of Mineral Engineering, University of Alaska Fairbanks Fairbanks, AK 99775-5800 USA
[2]US Department of Energy/National Energy Technology Laboratory, 3610 Collins Ferry Road, Morgantown, WV 26507-0880

Introduction

In recent years, mixed conducting perovskites of the general composition $La_xSr_{1-x}M_xM'_{1-y}O_{3-\delta}$ (where M = Co, Mn and Cr and M' = Fe and Al) have attracted considerable attention for possible applications as high temperature electrochemical oxygen membranes – devices that serve to separate oxygen containing gas mixtures due to difference in oxygen partial pressures on the two sides of the membrane. This concept is utilized in membrane reactors that can produce synthetic gas by direct conversion of hydrocarbons [1,2]. For the above-mentioned applications, the ABO_3 type oxides have to be dense and importantly show high ionic and/or electronic conductivity. To achieve this, the A-site cations are often substituted by a lower valence state, effectively forming oxygen vacancies and causing a change of valence state in B-site cation to maintain charge neutrality. The concentration of oxygen vacancies can also be tailored by substituting ions of smaller size but lower valence B sites. It has also been observed that the oxygen vacancies in many of these materials can be created by exposure to an environment having a sufficiently low thermodynamic oxygen activity. The formation of oxygen vacancies so essential for the functional properties in the material often leads to dimensional instability and strength degradation under reducing conditions. Thus, one of the important issues that need to be addressed is the structural, chemical and mechanical stability and reliability of these materials in application environments that are severely reducing ($P(O_2) \approx 0.2$ to10^{-16} atm.).

Much of the available literature has focused on membrane synthesis, characterization and functional properties such as: ionic-electronic conductivities [3], oxygen permeability [4], oxygen transport and diffusion [5]. However, there has been only a limited characterization of the thermo-mechanochemical behavior of these materials. In this paper, the thermomechanical and chemical stability of one such perovskite $La_xSr_{1-x}M_xM'_{1-y}O_{3-\delta}$ (where M = Cr and M' = Fe) membranes is examined. The perovskites processed as tubes are potential candidate material for membrane reactors for direct reduction of methane to syngas. The perovskites are evaluated for strength and toughness through C-ring tests and the fracture surfaces analyzed by X-ray diffraction (XRD) and Scanning Electron Microscopy (SEM).

Experimental

Two sets of membranes of the general composition $La_{0.2}Sr_{0.8}Fe_{0.8}Cr_{0.2}O_{3-\delta}$ and varying in particle size (LSFCO1 ≈ 1μm and LSFCO2 ≈ 5μm) were provided for testing by BP chemicals Inc., USA. The tubes were prepared by a proprietary process involving cold-isostatic pressing and sintering between 1250-1350°C for 4 hours in flowing air and then cooled to room temperature in flowing nitrogen. C-rings Rings cut from the tubes in were tested in diametral compression between two alumina platens in a hydraulic testing frame (MTS 858 MiniBionix II) [6]. The fracture strength (σ_f) and toughness (K_c) of the membranes tubes were evaluated in the temperature range (25-1000°C) and pressure (1 and 1.7 atm) in three different environments: air, 100% N_2 and 90%CO_2/10%CO. These test conditions at 1000°C in 0.17 MPa N_2 and in 0.17 MPa CO_2/CO (90/10) corresponded to oxygen partial pressure of $\log_{PO_2}$ = -4 atm and $\log_{PO_2}$ = –12.1 atm. respectively. After testing, the fracture surfaces were examined under SEM to identify the dominating flaws and possible fracture mechanisms. The surfaces were also examined by X-ray analysis to verify for any possible phase separation.

Post fracture hardness (H) and fracture toughness (K_C) of the membranes were measured. Measurements were made in a Vickers microhardness tester (Buehler, Micromet II) on ground and polished surfaces (< 0.5μm) with loads of up to 10N applied for 15s. The diagonal and crack lengths of ten indents were used to evaluate fracture toughness using the formula [7]

$$K_C = 0.016\left(\frac{E}{H}\right)^{1/2}\frac{P}{c^{3/2}} \qquad (1)$$

Where *2c* is the crack size, P is the indent load, E is the Young's modulus, H is the hardness.

Results and Discussion

The maximum and the average strength of sample set LSFCO-2 (429 MPa and 307 MPa respectively) were twice of that in LSFCO-1 (210 MPa and 167 MPa respectively). Microscopic analysis indicated that surface and volume flaws were the primary failure origins. However, although the fracture in both the sets were by cleavage, the morphology was distinct in observed features. In set LSFCO-1, the surfaces were smooth with apparent lack of features while in set LSFCO-2 microscopic cleavage planes and pore opening at triple point grain boundaries could be observed.

The strength of the oxide membrane tube decreases with increase in temperature and severity of reducing environment (Fig. 1). The strength degradation was markedly more severe in air (Log pO_2 = -0.7 atm) and CO_2/CO (Log pO_2 = -12 atm) in comparison with N_2 (Log pO_2 = -4 atm.) environment. However, LSFCO-1 indicated a higher resistance to strength degradation in comparison with LSFCO-2. Strength of the LSFCO-1 tubes decreased from 167 MPa to 108 MPa and 139 MPa in air and N_2 respectively, while in LSFCO-2, strength in N_2 (178 MPa) decreased rapidly to nearly half its value at the ambient condition. In air (113 MPa) and CO_2/CO (107 MPa), rapid degradation in strength was observed. Although similar trends in toughness (Kc) were seen, the recorded values were not as sensitive to the environment as strength measurements. A drastic drop in toughness in air followed by a slight recovery in N_2 and CO_2/CO was recorded. Fractographic observations indicated a breakdown of grain structure along with distinct relief in grain boundaries [6] in all conditions.

The hardness (*H*) and indentation toughness (K_{ind}) of LSFCO-1 was in the range of 5.2±0.5 GPa and 0.5-0.8 MPa$\sqrt{m}$ respectively. In comparison, LSFCO-2 showed a slightly reduced hardness of 4.4±0.5 GPa but increased toughness of 1-1.5 MPa$\sqrt{m}$ respectively. At room temperatures, the hardness increased in samples after testing with a concomitant decrease in toughness. The trends observed in indentation toughness values confirmed the similarly observed loss of toughness in air and recovery in N_2 and CO_2/CO [8].

At room temperature, X-ray analysis of the membranes indicated that the dominant phase in both the tubes was the primitive cubic perovskite phase. As shown in figure 3, mechanical testing at room temperature did not alter the structure. At elevated temperatures, traces of decomposition products were observed. In LSFCO-1, samples tested in air at 1000°C showed traces of

$(La,Sr)CrO_3$ and no decomposition in N_2. On the other hand, LSFCO-2 samples (decomposed to form $(La,Sr)CrO_3$ and $(La,Sr)Fe_{12}O_{12}$ in air and $(La,Sr)CrO_3$ in N_2 respectively.

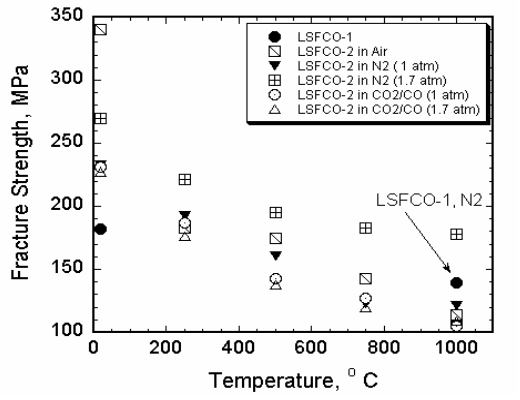

Figure 1. Effect of temperature and pressure on strength of LSFCO membrane tubes.

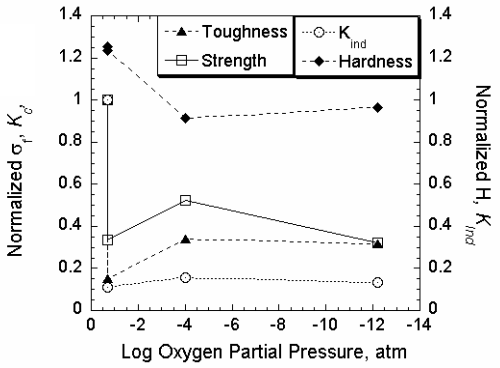

Figure 2. Strength, hardness and toughness of LSFCO membrane tubes as a function of environment

In the present study, the parent $SrFeO_{3-\delta}$ perovskites show a large oxygen deficiency even at room temperature in air. At elevated temperatures, enrichment of Sr at the grain boundaries and surfaces occur via a high diffusive path and leads to the additional formation of point defects. The formation of point defects enhances the diffusion of oxygen or metal component via grain boundary and often governs the oxygen permeation, reaction and degradation of perovskites [8]. Fracture surfaces of specimens tested below 750°C do not indicate an enrichment of Sr at the grain boundaries. This agrees well with an earlier observation indicating that below 800°C, vacancies are not mobile in many of the perovskites. The other point of interest is that at temperatures above 800°C, the vacancy populations in the perovskites are partly mobile and often lead to some local (micro domain) ordering. Studies involving Z-contrast imaging and EEL spectra have shown extended ordering in LSFCO analyzed as Brownmillerite like oxygen vacancy structures, with additional defects produced at elevated temperatures. Although, these transitions are reported above ~500°C, it has been observed that non stoichiometry in the oxide can increase considerably with increasing temperature and reducing conditions. Also, the ordered domains are observed to progressively grow with increasing temperatures until the reduction of the cubic perovskite structure cause some areas to collapse, thereby forming Aurvillus phases in the bulk that may restrict oxygen conductivity. Although, these transitions could not be directly linked to the distinctive morphological features observed in the fractured surfaces by an SEM it is highly probable they bear significant influence on the fracture process.

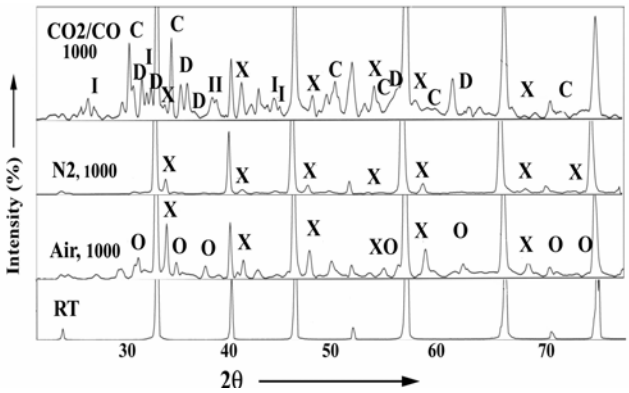

Figure 3. Phase separation upon mechanochemical degradation of LSFCO membrane tubes. The major phases formed are (X)-$(La,Sr)CrO_3$, (O) -$(La,Sr)Fe_{12}O_{12}$ and (C)- SrO. LSFCO-1 is more resistant to degradation in N_2

Conclusions

Oxygen transport perovskite membranes in reducing environment can undergo thermo-mechanochemical degradation that is significantly different from those observed in stress free conditions. The observed behavior has important significance in designing of reliable structures for gas separation and their long-term properties.

Acknowledgment

This research was sponsored by National Energy Technology Laboratory, US Department of Energy under grant number DE-FC26-99FT40054. We thank T.J. Mazanec and W.T Stephens for providing the samples.

References

1. T.J. Mazanec, *Solid State Ionics,* **70/71**, 11 (1994).
2. K. Huang, R.S. Tichy and J.B. Goodenough, *J. Am. Ceram. Soc*., **81**, 2565 (1998).
3. Y. Teraoka, H.M. Zhang, K. Okamoto and N. Yamazoe, *Mater. Res. Bull*. **23**, 51-58 (1988)
4. W.T. Stephens, T.J. Mazanec and H.U. Anderson, *Solid State Ionics,* **129**, 271 (2000).
5. C. Tsai, A.G. Dixon, Y.H. Ma, W.R. Moser and M.R. Pascucci, *J. Am. Ceram. Soc.,* **81**, 1437-44 (1998).
6. N. Nagendra, R. F. Klie, N.D. Browning and S. Bandhopadhyay, *Mat. Sci. Eng A* 341/1-2, 236-246, 2002
7. G.R. Anstis, P. Chantikul, B.R. Lawn and D.B. Marshall, *J. Am. Ceram. Soc*., **64,** 533-28 (1981)
8. N. Nagendra and S. Bandopadhyay, *Scripta Materialia***, 48/1**, 37-42, 2003
9. R.H.E. van Doorn and A.J. Burggraaf, *Solid State Ionics,* **128** , 65-78 (2000).

CO_2 Remediation via O_2/CO_2 Combustion Utilizing an O_2 Permeable Membrane

Howard G. McIlvried
Massood Ramezan

Science Applications International Corporation
PO Box 18689
Pittsburgh, PA 15236-8689

Arun Bose

National Energy Technology Laboratory
U.S. Department of Energy
PO Box 10940
Pittsburgh, PA 15236-0940

Introduction

Electric power generation is a major CO_2 emitter in the United States; roughly one third of the United States' carbon emissions come from power plants. Since electricity generation is expected to grow and fossil fuels will continue to be the dominant fuel source, fossil fuel based power generation can be expected to produce even greater amounts of CO_2 in the future. Thus, if power generation is to be done in an environmentally acceptable way, new approaches that reduce emissions of CO_2 (including capture and sequestration) must be developed. One promising concept is the use of oxygen-based combustion, using recycled flue gas to moderate combustion temperature. This approach produces a concentrated CO_2 stream that is much easier to prepare for sequestration than a typical flue gas stream. This concept is further enhanced by using an efficient oxygen permeable membrane for the production of O_2 in place of a conventional cryogenic air separation unit (ASU).

In a typical pulverized coal (PC) fired boiler, flue gas is produced with a CO_2 content of about 15% at essentially atmospheric pressure. Thus, the driving force for absorption of CO_2 from such a stream is quite low, requiring the handling of large gas volumes in large equipment. The result is not only increased capital costs but a significant increase in parasitic power requirements and a consequent decrease in efficiency.

Oxygen Transport Membranes

One option for increasing the CO_2 content of the flue gas is to use pure oxygen for combustion. This eliminates most of the nitrogen, which is the major component of flue gas. However, because combustion in pure oxygen results in temperatures higher than existing materials of construction can withstand, it is necessary to recycle some of the CO_2 rich flue gas as a temperature moderator.

The major difficulty with oxygen combustion is supplying the necessary oxygen. Large volume oxygen is typically supplied by cryogenic air separation units. These units are big power consumers, requiring up to 20% of the gross power production, and can have a significant impact on unit efficiency. A promising alternative to a cryogenic ASU is the use of oxygen selective ion transport membranes (ITM).

ITMs are ceramic membranes that, at the proper temperature, are selective for the diffusion of oxygen. Oxygen disassociates at the high pressure side of the ITM and diffuses through the membrane as oxygen ions. These ions recombine into molecular oxygen at the low pressure side of the membrane. However, if there is a reactive material, such as a fuel, at the low pressure side, the oxygen atoms may react rather than recombine. This can result in very efficient combustion.

There are two major options for incorporating membrane oxygen production into an oxygen-fired combustion system. The first option is to build the membrane unit external to the furnace, similar to the situation with a cryogenic ASU. The other much more interesting option is to place the ITM membrane directly in the furnace. This has two advantages. First, as indicated above, membranes may increase combustion efficiency. The second reason is that membranes require a high temperature to operate, and since high temperatures exist in the furnace, that is a logical place to locate them.

This can conveniently be accomplished in a fluidized bed combustor because of its uniform temperature and its high heat and mass transfer capabilities. In a fluidized bed combustor, it would be easy to intersperse membrane tubes and steam generation tubes. A typical membrane reactor consists of a ceramic tube, with compressed air being passed through the tubes. Oxygen passes through the membrane to the shell side, and depleted air exits the tube.

Case Studies

Three cases for incorporating an ITM-based oxygen unit into a power plant were evaluated using an ASPEN process simulator: (1) a base case, (2) a case using recycled CO_2 as a sweep gas in the ITM oxygen unit, and (3) an all coal case.

Base Case

Figure 1 presents a block flow diagram of the base case. Compressed air is heated to a temperature suitable for a membrane oxygen separation unit (1560^{o}F). Pure oxygen from this unit is mixed with cleaned recycle flue gas and used as the oxidant for combustion in a coal-fired boiler. The depleted air from the oxygen separation unit is sent to a gas turbine for power recovery, and the exhaust from the gas turbine goes through a heat recover steam generator (HRSG) to produce steam before it is vented to the atmosphere. The gross efficiency of the 273 MW_e cycle is approximately 31% (HHV). The flue gas is over 95 wt% CO_2 and can easily be prepared for sequestration.

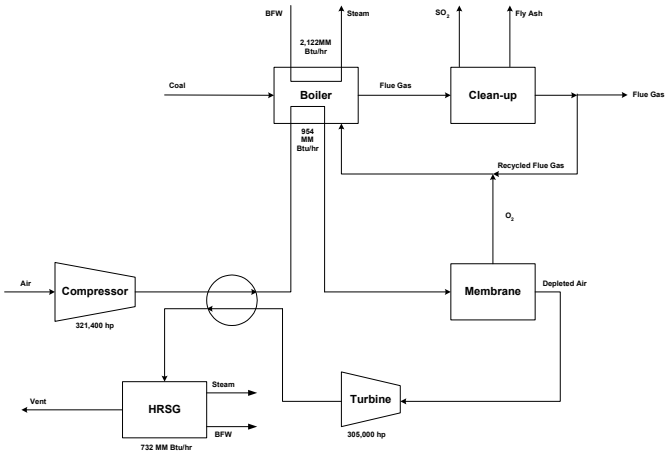

Figure 1. Block flow diagram for base case showing incorporation of an ITM oxygen unit with a PC fired boiler.

Case Using CO_2 Sweep Gas

This case, illustrated in Figure 2, is similar to the base case. The differences are that part of the recycled flue gas is heated in the furnace and utilized as a sweep gas in the membrane unit to reduce the partial pressure of oxygen and increase the oxygen flux in the

membrane separation unit and natural gas is used to increase the temperature of the depleted air which is then sent to an advanced gas turbine. The gross efficiency of this 491 MW_e cycle is approximately 36% (HHV).

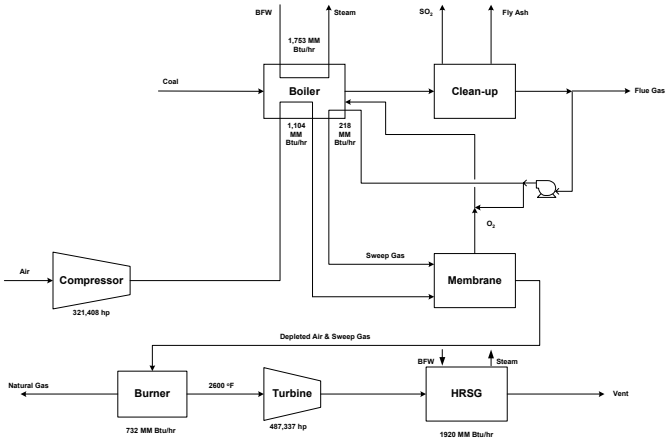

Figure 2. Block flow diagram for case showing utilization of a sweep gas to increase oxygen permeation rate.

All Coal Case

This case, as illustrated in Figure 3, is similar to the previous case, except that the depleted air gas turbine working fluid is heated inside the boiler, similar to a high temperature air furnace (HITAF) rather than using a natural gas burner. The gross efficiency of this 285 MW_e cycle is approximately 32% (HHV).

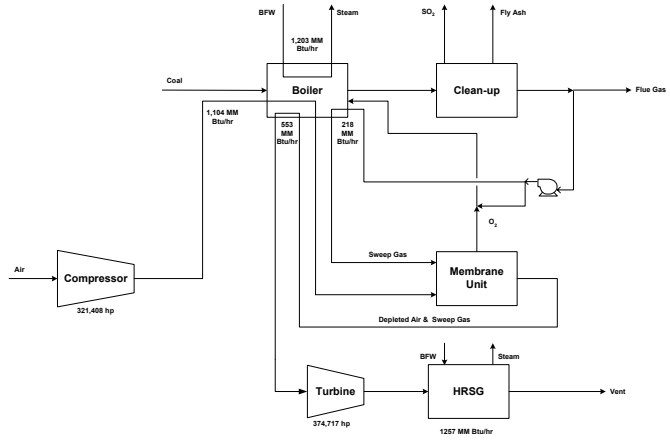

Figure 3. Block flow diagram for case utilizing coal as the only fuel.

Discussion

These preliminary case studies have shown considerable promise for the concept of using oxygen permeable membranes as a source of oxygen for coal combustion. Although these case studies did not include CO_2 sequestration, it is clear that a significant improvement in efficiency will result from sequestering the high concentration CO_2 stream from these cases compared to the low concentration CO_2 flue gas from a conventional pulverized coal fired boiler. After sulfur oxides removal from the flue gas, about all that will be required to prepare for CO_2 sequestration is drying, oxygen separation, and compression.

Theoretical Study on the Hydrogen Absorption Behavior of Palladium and its Alloys

Hitoshi Kurokawa [1], Yuhsuke Makino [1], Mutsumi Takahasi [1], Akira Endou [1], Seiichi Takami [1], Momoji Kubo [1], Naotsugu Itoh [2], Parasuraman Selvam [3], and Akira Miyamoto [1, 3]

[1] Department of Materials Chemistry,
Graduate School of Engineering, Tohoku University,
Aoba-yama 07, Sendai 980-8579, Japan

[2] Catalysis & Membrane Systems Group,
National Institute of Advanced Industrial Science and Technology,
AIST Tsukuba Central 5, Tsukuba, Ibaraki 305-8565, Japan

[3] New Industry Creation Hatchery Center, Tohoku University,
Aoba-yama 04, Sendai 980-8579, Japan

Introduction

Historically, the Pd-H system is a model system to study the most common regularities of hydrogen interaction with metals, and that the hydrogen separating capability of Pd and its alloy membranes is well known. Further, these membranes show very high selectivity for the permeation of hydrogen. Other applications include hydrogenation and dehydrogenation reactions, recovery, purification, and storage of hydrogen, hydrogen sensor, etc. [1-5]. The alloys of Pd, e.g., Pd-Ag, Pd-Cu, Pd-Au, etc., posses certain important characteristics, which may alleviate some of the shortcomings of pure Pd by lowering the β-hydride phase formation temperature and membrane cost as well as increasing the permeability of hydrogen as well as the mechanical properties. In the past, a great deal of experimental work has been carried out about the solubility and diffusivity of hydrogen in bulk materials. Nevertheless, the theoretical studies are interesting from a basic viewpoint. It is, in this context, the understanding of the metal/alloy-hydrogen systems, at the atomic level, is of paramount importance with respect to the development of membrane reactor, hydrogen recovery from petrochemical plants, fuel cell technologies and hydrogen storage systems.

In recent years, computational chemistry has become a powerful tool to design and develop new materials as well as to understand the mechanism of the interactions for the various processes at the atomistic level by taking the advantage of the tremendous progress made on both the theory and the computation spend. Several theoretical methods such as molecular dynamics (MD), Monte-Carlo (MC), quantum chemical calculation, etc. have been employed to extract information at the atomic and molecular scale. The first-principles calculations based on the density functional theory (DFT) have been performed for Pd-Ag-H system in order to understand the properties like the energetics of the hydrogen absorption, the energetic preference of hydrogen absorption site, equilibrium lattice constant, etc. [6]. Romanowski et al. [7] have also studied the interaction between hydrogen and transition metals and their alloys by DFT. Although, the first-principles calculations are quite useful to investigate the metal-hydrogen systems due to its accuracy and reliability, it may, however, force us to use extremely small cluster systems owing to the exorbitant computation time. Thus, it is not attractive for the real systems involving larger models such as the simulation of the storage processes of metal/alloy-hydrogen systems. Thus, a large-scale simulation method is imperative to elucidate the absorption behavior of hydrogen into the pure metals and their alloys.

In a previous study [8], we reported the successful development and demonstration of the new MC program for the hydrogen absorption characteristics of pure Pd and Pd-Ag alloys. The results were in good agreement with the experimental as well as the first-principles studies. In the present investigation, we further extend the study of the hydrogen absorption behavior of Pd-Ti and Pd-Cr alloys using MC program [8].

Computational Details

Monte-Carlo (MC) Method

The equilibrium absorption of hydrogen in metals and alloys may be calculated by the grand-cannonical Monte-Carlo (GCMC) method, employing our originally developed GCMC simulator "MONTA" [9]. However, the conventional as well the GCMC cannot treat the dissociative adsorption of hydrogen molecule and the subsequent absorption process. On the other hand, we have improved our GCMC program [8], in order to perform MC simulation, which takes into account of both the dissociation adsorption of hydrogen molecule and consequent absorption characteristics in metal/alloy-hydrogen systems.

Models, inteatomic potentials

As for the models of Pd and its alloys are concerned, a 4 × 4 × 4 super-cell having fcc structure and a lattice constant of 3.89 Å was considered. In the case of Pd metal, we used 256 atoms model. However, accurate atomistic models for Pd-Ti and Pd-Cr alloys may be difficult to consider, in particular the position of metal atoms in the unit cell. However, they can be modeled by partial substitution of Pd by Ti or Cr in the lattice. As a first step of the atomistic simulation using GCMC method, the effect of both the expansion of the unit cell and the strain in atomic level around the absorbed hydrogen atoms were ignored. The interatomic potentials are estimated by the Morse-type two-body potential function, which is described as:

$$U_{ij} = D\left[x^2 - 2x\right]$$

$$x = \exp\left[-\frac{\gamma}{2}\left(\frac{r_{ij}}{r_e} - 1\right)\right]$$

where r is the interatomic distance, D is the well depth, r_e is the equilibrium interatomic distance, and γ is the parameter, which determines the effective range of the potential. The interaction between hydrogen atoms is the almost repulsive one.

Solubility based on Sieverts' law

In order to evaluate the solubility of hydrogen in metals, we used the Sieverts' law, as described below:

$$\sqrt{\frac{p}{p^0}} = K_s x$$

$$\ln K_s = -\frac{\Delta S_s}{R} + \frac{\Delta H_s}{RT}$$

where p, p^0, K_s, ΔS_s, ΔH_s, and R are the hydrogen pressure, the standard pressure, the Sieverts' constant, the solution entropy of hydrogen, the solution enthalpy of hydrogen, and the gas constant, respectively.

Results and discussion

Parameter fitting

In order to determine the parameters for the interatomic potentials, we attempted to reproduce the solubility of the hydrogen in pure metals such as Pd [8], Ag [8], Ti, and Cr with a hydrogen pressure of 0.1 MPa, and the results are depicted in Figure 1. From this figure, it clear that the calculated values, by our improved GCMC program, for the hydrogen solubility in pure metals are in

excellent agreement with those obtained by Sieverts' law. Further, ΔH_s values were also calculated from the temperature dependent solubility of hydrogen, and ΔH_s were deduced from this data for the various metal-hydrogen systems. The computed ΔH_s values for the various system, viz., Pd, Ag, Ti, and Cr are – 9.5 [8], 67.7 [8], – 50, and 56.8 kJ / mol H, respectively. The corresponding experimental values are –10, 68, – 53, and 58 kJ / mol H, respectively. These results strongly indicate that the parameters employed for the interatomic potential functions are valid and hence they can be used for the MC simulation on the absorption of hydrogen in metal/alloy systems. The various parameters determined in this study are listed in the Table 1.

Table 1. Parameters for the Morse-type two-body potential function.

Atom pair	D [kJ / mol]	r_e [Å]	γ [Å $^{-1}$]
H-H	0.1848	2.886	11.429
H-Pd	17.3000	1.940	4.300
H-Ti	26.1000	2.069	5.000
H-Cr	12.5000	1.610	3.390

Hydrogen absorption in Pd alloys

In our previous study [8], we have investigated the energetic characteristics of Pd metal and Pd-Ag alloy towards hydrogen absorption. It was found that the most (energetically) favorable site for the hydrogen location is octahedral site in Pd lattice, which clearly reproduces the experimental results [1] as well as the theoretical findings using first-principles calculations [6]. Thus, the above studies clearly reveal that our improved GCMC simulator can perform the simulation of hydrogen absorption behavior and that the method can very well be extended to other Pd alloy-hydrogen systems. Therefore, in the present study, we investigate the hydrogen absorption characteristics of Pd-Ti and Pd-Cr alloys with 5 atom % of the dopant, i.e., $Pd_{0.95}Ti_{0.05}$ and $Pd_{0.95}Cr_{0.05}$. The conditions of GCMC simulation, viz., temperature and hydrogen pressure are set to 473 K and 0.1 MPa, respectively.

Figure 2 shows the integrated coordination number of hydrogen atoms absorbed in Pd-Ti alloy system. It is clear from this figure that the integrated coordination number of H-Ti system is close to 1. On the other hand, it almost 5 for H-Pd. These results suggest that the majority of hydrogen atoms absorbed into the octahedral sites consisting of at least one Ti atom. On the other hand, the integrated coordination number in H-Cr is practically zero (the figure is not reproduced here) and the integrated coordination number in H-Pd is 6. These results indicate that the hydrogen atoms tend to avoid Cr containing octahedral sites in the lattice. Our findings on the hydrogen absorption behavior of Pd-Ti and Pd-Cr alloys are clearly in line with their observation Berlag et al. [10]. They have suggested that when the alloying metals have a higher hydrogen solubility compared to Pd, they act as 'traps' for hydrogen in the Pd matrix. However, further investigations for various kinds of Pd-based alloys are required to understand clearly the various complicated phenomena in the hydrogen absorption behavior in metals and alloys. Such studies are currently in progress.

Conclusions

The hydrogen absorption behavior of Pd and its alloys, viz., Pd-Ti and Pd-Cr, were studied by GCMC simulator. The simulations were conducted at 473 K under the H_2 pressure of 0.1 MPa. The parameters for the Morse-type two-body potential function used here were determined so as to reproduce the solution enthalpy of hydrogen in pure metals. The present results suggest the different roles of Ti and Cr in Pd alloys with respect to the hydrogen absorption characteristics. Further work will be helpful in order to understand and design new alloy materials so as to achieve higher performance on the storage of hydrogen.

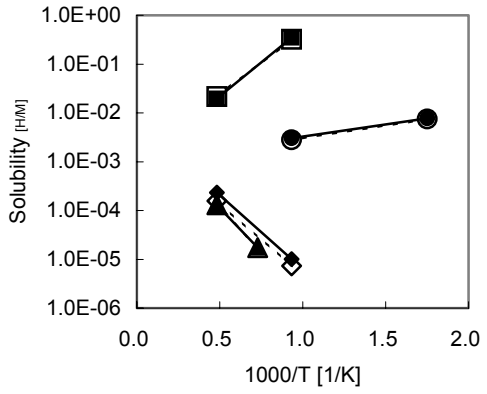

Figure 1. Solubility of hydrogen into the pure metals (○,●: Pd; △,▲: Ag; ◇,◆: Cr; □,■ : Ti). Open symbols: Sieverts' law; Filled symbols: MC simulation (this work).

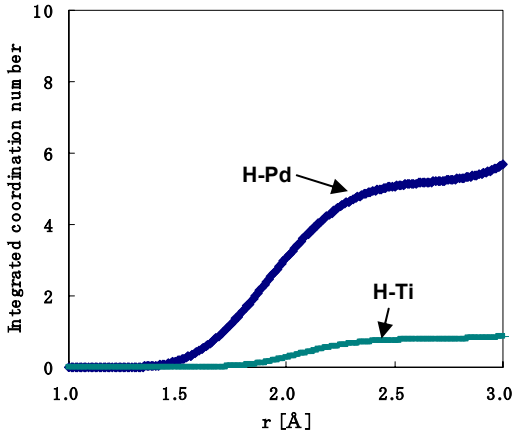

Figure 2. Relation between integrated coordination number and interatomic distances in Pd-H and Ti-H systems.

References

(1) Alefeld, G.; Völkl, J. *Hydrogen in Metals I. Basic Properties*, Springer-Verlag, Berlin, 1978.
(2) Alefeld, G.; Völkl, J. *Hydrogen in Metals II. Application-oriented Properties*, Springer-Verlag, Berlin, 1978.
(3) Wipf, *H. Hydrogen in Metals III. Properties and Applications*, Springer-Verlag, Berlin, 1997.
(4) Fukai, Y. *The metal-hydrogen system*, Springer-Verlag, Berlin, 1993.
(5) Lewis, F. A. *The Palladiumu Hydrogen System*, Academic Press, London, 1967.
(6) Løvvik, O. M.; Olsen R. A. *J. Alloys Comp.* **2002**, *330-332*, 332.
(7) Romanowski, S.; Bartczak,, W. M.; Wesolkowski, R. *Langmuir* **1999**, 15, 5773.
(8) Kurokawa, H.; Nakayama, T.; Kobayashi, Y.; Suzuki, K.; Takahashi, M.; Takami, S.; Kubo, M.; Itoh, N.; Miyamoto, A. submitted to *Catal. Today.*
(9) Hirotani, A.; Mizukami, K.; Miura, R.; Takaba, H.; Miya, T.; Fahmi, A.; Stirling, A.; Kubo, M.; Miyamoto, A. *Appl. Surf. Sci.* **1997**, 120, 81.
(10) Berlag, H.; Opara, L.; Züchner, H. *J. Alloys Comp.* **2002**, *330-332*, 434.

Perspectives on Membrane Technology for Advanced Gas Separations

Richard D. Noble

University of Colorado
Chemical Engineering Dept.
P.O. Box 424
Boulder, CO 80309

The use of polymer membranes for gas separations is a well-established separation technology. Membrane-based gas separation technology has developed during last 20 years to an annual business of $150 million. The major current separations are N_2 from air, H_2 separation and recovery, and CO_2 or H_2O removal from natural gas. The evolution of membrane technology to expand the temperature range of operation as well as provide the capability for additional separations will require new materials and/or processes. This talk will provide a brief historical focus and discuss the new materials and processes that can address the current limitations of commercial membrane technology.

The first large-scale industrial application was hydrogen separation started in 1980 by Permea. This was rapidly followed by the introduction of the first N_2 from air membrane separation system in 1982. In the late 1980's, cellulose acetate membranes for CO_2/CH_4 separation as well as new membrane materials for O_2/N_2, H_2/N_2 and H_2/CH_4. At this time, vapor separation membranes also made their first appearance as a commercial product. The mid-90's were the time frame for the introduction of polyimide hollow-fiber membranes for CO_2/CH_4 separation and membrane systems for C_3H_6/N_2 separations.

The use of new materials as membranes also requires support structures that can withstand the same operating conditions and provide the mechanical support. The evolution of sintered stainless steel and alumina membranes for filtration applications provided the support materials for high temperature and/or chemically challenging environments. Zeolite membranes are nanoporous inorganic crystalline structures that can provide highly selective separations up to 500ºC. Recent developments to synthesize thin zeolite films on metal or alumina supports should provide the high flux combined with selectivity needed to move this technology toward commercial development.

Additional new materials being evaluated as membrane materials are lyotropic liquid crystals and ionic liquids. Lyotropic liquid crystals form structured phases that have uniform pore structures down to 1.5 nm. The ability to polymerize these structures and "lock" them in place provides a means to fabricate a nanoporous polymer film. Ionic liquids are salts that are liquid at or near room temperature. Since they are non-volatile, this material could be used as a liquid membrane platform.

The addition of chemical selectivity into the membrane has long been attempted to overcome the "line of death" on a Robeson plot that represents the upper bound for gas selectivity versus permeability for polymers. One recent approach that has shown promise is the incorporation of zeolites or molecular sieves into polymer films (mixed matrix membranes). Another approach that has been evaluated for a long time is facilitated transport. Recent studies on the incorporation of Ag^+, Cu^+ and Co^{2+} complexes into polymer structures could lead to stable membranes for various applications such as olefin/paraffin and O_2/N_2 separations.

HIGHLY SELECTIVE MFI-ZEOLITE MEMBRANES FOR HYDROCARBON SEPARATIONS

Christophe CHAU, Mickaël SICARD, Philippe TERRASSE, Ronan Le DRED°*

*Institut Français du Pétrole, Catalysis and Separation Division, 1&4, avenue de Bois-Préau, 92852 Rueil-Malmaison - France, christophe.chau@ifp.fr

°ENSCMu-CNRS, Laboratoire des Matériaux Minéraux, 3, rue Alfred Werner, 68093 Mulhouse - France

Introduction

Zeolite membranes are emerging and promising membrane materials with high potential for gas separation, due to their chemical and thermal resistances, surface polarity and zeolite topology. To date, limitations to industrial and commercial development of zeolite membranes still exist and have to be overcome for successful implementation at industrial scale for gas separations *e.g.* in the field of gas treatment, refining and petrochemistry.

In order to highlight membrane textural integrity, appropriate characterization techniques and gas probe molecules have to be established. Characterization of zeolite membranes is of great importance and among various techniques, gas permeation is a non destructive characterization techniques that allows to evaluate the textural integrity of the zeolitic layer, the separation capability and the molecular transport phenomena involved through the zeolitic channels.

Using hydrocarbon mixtures for the characterization stage can provide particularly valuable data in the screening/selection of membrane materials provided that the experimental conditions are appropriate. The purpose of our study consisted in highlighting the separation performances of high quality MFI-zeolite membranes through a standard reliable and reproducible characterization procedure using hydrocarbonaceous mixtures at high temperatures.

Experimental

MFI-type zeolite membranes. Supported MFI zeolite membranes were prepared by hydrothermal treatment of a silica source using an organic compound as structure directing agent and porous alumina tubes. The synthesis procedure was optimized according to relevant modifications developed by IFP, Institut Français du Pétrole, France and ENSCMu-CNRS.

Gas permeation. These membranes were characterized by gas permeation at high temperatures using butanes (linear and branched isomers) as probe molecules and a gas permeation equipment developed within the Institut Français du Pétrole, with on-line gas-chromatographic analysis. Butanes were chosen to highlight the textural integrity of the synthesized membrane materials in severe conditions (pore apertures of the MFI-type zeolite around 0.55 nm, kinetic diameters: n-butane 0.43nm, isobutane 0.49nm).

Pure gas permeation. This characterization method allows to distinguish between defect-free MFI-type microporous membranes and non selective materials with macro or mesopores, or residual interparticles voids (Fig. 1).

N-butane permeation profile is in good accordance with microporous adsorption-diffusion mechanisms with a maximum of performance at about 180°C, where molecular loading and diffusion coefficients are high. At lower temperatures diffusivity is low, at higher temperatures the higher diffusivities do not compensate the lower molecular loadings.

First generation membranes (before optimisation of the synthesis procedure) revealed good permeances (2-8.10^{-7} mol/m^2.s.Pa). Isobutane permeance remains very low and below detection threshold for all samples, prepared by the first generation and the new synthesis procedure. As a result of our optimization, permselectivity appears to be infinite for n-butane with a very high permeance around 20.10^{-7} mol/m^2.s.Pa, which is about 10 times higher than any published results. In other words, besides a drastic increase of membranes permeability, gas separation capability and separation factors are not affected by material improvement. At this stage mixture gas separation is a prerequisite for highlighting membrane potential for hydrocarbon separations at high temperatures, in a domain where organic membranes can not compete with, *e.g.* by using linear and branched paraffins.

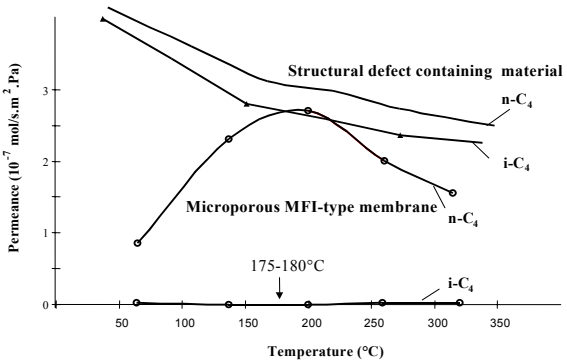

Figure 1. Single gas permeation for MFI zeolite membrane characterization (depicted here for the first generation's membrane IFP-23)

Mixture gas permeation. Characterization with mixture feedstocks (*e.g.* n-butane and isobutane, Fig. 2) at high temperatures revealed more representative of the separation performances of membrane materials as well as appropriate to highlight potential use in industrial applications.

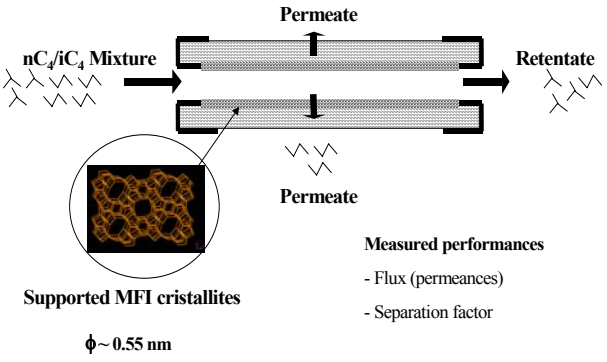

Figure 2. Characterization of MFI-type membranes by n-butane/i-butane mixture permation

On the other hand competitive adsorption, pore mouth blocking effet and/or single file diffusion may govern the molecular transport phenomena through zeolitic channels. More particularly, due to pore

size restrictions (ten membered-rings of MFI-type topology) and steric hindrance of hydrocarbons, molecular and pore wall interactions strongly affect hydrocarbons diffusion and adsorption in mixtures.

Experimental campaigns were carried out on high quality MFI-membranes with varying *e.g.* feed composition, sweep-gas flowrate and temperature, in order to determine the most adequate conditions for the characterization of the membrane separative properties.

Results and Discussion

The influence of isobutane content in n-butane/isobutane mixtures on molecular flux is studied with and without sweep gas at 175°C, where n-butane permeation is the highest (Fig. 3). The higher the isobutane concentration in the feed, the lower the transmembrane fluxes. The influence of isobutane content in n-butane/isobutane mixtures on molecular flux was studied with and without sweep gas.

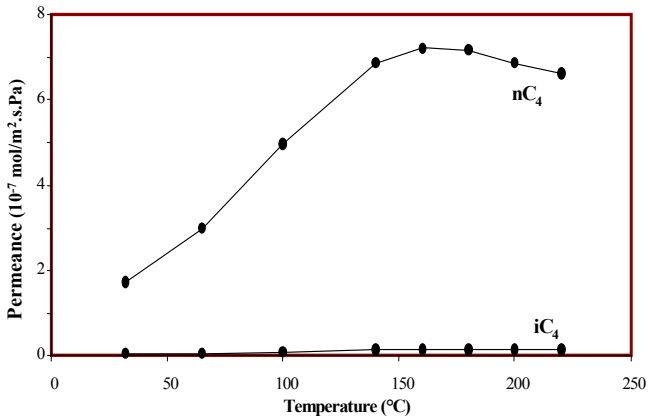

Figure 3. Butane mixture permeation for MFI zeolite membrane characterization

The effect of sweep gas flowrate is investigated and separation factors remain high by using a sweep gas, even at relatively high isobutane concentration (Fig. 4).

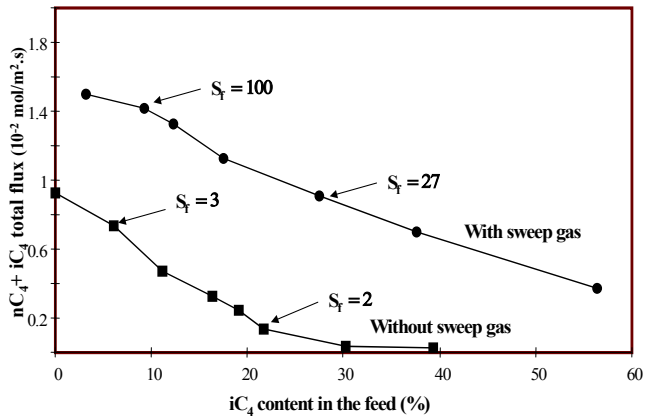

Figure 4. Effect of sweep gas on total flux and separation factor for varying butane mixtures

A comparison of separation performances is carried out among a series of very high quality membranes, taking into account more realistic and conditions (hydrocarbonaceous mixtures, high temperature) with a faster, reliable and reproducible procedure. Moreover the complex phenomena and interactions occurring in zeolitic channels and the influence of the intrinsic material properties may affect a direct correlation between pure gas and mixture permeation.

As a result a typical procedure is adopted and applied with hydrocarbonaceous mixtures to a great number of membrane materials with very high separation performances. A comparison of separation performances is carried out among a series of very high quality membranes with properties varying in a wide range. The behaviour comparison in gas mixture permeation helps select membrane samples, taking into account more realistic conditions (hydrocarbonaceous mixtures, high temperature) with a faster, reliable and reproducible procedure.

Conclusions

Characterization is a key stage of membrane science and effective separation measurements are of great interest to improve the understanding of *e.g.* hydrocarbon transport through high quality and highly permeable zeolite membrane materials. Competitive adsorption, pore mouth blocking effect and/or single file diffusion may govern the molecular transport phenomena through zeolitic channels. Mixture gas permeation, instead of pure gas permeation, appears therefore particularly adapted to highlight membrane effective performances at high temperature for applied purposes, especially in the field of refining, petrochemistry and gas treatment.

References

1. Chau, C.; Terrasse, P.; Sicard, M.; Le Dred, R.; *International Workshop on Zeolite Membrane Materials, July 1-4,* **2001**, Purmerend, the Netherlands

ZEOLITE MEMBRANES FOR FUEL ETHANOL PRODUCTION

Hidetoshi Kita,[1] Ken-ichi Okamoto,[1]
Tadahumi Yamamura,[2] and Jun Abe,[2]

[1]Department of Advanced Materials Science and Engineering, Yamaguchi University, Tokiwadai , Ube 755-8611, Japan
[2]Department of Industrial Machinery Design, Mitsui Engineering and Shipbuilding Co. Ltd., Tamano 706-8651, Japan

Introduction

Dehydration of solvents using hydrophilic polymer pervaporation membranes is a well-established technology.[1] However, these polymeric membranes have been limited to applying dehydration of solvents due to insufficiency of their thermal, mechanical and chemical stability. The recent development of hydrophilic zeolite membranes has made it possible to overcome the above limitations of hydrophilic polymeric membranes.[2, 3] The performance of these zeolite membranes is the most favorable one for pervaporation and vapor permeation membranes that have been published so far and is very high enough to put these membranes into practical use. In this work, we report the tubular type pervaporation and vapor permeation module with zeolite membranes for the fuel ethanol production. This can provide more energy efficient concentration of the ethanol to fuel-grade ethanol.

Experimental

NaA type zeolite membrane was grown hydrothemally on the surface of a porous cylindrical mullite support. The hydrothermal synthesis of NaA zeolite membrane was performed as follows. An aluminate solution was prepared by dissolving sodium hydroxide and aluminium hydroxide in distilled water. A silicate solution was prepared by dissolving sodium silicate in distilled water. The aluminate solution was added to the silicate solution and the resulting mixture was stirred vigorously, producing a homogeneous gel. The molar composition of the resulting gel was SiO_2/Al_2O_3=2.0, Na_2O/SiO_2=1.0 and H_2O/Na_2O=60. The porous support coated by the seed crystals of NaA zeolite was placed in the gel. After hydrothermal treatment at 100°C for 4 hours, the support was taken out, washed by water and dried in reduced pressure.

T-type zeolite membrane was also grown hydrothemally on the mullite support. The aluminosilicate gel used in the synthesis was prepared by mixing a colloidal silica solution and an alkaline aluminate solution. The molar compositions of the starting gel were SiO_2/Al_2O_3=54, (Na+K)/SiO_2=0.77, Na/(Na+K)=0.76, H_2O/(Na+K)= 20.75. After aging, the porous support coated by the seed crystals of T-type zeolite was placed in the gel. After hydrothermal treatment at 100℃ for 24 hours, the support was taken out, washed by water and dried.

Pervaporation and vapor permeation experiments were carried out using the apparatus described elsewhere.[4]

The zeolite membranes were characterized by X-ray diffraction. The Si/Al ratio of the zeolite was determined by ICP analysis. The surface morphology of zeolite membranes was examined by scanning electron microscopy.

Results and Discussion

Table 1 shows the flux and the separation factor of pervaporation and vapor permeation for water/alcohol mixtures through the A-type and T-type zeolite membranes. The membranes were selective for permeating water preferentially with the high permeation flux. Although the separation factor of the T-type zeolite membrane was slightly smaller than that of NaA zeolite membrane, T-type zeolite membrane was stable in acidic solution as reported previously.[5]

Table 1. Comparison of Pervaporation (50 and 75ºC) and Vapor permeation (105ºC) performance of A- and T-type zeolite membranes

Membrane	System (10 / 90 wt%)	Temp [ºC]	Flux [kg/m^{2}h]	Separation factor
A Zeolite	H_2O / MeOH	50	0.57	2100
		105	3.50	5700
	H_2O / EtOH	75	2.15	10000
		105	4.53	30000
	H_2O / *i*-PrOH	75	1.76	10000
T Zeolite	H_2O / MeOH	50	0.37	27
		105	1.74	45
	H_2O / EtOH	75	1.25	2200
		105	2.48	3900
	H_2O / *i*-PrOH	75	1.77	10000

Figure 1. Tubular type module with zeolite membrane for dehydration of ethanol.

Figure 1 shows tubular type module with NaA zeolite membrane. This plant is equipped with16 modules, each of which consists of 125 pieces of zeolite membranes and produces 99.8 wt% ethanol from 600 l/h, 90 wt% ethanol feed at module inlet temperature of 120ºC.

References

1. Huang, R. Y. M., Ed., *Pervaporation Membrane Separation Processes*, Elsevier, Amsterdam, 1991.
2. Kita, H.; Horii, K.; Ohtoshi, Y.; Tanaka, K.; Okamoto, K., *J. Mater. Sci. Lett*. **1995**, *14*, 206.
3. Morigami, Y.; Kondo, M.; Abe, J.; Kita, H.; Okamoto, K., *Separation Purification Tech*. **2001**, *25*, 251.
4. Kita, H.; Asamura, H.; Tanaka, K.; Okamoto, K. *Am. Chem. Soc. Symp. Ser*. **2000**, *744*, 330.
5. Tanaka, K.;Yoshikawa, R.; Ying, C.; Kita, H.; Okamoto, K., *Chem. Eng. Sci*. **2002**, *57*, 1577.

ZEOLITE FILM PACKING: APPLICATION TO SYNTHESIS OF ETBE IN A CATALYTIC DISTILLATION COLUMN

Yonghong Li [a], *Xigang Yuan* [b], *Shaomin Wu* [b],

[a] National Key Laboratory of C1 Chemical Technology, School of Chemical Engineering, Tianjin University, Tianjin 300072, People's Republic of China
[b] National Key Laboratory of Chemical Engineering, School of Chemical Engineering, Tianjin University, Tianjin 300072, People's Republic of China

Introduction

ETBE (ethyl tert-butyl ether) may become a better option for automotive fuel octane booster since it could be produced from bio-ethanol that can be obtained from renewable resources. In addition, ETBE has superior qualities since its low blending Reid vapor pressure, less than 55kPa, is required in some place during summer. This makes ETBE an interesting alternative to MTBE.

Acidic zeolites have been identified as good catalysts for the reaction of etherification because of their good activity, perfect selectivity, thermo-stability and reproducible response [1]. Nowadays, zeolites are commonly used in the configuration of extrudates or beads. Due to the size of the catalysts, there are some problems for them to be used in a catalytic distillation column such as difficulty in removing products out of the reaction zone promptly and higher pressure drop in the catalytic distillation column than that in conventional distillation column so as to increase energy consumption. Therefore, an operation configuration involving thin active zeolite film on a structured packing, with a large contact surface between reactants and the catalyst, combined with the short diffusion length, in the reaction zone of the catalytic distillation column is expected to ensure good mass transfer and heat transfer. A few kinds of methods for preparation of supported zeolite film or zeolite film packing have been developed so far [2−5], but the performance of the zeolite film packing applied to synthesis of ETBE in a catalytic distillation column has not been addressed.

The aim of the present study is to develop a novel type of zeolite film packing for synthesis of ETBE and exploit its unique advantages in a catalytic distillation column.

Experimental

Preparation of the zeolite film packing. The zeolite film packing was prepared using secondary hydrothermal growth on a precursor seed layer of BEA crystals over a pretreated Si-Al ceramic support with pyramids all over the surfaces. Chemical composition of the precursor solution of Al_2O_3: $30SiO_2$: 6TEABr: 10.5NaOH: $240H_2O$ (in molar ratio) was employed for the formation of the zeolite film at temperature of 145℃ for 40 hours (autogenous pressure) in a 150 cm^3 Teflon lined autoclave. After hydrothermal treatment twice, the sample was calcined at 450℃ for 4 hours in elevation of 1℃/min, modified by ion-exchanging with solution of 0.5M NH_4Cl aqueous and steamed at 350℃ for 3 hours in elevation of 1℃/min to form the acidic zeolite film packing.

Catalytic distillation. The catalytic distillation experiments were carried out in a laboratory-scale stainless steel column (Diameter of 30mm). The column consists of a total condenser with circulating alcohol at a temperature of 273 K as a coolant, a reboiler with a mantle heater, and a column body composed of the three sections: (1) a rectifying section of 200 mm height below the condenser, (2) a stripping section of 400mm height above the reboiler, (both sections were packed with triangle stainless steel gauze packings), and (3) a reaction-separation section of 1200 mm height packed with the acidic zeolite film catalytic packings located at the middle of the column. There were 15 theoretical plates per meter of the stainless steel gauze packing and 12 theoretical plates per meter of the zeolite film packings, as determined by total reflux distillation with benzene and tetrachloromethane.

When the catalytic distillation was carried out, ethanol and C_4-cut olefin were introduced, with positive displacement pumps, into the column body at the higher part and the lower part of the reaction-separation section after being preheated, respectively. The reflux ratio was controlled with a solenoid valve with a timer. Liquid level in the reboiler was maintained by adjusting the valve of the withdrawing pipe connected to a tank. The pressure was controlled with compressed nitrogen at top of the column. After the experiment had been conducted for 4 hours, the liquid streams were sampled from the top of the column and from the reboiler, simultaneously, every half an hour. The compositions of the samples were analyzed with SQ-206 gas chromatography. The experiment would not be finished until the compositions of the samples did not vary with time any more.

Results and discussion

Characterization of the zeolite film catalytic packing. The zeolite film packing was characterized by XRD, SEM, and pyridine-IR. The XRD shows that zeolite BEA film, with relative crystallinity of 99%, has formed. Fig.1 shows the external surface of the zeolite film packing. The sizes of crystals are about 500nm. The film is essentially continuous and free of cracks with a thickness of about 3 μm. The IR spectra show that there are both a lot of stronger Bronsted acidic centers and stronger Lewis acidic centers over the zeolite film.

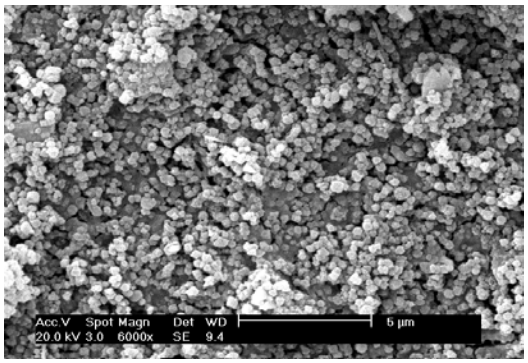

Figure 1. SEM image of the external surface of the zeolite film packing

Synthesis of ETBE in the catalytic distillation using the acidic zeolite film catalytic packings. Synthesis of ETBE from ethanol and isobutene is an exothermic reaction and the temperature highly influences the reaction rate. In the reaction-separation section, the exotherm causes some of liquid to be vaporized so that the compositions of the liquid phase and the vapor phase in this section are influenced by both the reaction and the amount of exotherm. In addition, the effect of pressure on boiling point temperature of the liquid in the column can result in a variation in the temperature of the reaction-separation section. Consequently, operating pressure influences the reaction rate. According to previous work [1], the right temperature for synthesis of ETBE over the zeolite BEA catalyst should be 85℃ that can be obtained in the reaction-separation section

of the column at pressure of about 500 kPa. Therefore, the investigations for the catalytic distillation were conducted at 500 kPa.

It is necessary to optimal the period when reactants flow through the reaction-separation section in order to ensure the sufficient contact between liquid reactants and the catalytic film. There are three factors that can influence on it. They are reflux ratio, reboil rate and space velocity. In this work, the effects of reflux ratio and reboil rate on the conversion of isobutene were investigated at the fixed space velocity of 1 h^{-1}. Also, influence of feed ratio of ethanol/isobutene on conversion of isobutene was concerned. The experiments were conducted by varying one of those operating conditions at the fixed the others.

First of all, ranges of feed molar ratio of ethanol/isobutene (F) corresponding to different conversion of isobutene (X) were investigated and were shown in Fig.2. Higher conversions of isobutene were obtained at the range of feed molar ratio from 1 to 2 where the conversion increases with increasing the feed ratio. It is noticeable that conversion of isobutene increases considerably with feed molar ratio of 1 to 1.1. On the other hand, lower conversions of isobutene were obtained at the range of feed molar ratio from 2.5 to 3 where the conversion decreases with increase of the feed ratio. This result indicates that increase of the feed ratio, in catalytic distillation, does not always advantage the conversion of isobutene, which is different from the situation in a reactor.

There is a distillation boundary in the system of ethanol/C_4–cut/ETBE because of the non-ideal mixture behavior. In non-reaction distillation, the compositions of distillate and the liquid in the reboiler are limited within some regions. According to the results of this experiment, there is an upper limited value in feed ratio of ethanol/isobutene for ETBE synthesis in a catalytic distillation process. As long as the value of feed molar ratio is less than 2, an ordinary distillation boundary can be removed by conducting the reaction and separation simultaneously and a higher conversion of isobutene can be obtained.

In addition, composition of the liquid in the reboiler should be taken into account. Since most extra ethanol may run down into the reboiler, there is a demand for a feed ratio of ethanol/isobutene as lower as possible. Therefore, the optimal value of the feed molar ratio, considering both conversion of isobutene and purity of the product in the reboiler, should be 1.1.

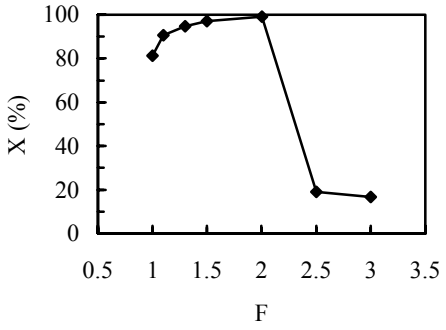

Figure 2. Conversion of isobutene as a function of feed molar ratio of ethanol / isobutene, pressure=500kPa, R=7, B=0.11m^3/h

Next, the effects of reflux ratio (R) on conversion of isobutene were shown in Fig.3. As increase of reflux ratio both can prolong the time for the contact between reactants and the catalysts and can improve the separation of the product from the reactants, there is always an increase in conversion of isobutene with increase of reflux ratio. Fig.3 also shows that the conversion does not vary so much by changing reflux ratio from 6 to 7. To minimize the consumption of energy, the optimal reflux ratio should be 6.

Finally, the variation of conversion of isobutene with respect to reboiler heat duty (B) was shown in Fig.4. The conversions are more than 90% at the range of reboil rate from 0.105 m^3/h to 0.125 m^3/h. The maximum conversion of isobutene appears at a reboil rate of 0.115 m^3/h. Further increase of reboil rate can cause some of the product in the reboiler to be vaporized and to run up into the reaction zone, which is disadvantageous to conversion of isobutene. Therefore, the optimal value of reboil rate can be 0.115 m^3/h.

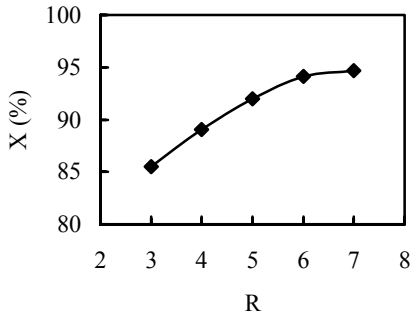

Figure 3. Conversion of isobutene as a function of reflux ratio, pressure=500kPa, F=1.3, B=0.11m^3/h

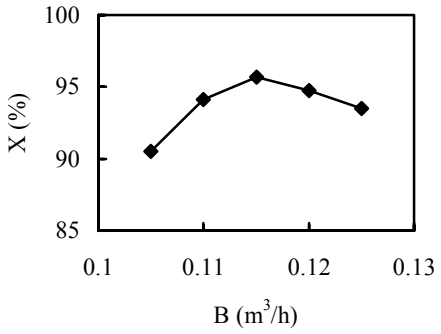

Figure 4. Conversion of isobutene as a function of reboil rate, pressure=500kPa, F =1.3, R = 6

Acknowledgment

The financial supports of the China Petroleum & Chemical Corporation and the fond of the National Key Laboratory of Chemical Engineering at Tianjin University are gratefully acknowledged.

References

[1] Li, Y., Yu, S., Chang, X., Wang, Y., Song, Y., *Acta Petrolei Sinica (Petroleum Processing Section)* in Chinese **2001**, 17(sup), 86.
[2] Oudshoorn, O. L., Janissen, M., Van Kooten, W. E. J., Jansen, J.C., Van den Bleek, C. M., Calis, H.P.A., *Chem. Eng. Sci.* **1999**, 54, 1413.
[3] Aoki, K., Kusakabe, K., Morooka, S., *AIChE J*. **2000**, 46(1), 221.
[4] Alfaro, S., Arruebo, M., Coronas, J., Menendez, M., Santamaria, J., *Micro. & Meso. Mater.* **2001**, 50(2-3), 195.
[5] Coutinbo, D., Balkus, J., Kenneth, J., *Micro. & Meso. Mater.* **2002**, 52(2), 79.

POLYIMIDES FOR BATTERY AND FUEL CELL MEMBRANES

Jennifer A. Irvin[1]*, Daniel Stasko,*[2] *Stephen Fallis*[1]*, Andrew J. Guenthner*[1]*, Cynthia Webber*[1]*, and John Blackwell*[3]

(1) Chemistry and Materials Division, Naval Air Warfare Center Weapons Division, Code 4T4220D, 1 Administration Circle, China Lake, CA 93555, Fax: 760-939-1617, irvinja@navair.navy.mil, (2) Department of Chemistry, University of Toledo, (3) Macromolecular Science and Engineering, Case Western Reserve University

Introduction

Although polymer electrolytes are crucial components of both lithium ion batteries (LIBs) and fuel cells (PEMFCs), the properties of existing polymer materials limit the performance of these devices. For example, the PEO-based polymers typically used in LIB membranes provide sufficient ion conductivity only above room temperature, which prevents their use at high altitude and in outer space. PEMFCs are conversely limited to low operating temperatures due to inadequate membrane thermal stability, which leads to increased catalyst poisoning and lower transport rates. [1] Thus, new polymer materials are needed to improve the performance of these devices.

The low conductivity of LIB membranes at low temperatures results from the mechanism of Li^+ transport, which involves highly temperature-dependent polymer chain segmental motions. If the Li^+ transport mechanism involves electric field-driven motion through open channels, however, high rates of transport over a large temperature range are possible.[2] The combination of molecular geometry and Li^+ affinity makes some crown ethers ideal candidates for these channels, provided they can be incorporated into a polymer matrix and aligned properly.

We have investigated crown ethers as components in high temperature fuel cell membranes, for which polybenzimidazoles, poly (ether ether ketone)s, polysulfones, and polyimides are considered candidates. Although most polyimides contain five-membered imide rings, polyimides in fuel cell membranes require six-membered imide rings[3] in order to exhibit sufficient hydrolitic stability under acidic conditions.[4] However, these six-membered ring polyimides are typically poorly soluble; solubility in polyimides can often be improved by incorporation of hexafluoroisopropylidene (HFIP) groups without detracting from polymer stability. [5]

Experimental

Synthesis. Crown ether-containing diamines were prepared as reported previously.[6] Copolyimides were synthesized by heating equivalent amounts of diamine and dianhydride in m-cresol at 200ºC for 15-24h. Terpolymers were prepared similarly, but the two diamines or two dianhydrides were dissolved together in m-cresol prior to addition of the other monomer. Polyimides were sulfonated according to a literature preparation.[7]

Characterization. Structural verification was accomplished using Bruker 400MHz ^1H and ^{13}C NMR and a Nikolet 710 FTIR. Elemental analysis (C, H, N) was performed by Galbraith Laboratories. Degree of sulfonation was determined by titration. (ref) Differential scanning calorimetry (DSC) was performed using a TA Instruments Model 2910 in nitrogen with a 10ºC/minute ramp from –40 to +300ºC. Thermogravimetric analysis (TGA) was performed using a TA Instruments Hi-Res TGA 2950 in nitrogen with a 5ºC/minute ramp to 500ºC. Proton conductivity was determined using electrochemical impedance spectroscopy (EIS) measurements with an EG&G Model 273A potentiostat/galvanostat equipped with a Princeton Applied Research 5210 lock-in amplifier and PowerSine software.

Results and Discussion

A variety of polyimides were prepared as delineated in Table 1. Initially, 1,4,5,8-naphthalenetetracarboxylic dianhydride (NTDA) and/or 4,4'-(hexafluoroisopropylidene)diphthalic anhydride (6FDA) were reacted with diamines to form polyamic acids, which were thermally converted to the polyimides. Diamines used were 2,2-bis(4-aminophenyl)hexafluoropropane (Bis-A-AF), anti-4,4'-diamino-dibenzo-18-crown-6 (C18), 4,4'-diaminodibenzo-24-crown-8 (C24), and/or 2,5-diaminobenzenesulfonic acid (DABS). A general scheme for the synthesis and subsequent sulfonation is shown in Figure 1. The crown ether-containing polyimides (1 and 2 in Table 1) were very poorly soluble, dissolving significantly only in m-cresol. To improve solubility, commercially-available HFIP-containing monomers, either 6FDA or Bis-A-AF, were incorporated into the polyimides. The resulting polyimides (5 and 9 in Table 1) are soluble in chloroform, DMF, NMP, and m-cresol; polymers 5 and 9 have been previously reported[8] but have not been investigated for use as electrolyte membranes. We have also prepared four terpolymers (3, 6s, 7, and 8); the terpolymers exhibit satisfactory solubility, processability, and film-forming properties.

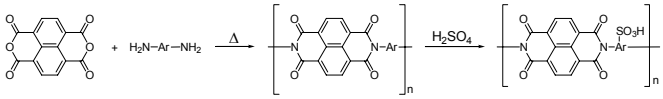

Figure 1. General synthesis and sulfonation of polyimides

Table 1. Summary of Polymer Formulations

	Monomers					
Polymers*	NTDA	6FDA	Bis-A-AF	C18	C24	DABS
1/1s	x			x		
2/2s	x				x	
3	x		x		x	
4s	x					x
5	x		x			
6s	x			x		x
7	x	x			x	
8	x	x		x		
9		x			x	

*Sulfonated polymers are denoted by an s following the polymer number

Incorporation of sulfonic acid groups was accomplished using two strategies, direct sulfonation of polymer materials using reactive reagents or incorporation of sulfonated monomer. The first case, post-polymerization sulfonation, was accomplished using concentrated sulfuric acid according to a literature preparation.[7] The resulting polymers (1s and 2s) were found to be somewhat soluble in hot methanol and in aqueous base. Verification of the extent of sulfonation using standard spectroscopic techniques proved difficult, though changes in solution properties suggested substantial substitution. Ion exchange capacity, and thereby the degree of sulfonation, was determined titrametrically. A significant degree of sulfonation was apparent in some cases with up to three sulfonate groups introduced per repeat unit. Polyimides 4s and 6s were prepared using a presulfonated diamine that allowed for a controlled degree of sulfonic acid incorporation into the polymer. As an internal check, the ion exchange capacity for these polymers was also measured and corresponded to one sulfonate group per repeat unit as expected (Table 2). While introduction of sulfonic acid groups in

this manner is more reliable and reproducible, the overall degree of sulfonation is much lower and more limited.

Proton conductivity (σ, S/cm) of the sulfonated polymers was accomplished using EIS. As expected, water content was found to be critical in the overall conductivity of the pressed samples (see Table 2). Dry conductivity values were very low at room temperature, ~10^{-7} S/cm. Conductivity was improved in moist samples with values reaching 10^{-2} S/cm at room temperature in fully hydrated samples.

Table 2: Proton Conductivity Measurements of Polymer Systems

Polymer	Wt % SO_3H	Approx. # SO_3H per repeat	σ of dry films*	σ at 10% water*	σ saturated w/ water*
6s	6 %	1	7x 10^{-8}	-	2x10^{-5}
4s	12 %	1	1x10^{-7}	5x10^{-7}	1x10^{-4}
1s	32 %	3	1x10^{-6}	-	1x10^{-2}

*All conductivity measurements performed at room temperature and presented in units of S/cm

These polymers have been found to be thermally stable, with 10% weight loss in air at approximately 400ºC (via TGA). This stability range will more than satisfy the high temperature requirement for fuel cell membranes.

Two different forms of order in the crown ether-containing polyimides have been detected via cryogenic differential scanning calorimetry (DSC; Figure 2) and X-ray diffraction (XRD) of powder samples (Figure 3). XRD indicates that both samples are semi-crystalline, and DSC indicates that the crystals melt at a temperature near to or above the thermal degradation point (320°C) of these polymers. The polyimide with the smaller, *anti*-18-crown-6 repeat unit is more crystalline with better crystalline order than the polyimide with the 24-crown-8 repeat unit, suggesting that the crystallinity is controlled by the tendency of the planar naphthylimide sheets to stack and pack into a crystalline array. This is more readily accomplished with smaller crowns that interfere less with the ordering process. Molecular models based on the X-ray data suggest structures in which the chain axes are in the plane of the film, and the crown ethers are stacked perpendicular to the surface. This type of structure should facilitate Li^+ transport.

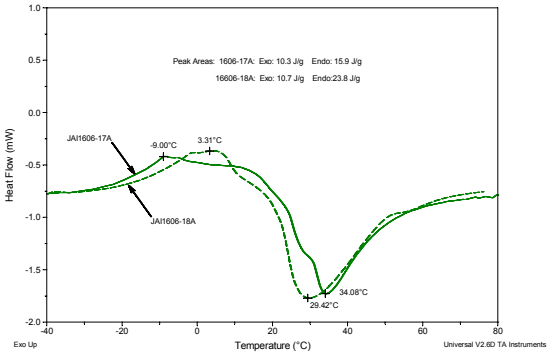

Figure 2. DSC thermograms of polymers 1 (solid line) and 2 (dashed line).

The second form of ordering appears to be present only at or below room temperature and is thus most easily detected via cryogenic DSC. A first-order transition (akin to crystallization) with a modest enthalpy change occurs in both polyimides at approximately 30°C (peak endotherm). Like crystallization, this ordering appears to require activation energy, leading to a maximum in the rate of ordering at -10 to 0°C. DSC scans show that the enthalpy of ordering is larger for the 24-crown-8 containing polyimide than for the *anti*-18-crown-6 polyimide. The most likely interpretation of this ordering phenomenon involves a conformational change in the crown ether repeat units. Whether such changes are sufficient to induce crystal-crystal transformations in these polyimides is presently unknown.

Conclusions

Several polyimides have been prepared; incorporation of HFIP groups improves solubility without detracting from thermal stability. Sulfonation of several of these polymers yielded materials with room temperature proton conductivities reaching 0.01 S/cm. Some evidence of crown ether channel formation has been seen; some of these polymers may be useful as LIB electrolytes.

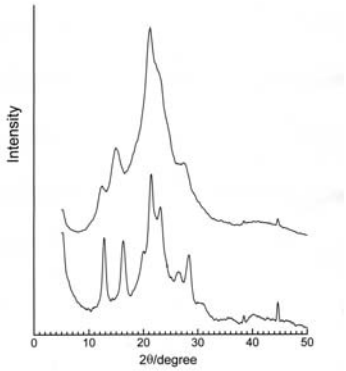

Figure 3. X-ray diffraction patterns for the polymers 1 (bottom) and 2 (top).

Acknowledgements. This work was supported by the Office of Naval Research's ILIR program and by NASA Glen Research Center.

References

1. Rikukawa, M.; Sanui, K., *Prog. Polym. Sci.* **2000**, *25*, 1463-1502.
2. Scanlon, L. G., Jr.; Krawiec, W. T.; Giannelis, E. P., *US Pat. No.* 6,010,805, **2000**.
3. a)Vallejo, E.; Pourcelly, G.; Gavach, C.; Mercier, R.; Pineri, M., *J. Membr. Sci.* **1999**, *160*, 127-137. b) Zhang, Y.; Litt, M.; Savinell, R. F.; Wainright, J. S., *Polym. Prepr. (Am. Chem. Soc., Div. Polym. Chem.)* **1999**, *40 (2)*, 480-481. c) Genies, C.; Mercier, R.; Sillion, B.; Cornet, N.; Gebel, G.; Pineri, M., *Polymer* **2001**, *42*, 359-373. d) Fang, J.; Guo, X.; Harada, S.; Watari, T.; Tanaka, K.; Kita, H.; Okamoto, K., *Macromoecules* **2002**, *35 (24)*, 9022-9028.
4. Genies, C.; Mercier, R.; Sillion, B.; Petiaud, R.; Cornet, N.; Gebel, G.; Pineri M., *Polymer* **2001**, *42*, 5097-5105.
5. P. E. Cassidy, *J. Macromol. Sci.-Rev. Macromol. Chem. Phys.,* **1994,** C34, 1.
6. Zarras, P.; Lindsay, G. A.; Chafin, A. P.; Miles, M. H.; Merwin, L. H.; Fallis, S.; Webber, C.; Yee, R. Y.; Irvin, J. A., Polymer News, 2001, 26 (10), 335-340.
7. Zaidi, S. M. J.; Mikhailenko, S. D.; Robertson, G. P.; Guiver, M. D.; Kaliaguine, S., J. Membr. Sci., 2000, 173, 17-34.
8. a) Togano, T.; Takiguchi, T.; Takao, H.; Hanyu, Y.; Asaoka, M.; Iwaki, T., *Eur. Pat. Appl.* EP499,159, August 19, 1992. b) Russanov, A. L.; Bulycheva, E. G.; Elshina, L. B.; Askadskiy, A. A.; Vlasov, U. M.; Rogozhnikova, O. Yu., *Polym. Prepr. (Am. Chem. Soc., Div. Polym. Chem.)* **1998**, *39 (2)*, 853-854. c) Pethrick, R. A.; Wilson, M. J.; Affrossman, S.; Holmes, D.; Lee, W. M., *Polymer* **2000**, *41*, 7111-7121.

APPLICATION OF SANS IN ANALYSIS OF FUEL CELL CATHODE ION EXCHANGE MEMBRANES

Riza Kizilel[1], Nasrin Khalili[2], Giselle Sandi[3], and Robert J. Selman[1]

[1]Department of Chemical and Environmental Engineering, and [2]Environmental Management Program, Illinois Institute of Technology, Chicago, Illinois 60616;
[3]Chemistry Division, Argonne National Laboratory, 9700 South Cass Ave, Argonne, IL 60439

Introduction

One of the fundamental components of a fuel cell is the membrane electrode assembly. The electrode is coated on one side with a thin platinum catalyst layer and the electrode, catalyst, and membrane together form the membrane electrode assembly (MEA). Since it is the heart of the fuel cell, more studies are concentrated on synthesis of MEAs.

High or low catalyst loaded cathode material (MEA) prepared by different techniques can be obtained commercially. In most cases high loading helps the system works better but the higher the amount of platinum the more costly is the process. The characterization of new and used MEAs using advanced analytical methods is a key element to determine the problems associated with operations and operating conditions.

In this work, a fuel cell is being used for slightly different purpose from its usual usage. Metal contaminants in acidic solution are removed by electrochemical process which has a cathode fuel cell (**Figure 1**). The contact with the acidic solution was shown to affect negatively the structure and the performance of the MEA. Since the focus of our work was the determination of the effect of Pt loading on the cell performance and ionic flux, a series of experiments were carried out to analyze the impact of process performance on the MEA structure. In each of them overloading (a continuous slow rise in the voltage necessary to maintain a constant current) appeared to be a major problem (**Figure 2**). To solve the problems associated with the cost and the need for a high Pt loading, it was decided to prepare and fully characterize a range of MEAs in our laboratory. Therefore, the structural characterization focused on Small Angle Neutron Scattering (SANS). The results obtained in these studies will help to lower the cost of operation and to find the optimum structure needed for the process to reach its maximum efficiency.

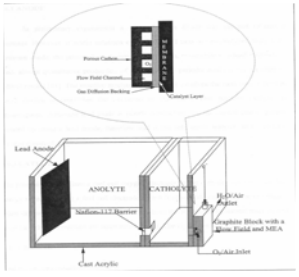

Figure 1: Experimental Setup for regeneration of chromic acid and removal of metal contaminants

Experimental

MEA Preparation. MEAs are prepared by following the procedure described in reference (1).

Characterization Methods.

Powders used in SANS are prepared by first scratching the electrodes from the MEA and then grinding them into fine particles. Four different types of powders were used during the characterization. Specifically, they are Pt-C mixture (Electro-Chem), MEA before used in electrochemical cell (EC), MEA after used in EC without impurities, and MEA after used in EC with impurities.

The SANS measurements were performed at the SAND time-of-flight SANS instruments at the Intense Pulsed Neutron Source, Argonne National Laboratory. Cylindrical Suprasil sample containers with a neutron optical path length of 1 mm were used. SAND provides data in a Q range of 0.001 to 1 $Å^{-1}$ in a single measurement. All samples were studied as dry powders. Additionally, a contrast-variation SANS study was performed on each sample by preparing the powdered sample as slurries in mixtures of normal and deuterated toluene with deuterated toluene proportions of 0, 25, 50, 75 and 100 %. In preparing the slurries, the powder was slowly evacuated to avoid air bubble formation prior to adding the solvent. The scattering from an empty cell was used for background correction in these measurements (2).

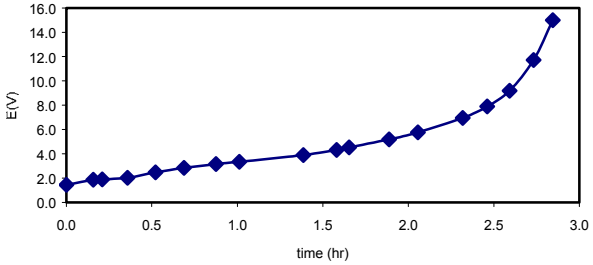

Figure 2: The impact of low platinum loading on potential (E(V))

Results and Discussion

Previous results have shown that a new membrane process can be used to remove the contaminants from hard chromium plating baths. Although energy required to operate the cell was decreased theoretically, experimental results showed that energy consumption during the experiment is still too high. Fortunately, the process removal rate for metal contaminants was observed to be same level of removal rate in porous pot process.

SANS data helps to draw a clear picture of the morhphology of MEAs electrodes. The plot of I (intensity) vs q (scattering vector) is the key element to determine the diameter of agglomerate, and pore size (**Figure 3**).

To analyze the results, SANS data can be fit into an equation derived by Beaucage, B., (2).

$$I(q) = G\exp\left(\frac{-q^2 {R_g}^2}{3}\right) + \left(L_i {q_i}^*\right)^P$$

where

G: Guinier prefactor
Rg Particulate radius of gyration
Li: characteristic length scale
I: Scattering Intensity
qi* : function of q scaled to cut of power law scattering
$q = 4\pi\mathrm{Sin}(\theta/2)/\lambda$ where θ is the scattering angle and λ is the wavelength

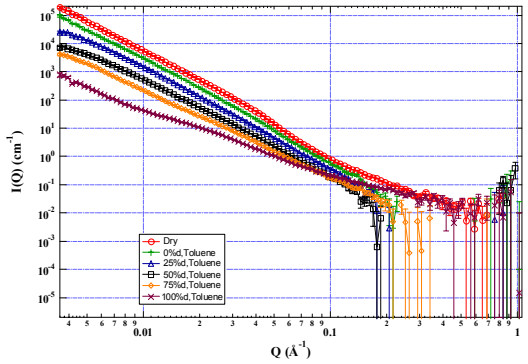

Figure 3: Contrast Variation SANS Data

The fitting shows that dry Pt-C powder has an agglomerate of two layers. The intensity at high values, unfortunately, does not help to define the first layer. But the second layer shows a gyration radius of ~60Å and power law exponent of 3.3. The latter value also indicates a disordered structure in this mixture.

Addition of Nafion to the MEA decreases the gyration radius to 48Å, whereas the power law decreases to 3.19. These two parameters show that the addition of nafion and the application of high pressure help to attach smaller particles to each other in the second layer. Although the disorder level is decreasing, it is still at the high levels.

MEAs were tested in two different cells. One of them is the 2.5 M chromic acid solution without metallic impurities. This electrochemical process increases the potential of the cell in less than two hours. Two layers were observed in the SANS results fitting, however, and the radius of gyration, increases to 100 Å. The disorder level (power law) remains fairly constant at 3.25.

When metallic impurities (Cu,Fe,Ni) are added to chromic acid, another layer is formed because of the impurities. The results show that the impurities diffuse through the second layer first and then form the third one. Radius of gyration in the second layer reaches up to 182.4 Å which means a 277% increase. The disorder level of this layer is at the highest level which is 3.37. Third layer clearly indicates a clogged surface formed during the process. This last layer has a gyration radius of 36.7 Å and a power law of 2.1, indicated a more ordered structure. **Table 1** shows the fitting results for each experiment.

Contrast analysis helps to characterize the porous structure of the materials. The Modified Guinier plot (**Figure 4**) at low Q levels determines the porosity of the materials. **Table 2** shows that there are still available pores inside the agglomerates but they are inaccessible because of the clogged outer region.

Table 1: Relevant parameters obtained from SANS data

		Pt-C	New MEA	Used MEA w/o impurities	Used MEA with impurities
1st Layer	length scale	6.876	7.6109	9.1572	5.6916
	exponent	3.267	3.1539	3.3404	3.0762
2nd Layer	guiner i(0)	183.21	26.323	219.57	6414.1
	guiner rg	60.024	48.422	100.41	182.42
	length scale	10.652	12.131	12.526	8.3657
	exponent	3.3293	3.1938	3.2504	3.3703
3rd Layer	guiner i(0)	-	-	-	5.9373
	guiner rg	-	-	-	36.695
	length scale	-	-	-	12.829
	exponent	-	-	-	2.1476
	reduced chi squared	5.296	11.193	7.3866	1.9676

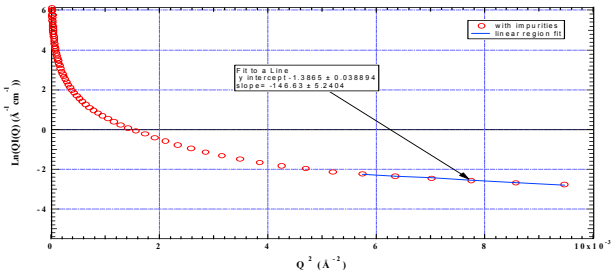

Figure 4: Modified Guinier Plot

Table 2: Morphology of the pores

	Pt-C	Pt-C/Nafion (new)	Used w/o impurities	Used with impurities
Porous Radius (Aº)	27.1	26.8	22.8	24.2

Acknowledgment

Work at Argonne was performed under the auspices of the U.S. Department of Energy, Office of Basic Energy Sciences, Division of Chemical Sciences, Geosciences, and Biosciences under contract number W-31-109-ENG-38. The help from the IPNS personnel is greally appreciated.

References

1. Wilson, M.S., Valerio, J.A. and Gottesfeld, S., *Electrochim. Acta*, 40(3), 355, (1995).
2. Littrell, K., Khalili, N., Campbell, M., Sandi, G. and Thiyagarajan, P. , *Chemistry of Materials* 14 (1), 327-333 (2002).
3-Beaucage, *G,. Journal of Applied Crystallography* 1996, 29, 134.

Novel PEEK Membranes for Fuel Cell Applications

Maria Gil [1], *Xiangling Ji*[1], *Xianfeng Li*[2], *Hui Na*[2], *J. Eric Hampsey*[1] *and Yunfeng Lu*[1]

(1) Chemical Engineering Department, Tulane University, 300 Lindy Boggs Center, Tulane University, New Orleans, LA 70118, ylu@tulane.edu, (2) Department of Chemistry, Jilin University, huina@jlu.edu.cn

Introduction

Proton exchange membrane fuel cells (PEMFC) are promising power sources for vehicles and portable devices [1,2]. Membranes currently used in PEMFC are perfluorinated polymers such as Dupont Nafion®. Even though such membranes have demonstrated good performances and long-term stability, their high cost and methanol crossover makes them unpractical for large-scale production. Among the desired characteristics of a cation-exchange membrane for PEM fuel cells applications are: high ionic conductivity, minimal water/methanol transport, high resistance to dehydration, low gas permeability, low swelling, high mechanical strength, high resistance to oxidation, reduction and hydrolysis and low cost. Sulfonated aromatic polyether ether ketones (S-PEEK) based membranes have been studied due to their good mechanical properties, thermal stability and conductivity [3, 4]. In the present study, poly(aryl ether ether ketone) (PEEK) polymeric membranes fabricated from sulfonated monomer have been evaluated for possible fuel cell applications. The sulfonated PEEK membranes were characterized by measuring the ion exchange capacity, water swelling, proton conductivity, methanol diffusivity and thermal stability.

Experimental

Membrane Preparation. 1.0 g sulfonated PEEK was dissolved into 30ml DMF. The solution was cast into thin films of 30 µm – 60 µm thickness on a 10 cm x 10 cm glass slide, which was placed into an oven at 50°C and dried for 3 days. A dry membrane was peeled off from the substrate with deionized water, and was submerged into 1.5M H_2SO_4 solution overnight. Finally, the membranes were rinsed with deionized water and dried under vacuum for one day.

Membrane Characterization

Swelling Degree. Membrane samples were equilibrated in water at 25°C for 24 h. They were then removed from the water, quickly dry-wiped and immediately weighed. Subsequently, they were dried at 100°C and again weighed. The swelling degree was calculated as follows:

$$SD = m_{wet}/m_{dry} - 1 \qquad (1)$$

Ion-Exchange Capacity (IEC). The IEC was determined through titration. The membranes in H^+ form were immersed in 1M NaCl solution for 24 h to liberate the H^+ ions (the H^+ ions in the membrane were replaced by Na^+ ions). The H^+ ions now in solution were then titrated with 0.01M NaOH.

Proton Conductivity. The proton conductivity of the fully hydrated polymer membrane samples was determined by AC impedance spectroscopy over a frequency range of $1x10^3$ Hz to $1x10^6$ Hz using a Solartron 1260 gain phase analyzer.

Methanol Diffusion Coefficient. Diffusion coefficients were determined using an H-cell arrangement. 1M Methanol was placed on one side of the H-cell and water was placed on the other side. Magnetic stirrers were used on each compartment to ensure uniformity. Methanol analyses were done using a Hewlett Packard GC chromatograph. Peak areas were converted to methanol concentration using a calibration curve.

Thermal Stability. The thermal stability of the membranes was analyzed using a TA instrument SDT 2960 simultaneous DTA-TGA. The sample (~10mg) was heated from 25°C to 900°C at a rate of 10°C/min under a nitrogen atmosphere.

Results and Discussion.

Methanol Diffusion. S-PEEK polymeric membranes prepared from the sulfonated monomer exhibited methanol diffusion coefficients of $3x10^{-7}$ to $5x10^{-8}$ cm^2/s depending on the degree of sulfonation of the starting monomer. These values are significantly lower than that of Nafion® membranes ($2x10^{-6}$ cm^2/s). Such results are expected for S-PEEK membranes and can be attributed to less pronounced hydrophilic and hydrophobic domains within the membrane and to a smaller flexibility of the polymer backbone. These characteristics reduce the hydrodynamic solvent transport (water and methanol), which may help reduce the problems associated with water and methanol crossover for direct methanol fuel cells [4].

Conductivity. Proton conductivities at 25°C of the S-PEEK membranes (shown on Figure 1) are about 13-42 % that of Nafion 117 determined in [5]. The conductivity values are acceptable to obtain good fuel cell performances.

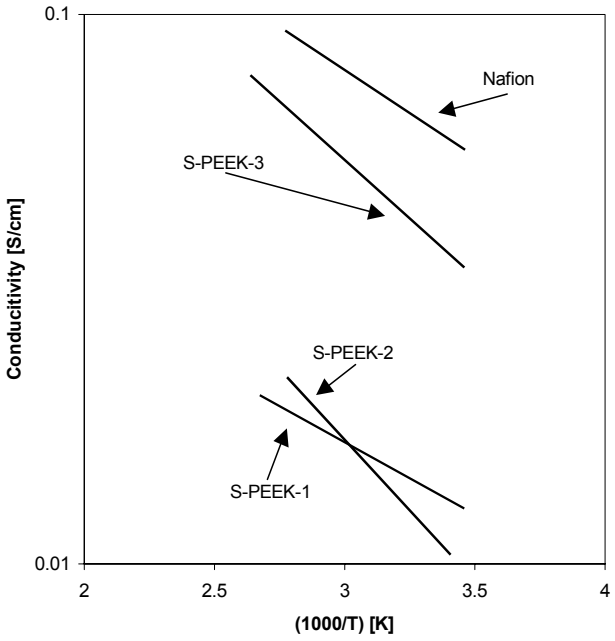

Figure 1. Proton conductivity of fully hydrated Nafion [4] and S-PEEK polymeric membranes prepared from sulfonated monomer.

Thermal stability. The thermal degradation of the S-PEEK membranes starts in the range of 250-270°C and these values are similar to the ones obtained for cross linked polyaryl blend membranes [6]. Three weight loss steps are observed in Figure 2. The first weight loss step corresponds to water loss. The second weight loss step is attributed to the splitting-off of sulfonic acid groups in the PEEK membrane [7]. The third weight loss step corresponds to sulfonic acid decomposition. According to the thermal analysis, the S-PEEK membranes are thermally stable within the temperature range for PEMFC applications.

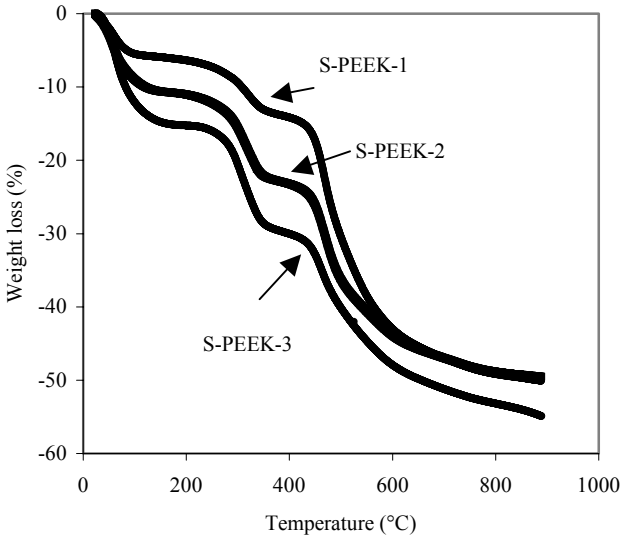

Figure 2. TGA curves of S-PEEK membranes

Comparison with Nafion® membranes.

S-PEEK polymeric membranes prepared from the sulfonated monomer show some similarities with Nafion membranes in IEC and water swelling properties depending on the degree of sulfonation of the PEEK, see Table 1. The main differences between S-PEEK ad Nafion® membranes are ionic conductivity and MeOH diffusion coefficient. Even though the ionic conductivities are lower than that of Nafion®, they are still suitable for PEMFC applications and the lower MeOH diffusion coefficients should reduce methanol crossover in direct methanol fuel cells.

Table 1. Comparison of Nafion and S-PEEK membranes

	S-PEEK 1	S-PEEK 2	S-PEEK 3	Nafion®
Ion Exchange Capacity (IEC)	0.712	1.511	1.465	0.91
Water Swelling (%)	13	37	54	38
Conductivity at 25°C (S/cm)	0.011	0.013	0.035	0.083
MeOH diffusion coefficient at 25°C (cm^2/s)	$5x10^{-8}$	$3x10^{-7}$	$3x10^{-7}$	$2x10^{-6}$

Conclusions

S-PEEK membranes with 0.7-1.5 mmol/g ion exchange capacity exhibited a high proton conductivity (> 0.01 S/cm at room temperature), good thermal stability and methanol diffusion coefficients significantly lower than that of Nafion® (PEM of choice for hydrogen/air fuel cells), making S-PEEK membranes a good alternative to reduce problems associated with high methanol crossover in direct methanol fuel cells.

References

1. Appleby, A.J., *Recent developments and applications of the polymer fuel cell.* Philosophical Transactions of the Royal Society of London, Series A: Mathematical, Physical and Engineering Sciences, 1996. **354**(1712): p. 1681-1693.
2. Shoesmith, J.P., *et al.*, *Status of solid polymer fuel cell system development.* Journal of Power Sources, 1994. **49**(1-3): p. 129-42.
3. Kreuer, K.D., *On the development of proton conducting materials for technological applications.* Solid State Ionics, 1997. **97**(1-4): p. 1-15.
4. Kreuer, K.D., *On the development of proton conducting polymer membranes for hydrogen and methanol fuel cells.* Journal of Membrane Science, 2001. **185**(1): p. 29-39.
5. Zawodzinski, T.A., Jr., *et al.*, *Determination of water diffusion coefficients in perfluorosulfonate ionomeric membranes.* Journal of Physical Chemistry, 1991. **95**(15): p. 6040-4.
6. Kerres, J., *et al.*, *Application of different types of polyaryl-blend-membranes in DMFC.* Journal of New Materials for Electrochemical Systems, 2002. **5**(2): p. 97-107.
7. Zaidi, S.M.J., *et al.*, *Proton conducting composite membranes from polyether ether ketone and heteropolyacids for fuel cell applications.* Journal of Membrane Science, 2000. **173**(1): p. 17-34.

Synthesis and Characterization of Pyridine-Based Polybenzimidazoles as Novel Fuel Cell Membrane Materials

*Lixiang Xiao, Haifeng Zhang, Eui-Won Choe, Eugene Scanlon, L. S. Ramanathan and Brian C. Benicewicz**

NYS Center for Polymer Synthesis,
Department of Chemistry, Rensselaer Polytechnic Institute, Troy, NY 12180

Introduction

Fuel cells based on solid polymer electrolytes have attracted much attention recently due to their promise as high energy density power sources for both mobile and stationary applications. In particular, high temperature polymer electrolyte membranes operational above 120°C without humidification offer many advantages including fast electrode kinetics and high tolerance to fuel impurities.[1] However, the current widely used sulfonated perfluoropolymer membranes such as Nafion® rely on the presence of water to solvate and transport the protons and therefore operate in a limited temperature range and encounter water-management problems.

Acid doped polybenzimidazole (PBI) has emerged as a promising candidate for a low-cost and high performance fuel cell membrane material. It has been shown that this polymer electrolyte membrane exhibits high ionic conductivity at temperatures up to 200°C, low gas permeability, excellent oxidative and thermal stability,[2] and nearly zero water drag coefficient.[3] However, additional progress is still needed for the large-scale application of PBI in fuel cells. Furthermore, the conventional method to prepare acid doped PBI membranes involves a multi-step process while the mechanical properties of the resulting membranes are largely limited by the low molecular weight of PBI used in previous studies.

In this paper, we report the synthesis of a series of high molecular weight (as indicated by the inherent viscosity, I.V.) polybenzimidazoles (PBIs) with additional main chain pyridine groups, using polyphosphoric acid (PPA) as both solvent and polycondensation reagent. A novel process, termed as PPA process,[4] has been developed to prepare pyridine-based PBI (PPBI) membranes loaded with high levels of phosphoric acid by direct-casting of the PPA polymerization solution without isolation or re-dissolution of the polymers, followed by a sol-gel transition induced by the hydrolysis of PPA into phosphoric acid. In addition, we studied the effect of the incorporation of pyridine groups on the properties and film formation process.

Experimental

Materials. Pyridine dicarboxylic acids (2,4-, 2,5-, 2,6- and 3,5- PDAs) were purchased from Acros and purified by recrystallization from dilute hydrochloric acid before use. 3,3′,4,4′-Tetraaminobiphenyl (TAB) was donated by Celanese Ventures, GmbH and used as received. Polyphosphoric acid (115%) was used as supplied from Aldrich Chemical Co.

Polymerization. The general procedure for the synthesis of pyridine-PBIs (PPBIs) is described as follows: Purified pyridine dicarboxylic acid (12.534g, 0.075mol) and TAB (16.074g, 0.075mol) were added to a three-neck resin reaction flask in a nitrogen atmosphere glove box, followed by 220 grams of polyphosphoric acid. The reaction mixture was stirred using a mechanical overhead stirrer under nitrogen and the reaction temperature was ramped to 190°C and maintained for 18hrs at 190°C. The reaction mixture became more viscous and developed a dark brown color. A small amount of the reaction mixture was poured into water to isolate a brown mass. The mass was pulverized, neutralized with ammonia hydroxide, washed thoroughly with water, and dried in a vacuum oven for 24 hours at 100°C to obtain the pyridine PBIs for further characterization.

Film Formation. The polymer films were prepared by casting the polymerization solution directly onto glass plates using a Gardner film applicator. The polyphosphoric acid solvent was hydrolyzed to phosphoric acid by exposing the films for 24h at 25°C and relative humidity 40±5% to obtain polymer electrolyte membranes for film properties and fuel cell testing.

Characterization. I.V. was measured at a concentration of 0.2 g/dL in concentrated sulfuric acid at 30°C. The acid doping level was determined by titrating a piece of membrane sample with standardized sodium hydroxide solution. The sample was then washed with water, dried in a vacuum oven to obtain the dry weight of polymer for calculation. The membrane mechanical property was tested utilizing a United Tensile Tester (SSTM-1-PC) following the ASTM standard D882-97 (Type V specimens). Ionic conductivity was measured by a four-point ac impedance method using a Zahner IM6e spectrometer over the frequency range from 1Hz to 100KHz. Fuel cell testing was conducted using a single cell test station (Fuel Cell Technologies) equipped with mass flow controllers.

Results and Discussion

We investigated the synthesis of pyridine-based PBI starting from 2,4-, 2,6-, 2,5- and 3,5-pyridine dicarboxylic acids in polyphosphoric acid as shown in scheme 1.

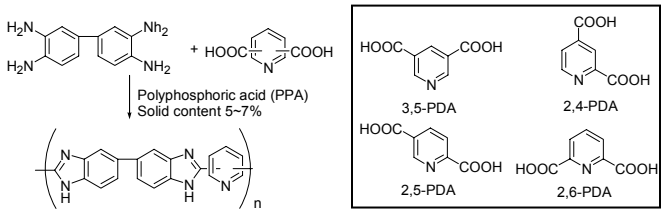

Scheme 1. Synthesis of pyridine-based polybenzimidazoles.

Table 1 summarizes the I.V. and solubility data. After appropriate purification of monomers, three of the four monomers polymerized to give high I.V. PPBIs with properties influenced by the substitution pattern on the pyridine ring as discussed later. The 2,6-PDA monomers did not undergo polycondensation to yield a high polymer, probably due to its limited thermal stability as suggested from the GC-MS spectrum and DSC curves.[5]

Table 1. Inherent Viscosity and Solubility Data of the PPBIs

Polymer	Monomer purity	$\eta_{inh.}$ (dL/g)	Solubility	
			DMAc[a]	Phosphoric acid[b]
2,5-PPBI	As received	0.8		
	Recrystallized	2.5-3.1	S	S (≤ 1%)
3,5-PPBI	As received	0.6		
	Recrystallized	1.3-1.9	S	S (≤ 5%)
2,4-PPBI	As received	0.3		
	Recrystallized	1.0	S	S
2,6-PPBI	As received	0.2		
	Recrystallized	0.6	S	S

[a] Determined by refluxing in dimethylacetamide (DMAc) for 3h.
[b] S: Soluble up to a certain weight percentage.

The solubility of the polymers in dimethylacetamide (DMAc) and phosphoric acid were assessed as shown in Table 1. Overall, the incorporation of the pyridine-group into the polymer backbone increased their solubility relative to the non-pyridine containing PBI. In particular, the meta-oriented 3,5-PPBI showed remarkably high solubility in phosphoric acid of up to 5%, most likely attributable to the strong interaction between the phosphoric acid and the polymer.

When cast from the polymerization mixture, thin films of 2,5-PPBI absorbed moisture from the atmosphere. A sol-gel transition then occurred via the hydrolysis of PPA to phosphoric acid. The subsequent drain-off of the excess phosphoric acid and water increased the solid content and gave rise to strong polymer electrolyte membranes. The acid doping levels of the resulting 2,5-PPBI membranes were approximately 15-25 moles of phosphoric acid per repeat unit of PPBI. The tensile strength and the elongation at break of such 2,5-PPBI membranes varied from 1.0 to 2.5Mpa and from 250% to 300%, respectively, depending upon the different acid doping levels.

In contrast, the 3,5-PPBI showed very different behavior when cast from the PPA polymerization mixture (solid content 5~7%). The 3,5-PPBI polymer retained all the phosphoric acid generated during the PPA hydrolysis process, and liquid drain-off was not observed.

A key feature of a fuel cell membrane is its proton conductivity. As depicted in Figure 1, 2,5-PPBI membranes prepared from the novel PPA process exhibited very high conductivities of around 0.2 S/cm at 160-180^{o}C as a result of the high acid doping level. It also suggests that the incorporation of pyridine groups as an additional nitrogen containing heterocycle increased the basicity of polymer backbone and enhanced the interaction of phosphoric acid and the polymer.

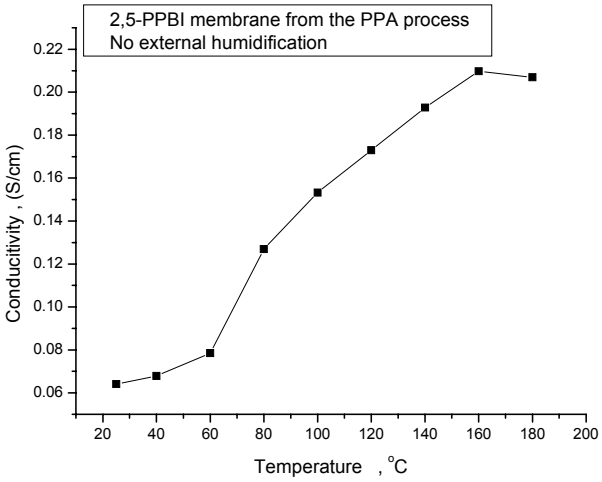

Figure 1. The conductivity of 2,5-PPBI membrane as a function of temperature without external humidification.

Preliminary fuel cell tests illustrated in Figure 2 demonstrate that these membranes prepared from the novel PPA process can be used successfully in high temperature fuel cells operational without any external humidification. As seen from the Figure 2, higher operational temperatures provided better cell performance. The optimization of film composition and the membrane electrode assembly (MEA) fabrication technique is in progress.

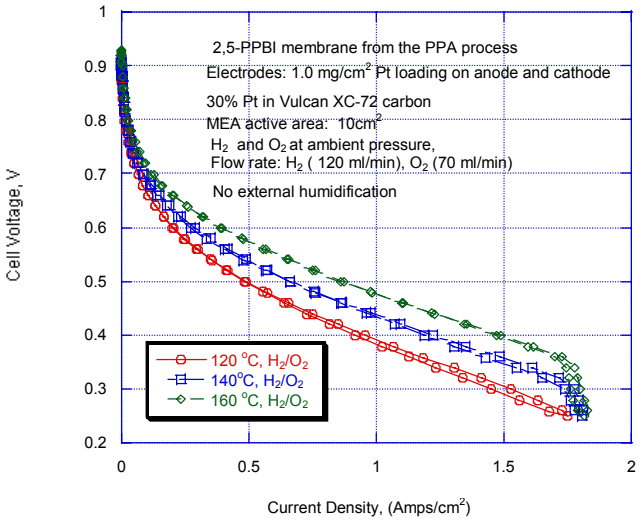

Figure 2. Cell voltage vs. current density curves for a fuel cell based on the 2,5-PPBI membrane from the PPA process.

Conclusion

A series of polybenzimidazoles (PBIs) with additional main chain pyridine groups have been synthesized using polyphosphoric acid (PPA) as both solvent and polycondensation reagent. After appropriate purification of starting materials and optimization of polymerization conditions, three of the four monomers (3,5-, 2,5-, 2,4-pyridine dicarboxylic acids) polymerized to yield high I.V. pyridine-based polybenzimidazoles with properties influenced by the substitution pattern on the pyridine ring. The incorporation of the pyridine group as an additional nitrogen-containing aromatic heterocycle increased the basicity of the polymer and improved the solubility of the polymer in acid while retaining the inherently high thermo-oxidative stability of the polybenzimidazoles.

The PPA process offers a revolutionary method to prepare pyridine-based polybenzimidazole membranes with high acid doping levels, which contribute to their unprecedented high proton conductivities of 0.2 S/cm at 160^{o}C-180^{o}C.

Preliminary fuel cell tests have demonstrated the feasibility of the novel PPBI membranes from the PPA process for operating a fuel cell at temperatures in excess of 120^{o}C without any external humidification or pressure requirements.

Acknowlegements. The authors thank Celanese Ventures, GmbH for financial and technical support. NYSTAR is gratefully acknowledged for partial support in establishing The Fuel Cell Test Laboratory at Rensselaer.

References

[1] Yang C., Costamagna P., Srinivasan, Bemziger J. and Bocarsly A. B., *J. Power Source*, **2001**, 109, 1
[2] Wang J. T., Savinell R. F., Wainright J., Litt M. and Yu H., *Electrochim. Acta*, **1996**, 41(2), 193
[3] Weng D., Wainright J. S., Landau U. and Savinell R. F., *J. Electrochem. Soc.*, **1996**, 143, 1260
[4] Krishnamurthy B., Zhang H., Ramanathan L. S., Xiao L., Scanlon E., Choe E. W. and Benicewicz B. C., 202nd ECS meeting abstract, Salt Lake City, Oct 2002
[5] Xiao L., manuscript in preparation.

POLYPHOSPHAZENE-BASED POLYMER ELECTROLYTE MEMBRANE FUEL CELLS

Serguei. N. Lvov[1], Xiangyang Zhou[1] , Elena Chalkova[1] , Jamie A. Weston[1] , Catherine M. Ambler[2], Andrew E. Maher[2],Richard M. Wood[2] and Harry R. Allcock[2]

[1]The Energy Institute &
Department of Energy and Geo-Environmental Engineering
[2]Department of Chemistry
The Pennsylvania State University
University Park, PA 16802, USA

Introduction

Polymer electrolyte membrane fuel cells (PEMFCs) are efficient electrical power sources. Nafion (DuPont) is the most widely studied polymeric membrane for fuel cell applications due to its good mechanical properties, chemical stability, and high ionic conductivity. However, Nafion is limited to operating temperatures below 100°C due to the tendency of the membrane to dehydrate, resulting in decreased proton conductivity and reduced mechanical stability. The Nafion membranes also suffer from high electro-osmotic drag of water as well as high methanol permeability. To alleviate these problems several approaches have been used to improve Nafion-based MEAs. Polyphosphazene-based proton-conducting membranes are promising materials for use in both H_2/O_2 and direct methanol fuel cells. Polyphosphazenes (POPs) are hybrid inorganic/organic polymers with a –P=N– backbone that is particularly stable to free-radical skeletal cleavage reactions. The chemical and physical properties of polyphosphazenes are highly tunable due to a wide array of side groups, which may be incorporated into these polymers. In this paper we summarize the results of our studies on the newly developed POP-based proton conducting membranes to be used in PEMFCs.

Synthesis

Up to now three kinds of proton conducting poly(aryloxyphosphazenes) have been synthesized and tested in our laboratories. Sulfonated polyphosphazene membranes were fabricated using the methods described by Pintauro and co-authors [1]. Phosphonated polyphosphazene membranes were synthesized as described in detail elsewhere [2]. Synthesis of the sulfonamide functionalized polyphosphazene membranes is described in reference [3]. All cross-linking was achieved through ^{60}Co γ-radiation at the dosage levels up to 40 Mrad. The main characteristics of the polyphosphazene membranes of interest and Nafion 117 (cross-linking radiation dosages, ion exchange capacities (IEC), equilibrium water swelling, and conductivities) are given in Table 1.

Table 1. Polyphosphazene and Nafion membrane properties at ambient conditions (22°C and 1 bar).

Polymer	Radiation (Mrad)	IEC (meq/g[1])	Swelling (%)	Conduc-tivity (S cm^{-1})
Nafion 117	N/A	0.91	30	0.100
Sulfonated POP	20	1.07	38	0.035
Phosphonated POP	40	1.35	14	0.025
Sulfonimide POP	40	0.99	42	0.058

Experimental Systems

Experimental systems for studying the conductivity, methanol permeability, and fuel cell performance of the proton conductive membranes over a wide range of temperatures have been developed in our laboratories.

Proton Conductivity. The proton conductivity of several polymer electrolyte membranes including sulfonated and phosphonated poly[(aryloxy)phosphazenes] was determined at temperatures up to 120°C [4]. Nafion 117 membranes were also tested using the same methods in order to determine the reliability of our approach. The electrical conductivity of protons in water-equilibrated membranes was determined using a four-electrode AC impedance method. The membrane holder was made from Teflon and stainless steel. Two Pt wires are used as reference electrodes for detecting the potential drop along the strip of a membrane. The ends of the membrane strip were pressed against stainless steel sheets that were used as counter electrodes for providing an electrical current along the membrane. The Pt and stainless steel electrical leads were coated with Teflon to ensure good electrical insulation between one another and between electrodes and the body of an autoclave. The entire membrane was immersed in high purity water that was prepared using a Milli-Q gradient system (Millipore Inc.). An electrochemical test station (Gmery Instrument. Inc.) was used to carry out the impedance spectroscopy measurements. It was found that the electrochemical system that we use is close to a pure resistor and the value of the resistance was defined as the average module between 0.01 and 1000 Hz.

Methanol Permeability. Permeability measurements of sulfonated and phosphonated polyphosphazenes membranes at room temperature and pressures were carried out using the method outlined in reference [5]. The measurements at elevated temperatures and pressures were carried out for the same polyphosphazenes using the modified experimental system [4,6], which was specially constructed to be used at high temperatures and pressures. The system consisted of the upper and lower chambers separated by the membrane to be tested. An aqueous methanol solution is pumped into the lower chamber using a high pressure liquid chromatography pump at a particular flow rate to keep the methanol concentration constant. A pressure relief valve was used to keep the pressure constant. It was also found that there was a vigorous convection in the upper chamber because of the temperature gradient and a possible concentration gradient in the bulk of the upper chamber can be minimized. Therefore, the developed design allowed for the pressure on both sides of the membrane to be kept equal and for minimizing the formation of a concentration gradient in the upper chamber.

Methanol passes through a polymer membrane from the lower chamber of the cell to the upper chamber by molecular diffusion. Tests were conducted at temperatures up to 120°C and pressures up to 90 psi. Solution samples were taken by a syringe from the upper chamber once the methanol solution had been pumped through the lower chamber for 3.5 hours. The methanol concentration of the samples was determined by gas chromatography.

Fuel Cell Measurements. A proton conducting sulfonimide polyphosphazene membrane has been used to prepare a membrane electrode assembly (MEA) [7]. The MEA was tested in an H_2/O_2 fuel cell that was obtained from Fuel Cell Technologies, Inc. Hydrogen and oxygen were humidified and pre-heated, if necessary, before entering the fuel cell. Flow rates and pressure of gases were monitored. The voltage-current measurements were carried out using an electronic load (Hewlett Packard Co.) and electrometer (Keithley Instruments, Inc.).

Results of Measurements and Discussion

The results for proton conductivity obtained at elevated temperatures [4] show that the sulfonated and phosphonated polyphosphazenes have significant increases in conductivity with increasing temperature, although these values remained lower than that of Nafion 117 (measured in our laboratory). However, the activation energy values obtained in the present study for the Nafion 117 and the sulfonated and phosphonated polyphosphazene membranes are similar. A difference of only 0.4 kJ/mol was found between the sulfonated derivative and the Nafion 117 sample, while the phosphonated material was about 1.1 kJ/mol less than the Nafion 117 sample. It was found that the conductivity values of the new membranes are not yet ideal, but they are still within a range that holds potential for viable fuel cell applications. Further modifications of these systems are ongoing in order to improve the proton conducting materials and their performance.

The results for the methanol permeability measurements of sulfonated and phosphonated polyphosphazenes at ambient temperatures have shown a significantly lower capacity for methanol cross-over when compared to Nafion 117, leading them to be promising candidates for further DMFC testing [4-6]. At the elevated temperatures explored in this study, it was found that while the gap in methanol cross-over value has been closed significantly for the sulfonated materials, there still remains a large difference between the phosphonated membrane and that of Nafion 117. At 120°C, the sulfonated polyphosphazene membrane exhibits a similar methanol permeability (8.1×10^{-6} cm^2 s^{-1}) to that of Nafion 117 as measured by the present authors, whereas the permeability of the phosphonated polyphosphazene membrane is about nine times lower than that of Nafion 117. This property may permit a more efficient fuel cell operation with the phosphonated polyphosphazene membrane than otherwise expected, because the methanol concentration used in the operating cell can be increased significantly above the level that would be possible in other systems without encountering problems with system poisoning. With respect to the activation energy of the diffusion transport, both the sulfonated and phosphonated polyphosphazene membranes have shown much greater values than that of Nafion 117. The sulfonated derivative was found to have a value of 41.4 kJ/mol and the phosphonated species was 36.8 kJ/mol, whereas Nafion 117 has a value of 22.4 kJ/mol. This difference is thought to indicate that alternative diffusion mechanisms are involved in the transport through the polymeric membranes.

The selectivity of proton conductive membranes was calculated as a ratio of the electrical conductivity and permeability and used to compare the new membranes with Nafion 117. It was found that the sulfonated polyphosphazene is superior (in terms of selectivity) to Nafion 117 at temperatures below 85°C while the phosphonated polyphosphazene is superior to Nafion 117 over a wide temperature range from 22 to 125°C.

Sulfonimide polyphosphazene has been investigated as a proton conducting electrolyte membrane to make an MEA and to test it in a hydrogen/oxygen fuel cell. The membrane of 0.01 cm thickness was cross-linked via gamma radiation of 40 Mrad. The electrodes were prepared by applying an ink, containing Pt on carbon (Vulcan XC-72R), water, and a Nafion solution in a mixture of lower aliphatic alcohols, to ELAT/NC/D5/V2 carbon cloth with 20% wet proofing. The catalyst loading was 0.33 mg/cm^2 for both the anode and the cathode. The sulfonimide polyphosphazene-based MEAs were pressed at elevated temperature and pressure. For the Nafion based MEA, Nafion 117 (E.I. du Pont de Nemours & Co., Inc.) membranes were fabricated using direct ink application to the membrane and the ink composition was the same as for the sulfonimide polyphosphazene based MEAs. The Nafion-based MEAs were pressed at elevated temperature and pressure, too. Uncatalyzed 10% Teflon-bound carbon cloth was used as the gas diffusion backing on both sides of the MEA.

The cell voltage and current density of the fuel cell were measured at temperatures of 22 and 80°C [7]. The voltage-current curve obtained for the Nafion 117 MEA at 80°C was found to be similar to that reported under similar conditions (0.33 mg cm^{-2} catalyst loading for both the anode and cathode; H_2 and O_2 pressures are 3 and 5 bar, respectively; humidification temperature of 95°C for both the anode and cathode) [8]. Results from our Nafion-based MEA tested at 80°C indicate a limiting current density of 1.24 A cm^{-2} and a maximum power density of 0.45 W cm^{-2}. Our data parallels that found in the fuel cell tests conducted by Wilson and Gottesfeld [8] on Nafion 117 MEAs within an H_2/O_2 fuel cell system, which indicated a limiting current density of 1.37 A cm^{-2} and maximum power density of 0.50 W cm^{-2} at 80°C.

The observed limiting current densities of 1.12 A/cm^2 and 1.29 A/cm^2 were found for the sulfonimide polyphosphazene MEA at the ambient and elevated temperatures, respectively. The greatest power for the sulfonimide polyphosphazene MEA at 80°C was 0.47 W cm^{-2} and was achieved when hydrogen and oxygen were humidified at 10°C above the fuel cell temperature, which prevented dehydration of the membrane. On the other hand, the greatest power for the MEA at room temperature was 0.36 W cm^{-2} and was obtained without need of humidification. Thus, the maximum power density for the sulfonimide polyphosphazene-based fuel cell was found to be comparable to our Nafion-based MEA, as well as to the results of Wilson and Gottesfeld [8] for Nafion 117 based fuel cells. However, the tailorability of the sulfonimide polyphosphazene system permits significant flexibility in possible modifications to the side group structure. This should allow for optimization the MEA preparation process and achievement of a higher fuel cell performance.

Acknowledgement. This work was funded by the United States Department of Energy under Contracts DE-PS02-98EE504493 and DE-FC36-01GO11085 and by Los Alamos National Laboratory under Subcontract W7405ENG36.

References

1. Guo, Q.; Pintauro, P. N., Tang, H., O'Connor, S. *J. Membr. Sci.* **1999**, ***154***, 175.
2. Allcock, H. R.; Hofmann, M. A.; Ambler, C. M.; Chalkova, E.; Lvov, S. N.; Zhou, X. Y., Weston, J. A. *J. Membr. Sci* **2002,** *201*, 47.
3. Hofmann, M. A; Ambler, C. M.; Maher, A. E.; Chalkova, E.; Zhou, X. Y. ; Lvov, S. N.; Allcock, H. R *Macromolecules* **2002,** *35*, 6490.
4. Zhou, X. Y.; Weston, J.A.; Chalkova, E., Hofmann, M. A; Ambler, C. M.; Allcock, H. R.; Lvov, S.N. *Electrochmica Acta,* **2002**, in press.
5. Fedkin, M. V.; Zhou, X.Y; Hofmann, M.A.; Chalkova, E.; Weston, J.A.; Allcock, H.R.; Lvov, S.N. *Materials Letters*, **2002**, *52***,** 192.
6. Zhou, X. Y.; Hofmann, M. A; Weston, J.A.; Chalkova, E.; Allcock, H. R.; Lvov, S.N. In *Direct Methanol Fuel Cells*; Narayanan, S., Zawodzinski, T. and Gottesfeld, S., Eds.; The Electrochemical Society Proceedings Series: Pennington, NJ, **2002**, pp. 34-41.
7. Chalkova, E.; Zhou, X. Y., Ambler, C. M.; Hofmann, M. A; Weston, J.A.; Allcock, H. R, Lvov, S. N. *Electrochem. and Solid State Lett.* **2002,** *5*, A221-A222.
8. Wilson, M.S.; Gottesfeld, S. *J. Appl. Electrochem.* **1992**, *22*, 1.

APPLYING A MEMBRANE REACTOR TO HYDROGENATE ACETOPHENONE WITH SIMULTANEOUS PRODUCT SEPARATION

Detlev Fritsch and Gisela Bengtson

GKSS Research Centre, Max-Planck-Strasse 1, D-21502 Geesthacht, Germany

Introduction

The stereoselective hydrogenation of acetophenone yields chiral (R)- or (S)- 1-phenylethanol [1], finding application as fragrance or intermediate in pharmaceutical industry. Besides other catalysts, also palladium was used, complexed to the biopolymer chitosan and immobilised to silica [2]. Chitosan is known as a membrane material for de-watering in pervaporation (PV) [3]. For use in a catalytic membrane reactor, however, a more hydrophobic, organophilic membrane material suited to extract acetophenone and the desired product will be required. Related to our work of hydrodechlorination of chloroaromatics [4], we tested membrane-bound Pd-catalysts successfully for this reaction. The possible products are shown in Figure 1.

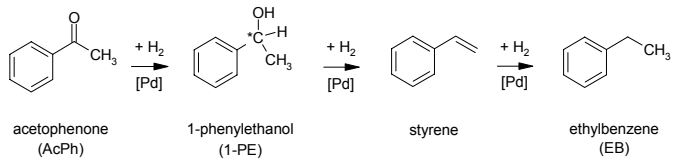

Figure 1. Possible products of the acetophenone hydrogenation

Results and Discussion

We selected the polyether-*b*-amide, PEBA 4033, as an organophilic membrane material. Catalytic active Pd was introduced by a solution-casting-reduction method developed previously [5]. Either direct incorporated Pd nano-clusters of about 10 w% and 3 nm size or newly developed organic/organic/inorganic blend membranes with 2 w% Pd were applied. With these blends of Pebax/polyvinylpyrrolidone/silica the cluster size could be reduced to 1.8 nm and the activity increased notable. At 30°C and 0.1 w% acetophenone in the feed, a conversion of 0.1 mol/g(Pd) * h resulted in the PV mode (see Figure 2, mode B). The membrane material not only serves as catalyst support, but also acts as solid (immobile) extractant able to enrich acetophenone in the membrane by a factor of about 100. Two different process set-ups were tested (see Figure 2). Applying method A, the educts acetophenone and H_2, both dissolved in water, are enriched in the membrane, react at the catalyst, and product leaves the membrane. Method B is the PV mode where educt is extracted into the membrane and product may be detected in the permeate and retentate [4]. Surprisingly, both methods yielded completely different selectivity with the same membrane catalyst. With method A 1-phenylethanol was the main product, besides small amounts of ethylbenzene detected only in the membrane. Method B (PV) generated small amounts of 1-phenylethanol found in the retentate, whereas in the permeate ethylbenzene was detected as the main product. In no case ethylcyclohexane was detected, being the main product of acetophenone hydrogenation by Pd or Pt on carbon catalysts in liquid phase batch processes [6].

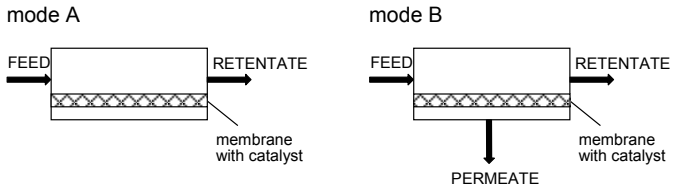

Figure 2. Two modes of membrane catalyst application

Conclusion

In summary, the operation mode of the membrane based Pd-catalyst controls the product selectivity. Also the membrane polarity will contribute to selectivity together with the selected solvent. We will expand our research using stereo-selective, membrane hosted catalysts to generate enantiomeric pure products.

References

[1] S. Wallbaum, J. Martens, Tetrahedron-Asymmetry 3 (1992) 1475-1508.
[2] Mao-Ya Yin, Guo-Li Yuan, Yong-Qiang Wu, Mei-Yu Huang, Ying-Yan Jiang, J. Mol.
Catal. A-Chem. 147 (1999) 93-98.
[3] T. Uragami, K. Takigawa, Polymer 31 (1990) 668-672.
[4] G. Bengtson, H. Scheel, J. Theis, D. Fritsch, Chem. Eng. J. 85 (2002) 303-311.
[5] L. Tröger, H. Hünnefeld, S. Nunes, M. Oehring, D. Fritsch, J. Phys. Chem. B 101 (1997)
1279-1291.
[6] P. Tundo, S. Zinovyev, A. Perosa, J. Catal. 196 (2000) 330-338.

CHARACTERIZATION OF POLYMER NANOCOMPOSITES USED IN RECHARGEABLE SYSTEMS

[1]Giselle Sandí, [3]Riza Kizilel, [3]Humberto Joachin, [1]Kathleen A. Carrado, [1]Sönke Seifert, [2]Luis Smith, and [4]Rex E. Gerald

[1]Chemistry, [2]Materials Science, and [3]Chemical Technology Divisions, Argonne National Laboratory, 9700 South Cass Ave., Argonne, IL 60439
[4]Chemical and Environmental Engineering Department, Illinois Institute of Technology, Chicago, IL 60616

Introduction

Nanocomposite materials of poly(ethylene oxide) (PEO) and phyllosilicates were first suggested by Ruiz-Hitzky and Aranda (1) as candidates for polymer electrolytes. Within these materials, the polymer chains are intercalated between the silicate layers. The polymer chains then provide a mobile matrix in which cations are able to move. A considerable amount of interest has been shown in nanocomposites of PEO and montmorillonite, a layered aluminosilicate clay. When this composite contains $LiBF_4$, it displays conductivities up to 2 orders of magnitude larger than those of PEO itself at ambient temperatures (2). However, the addition of lithium salts, which are needed to obtain such conductivity values, is not desirable for two reasons: a more complicated synthetic route and a transference number for lithium that is not unity.

We have prepared a series of nanocomposites containing PEO intercalated in the layers of hectorite clays. These clays, also called phyllosilicates, belong to the family of smectite clay minerals. They are composed of two tetrahedral silicate layers sandwiching a central octahedral layer in a so-called 2:1 arrangement. In hectorite, isomorphous substitutions in the lattice of Li(I) for Mg (II) in the octahedral layers cause an overall negative charge that is compensated by the presence of interlayer, or gallery, cations. A significant amount of interlayer water is also present and the cations are easily exchangeable. A large degree of preferential orientation in films prepared by natural occurring clays tends to occur, however, due to their large platelet size (up to 1 μm). This can lead to non-conducting planes being perpendicular to the current path and thus reduce the conductivity. To avoid this problem, we followed a method developed by Carrado et al. (3) which involves direct hydrothermal synthesis and crystallization of hectorite with smaller platelet size, termed synthetic lithium hectorite (SLH). Organic molecules can be either incorporated directly from the gel or by subsequent intercalation.

Experimental

Clay Preparation. Precursor clay gels are of the composition: 1.32 LiF, 5.3 Mg(OH)2, 8 SiO2, n H2O, to correlate with the ideal hectorite composition of $Li_{0.66}[Li_{0.66}Mg_{5.34}Si_8O_{20}(OH,F)_4]$. A typical reaction begins by suspending the LiF with stirring in water. Separately, $MgCl_{2.6}H_2O$ is dissolved in water and mixed with 2 N NH_4OH to crystallize fresh $Mg(OH)_2$. Prior to use, this brucite source must be washed several times with water to remove excess ions. It is then added wet to the LiF solution. This slurry is stirred for 15-30 min before addition of silica sol (ludox HS-30, Na^+-stabilized, 30%). The total volume is increased to afford a 2 wt% solids suspension, and is stirred and refluxed for 40-48 hours. Solids are isolated by centrifugation, washed, and air-dried.

Film Preparation. Colloidal suspensions of 1 g SLH/100 ml deionized water were stirred for one-half hour. The desired amount of PEO (100,000 average molecular weight, Aldrich) was then added, and the mixture stirred for 24 hours. Mixtures contained 0.6, 0.8, 1.0, and 1.2 g of PEO/g of clay. Films were prepared by casting the slurries onto Teflon-coated glass plates and partially air-drying them. Further drying was carried out at 397 K under an inert atmosphere for 48 hours. The typical thickness of the films was about 40 μm.

Characterization Methods. X-ray powder diffraction (XRD) patterns of SLH and PEO powders were determined using a Rigaku Miniflex, with Cu Kα radiation and a NaI detector at a scan rate of 0.5° 2Θ/min and step size of 0.05.

In situ small angle x-ray scattering (SAXS) was carried out at the Advanced Photon Source, (Basic Energy Sciences Synchrotron Research Center CAT), Argonne National Laboratory. The SAXS intensity of the investigated material I(q) is the function of the angle of scattering (2θ) and the wavelength (λ) of the applied radiation. This relation can be expressed as $q = 4\pi \sin\theta/\lambda$. Monochromatic X-rays (18 keV) are scattered off the sample and collected on a 15 x 15 cm2 CCD camera. The scattered intensity is corrected for absorption and instrument background. The instrument was operated with a sample-to-detector distance of 332 mm to obtain data at $0.1 < q < 3.0$ $Å^{-1}$. For these studies, a specially designed sample holder was used to heat the sample and collect SAXS data at the same time. **Figure 1** shows a diagram of the sample holder. Films of about 1.25 cm in diameter and 40 μm in thickness were placed in the sample holder and held using kapton tape. The furnace temperature program was set to ramp from room temperature to 150 °C at 5 °C/min, and the gas flow of nitrogen was started at room temperature. SAXS data were collected at room temperature, 60, 80, 100, 120, and 150 °C in order to compare the structural results with the conductivity values.

AC impedance measurements as a function of temperature were obtained on films in sealed cells with lithium foil as the counter and working electrode, using a Solartron SI 1256 electrochemical interface and 1254 frequency response analyzer. A Tenney Junior Environmental Test Chamber was used to control the temperature of the cell with a precision of ± 0.5 °C.

Wideline ^7Li NMR experiments were recorded at six temperatures in the range 220-360 K on a Bruker AVANCE 360 MHz spectrometer using a B_1 field that delivered a 90°pulse of 7.7 μs. Magic angle spinning (MAS) ^7Li NMR experiments were recorded at room temperature on a Varian INOVA 300 MHz spectrometer using a 90°pulse of 2.5 μs, and a rotor.

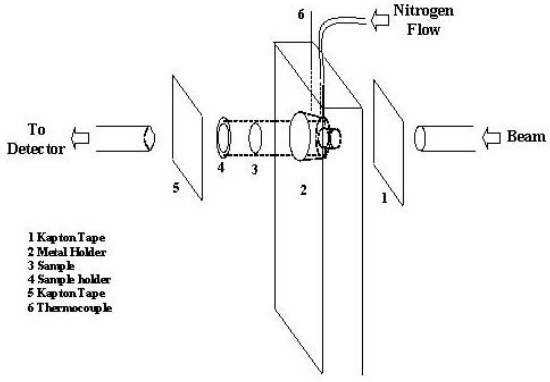

Figure 1. Schematic diagram of the sample holder used for in situ SAXS studies.

Results and Discussion

Understanding the structural changes of the PEO component in the nanocomposite films upon heating is crucial for predicting the conductivity of these materials. *In situ* SAXS is an excellent

technique for deriving such information because of this particular instrument's time-resolving capability and its high flux.

Figure 2 shows SAXS data obtained from a film made of PEO/SLH 1.2:1 mass ratio. The data was collected at room temperature. This figure was chosen because it shows clearly the peaks that correspond to SLH and PEO. The d001 peak is broader than that presented in the XRD plots because it is plotted here as Q in $Å^{-1}$, but the spacing differs only by 0.42 Å. SAXS data was then collected at 60°C and the results are shown in **Figure 3**. It is clear that the structure of the polymer has changed as indicated by the near complete disappearance of the PEO crystalline peaks. It is therefore assumed that the polymer chains have relaxed inside the clay layers. Other evidence of such relaxation is the decrease in d001 spacing, which indicates a more dense polymer phase. Under these circumstances, the polymer matrix is more mobile and the lithium ions associated with the polymer can have higher transference number, leading to a higher conductivity as found by Sandí et al. (4). The samples were also heated at 80, 100, 120, and 150 °C. Except for complete disappearance of the PEO peaks at 80 °C, there are no other polymer structural changes.

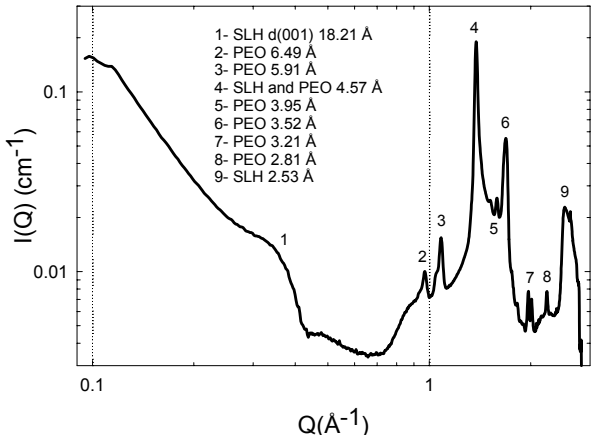

Figure 2. In situ SAXS of a PEO/SLH 1.2:1 mass ratio film taken at room temperature. The inset shows the diffraction peaks attributed to PEO and SLH.

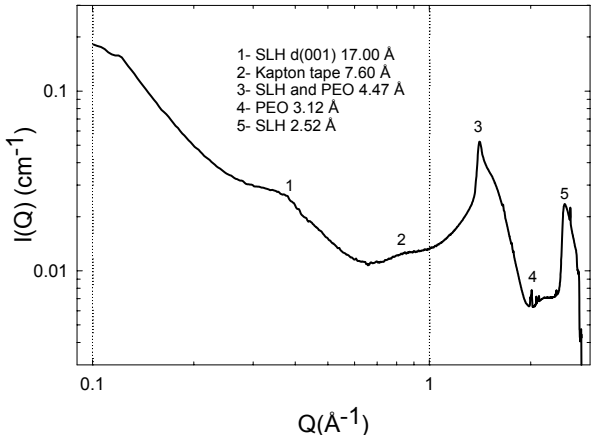

Figure 3. In situ SAXS of a PEO/SLH 1.2:1 mass ratio film taken at 60 °C. The sharp peaks from PEO have broadened, indicating that the PEO has lost its crystallinity. The sample was heated under nitrogen at 5°C/min.

Wideline ^{7}Li NMR spectra of PEO/SLH nanocomposite films revealed a single peak over the temperature range studied. The spectrum at each temperature was decomposed into a sum of two line functions, a narrow Lorentzian and a broad Gaussian. **Figure 4** (top) shows plots of the linewidths of both line functions vs. temperature for three film compositions. **Figure 4** (bottom) maps the integrated Lorentzian component of the spectrum vs. temperature. A ^{7}Li MAS spectrum (**Figure 4**, inset) shows an intense and narrow (<1 kHz) centerline, and a weak, broad manifold of spinning side bands (>80 kHz). These data are consistent with two lithium ion environments in PEO/SLH nanocomposite films. The Lorentzian spectral component is consistent with mobile lithium ions, and become narrower as the temperature of the nanocomposite is increased. In addition, the fraction of the spectral intensity due to the Lorentzian component changed with temperature, increasing to a maximum value of 55-60%, consistent with the stoichiometry of SLH. The Gaussian spectral contribution indicates a large static quadrupolar coupling (>80 kHz), consistent with the static lithium ions locked in the silicate layers.

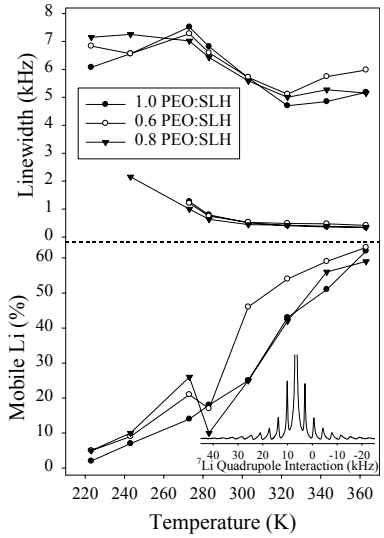

Figure 4. Linewidths of the Lorentzian and Gaussian functions that comprise the ^{7}Li NMR spectrum recorded at different temperatures (top). Percent of spectral intensity from the integrated Lorentzian line function, which is attributed to the fraction of lithium that is mobile (bottom). ^{7}Li MAS spectrum at 273 K (inset).

Based on the NMR results, significant ionic conduction and a high Li transference number can be expected at temperatures above 330 K.

Acknowledgment

This work was performed under the auspices of the U.S. Department of Energy, Office of Basic Energy Sciences, Division of Chemical Sciences, Geosciences, and Biosciences under contract number W-31-109-ENG-38.

References

1. Ruiz-Hitzky, E., Aranda, P. *Adv. Mater*., **1990**, *2*, 545.
2. Wong, S., Vaia, R. A., Giannelis, E. P., Zax, D. B., *Solid State Ionics*, **1996**, *86-88*, 547.
3. (a) Carrado, K. A.; Winans, R. E.; Botto, R. E. US Patent 5,308,808. (b) Carrado, K. A. *Appl. Clay Sci*., **2000**, *17*, 1.
4. Sandí, G.; Carrado, K. A.; Joachin, H.; Lu, W.; Prakash, J. *J. Power Sources*, **2002**. In press

EVALUATION OF FERRITES FOR THE MEMBRANE APPLICATIONS

X.-D. Zhou [1] Zili Chu [2], J. Yang[1], W. B. Yellon[2], W. J. James[1] and H. U. Anderson [1]

1: Materials Research Center, University of Missouri-Rolla, Rolla, MO 65401
2: Department of Physics, University of Missouri-Columbia, Columbia, MO 65211

Introduction

The perovskite-type oxides encompass a large variety of chemical compositions that contribute to their diverse and unique properties. It is the intent of this presentation to study the structural, electric and magnetic properties of ferrites with an emphasis on the compounds of $La_{0.60}Sr_{0.40}FeO_{3-\delta}$, which are particularly interesting in oxygen membrane and the intermediate temperature solid oxide fuel cells. Initial studies on ferrite materials have showed that the structure plays an important role in electrical and catalytic properties and that the electrical, catalytic and magnetic properties have an inter-relationship that is commonly related to the electronic structure and oxygen vacancy concentration. Therefore, it is critical to study the ferrite materials from the atomic structure point of view, for example the hybridization of transitional metal and oxygen orbitals that plays a dominant role in the properties such as the generation of oxygen vacancies, holes, and spin state of the transitional metals. This interrelationship is shown in the (La, Sr)(Fe, Co)$O_{3-\delta}$ system. For 20% Co compound, electrons (holes) move indirectly between Co ions via an O ion rather than directly between Co ions, i.e., the fluctuation of the charges of O ions as well as Co ion causes electrons (holes) to move with a complicated interaction between the generated holes and electrons [1]. The effects of Fe doping in $La_{0.67}Sr_{0.33}CoO_3$ showed that no apparent structure change was introduced by Fe doping up to x=0.3, but the Curie temperature T_c, magnetization M and electrical resistivity are lowered by Fe substitution [2]. A smaller localization length and a more severe disorder in the lattice due to Fe doping were observed. Previous research showed that two transitional metals, Fe and Co, at B site of ABO_3 allowed a better performance compared to only Co or Fe located at B site. For example, cobaltites exhibit a significant weight loss when the annealing temperature is higher 1000ºC (in some case 800ºC) and a higher resistivity and oxygen diffusivity were observed in ferrites.

Experimental

The Pechini method [3, 4] was used to synthesize nanocrystalline particles[2], in this process a polymeric solution was formed due to a chelating reaction between cations and chelants. The polymeric solutions were also used as the thin film sources, which were used to fabricate thin films by spin coating and thermal processing. Electrical conductivity was measured by four-probe method at the temperature from 150 – 1000ºC in a wide range of oxygen activities (10^{-25} to 1). Thermogravimetric analysis was conducted at 1000 and 1200ºC in O_2, air and Ar. Mössbauer spectroscopy and neutron diffraction were performed at room temperature on the sintered and quenched specimens. During the quenching experiments, the specimens were first heated at 1000°C with a flowing gas atmosphere of N_2, air, or CO/CO_2 mixtures for 24 hours, and then quenched to room temperature. For Neutron Diffraction (ND) studies, samples were contained in 3 mm V metal cells and data were collected at 1.4785 Å over a range of 5º-105º (2θ). Rietveld refinement was carried out using the FULLPROF code, in which the magnetic ordering was taken into account because of the sensitivity of neutron diffraction to the magnetic ordering of the Fe atoms.

Results and Discussion

Figure 1 shows powder Neutron Diffraction Patterns of $La_{0.60}Sr_{0.40}FeO_{3-\delta}$ quenched at various gas environments. The powder Neutron Diffraction results showed that all specimens were single phase with an exception of the sample quenched with 90%CO/10%CO_2, in which peak broadening and asymmetry took place that indicated a decomposition of the sample. Four models [5] were used to fit the data for each sample and all results seemed reasonable. However, there did exist different preferred models for the reduced samples than for the air- and N_2- quenched samples and the neutron diffraction patterns for the samples quenched from the reducing atmosphere are significantly different with those quenched from air or N_2. The diffraction peak splitting for the reduced samples is dramatically reduced compared to the N_2- and air- treated samples. The first diffraction peak (~ 19°) is much stronger in the reduced samples than in the air- or N_2- quenched samples. This peak proves to be purely magnetic and the change reflects a large increase in magnetic moment for the reduced samples vis-à-vis the air- and N_2-quenched samples [5].

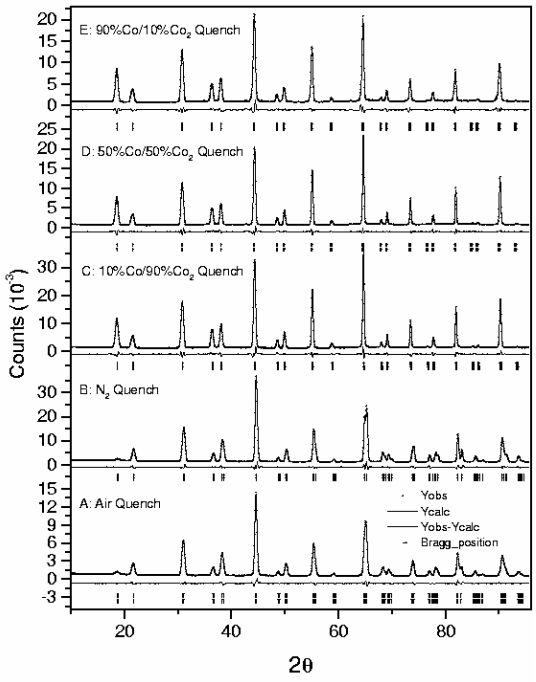

Figure 1. Powder Neutron Diffraction patterns of $La_{0.60}Sr_{0.40}FeO_{3-\delta}$ quenched at various gas environments.

Further study was then performed on the electrical conductivity of $La_{0.60}Sr_{0.40}FeO_3$ at the low pO_2, in which oxygen vacancy concentrations were increased. Figure 3 shows the plot of $\log(\sigma)$ vs. $\log(pO_2)$ at 1000ºC with a control over the oxygen activity being made by using a mixture of CO/CO_2, from which the pO_2 can be determined thermodynamically. In figure 3, a transition from p-type to n-type of conductor is obvious at relative low pO_2, at which the majority carriers changed from the holes to electrons because of the valence state decreases in Fe due to the further loss of oxygen. The

oxygen vacancies are generated at high temperature due to loss of oxygen, which results in a higher oxygen vacancy concentration and a lower hole concentration.

In addition to the conductivity, oxygen vacancy concentration also plays a key role in the function of cathodes, in particular in the catalytic properties. Determination of the oxygen vacancy level has been performed by thermogravimetric analysis (TGA) and neutron diffraction. TGA simply measures the weight changes with the variable being time, gas environment and temperatures. Neutron diffraction was performed on the samples which were quenched at 1000ºC from different oxygen activities. A large decrease in 3-δ was observed when the was gas changed from 90%CO to 99%CO. XRD results showed that $La_{0.60}Sr_{0.40}FeO_3$ decomposed in the 99% CO atmosphere. The consistence results between TGA and neutron diffraction confirmed that the quenching experiment could be used to study the ferrites under reducing conditions.

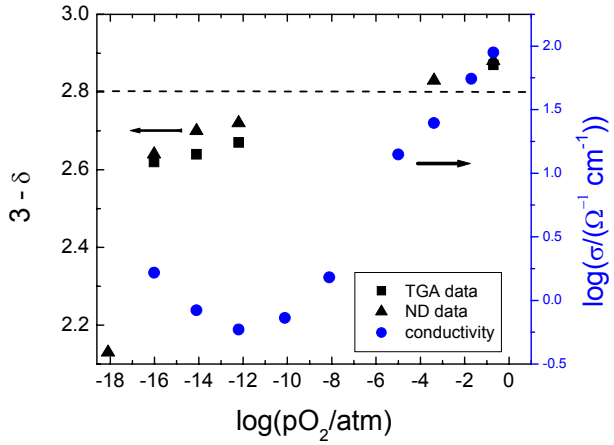

Figure 2. Log(σ) and 3-δ as a function of log(pO_2) for $La_{0.60}Sr_{0.40}FeO_{3-\delta}$.

Figure 3 shows Nèel Temperature and Fe-O-Fe angles as a function of pO_2, at which the specimen was quenched. The bonding angles of Fe-O-Fe were increased with decreasing oxygen partial pressures. Because the bonding lengths were nearly constant, the increasing of the bonding angle increases the overlap between Fe and O atomic states that results in an increase in the superexchange interaction between Fe and Fe. The Fe-Fe super-exchange interaction is highly dependent on the Fe-O-Fe bond angle and the superexchange through the oxygen atoms that is more effective when the Fe-O-Fe paths are close to linear [6]. It is also found that the increase in the superexchange interaction results in an increase in Nèel temperature, as shown in Figure 3. The Fe moments for the three reduced samples refine between 3.72 and 3.82 μ_B while the moments for the other two samples are much smaller (1.4 μ_B and 1.2 μ_B for the air- and N_2- quenched samples, respectively) [5].

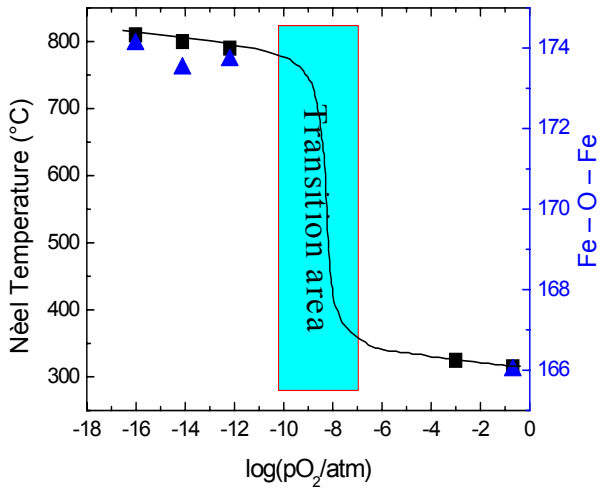

Figure 3. Nèel temperature and Fe – O – Fe angle of the specimens quenched at various oxygen partial pressures (pO_2).

Acknowledgement. The support by DOE under contract UAF99 – 0038 is highly appreciated.

References

(1) Takahashi, H.; Munakata, F.; and Yamanaka, M. *Phys. Rev. B.* **1998**, *57,* 15211.
(2) Sun, Y.; Xu, X.; Zhang, Y. *Phys. Rev. B.* **2000**, *62*, 5289.
(3) Pechini, M., U.S. Pat., No. 3,330,697, **1967**
(4) Anderson, H. U., Chen, C.-C., and Nasrallah, M. N., U.S. Pat., No. 5,494,700, **1996**.
(5) Chu, Zili, University of Missouri-Columbia, Dissertation, **2002.**
(6) J. B. Goodenough, Magnetism and Chemical Bond, Edited by F. A. Cotton (Interscience Publishers, London, 1976) Vol. 1, p. 170

Effect of water adsorption on MFI-type zeolite membrane prepared by *in situ* hydrothermal crystallization

Masahiko Matsukata, Tomoyuki Nara*, Eiichi Kikuchi**
*Sylvain Miachon**, and Jean-Alain Dalmon***

*Department of Applied Chemistry
Waseda University
3-4-1 Okubo
Shinjyuku-ku
Tokyo, 169-8555

**Insititut de Recherches sur la Catalyse
CNRS
2 Avenue Albert Einstein
69626 Villeurbanne Cedex
France

Introduction

Zeolite membranes have recently attracted considerable attention because they allow us to perform difficult liquid and/or gas separations. MFI-type zeolite membrane has extensively been studied. *In situ* crystallization is the most common method for synthesis of supported MFI type zeolite membranes.

In this study, we synthesized MFI zeolite membranes on porous α-alumina support tubes by in situ hydrothermal synthesis. In this method it is likely that alumina was dissolved into a synthesis gel from α-alumina support tubes during crystallization. Hence, the permeation properties of membranes synthesized by this method would be greatly affected by water adsorption. In order to investigate the effect of water adsorption on the permeation properties of MFI-type membranes, permeation tests were carried out using the membranes dried at room temperature after soaking them in deionized water.

Experimental

Membrane preparation. MFI-type zeolite were crystallized on porous α-alumina support tubes by in situ hydrothermal synthesis. The permeation zone was approximately 3 cm long. A gel was prepared with the following molar composition: 1 SiO_2:0.45 TPAOH (tetrapropylammonium hydroxide):22.7 H_2O[1]. After being stirred for 72 h, the gel was centrifuged for the purpose of removing the impurities. The support was put into the gel and crystallization was carried out at 170°C for 72 h. TPA cation contained in the membrane was removed by the calcination in air at 500°C for 5 h.

Characterization. The structure of products was analyzed by X-ray diffraction (XRD) with Cu K_α radiation.

Permeation tests.

The permeation test of mixed gas of H_2/n-C_4H_{10} was carried out in the temperature range of 30-300°C with the membranes which were dried at room temperature after soaking them in ion-exchanged water. The permeances were measured during heating and cooling.

In order to investigate the influence of water adsorption in the zeolite membranes on permeation properties, single gas permeation tests using H_2 were carried out in the temperature range of 30-300°C using a membrane dried at room temperature after soaking it in deionized water. The permeation test was started at 303 K after the water treatment of membrane. The temperature was raised up to 673 K and then fell to 303 K. The permeances were measured after the permeation reached a steady-state at each temperature. Two kinds of gas were used as feed gas: one was H_2 gas containing 500 ppb water stream and another was H_2 gas stream dried with a liquid nitrogen trap.

The permeate through the membrane in the single gas permeation test for H_2 at 100°C was analyzed for water by using Q-mass. The membrane was heated from 30 to 100°C with a rate of 6°C min^{-1} and held at this temperature. To prevent the pump of Q-mass from drawing air from the outlet of the apparatus, He gas was fed into the permeate side.

Results and Discussion

Figure 1 shows the XRD pattern for the MFI membrane synthesized. From the XRD pattern observed, MFI zeolite crystals were nicely grown on the support tube. **Figure 2** shows the gas permeation results of a 50:50 H_2/n-C_4H_{10} mixture. Separation factor

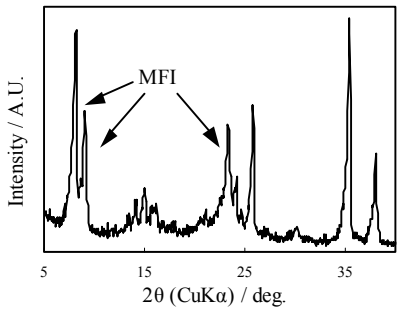

Figure 1. XRD pattern for MFI zeolite membrane.

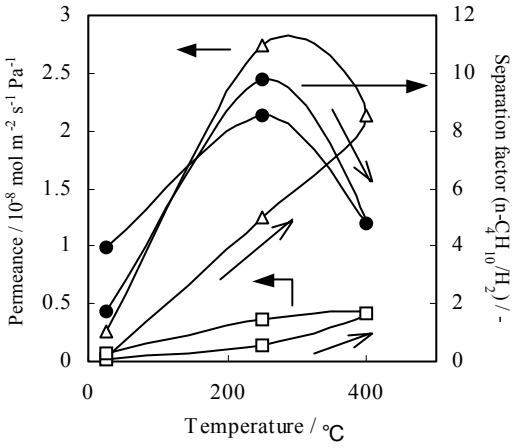

Figure 2. Mixed gas (n-C_4H_{10}/H_2) permeation results using the membrane treated with water. ●:separation factor (n-C_4H_{10}/H_2), △:n-C_4H_{10} permeance, □:H_2 permeance

(n-C_4H_{10}/H_2) was around 10 at 250°C during heating, supporting that the concentration of the defects (or pinholes) in the membrane is low. The separation factor of n-C_4H_{10}/H_2 measured during cooking was less than that observed during cooling. Based on this result, we suppose that the observed difference in the permeances during heating and cooling was due to the desorption of water adsorbed in the membrane.

The results of the single gas permeation of H_2 through the membrane treated with water are shown in **Figure 3.** The solid curve represents the results of single gas permeation tests using a dried H_2 gas stream, and the broken one represents the results of those using H_2 gas containing 500 ppb water stream. It should be noted that the

results of the tests using a dried H_2 gas stream and those using dried H_2 gas stream were different from each other. Even a small amount of water (ca. 500 ppb) influenced the permeation properties of the membrane. In these two cases, the permeances measured during cooling were higher than those during heating. It might be attributed to the removal of water adsorbed in the micropore of zeolite during heating up to 300°C.

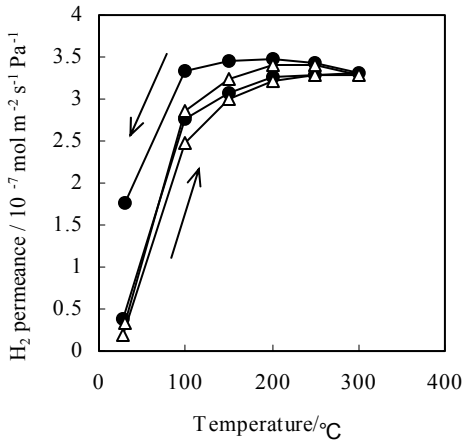

Figure 3. Single gas permeation tests for H_2 using the membrane treated with water. △:H_2 gas containing 500 ppb water stream, ●:Dried H_2 gas stream.

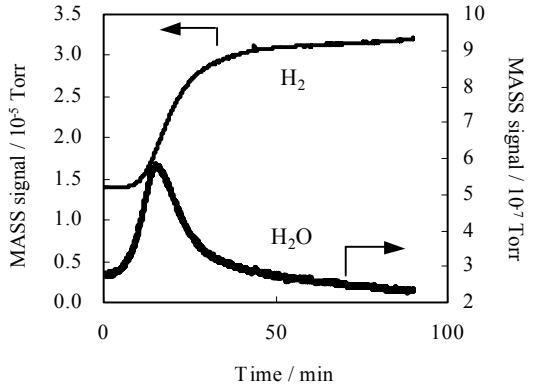

Figure 4. Composition of the permeate in the H_2 permeation test at 100°C. The membrane was heated up to 100°C after the water adsorption.

In order to confirm this assumption, the composition of the permeate side during the H_2 permeation at 100°C was analyzed by Q-mass. **Figure 4** shows the results. The signal intensity of H_2 started to increase at around 15 min while that of H_2O did earlier, at around 7 min. Water was strongly adsorbed in the membrane and blocked the permeation of H_2. Such adsorbed water was partially released to the permeate side, leading to the increase in the permeance of H_2.

From the results obtained in this study, it was suggested that the desorption of water was attributed to the lager permeances measured during cooling as compared with those obtained during heating.

Concluding remarks

The permeation properties of a MFI-type zeolite membrane were influenced by the water adsorbed in the membrane. Even 500 ppb water stream influence the single gas permeation properties of the membrane. These properties of the membranes might be caused by strong hydrophilicity of highly aluminated MFI-type zeolite formed in the *in situ* crystallization method.

References

1. J. Ramsey, A. Giroir-Fendler, A. Julbe, J.-A. Dalmon, French Patent 9,405,562 (1994).

TUBULAR TYPE PERVAPORATION MODULE WITH SILICALITE MEMBRANES FOR DEHYDRATION OF BIOMASS ALCOHOL

Hidetoshi Kita,[1] Xiangshu Chen,[1] Xiao Lin,[1] Ken-ichi Okamoto,[1] Tadahumi Yamamura,[2] and Jun Abe,[2]

[1]Department of Advanced Materials Science and Engineering, Yamaguchi University, Tokiwadai , Ube 755-8611, Japan
[2]Department of Industrial Machinery Design, Mitsui Engineering and Shipbuilding Co. Ltd., Tamano 706-8651, Japan

Introduction

Pervaporation has gained widespread acceptance as an effective process for separation of azeotropic mixtures. [1] It has been applied to the dehydration of organic liquids and many fundamental works have been carried out using polymeric membranes. However, membranes that have both high selectivity and high flux are not commonly available. Furthermore, polymeric membranes have been limited to applying dehydration of solvents due to insufficiency of their thermal, mechanical and chemical stability. The recent development of zeolite membranes has made it possible to overcome the above limitations. Zeolite A membranes have been successfully applied to remove water from aqueous solutions on a large scale.[2] In contrast, silicalite membranes exhibited preferential organic compound permeation from water such as ethanol/water mixtures because silicalite zeolite not only has strong hydrophobic property but also preferentially adsorbs organic compounds.[3] Recently we have reported high-performance silicalite membranes on porous tubular supports could be prepared by a single hydrothermal treatment.[4] Here, the tubular pervaporation module with silicalite membranes is investigated in order to develop more energy efficient concentration of the biomass ethanol.

Experimental

A clear solution for synthesis of silicalite membranes was prepared by mixing and stirring tetraethylorthosilicate (TEOS), tetra-n-propylammonium hydroxide (TPAOH), and water at room temperature for 1 hour. The resultant molar composition is 1:0.17:120 (SiO_2: TPAOH: H_2O). A mullite tubular support with 50 cm in length and a pore size of 1 μm was vertically immersed in the solution. Crystallization was carried out at 185 °C for 40 hours. After crystallization, the sample was taken out, washed carefully with hot distilled water, dried at 100 °C for several hours, and then calcined at 400 °C for 40 hours with heating rate of 1 °C/min.

Pervaporation experiments were carried out using the apparatus described elsewhere.[4] The zeolite membranes were characterized by X-ray diffraction and electron probe microanalysis (EPMA). The surface morphology of zeolite membranes was examined by scanning electron microscopy (SEM).

Results and Discussion

Silicalite membranes were prepared by a single hydrothermal treatment on porous tubular supports. Silicalite crystals slowly grew onto the unseeded supports leading to formation of an incompact crystal layer as shown in Figure 1. On the other hand, the higher crystallization temperature (185ºC), the faster crystal growth rate is the favorable condition for preparation of silicalite membranes with high pervaporation performance for separation of ethanol from aqueous solutions. EPMA characterization indicates the Si content in depth of 1 μm from the top crystal layer was 100 at. % without detection of Al. The Al content in the crystal layer was also negligible levels. The EPMA result confirms that the high siliceous MFI membrane was obtained on the mullite tube.

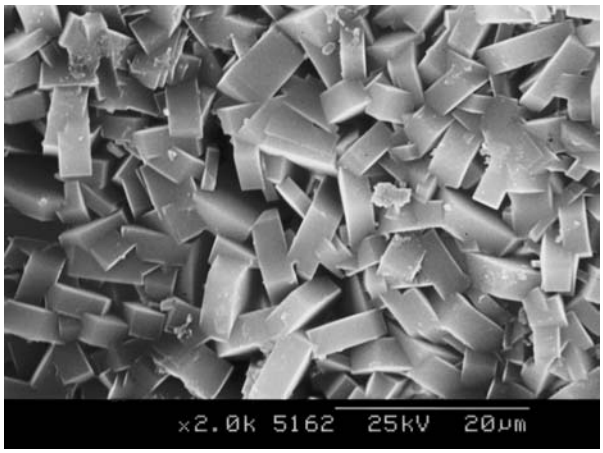

Figure 1. SEM photo of the surface of silicalite membrane prepared at 175ºC for 30h.

The pervaporation results for the silicalite membranes synthesized under typical conditions are listed in Table 1, which clearly shows that our silicalite membranes exhibit high flux and high separation factor. The tubular type module with 50 cm membrane was composed of 7 silicalite membranes. Membranes sealed one end of a support tube is inserted alternatively. Thus, pervaporation using zeolite membranes may have an opportunity for making a significant contribution to more energy efficient production of the ethanol from biomass.

Table 1. Pervaporation Performance of Silicalite Membranes at 60ºC

Synthesis condition		System(A /B)	Flux	$\alpha_{A/B}$
Temp [ºC]	Time [h]	[A 5wt%]	[kg/m^{2}h]	-
175	30	EtOH / H_2O	1.23	46
185	20		1.25	79
185	24		1.24	82
185	40		1.25	96
185	40	Acetone / H_2O	1.43	460
185	40	MEK / H_2O	0.36	1000

Acknowledgement. This research was partly supported by the MAFF project of Bioenergy Conversion in Japan.

References

1. Huang, R. Y. M., Ed., *Pervaporation Membrane Separation Processes*, Elsevier, Amsterdam, 1991.
2. Morigami, Y.; Kondo, M.; Abe, J.; Kita, H.; Okamoto, K., *Separation Purification Tech*. **2001**, *25*, 251.
3. Sano, T.; Yanagishita, H.; Kiyozumi, Y.; Mizukami, F.; Haraya, K. *J. Membr. Sci.* **1994**, *95*, 221.
4. Lin, X.; Kita, H.; Okamoto, K. *Ind. Eng. Chem. Res.* **2001**, *40*, 4069.

Driving Force for Pervaporation through Zeolite Membranes

Travis C. Bowen, Shiguang Li, Richard D. Noble*, and John L. Falconer

Department of Chemical Engineering, University of Colorado, Boulder, CO 80309-0424

Introduction

Zeolites are crystalline structures made mostly of SiO_2 with uniform, molecular-sized pores. Zeolite membranes can separate mixtures by molecular sieving, selective adsorption, and/or diffusion differences. Hydrophobicity or hydrophilicity of the zeolite is important for selective adsorption in organic/water separations. Isomorphous substitution of silicon by other elements in the zeolite framework has been shown to change the relative hydrophobicity/hydrophilicity of the membrane. Germanium substituted ZSM-5 zeolite membranes were more hydrophobic than silicalite-1 membranes prepared by a similar procedure. Although only small changes in the unit cell parameters and lattice vibration frequencies were observed when Ge was substituted for Si in MFI zeolite powders, the adsorption properties could change with substitution due to the changes in the T-O-T bond angle and T-O bond length [1].

Experimental

A Ge-ZSM-5 (Si/Ge = 41) zeolite membrane was synthesized by in-situ crystallization on the inner surface of a porous stainless steel tube. Characterization by XRD and SEM showed that the membrane had an approximately 30-μm thick layer of intergrown crystals with the ZSM-5 structure (~0.53-nm XRD pore size). The membrane had a n-C_4H_{10}/i-C_4H_{10} ideal selectivity of 2.1 at 473 K and a 0.2 g/m^2·h 1,3,5-tri-isopropyl benzene (0.85-nm kinetic diameter) flux at 303 K, indicating that it had few non-zeolite pores larger than 0.85 nm.

Results and Discussion

This membrane removed organics from 5 wt% organic/water mixtures by pervaporation. The organics included acetic acid, propionic acid, methanol, ethanol, 1-propanol, 2-propanol, 1-butanol, acetone, methyl ethyl ketone (MEK), methyl acetate, ethyl acetate, propionaldehyde, and diethyl ether, which were all smaller than the zeolite pore size. These organics exhibited more than a 500-fold range of fugacities and, in general, the organic/water separation factors increased with organic feed fugacity at 303 (Fig. 1), 313, 323, and 333 K. At 303 K, ethanol had an organic/water separation factor of 47, a 0.22 kg/m^2·h total flux, and a 1.30 kPa fugacity. The lowest separation factor was 2.7 for acetic acid, which had a fugacity of 0.12 kPa at 303 K and its total flux was 0.075 kg/m^2·h. The highest separation factor was 1200 for diethyl ether at 333 K. This mixture had a 147 kPa fugacity and its total flux was 1.23 kg/m^2·h. The organic fluxes exhibited a similar dependence on organic fugacity and also decreased with increasing organic heats of adsorption, in general. The water fluxes did not correlate with feed fugacities, but instead generally decreased with increasing organic sizes. Although low organic concentrations were present, water fluxes were significantly lower than the pure water fluxes of 0.22 and 0.66 kg/m^2·h for 303 and 333 K, respectively, indicating that the organics preferentially adsorbed on the zeolite and inhibited water adsorption and transport. Therefore, the separation occurred mainly by selective adsorption.

Fugacity ratios predicted a selectivity inversion for 1-butanol/acetic acid separations from 1-butanol/acetic acid/water mixtures. Three concentrations of equal molar ratios of 1-butanol and acetic acid in water were used. For increasing organic concentration, the 1-butanol/acetic acid separation factor decreased and became less than one. This was the same trend exhibited by the 1-butanol/acetic acid fugacity ratios.

Pervaporation separation factors for the binary and ternary mixtures separations were divided into a membrane contribution (α_{mem}) and an evaporation contribution (α_{evap}):

$$\alpha = \alpha_{evap} \cdot \alpha_{mem} \tag{1}$$

where

$$\alpha_{evap} = \frac{\hat{f}_a / \hat{f}_b}{x_a / x_b} \tag{2}$$

which is an equilibrium separation factor. Membrane quality was investigated and different membranes were compared using this evaluation. As temperatures increased, α_{mem} increased for most of the mixtures and the separation factors were higher than α_{evap} for all of the mixtures at 333 K. This indicates that the membrane selectivity was higher than what could be obtained by ordinary distillation.

Separation factors for hydrophobic and hydrophilic zeolite membranes reported in the literature also correlated with feed fugacities. Separation factors for the hydrophobic membranes increased as the organic/water feed fugacity ratio increased, but separation factors for the hydrophilic membrane increased as the water/organic feed fugacity ratio increased.

The driving force for transport through zeolite membranes is the coverage gradient across the zeolite layer. For pure liquid feeds, the fugacity is usually sufficiently high that the adsorption sites are saturated and intracrystalline flow is not dependent on the feed fugacity [2]. However, in mixtures, molecules compete for adsorption sites and a higher fugacity probably correlates with a higher competitive adsorption coverage at the feed-membrane interface. Using the relationship of selectivity and fugacity, measurements of pervaporation separations for a few mixtures in a given zeolite membrane should allow qualitative prediction of other mixture separations.

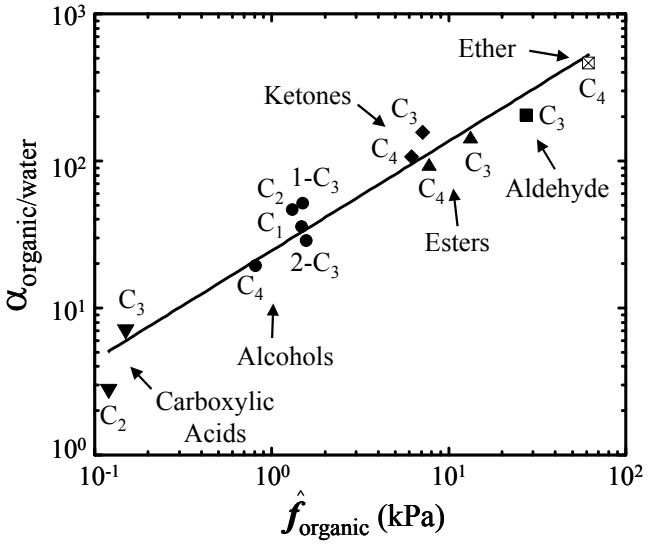

Figure 1: Organic/water separation factor for pervaporation of 5 wt% organic/water mixtures through a Ge-ZSM-5 membrane at 303 K. The line is fit to the data.

Conclusions

Separation factors for pervaporation of organic/water mixtures through zeolite membranes correlate with the fugacities of the feed components, and this correlation allows qualitative predictions of separation performance. Competitive adsorption coverages, and therefore the driving forces for transport, depend on the feed fugacities.

References

[1] H. Kosslick, V. A. Tuan, R. Fricke, C. Peuker, W. Pilz, and W. Storek, J. Phys. Chem., (1993) 97, 5678.

[2] M. Nomura, T. Yamaguchi, and S.-I. Nakao, J. Membr. Sci., (2001)187, 203.

Zeolite Membrane for Dehydration of Biomass Alcohol : Contribution to Mitigation of Global Warming

Shinichi Ichikawa*, Satoru Tanaka, Takashi Nakane, Masanobu Aizawa, Kiminori Sato, Takehito Mizuno, Hiroyuki Chida.
Bio Nanotec Research Institute, Inc., 3-42-3 Nihonbashi Hamacho,Tokyo,Japan. s-ichikawa@BNRI.co.jp

Introduction

The use of biomass alcohol is actively planned worldwide as one of the most viable solution to environmental and energy problems in the 21st century.

Let us consider biomass ethanol and its relation to mitigating global warming. Ethanol is produced through fermentation of biomass created by photosynthesis under the sun with carbon dioxide and water that are available in nature. This is then purified to create sufficiently high concentration of ethanol for use as fuel. The ethanol when it is combusted releases CO_2 into the air, but it is reused in the photosynthesis. Thus the carbon-neutral cycle as depicted in Figure 1 provides energy without increase of CO_2 concentration in the atmosphere.

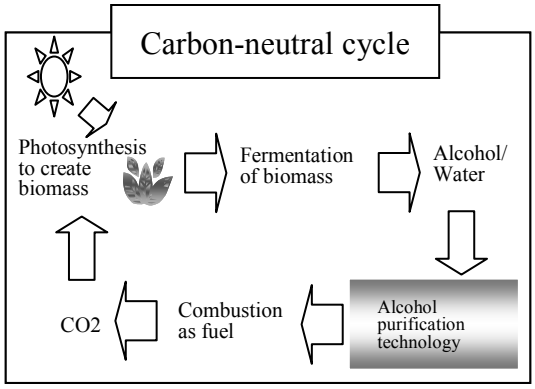

Figure 1. A scheme to mitigate global warming.

Where should we use the ethanol? "Gashol" is one place that has large potential and commercial impact for global contribution where dehydrated ethanol is added to gasoline for automobiles. Suppose half of the 900 million tons of sugarcane produced in the world is applied to biomass ethanol, the effect is extremely large. Implementation of Gashol has already begun in the U.S.A. and in Europe. And the projected increase in ethanol by 2010 is double to triple of the present amount. Meanwhile, Japan needs to decrease CO_2 emission by 6% on average by 2008 to 2012 based on the level of 1990 due to its ratification of the Kyoto protocol. This would be a very difficult goal to meet if not impossible. Introduction of biomass ethanol into the energy source market in Japan would have an immediate effect of 1% reduction in CO_2 emission. This would be the largest contribution by a single approach.

The biomass ethanol produced after fermentation requires purification. This is currently done by a series of distillation which must include azeotropic distillation that is complicated, costly and needs solvents. An alternative approach for the purification process is the zeolite membrane technology.

We have developed a highly efficient zeolite membrane that can provide high purity (more than 99.9 %) ethanol. The membrane system offers simple, safe and less energy-consuming production of ethanol which can be used for automobiles, power plants and elsewhere.

In particular, our zeolite membrane gives much higher flux under pervaporation mode compared to published results on membranes thus far which makes it an universally acceptable technology .

Preparation and Evaluation of Membrane

Zeolites are entering a new era of nanotechnology [1]. The use of zeolites for separation at the molecular level is expected to increase due to their ordered structure in the sub-nanometer range. The zeolite type chosen for the dehydration from ethanol/water mixture is sodium-A which is highly hydrophilic.

The membrane is formed by first introducing seed crystal onto the outer surface of a ceramic tube followed by hydrothermal synthesis. Optimization of every procedure is necessary to create a high performance membrane that is crystalline and continuous without pin holes.

The evaluation of the membrane is done by pervaporation. At the temperature of 75 degree Celsius or lower, the feed mixture (90wt% ethanol / 10wt% water) is introduced to the membrane which preferentially adsorbs and passes water, And the water is pumped by vacuum through the inside opening of the ceramic tube (Figure 2). The weight and components of the liquid permeated are measured and analyzed. The performance of the membrane is expressed as flux Q [Kg/m^2h] and separation factor alpha equal to $(Yi/Yj)/(Xi/Xj)$ where i denotes water and j denotes alcohol, and X denotes feed and Y denotes permeate. Alpha values of 10000 would correspond to about 99.9% purity of ethanol attained.

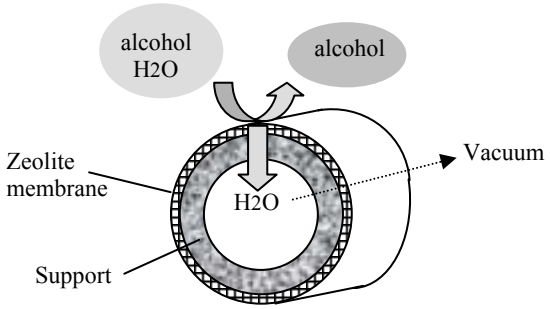

Figure 2. Dehydration of alcohol by pervapration.

Results and Discussion

By the method of pervaporation described above, our newly developed membrane gave redproducible flux of 3.5 [Kg/m^2h]. Also, values as high as 4.0 [Kg/m^2h] could be attained for certain synthesis conditions. The alpha values ranged between 20000 and 40000. These fluxes and separation factors are very high compared to published data on A-zeolite as well as T-,X-, and Y-zeolites which range between roughly 1 to 2 [Kg/m^2h] for the flux and about 10000 maximum for the separation factor [2,3].

Sodium-A type zeolite has a relatively low ratio of Si to Al and the sodium cations are placed in the alpha-cage pores. Therefore the pores are very hydrophilic channel convenient for selective adsorption and transport of water molecules. Also, the alpha-cage is such that it can pass water molecules but not ethanol molecules, thus functioning as a molecular sieve as well.

The X-ray diffraction of the film in its supported form without destruction was measured and only the peaks for A-type zeolite were detected as shown in Figure 3. The crystalline film is so thin that the peak intensities for the support alumina appeared very large.

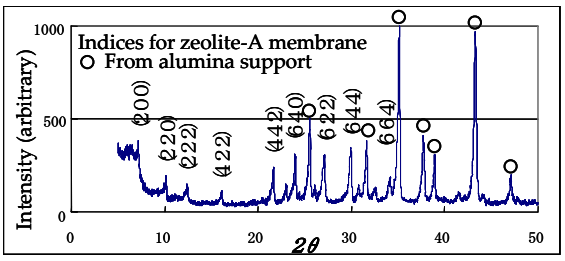

Figure 3. X-ray diffraction pattern.

Analyses of our high-performance membrane by SEM (Scanning Electron Microscopy) from low to high magnification observed perpendicular to the film as well as at its cross section indicated that Na-A zeolite crystal is densely intergrown and forms a continuous thin film.

On the other hand, membranes showing poor performance in terms of flux and separation had problems characterized by existence of amorphous phase, pinholes or cracks in the film or the thickness was too large.

HRTEM (High Resolution Electron Microscopy) showed some interesting features suggesting a kind of ordered interface between crystalline domains in addition to direct observation of the alpha-cage itself. There is no clear indication so far of grain boundary suggesting participation of molecular sieving in that region. Further studies with HRTEM and FIB-STEM (Focused Ion Beam – Scanning Transmission Electron Microscopy) are pursued to understand the relation between the physical structure of the film and its membrane characteristics.

The mechanism of water transport in the pores is difficult to understand while some simple models for gas diffusion have been reported in the past. Suggestions are made for further studies at the molecular level.

Conclusions

We have developed a sodium-A zeolite membrane with high flux and high separation factor for dehydration of ethanol/water mixture. The membrane is a densely intergrown crystalline thin film. The supported membrane elements are integrated into a module to form a total system which takes in biomass ethanol and delivers out purified ethanol. Demonstration and commercial systems are now available for testing and on-site operation.

In addition to biomass alcohol, a wide range of research has started where new types of zeolite membrane are developed for application to liquid and gas separation under mild or extreme operational conditions which use have large impact on improving or completely changing the approach to chemical processes in industry.

Lastly, we would like to thank Dr.Ryu for sample preparation and for taking the bright-field images by HRTEM and also to Professor Terasaki and Professor Ohsuna for their advice, all at Tohoku University.

References

(1) Davis, M. E., Nature, **2002**, 417, 813.
(2) Okamoto, K.; Kita, H.; Horii, K.; Tanaka, K.; Kondo, M. Ind. Eng. Chem. Res., **2001**, 40, 163.
(3) Kita, H. Kagaku Kogyo, **2002**, 53, 704.